Towards Defining Mechanisms involved in β-Lactam Resistance using Serial Crystallography



Anka Lucic

St. Cross College, University of Oxford

Hilary Term 2021

A Thesis Submitted to the Board of the Faculty of Physical Sciences of the University of Oxford in Partial Fulfilment of the Requirements for the Degree of Doctor of Philosophy

Acknowledgments

Like all scientific research, the work in this thesis would not have been possible without the love, help and support of many people. I would like to thank Chris and Allen for offering me the opportunity to work on such a fascinating project and Charlotte and Garrett for accepting unto the SABS CDT. I am eternally grateful to Thomas, Mike, Ian, Chris Lohans, Adam, Zahn, Jenny and Jürgen for assisting me in navigating the Schofield lab at the start of my DPhil. Both myself and the lab equipment appreciate this guidance. My thanks to Pierre, Agata, Robin, Danny, Ibrahim, Selena and all those at Diamond Light Source who regularly stayed through the night to assist us with data collection.

This project was a huge collaborative effort which would not have been possible without assistance from Tika, Alen, Anete, Phil, Cat, Gareth, Karina, Jos and Patrick. Jim Spencer and his group were vital in helping us expand our understanding of faropenem hydrolysis. My thanks to Peter Trapencieris and his group who synthesised bicyclic boronate **3** and were very generous with their help. Our XFEL beamtimes at LCLS, SACLA and EuXFEL would not have been possible without Jan Kern, Aaron Brewster, Franklin Fuller, Anton Barty, Lois Pollack and their respective groups; a big thanks to them and the countless people who help manage and operate these XFELs on a daily basis.

The friendships I have made during my time at Oxford have truly made my time here unforgettable. Joanna, Leah, Karen, Grace, Chiara, Ben, Marcin, Ollie and Bhaskar, you made day to day life in the lab a greatly rewarding experience. My thanks to all my friends from St. Cross College and the DTC with whom I have made some fantastic memories over the years. Andy, Priya, Justina, TMB and many others deserve all my thanks for supporting me and proofreading this thesis multiple times. Last but by no means least I would like to thank my cat Pushkin, my parents, Maria and Ivan, and my brother Lazar for their unconditional love and support, which helped guide me throughout these four years.

Abstract

Antimicrobial resistance is one of the biggest threats to contemporary medicine, with an increasing number of bacteria showing multi-drug resistance. Bacteria have developed mechanisms to survive β-lactam antibiotic treatment, including by the production of β-lactamases (BLs). BLs hydrolyse the β-lactam ring of vital antibiotics, including penicillins and carbapenems, the latter often described as a "last resort" antibiotic. As described in the Introduction, BLs are divided into two mechanistic groups: serine-β-lactamases, which use a nucleophilic serine to hydrolyse β-lactams (SBLs) and metallo-β-lactamases (MBLs), which use one or two zinc ions to aid hydrolysis. My work focussed on understanding the mechanism by which the MBL Verona Integron metallo-β-lactamase 2 (VIM-2) hydrolyses carbapenems using conventional and serial crystallographic methods.

Chapter 2 describes crystallographic, NMR and kinetic studies on VIM-2 and other MBLs and SBLs. Structures of faropenem complexed with VIM-2, the MBL L1 and the SBL KPC-2 (with the University of Bristol) show all three BLs hydrolyse faropenem, with VIM-2 and KPC-2 opening the tetrahydrofuran (THF) side chain. These observations were confirmed by NMR studies, although these also showed that L1 opens the THF ring in solution. Both tautomerisation of the nascent product (enamine to imine) along with epimerisation at the ring junction position were observed. Crystallographic and solution studies with VIM-2 and biapenem indicated the presence of several products, with both imine and enamine complexes being observed at the active site.

The work of Chapters 3 and 4 focused on serial crystallographic studies with penicillin binding protein 5 (PBP5) and VIM-2. The aim with VIM-2 was to perform time resolved crystallography using an X-Ray Free Electron Laser (XFEL) to capture the reaction intermediates during carbapenem hydrolysis. PBP5 was initially used to compare and contrast different sample delivery methods for XFEL analyses as it was easier to produce in larger quantities. Multiple resting state datasets of PBP5 and VIM-2 were collected, both at XFELs and at Diamond Light Source using serial data collection; however, no time resolved structures were captured with VIM-2 and the carbapenem ertapenem. A structure of PBP5 in the format of an acyl-enzyme complex with ertapenem was captured, at 2.9 Å resolution. The XFEL studies indicated that VIM-2 is a good candidate for time resolved studies, however, new crystallisation conditions are needed to visualise structural intermediates.

Chapter 5 describes structural and solution studies with VIM-2 and three bicyclic boronates, one with a thioether side chain which is a potent, broad spectrum inhibitor of SBLs and MBLs, and two with a sulfonamide type side chain.

Overall, the studies performed in this thesis expand our understanding of how VIM-2 hydrolyses carbapenems and penems and of how to potently inhibit a broad range of BLs, including by boronates which are a promising clinically relevant inhibitor class.

Table of Contents

Acknowledgments ..... *ii*

Abstract ..... *iii*

List of Abbreviations *1*

Chapter 1 - Introduction *4*

Penicillins and other β-lactams **4**

Penicillin and Penicillin Binding Proteins 7

Structure and Function of PBPs: Low vs High Molecular Weight 9

The Rise of Antibiotic Resistance and Resistance Mechanisms 11

β-Lactamases: How do they work? **13**

Metallo-β-lactamases (MBLs) 16

Serine-β-lactamase vs Metallo-β-lactamase Mechanism 19

Comparison of B1 Structures 21

Verona Integron Metallo-β-lactamases (VIMs) 22

Categorising VIMs 23

Inhibitors of β-lactamases **24**

The Development of Bicyclic Boronates 26

Serial Crystallography and XFELs **30**

How do XFELs work? 33

Reaction Initiation 34

Sample Delivery Methods at XFELs 35

Aims *39*

References **39**

Chapter 2 – Biophysical and biochemical studies on the β-lactamase catalysed hydrolysis of Faropenem and Biapenem 55

Abstract 55

Introduction 55

Materials and Methods 63

Transformation and Starter Culture 63

VIM-2 Protein Production 64

VIM-2 Nickel Affinity Purification 64

VIM-2 Gel Filtration Purification 65

His tag Cleavage and Reverse IMAC purification 66

Crystallisation of VIM-2 66

Data Collections at Synchrotrons 69

Soaking Compounds into Crystals and Data Collection 71

Data Processing and Refinement 72

PDB Deposition 75

NMR Studies 75

Kinetics Experiments 76

Results 77

Protein Production and Purification 77

Crystallisation of VIM-2 78

Data Collection and Soaking 79

Faropenem Kinetic Assays 81

Faropenem Datasets and Crystallography 82

Biapenem Kinetic Assays 98

Biapenem Crystallography Dataset 100

Biapenem NMR Data 105

Conclusions 108

References **113**

Chapter 3 – Testing XFEL sample delivery methods with PBP5 ..... ***122***

Abstract **122**

Introduction **122**

Materials and Methods **125**

Protein Production 125

Protein Purification 126

Broad Screen Crystallisation Trials 126

Macrocrystal Optimisation 127

Seeding Crystals 130

Batch Crystallisation Trials 130

Gel Extruder Data Collection at I24 131

Crystallisation of PBP5 Cysteine C- Terminal Variant at LCLS 133

Data Collection at LCLS 133

Sample Delivery at LCLS 134

Gel Extruder Data Collection of PBP5 wildtype at VMXi 134

Fixed Target Data Collection of PBP5 Cysteine Variant at I24 135

Macrocrystallisation of PBP5 with Ertapenem 137

Data Collection and Processing of PBP5 Macrocrystals with Ertapenem 139

Batch Method Optimisation of PBP5: Ertapenem Microcrystals 139

Data Processing of Serial Crystallographic Data 139

Results **141**

PBP5 Crystallisation 141

PBP5 Resting State Serial Data Collection at Diamond Light Source 143

LCLS Data Collection 145

Resting State Structure Comparison 147

PBP5: Ertapenem Macrocrystal Datasets 151

PBP5: Ertapenem Microcrystal Datasets 154

Conclusions **160**

References **163**

Chapter 4 – XFEL experiments using VIM-2 ..... ***169***

Abstract **169**

Introduction **169**

Materials and Methods **171**

Recombinant VIM-2 Production and Purification 171

VIM-2 Crystallisation 171

Batch Crystallisation of VIM-2 172

Broad Screening VIM-2 172

Fixed Target Data Collection 173

Data Collection at EuXFEL 173

Data Processing at EuXFEL using CrystFEL 175

OnDA and Cheetah-Real Time Data Analysis 177

Sample Delivery at EuXFEL 179

Data Collection at SACLA 180

Sample Delivery at SACLA 181

Data Collection and Processing at SACLA 182

Results **183**

VIM-2 Purification and Crystallisation 183

Batch Crystallisation of VIM-2 186

VIM-2 Fixed Target Data Collection 187

VIM-2 Data Collection at EuXFEL 190

Data Collection at SACLA 193

VIM-2 Data Collection at SACLA 194

Conclusions **198**

References **201**

Chapter 5 – Studies on Bicyclic Boronate Inhibitors with VIM-2 ..... ***206***

Abstract **206**

Introduction **206**

Materials and Methods **210**

Synthesis 210

Protein Production and Purification 210

VIM-2 Crystallisation 210

VIM-2 Data Collection and Refinement 211

Kinetic Studies 212

MIC Experiments 213

Results **214**

Synthesis of boronates 3, AK4 and AK110 214

Kinetics 214

Microbiology 216

Crystallisation 217

Conclusions **227**

References **230**

Chapter 6 - Discussion and Future Work ***236***

Carbapenems and Penems **236**

XFELs and Serial crystallography **243**

Future work **246**

References **254**

Appendix 260

List of Abbreviations

2TY: 2x Tryptone Yeast Extract

ADE: Acoustic Droplet Ejection

AGIPD: Adaptive Gain Integrating Pixel Detector

BJP: *Bradyrhizobium japonicum* β-lactamase

BL: β-lactamases

CCD: Charge coupled device

CCP4: Collaborative Computational Project 4

cctbx: Computational Crystallography Toolbox

CLSI: Clinical and Laboratory Standards Institute

Co-MESH: Concentric Mesh

COSY: Correlated Spectroscopy

COOT: Crystallographic Object Orientated Software

CTX-M: Cefotaxime β-lactamase

E. coli: *Escherichia coli*

DAQ: Data Acquisition System

DHP-1: Dihydropeptidase 1

DMM: Double Multilayer Monochromator

EDTA: Ethylenediaminetetraacetic acid

eLBOW: electronic Ligand Builder and Optimization Workbench

ESBL: Extended serine-β-lactamase

EuXFEL: European X-Ray Free Electron Laser

GDVN: Gas Dynamic Virtual Nozzle

GUI: Graphic User Interface

HEPES: 4-2-Hydroxyethyl 1 piperazineethyanesulfonic acid

HSQC: Heteronuclear Single Quantum Coherence

IC_{50}: Inhibitory Concentration

IMAC: Inhibitory Metal Affinity Chromatography

IMP: Imipenemase

KPC: *Klebsiella pneumoniae* carbapenemase

LB: Lysogeny broth

LCLS: Linac Coherent Light Source

LCP: Lipid Cubic Phase

Ldt: L, D transpeptidase

LLG: Log Likelihood Gain

MBL: Metallo-β-lactamase

MFX: Macromolecular Femtosecond Crystallography

MIC: Minimum Inhibitory Concentration

MLRF: Maximum Likelihood Rotation Function

MPI: Message Passing Interface

NDM: New Delhi Metallo-β-lactamase

NMR: Nuclear Magnetic Resonance

OD: Optical Density

OXA: Oxacillinase

ONDA: Online Data Analysis

PALFEL: Pohang Accelerator Laboratory XFEL

PBP: Penicillin Binding Protein

PDB: Protein Data Bank

PEG: Polyethylene glycol

PYP: Photoactive Yellow Protein

RMSD: Root Means Squared Deviation

SACLA: Spring 8 Angstrom Compact Free Electron Laser

SAR: Structure Activity Relationship

SASE: Self Amplified Spontaneous Emission

SBL: Serine-β-Lactamase

SEC: Size Exclusion Chromatography

SFC: *Serratia fonticala Carbapenemase*

SFX: Serial Femtosecond Crystallography

SHINE: Shanghai High Repetition Rate XFEL

SHV: Sulfhydryl Variable β-lactamase

SLAC: Stanford Linear Accelerator Center

SMB: Serratia Metallo-β-lactamase

SOC: Super Optimal broth with Cabolite repression

SPM: São Paulo Metallo-β-Lactamase

SSX: Serial Synchrotron Crystallography

SWISSFEL: Swiss XFEL

TEM: Temoniera β-Lactamase

TFZ: Translation Function Z

THF: Tetrahydrofuran

TLS: Translation Liberation Screw

TOCSY: Total Correlated Spectroscopy

trSFX: time resolved Serial Femtosecond Crystallography

UTI: Urinary Tract Infection

VIM: Verona Integron Metallo- β-Lactamase

VMXi: Versatile Macromolecular Xtallography *in situ*

XFEL: X-Ray Free Electron Laser(s)

Chapter 1 - Introduction

The first isolated antibiotic, at least in modern times, was known as salvarsan, which was used to treat syphilis.[1] Salvarsan was developed in 1910 and was the output of the first screening programme for the purposes of drug discovery using synthetic compounds. In 1932 came the discovery and development of the sulfonamides, the first broad spectrum antimicrobials suitable for clinical use.[2] However, it was the observation of the activity of penicillin by Alexander Fleming in 1928, followed by the efforts Norman Heatley and others at the University of Oxford, that led to the rise of broad spectrum antimicrobials which were readily available to the public.[3,4] Dorothy Hodgkin validated the proposal by Edward Abraham that penicillin contains the now famous four membered β-lactam ring.[5] Since the discovery of penicillin in the early 20th century, β-lactams have risen to be the most widely used class of broad spectrum antibiotics to this day.[6]

Penicillins and other β-lactams

It is thought that all β-lactams use the same molecular mechanism to kill bacteria, i.e. they mimic the D-Ala-D-Ala moiety (or equivalent) in the cell wall peptidoglycan substrate of penicillin binding proteins (PBPs) and reacts with a nucleophilic serine in the PBP active site (**Figure 1B**) (PBPs)[7] to form a stable acyl-enzyme complex, so inhibiting the PBPs and hence cell wall biosynthesis.

To improve on the potency and activity spectrum of the penicillins, new β-lactam subclasses were developed, including the cephalosporins, monobactams and carbapenems, the latter of which are often described as the "last resort" antibiotics.[8] The different β-lactam subclasses all contain the same four membered β-lactam ring with various five or six membered rings attached to it, except for the monocyclic monobactams (**Figure 1A**). The originally isolated penicillins and cephalosporins are naturally produced β-lactams from fungi, such as *Penicillium* and *Acremonium*, though they are also produced by some bacteria.[9] Later, new derivatives of penicillins and cephalosporins were developed

with enhanced potency and β-lactamase resistance. Carbapenems are based off of the compound thienamycin, a natural product from *Streptomyces cattleya*.[10] The first synthetic carbapenems were first developed in 1976.[8]

Carbapenems are amongst the most broad spectrum of the β-lactam antibiotics and inhibit the activity of many β-lactamases, which is why they are known as the "last resort" antibiotics.[8,10] Due in part to adverse side effects, such as seizures, carbapenems and the related penems are rarely used to treat mild bacterial infections.[11] Penems are very similar in chemical structure and activity to the carbapenems, except that they have a thiazoline ring attached to the β-lactam ring instead of the pyrroline ring observed in carbapenems (**Figure 1A**).[12] The penems are synthetic compounds that combine the properties of cephalosporins and penicillins by producing a compound with a five membered ring annealed to the β-lactam with a double bond conjugated with the β-lactam nitrogen.[12–14]

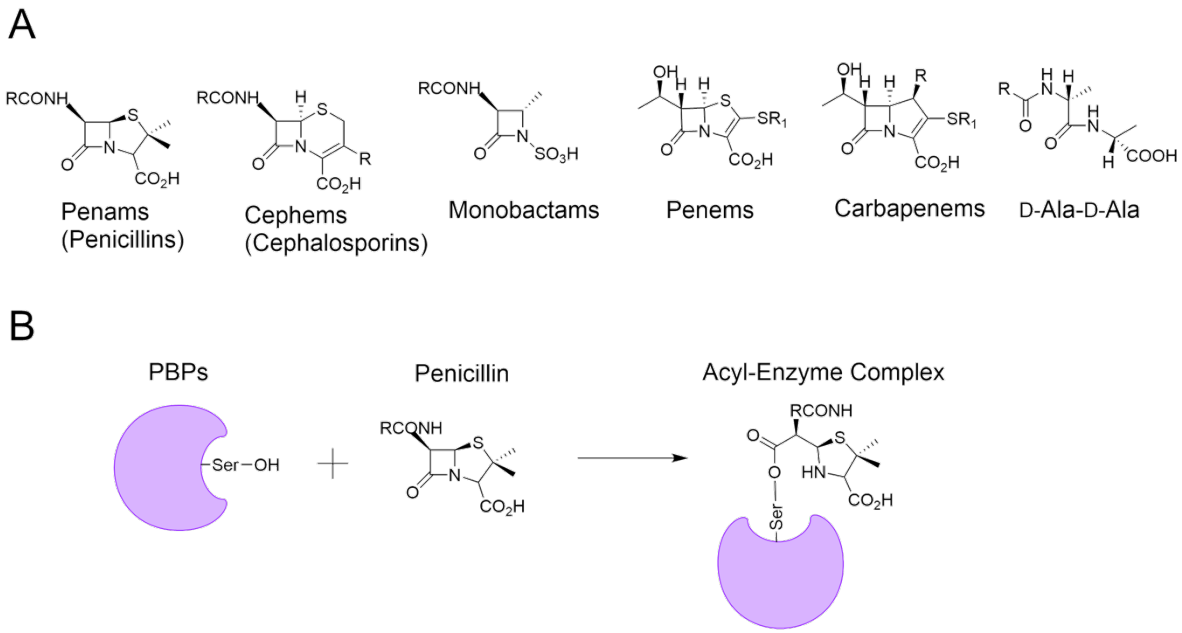


Figure 1: Different classes of clinically used β-lactams and their mechanism. A) The different sub-classes of β-lactams and the typical D-Ala-D-Ala PBP substrate. Note the similarity between the substrate and the β-lactam inhibitors. The β-lactam ring creates strain in the structure, making it more susceptible to nucleophilic attack compared to a normal amide. Addition of a second fused ring further increases the strain, which is likely in part why most clinical β-lactams antibiotics have a fused five or six membered ring.[18] B) A simplified diagram of how penicillins inhibit the activity of PBPs in bacterial cell walls.

Most of the β-lactams were developed during the golden age of antibiotics, which occurred between the 1950s and 1970s. Other non β-lactam drugs were also developed during this time such as cycloserines and ribosome targeting drugs.[15] It was also during the golden age of antibiotics that methicillin resistant *Staphylococcus aureus* (MRSA) started to appear, along with a general increase in the presence of multi resistance bacteria, even though bacteria capable of inactivating penicillin had been observed much earlier.[5,16]

Penicillin and Penicillin Binding Proteins

Bacteria are characterised as either being Gram-positive or Gram-negative, terminology used to describe differences that can be found in the cell wall structure of bacteria.[17] This nomenclature comes from the test used to differentiate the two groups of bacteria; where the bacteria are stained with Gram stain. The absorbance of the stain depends on the structure of the bacterial cell wall, with Gram-positive bacteria retaining the dye unlike Gram-negative bacteria.[17] Bacteria that are classified as Gram-positive have a peptidoglycan outer layer, a periplasmic space in between and a plasma membrane in the inner layer. Examples of Gram-positive bacteria include *Streptococcus pneumoniae* and *Bacillus cereus*. On the other hand, Gram-negative bacteria have an additional outer membrane referred to as the lipopolysaccharide layer; they include bacteria such as *Pseudomonas* and *Salmonella spp.* (**Figure 2**).

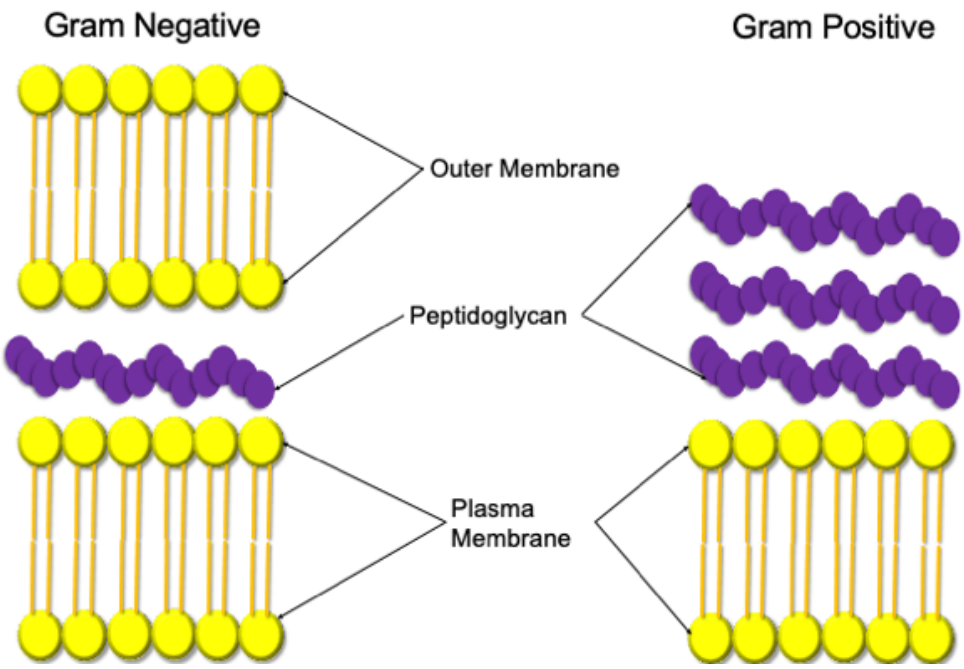


Figure 2: Diagram showing a comparison of Gram-positive vs Gram-negative bacteria. Note the extra outer membrane layer present in Gram-negative bacteria and the thicker peptidoglycan in Gram-positive bacteria.

PBPs are transpeptidase enzymes that play a key role in bacteria, since they catalyse part of the last steps of peptidoglycan biosynthesis. Peptidoglycans are vital for bacterial survival and are a key part of the bacterial cell wall, both in Gram-positive and Gram-negative bacteria (**Figure 2**).[19] All bacteria have transpeptidases/PBPs with many having more than one type. *Mycobacterium tuberculosis* for instance, has both PBPs and another class of transpeptidases known as L,D-transpeptidases (Ldts).[20,21]Despite not having a nucleophilic serine, instead employing an analogous cysteine, the Ldts are still inhibited by certain β-lactam antibiotics.[22]

The number of PBPs present varies with different species of bacteria; *E. coli* have 12 classes of PBPs.[7] These vary in molecular weight, with PBP1 being the highest molecular weight and PBP12 being the lowest.[23] High molecular weight PBPs are large, multi-domain proteins that are involved in peptidoglycan insertion into the cell wall by catalysing transpeptidase reactions.[24] They are also thought to have a role in cell morphology, with their respective knockouts showing dramatic differences in cell shape and size.[25] These high molecular weight PBPs tend to be partly hydrophobic on their surface, due to their association with the cell membrane. Most of these PBPs have two domains that are joined together by a β-strand rich linker region, alongside a cytoplasmic tail and a transmembrane anchor (**Figure 3**).[26]

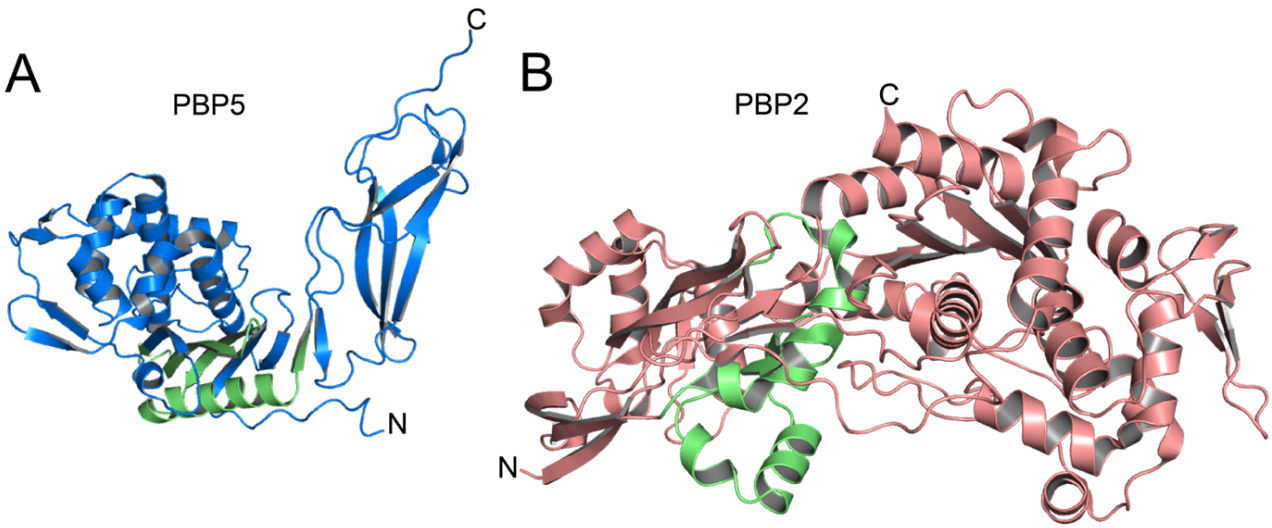


Figure 3: **Comparing a low and a high molecular weight PBP**. A) shows a view of a crystal structure of PBP5 from *E. coli* (5J8X[27]) which is a low molecular weight carboxypeptidase PBP (42kDa). B) shows a view of PBP2 from *E.coli* PBP2 (6G9P[28]) clearly contains a rich β-strand linker region between its two domains, whereas PBP5 only consists of two relatively small subdomains. The figure was made using Pymol.[29]

Structure and Function of PBPs: Low vs High Molecular Weight

Most PBPs have DD-peptidase activity with some being carboxypeptidases.[26] The DD-peptidase reaction follows an established three step outline mechanism. The first step involves the formation of a non-covalent complex between the enzyme and the peptidoglycan peptide (-L-Ala-γ-D-Glu-Ala or -L-Lys-D-Ala-D-Ala). Next, the nucleophilic serine in the active site attacks the carbonyl carbon of the D-Ala-D-Ala peptide bond forming an acyl-enzyme intermediate with the release of the C-terminal D-Ala (**Figure 4**). The final step in the reaction either involves the release of the hydrolysis product in the case of the carboxypeptidases, or the cross linking with another peptidoglycan strand in the case of the transpeptidases.[23]

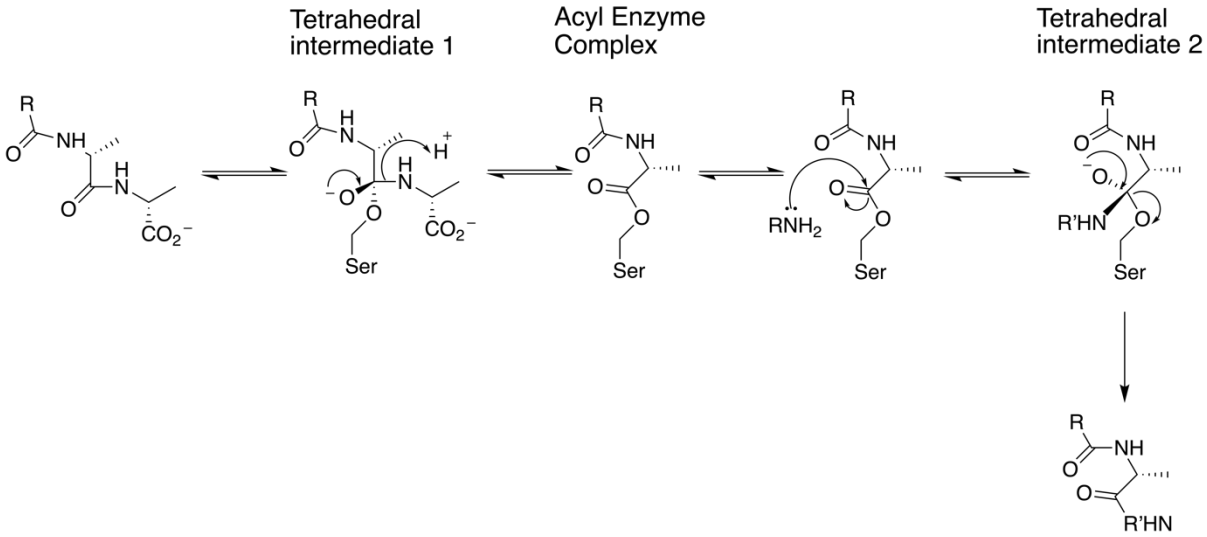


Figure 4: Simplified scheme of a transpeptidase mechanism. Note the formation of the tetrahedral intermediates, which are also seen with the very initial binding of β-lactams to PBPs.[26]

The transpeptidase reaction with PBPs is catalysed by the Penicillin Binding (PB) or N-terminal domain, with the residues in the PBP active site being conserved across the PBP family. The nucleophilic serine is positioned on the α2 helix and is typically followed by a lysine, giving a SXXK motif.[23] This domain is made up of two subdomains, the first having a five stranded β-sheet fold which is surrounded by three α-helices; the second is an all helical domain (**Figure 5**). The active site is located between these two domains.[23]

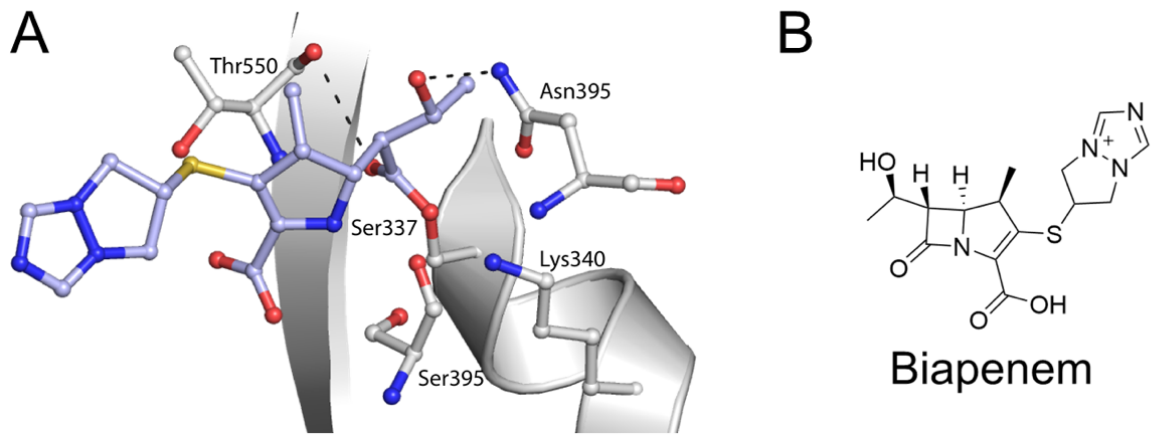


Figure 5: View of PBP2x active site (PDB 2ZC3[30]) complexed with a biapenem derived product. Like all PBPs the active site contains a SXXK motif and several other polar residues which interact with the substrate. The structure shown on the right is biapenem.[29]

In this thesis, PBP5 was used to study the mechanism of β-lactams and XFEL sample delivery methods. It is considered important to study a range of PBPs in order to develop broad spectrum, effective antimicrobial therapeutics. PBP5 is a low molecular weight PBP (~42kDa).[31] Like most other low molecular weight PBPs, PBP5 is made up of two domains; its N-terminal domain which binds to substrate and β-lactams, which has a mainly α-helical structure, and its C-terminal domain that interacts with the cytoplasmic membrane which mostly consists of β-sheets (**Figure 3**). PBP5 is a carboxypeptidase, having no transpeptidase activity and clearly plays a large role in cell morphology, with PBP5 knockouts showing alterations in cell shape.[32]

The Rise of Antibiotic Resistance and Resistance Mechanisms

Despite their effectiveness, antimicrobial resistance against β-lactams is a growing threat in modern medicine. So-called superbugs such as MRSA, *Pseudomonas* and *Enterobacter*[33] have become a massive challenge to overcome, especially in environments such as hospitals where patients are more vulnerable to secondary infections. This has also made it increasingly harder to treat previously treatable diseases. Tuberculosis, for instance, which was once relatively treatable with standard

antibiotics such as streptomycin[34] (though, normally, not β-lactams) has become extremely difficult to treat, with many strains of *Mycobacterium tuberculosis* showing multi drug resistance.[34,35]

At the societal level, there are several different causes for the increase in antibiotic resistance, one being over use and misuse of antibiotics, with billions of doses per year worldwide being prescibed.[36] Overuse in agriculture is another problem, with many farming practices relying heavily on antibiotic treatment of farming products.[36] These and other factors have promoted widespread antibiotic resistance particularly in developing countries, or in places where there is a high volume of sick people, leading to a high mortality rate. It has been proposed that by 2050, 10 million people could die from antibiotic resistance if nothing is done to tackle antimicrobial resistance.[37]

At the molecular level, bacteria have developed multiple mechanisms of resistance over many years.[38] These include the acquisition and increased expression of efflux pumps that remove antimicrobial agents from the cell;[39] thicker cell walls can make it harder for antibiotics to enter the bacteria cytoplasm and periplasm.[40] Another mechanism of resistance involves overproduction of PBPs and other transpeptidase enzymes to decrease the effects of β-lactam inhibition.[41,42] Decreased porin expression has also led to a decreased antibiotic uptake in bacteria.[43] However, the most prevalent method of β-lactam resistance, is mediated *via* β-lactamases, which hydrolyse the β-lactam ring, so inactivating penicillins and related β-lactam antibiotics.[44] Before the use of antibiotics, β-lactamases had probably existed as a survival mechanism for billions of years; however, the transfer of plasmids expressing β-lactamases into other microbes is leading to an increase in multi drug resistant bacteria. β-Lactamases can be subdivided into two main mechanistic groups: the serine-β-lactamases (SBLs) and metallo-β-lactamases (MBLs).[44]

β-Lactamases: How do they work?

Likely because they initially evolved from PBPs, the SBLs have a similar overall fold consisting of the same two domains as PBPs and a nucleophilic serine which also forms an acyl-enzyme complex (**Figures 6-8**).[45] SBLs are likely ancient enzymes, having been produced by bacteria for several billions of years.[45] Serine-β-lactamases, can be split into three different Ambler classes:[44] A, C and D, with each group preferentially hydrolysing different classes of β-lactams. Through selection SBLs appear to have evolved compared to PBPs, since they can hydrolyse β-lactams by forming a hydrolytically labile acyl-enzyme complex, then releasing the inactive hydrolysed product (**Figure 6**).[45] Many SBLs have little activity against carbapenems as many evolved before the widespread use of carbapenems, however, there has been an emergence of extended spectrum SBLs (ESBLs) such as OXA-48 that have been shown to hydrolyse carbapenems efficiently.[46]

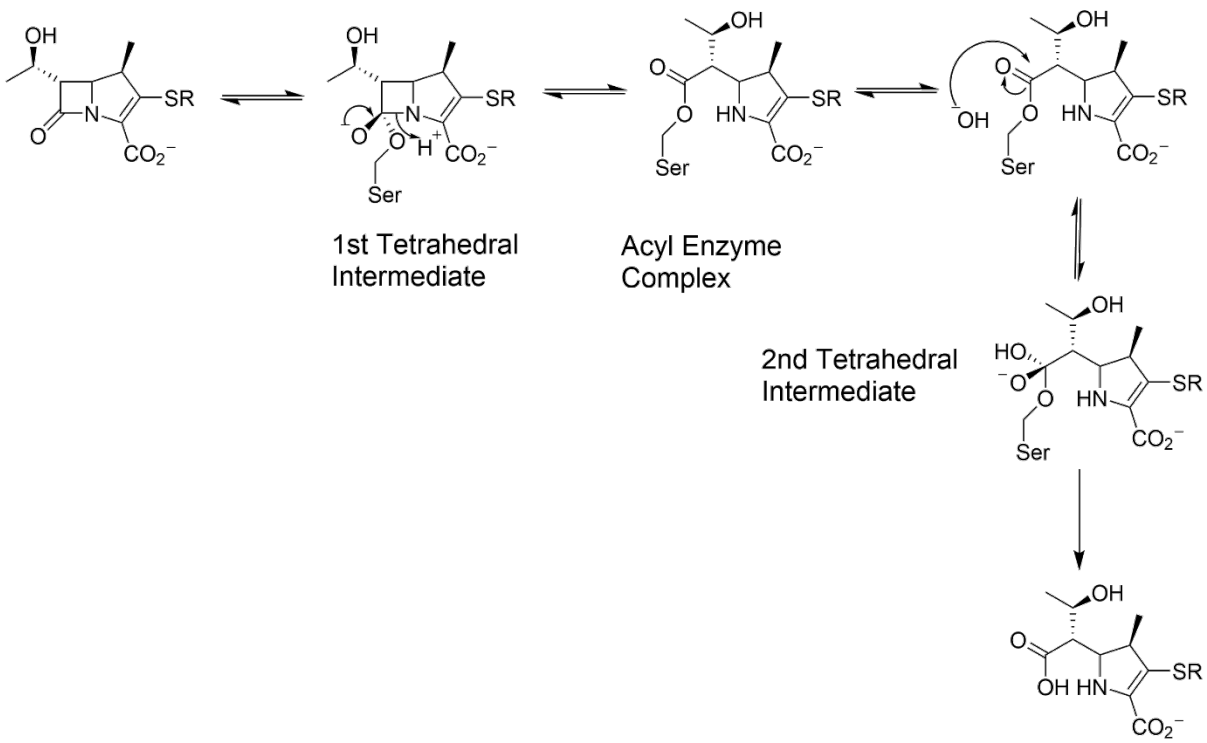


Figure 6: SBL mechanism for hydrolysis. Note, the formation of the 1st tetrahedral intermediate, acyl-enzyme complex and 2nd tetrahedral intermediate; analogous intermediates are present in transpeptidase mechanisms with D-Ala-D-Ala type substrates (**Figure 1**).

Although presently less common than SBLs, the Ambler class B MBLs are a growing clinical threat due to the lack of clinical inhibitors and their endemic spread across several regions.[47,48] The first MBL to be discovered was BcII in 1966 from *Bacillus cereus*.[49] Pioneering work showed that *B. cereus* produced a β-lactamase with cephalosporinase activity.[49] However, the activity was inhibited by the metal chelator Ethylenediaminetetraacetic acid (EDTA), indicating that the enzyme had a different mechanism in comparison to the SBLs and that this mechanism involved the use of metal ions (**Figure 9**).[50]

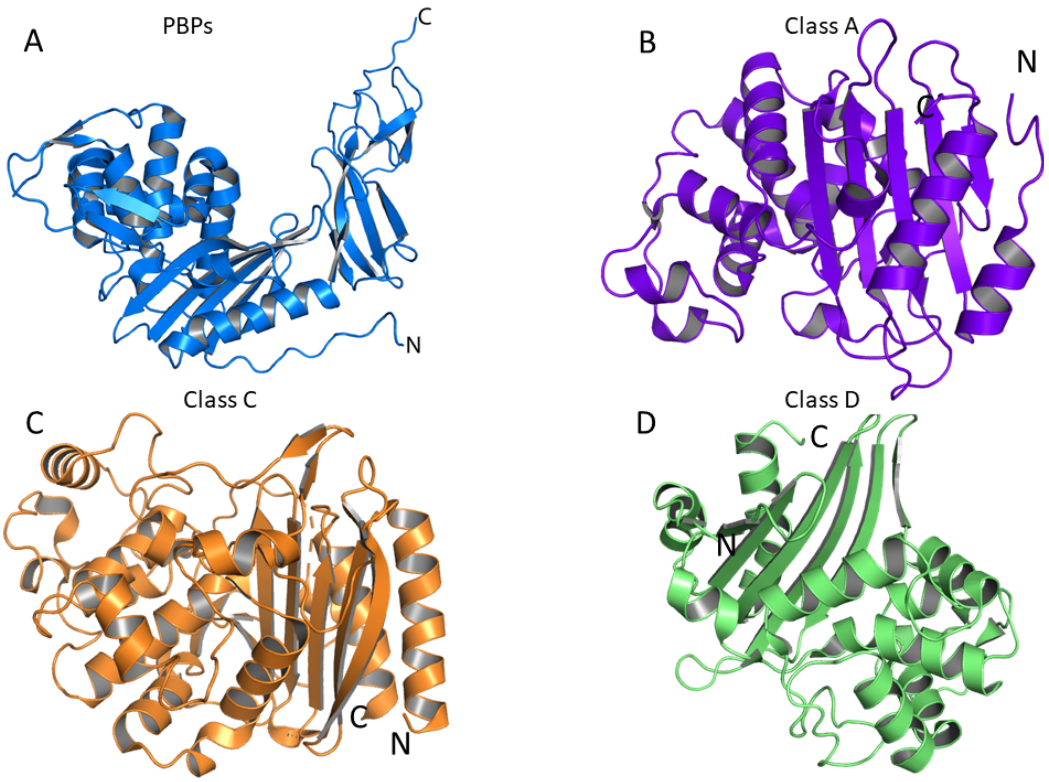


Figure 7: **PBP5 compared to the three different classes of SBLs**. All three SBL Ambler classes have the same PBP binding domain as seen in PBP5 (A PDB: 5J8X[27]). There are variations in the numbers of helices and β-sheets, AmpC (C PDB: 3FKW[51]), for instance, is much more helix rich compared to KPC-3 and OXA-10 (B and D, PDB: 6QWD[52] and 1EWZ[53]).[29]

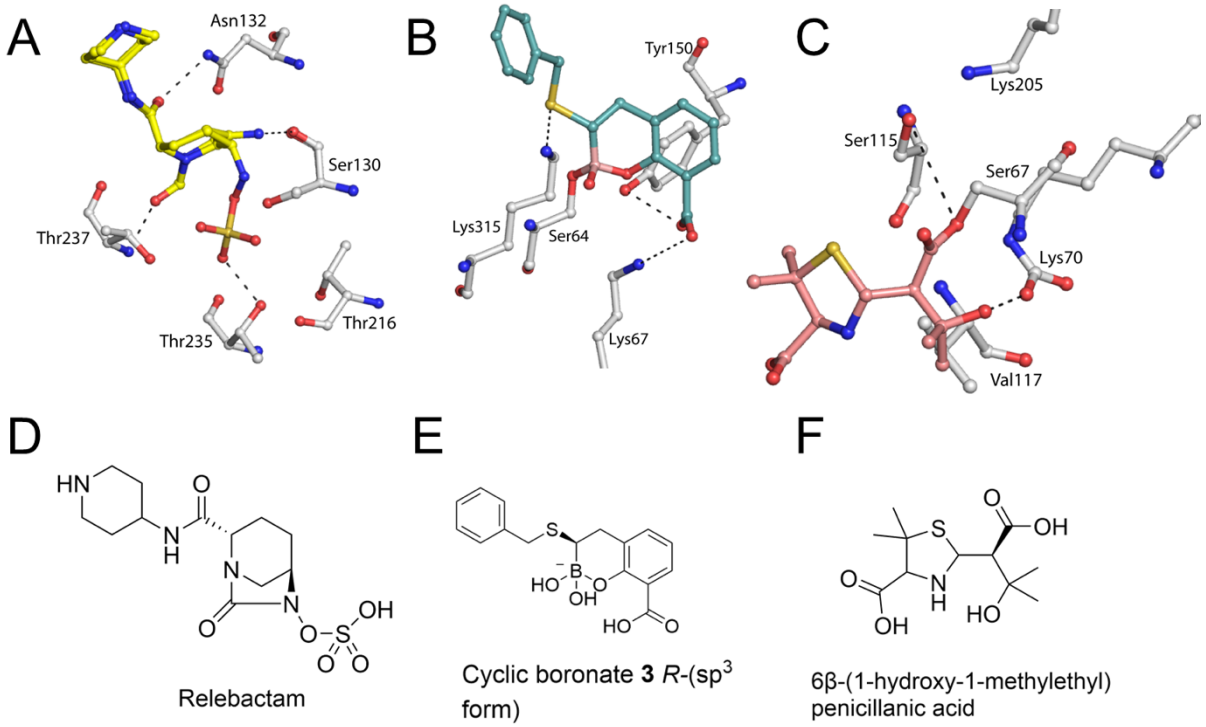


Figure 8: Views from active sites of different classes of SBLs. Views of A) *Klebsiella pneumoniae* 3 (KPC-3) complexed with relebactam (PDB: 6WQA[52]), B) AmpC complexed with bicyclic boronate **3** (PDB: 6YPD[54]) and C) Oxacillinase 10 (OXA10) complexed with a penicillin; note in this case the active site lysine is carbamylated (PDB: 1K54[55]).[29] D, E and F show the ChemDraw structures for relebactam, **3** and penicillanic acid.

No new MBLs were reported for at least 20 years after the discovery of BcII, leading many to believe that these new β-lactamases were clinically irrelevant.[50] After 1980, however, it became clear that MBLs has evolved to play an important role in antimicrobial resistance, with clinically pathogenic bacterial strains of MBLs being found in bacteria such as *Pseudomonas aeruginosa, Aeromonas hydrophila, Serratia marcescens* and *Elizabethkingia meningoseptica*.[50] MBL genes are expressed on either chromosomes or plasmids on mobile gene cassettes.[56] These gene cassettes can be inserted into integrons (Verona Integron metallo-β-lactamases or VIMs) or are bracketed into composite transposons (New Delhi Metallo-β-lactamases or NDMs).[57,58] Both of these are mobile DNA elements meaning that DNA can be moved to different parts of the genome in a single cell. Integrons are genetic

elements that can be integrated and expressed in different plasmids.[59] Integrons enable the movement of genetic material between different bacteria, making MBLs a significantly greater threat than initially thought. Often these mobile gene elements also encode for resistance for non β-lactam antibiotics such as aminoglycosides.[60]

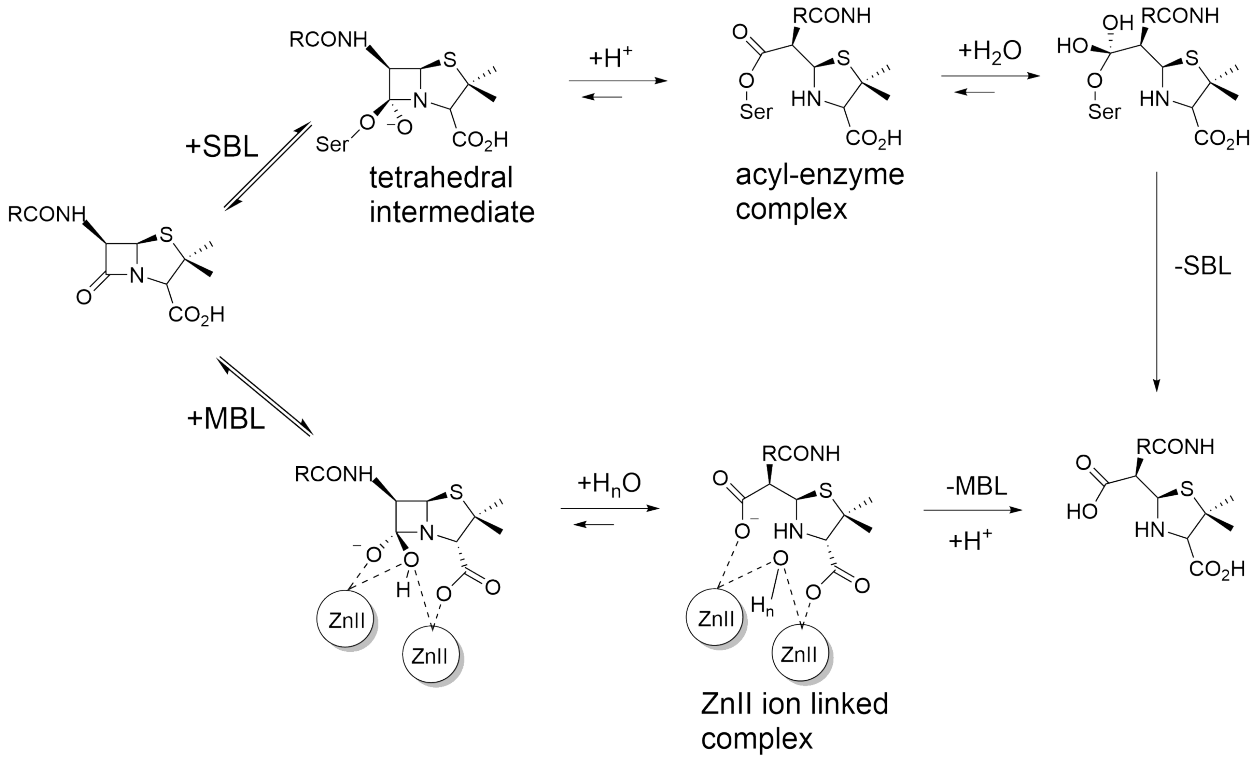


Figure 9: **Simplified diagram comparing outline mechanisms for hydrolysis of a penicillin via metallo and serine-β-lactamases**. Despite the same, or similar, inactive products being formed, the SBLs and MBLs are both structurally and mechanistically distinct. Both mechanisms involve the formation of tetrahedral intermediates; however, the SBLs forms a covalent acyl-enzyme intermediate with the substrate, whereas the MBLs do not.

Metallo-β-lactamases (MBLs)

Unlike SBLs, MBLs likely did not evolve from PBPs, but from a completely different group of enzymes (metallo-hydrolases), making them both structurally and mechanistically different from the SBLs.[60,61] Although not as prevalent as SBLs, MBLs are endemic in several regions of the world.[33,48] MBLs are classified as Ambler Class B β-lactamases and consist of an αβ/βα fold with one or two zinc ions in

their active site (**Figure 10**). The MBL active site is located in a shallow groove between the αβ interface.[60] Despite this, there is often little sequence similarity between different MBLs, with as little as 10% homology between the different MBL types.[62] MBLs can be divided into three subclasses: B1, B2 and B3, which have different affinities towards different β-lactams; the B1 MBLs are the most common and the most clinically relevant.[63]

B1 MBLs include widespread enzymes, such as the NDMs, the VIMs and the São Paulo metallo-β-lactamase (SPMs).[62] They are generally broad spectrum β-lactamases that can even hydrolyse carbapenems but, at least efficiently, not monobactams. They typically (B1 and B3 subclasses) use two zinc ions to hydrolyse the β-lactam ring; the B2 MBLs only use one zinc ion (**Figure 10**).[64] With the B1 MBLs, both the zinc ions both are bound by three different residues; zinc 1 binds to His116, His118 and His196 whereas zinc 2 binds to Asp120, Cys221 and His263 (**Figure 10**).[49] In resting state B1 MBL structures, a water and/or hydroxide ion molecule bridges between the two zinc ions. During the reaction, the Lewis acidity of the first zinc ion (Zn1) activates water for nucleophilic attack of the β-lactam ring. The second zinc ion (Zn2) stabilises the anionic intermediate before the release of the product.[65]

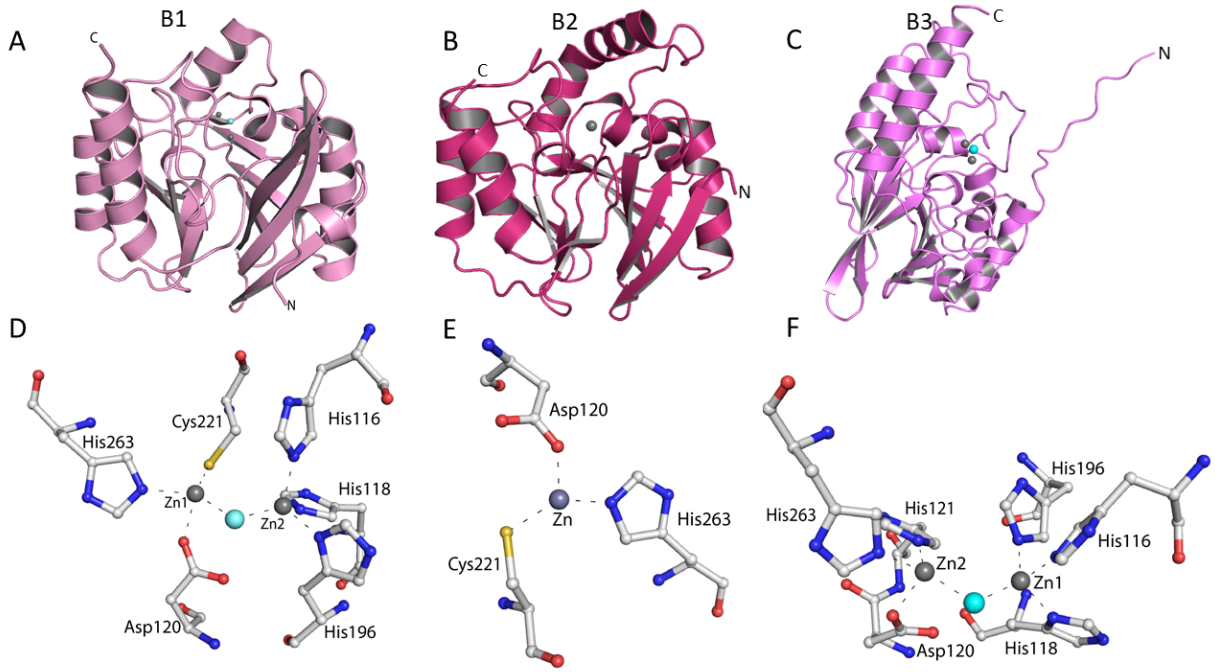


Figure 10: Image comparing structures of the three subclasses of MBLs. A and D show the tertiary structure and the active site of VIM-2 (4BZ3[66]). VIM-2 is a di zinc B1 MBL like the B3 MBL L1 (2QJS[67]), which is shown in C and F, however, VIM-2 uses a cysteine instead of a second histidine to bind Zn2. Both VIM-2 and L1 have a metal bridging water or hydroxide in the active site, which acts as a nucleophile during the hydrolysis of β-lactams. Likely due in part to a mutation in the normal Zn1 binding site, CphA (B and E, PDB 1X8G[64]), a B2 MBL only uses one zinc.[55] All three groups of MBLs have an overall similar αβ/βα fold with stronger homology between the B1 and B2 MBLs compared to the B3 MBLs.[29]

The B2 MBLs are distinctive in that they only have one zinc ion in their active site, since residue 116 is an asparagine not a histidine, resulting in weak or no binding of zinc 1 (**Figure 10**). Furthermore, B2 MBLs, such as CphA, preferentially hydrolyse carbapenems, with only weak activity against penicillins and cephalosporins.[68] B1 and B2 enzymes have a 14-24% sequence homology. The B3 enzymes, such as L1, also have two zinc ions in the active site, however, His121 binds to the second zinc ion, rather than a cysteine as in B1 and B2 MBLs.[61] These enzymes are mostly cephalosporinases and penicillinases with weak activity towards carbapenems. The sequence similarity between MBLs from the three MBL subclasses ranges from 2 to 14%.[69]

Serine-β-lactamase vs Metallo-β-lactamase Mechanism

The SBL or MBL mechanism can vary depending on the β-lactam substrate in question. In penicillin hydrolysis, for instance, analogous hydrolysis products are typically produced for both SBLs and MBLs (**Figure 9**), but this is not always the case. Both the SBL and MBL reaction mechanisms involve the formation of an initial tetrahedral intermediate, but whereas the SBLs form an acyl-enzyme complex and then another SBL tetrahedral intermediate, MBLs form an anionic intermediate before their products are released (**Figure 9**).[70]

Most MBLs and SBLs produce at least two hydrolysis products when hydrolysing carbapenems. Recent work has led to the proposal that the major initial hydrolysis product is an enamine, which can then tautomerise to form an imine with either (*S*) or (*R*) stereochemistry at the C2 position.[71] Class D SBLs, however, have been known to produce a separate type of carbapenem derived product, i.e. the β-lactones, when hydrolysing 1β-methyl substituted carbapenems (**Figure 11**).[72] β-lactone formation involves an attack by an alcohol of the carbapenem hydroxyethyl side chain onto the carbonyl group of the acyl-enzyme complex, i.e. the hydroxyethyl efficiently replaces water as a nucleophile.[72] Like the imine hydrolysis products, the imine lactone also forms epimers at the C2 position (**Figure 11**). It has been shown that the lactone products are capable of inhibiting the activity of SBLs and MBLs.[72]

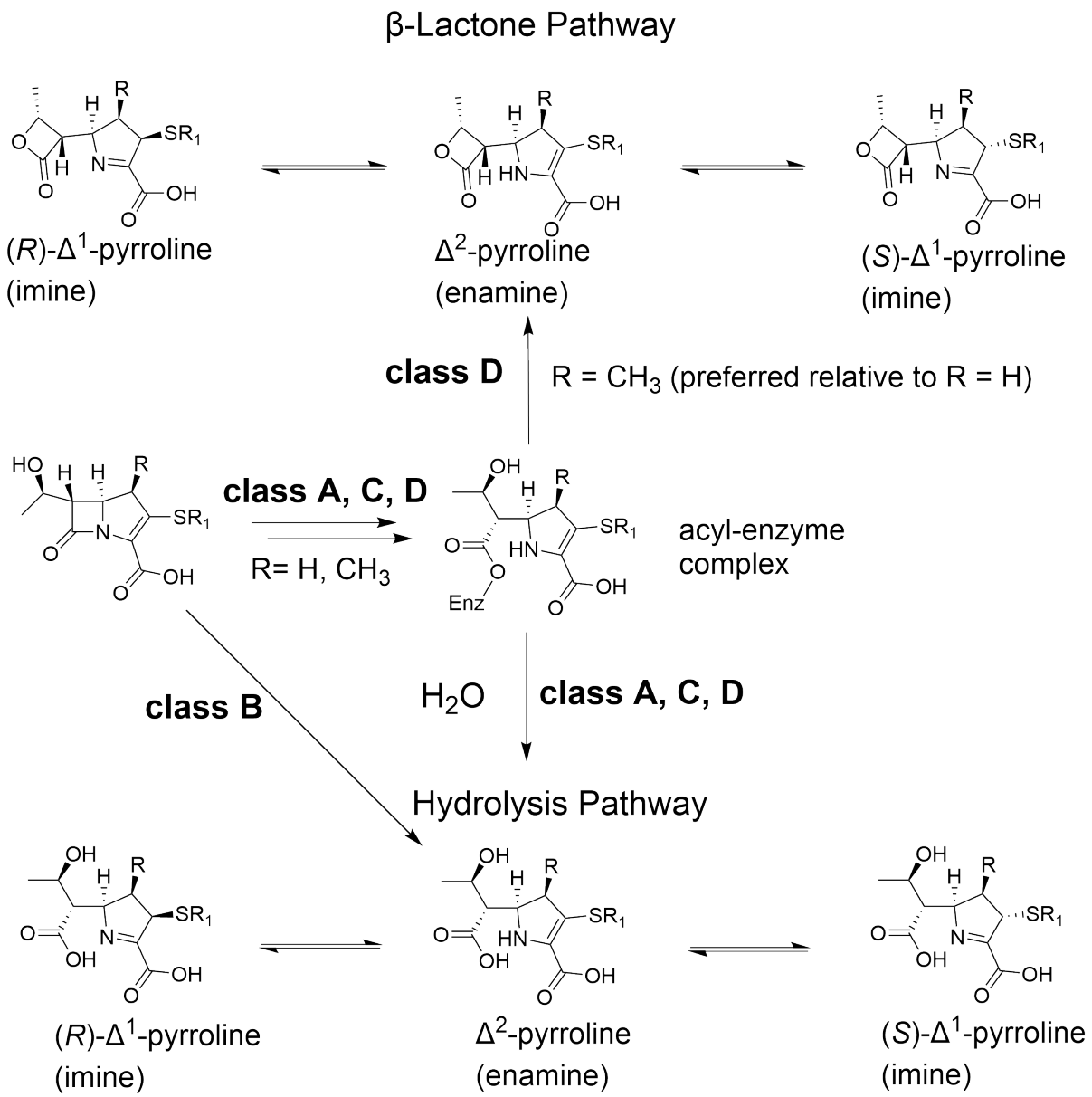


Figure 11: carbapenem hydrolysis mechanism. Both the hydrolysis product and the lactone product tautomerise to give an imine stereoisomer.

Understanding the reaction mechanisms for the hydrolysis of different β-lactams is proposed to be useful for the development of any new, broad spectrum antimicrobial therapeutics. Understanding structural changes that occur in the enzymes may be helpful in developing drugs that have a strong affinity for a broad range of β-lactamases. In my work, the B1 MBL VIM-2 was used as a model for analysing the reaction mechanisms of di zinc MBLs with carbapenems and penems.

Comparison of B1 Structures

The B1 MBLs have highly conserved zinc binding elements and a similar overall αβ/βα fold.[73] The B1 MBLs comprise the most clinically relevant MBLs, with multiple bacterial strains producing the VIM, imipenemases (IMP) and NDM B1 MBLs. However, there are differences between the non-zinc binding residues present in the active site loops which contribute to differences in affinity and turnover rates between the different MBLs.

In 2017 There were a total of 47 reported IMP variants; the IMPs are most predominant in Japan and other parts of South East Asia.[49,74] The IMP genes are expressed in *Pseudomonas aeruginosa* and *Enterobacteriaceae*, although they have been discovered in other bacteria.[75] IMPs commonly seem to be expressed *via* a class 1 integron cassettes along with other antibiotic resistance genes.[76] NDMs are a more recently discovered B1 MBL, with the first documented case being in 2008 form *K. pneumoniae* and *E.coli*, though NDMs are spreading rapidly.[47,77]

Despite little overall sequence similarity between IMPs, NDMs and VIMs (around 30%), there are several conserved structural features between the three different B1 MBLs.[73] One of these is the presence of a basic residue within 6 Å of the Zn2 zinc ion. In IMPs and NDMs this is Lys224, but in most (but not all) VIMs this residue is Arg228 (**Figure 12**).[49,78] Moreover, all of IMPs, NDMs and VIMs have a hydrophobic L3 loop, which provides a hydrophobic binding surface for the β-lactam substrates and all have an Asn233 which interacts with the new carboxylate of the product.[49]

There are differences in the active site cavities of the VIMs and NDMs. Comparisons of the crystallographically observed NDM-1 and VIM-2 active sites suggest that the NDM-1 active site may be more open and has more hydrophobic residues than VIM-2 on its L3 and L10 loops.[49,79] This, in combination with a lack of strong sequence similarity between VIMs and NDMs, suggests that the

development of any broad spectrum B1 inhibitors could focus on mimicking substrate interactions as well as any intermediates formed during substrate hydrolysis.

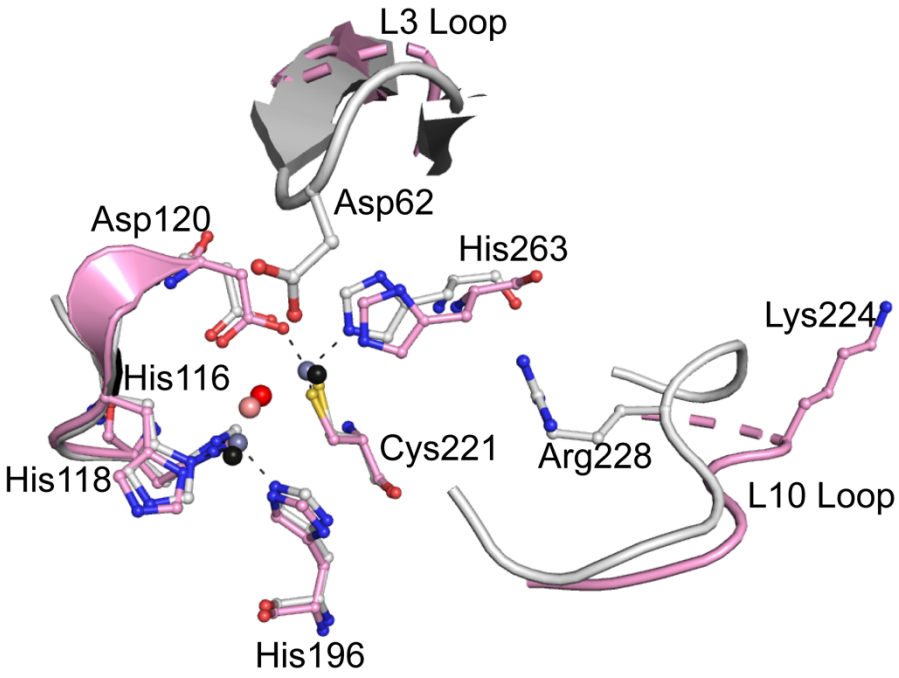


Figure 12: Comparison of active sites between VIM-2 (light grey) and NDM-1 (pink) (PDB codes: 4BZ3 and 6TWT[66, 79]). Note the different basic residues and the different positioning of the L10 and L3 loop. However, the basic structure is the same with the same zinc binding residues.[29]

Verona Integron Metallo-β-lactamases (VIMs)

The VIMs are B1 MBLs that were originally identified in 1997 in Verona, Italy in the Gram-negative bacteria *Pseudomonas aeruginosa*.[80] The VIM MBL subfamily is one of the most widely distributed MBL subfamilies across the world with over 46 variants identified in patients, with some variants only differing from VIM-1 by one residue whereas others have a 50% sequence difference.[69] VIM MBL genes are expressed on the class I integron as a gene cassette containing the bla_{VIM} gene.[76]

All variants of VIM have the same overall αβ/βα fold structure, with two zinc ion the active site that is surrounded by two loops involved in substrate binding, a hydrophobic L3 loop (residues 60-66) and a hydrophilic L10 loop (223-242).[69,81] The VIMs are small proteins, being approximately 25 kDa in size.[69]

All VIMs are broad spectrum β-lactamases, hydrolysing all β-lactam antibiotics except for the monobactams.[69] However, due to slight variations in their sequences, substrate affinities and their turnover rates may vary substantially between the different variant-substrate combinations.[69] Although some variants have been studied fairly intensely (VIM-1 and VIM-2), little structural information is currently available for most VIM variants.[69,73]

Categorising VIMs

Based on sequence similarity, identified VIM variants can be classified into five different clusters, i.e., the VIM-1, VIM-2, VIM-7, VIM-12 and VIM-13 clusters.[69] High sequence similarity can still be seen between some of the clusters, with over 90% similarity between VIM-2 and the VIM-1 cluster.[69] The changes observed between the different variants are mostly observed in the N-terminus region and at the last couple of residues at the C-terminus, although some variation can be seen in the L3 and L10 loops. An example of the latter is between VIM-1 and VIM-2, where residue 228 in L10 is a serine in VIM-1, but an arginine in VIM-2.[78]

Small changes in the VIM active site loops are what causes the variations in substrate turnover and is most likely the source of variation in IC_{50} values with inhibitors.[69] VIM-1 has been shown to have a significantly higher turnover rate with meropenem in comparison to VIM-2. However, VIM-2 has a higher affinity and turnover rate for imipenem when compared to VIM-1.[69] Residue 228 seems to play a particularly important role when it comes to substrate and inhibition recognition.[63,78] An R228L substitution from VIM-2 to VIM-24 has been shown to give bacteria producing VIM-24 an increased resistance against cephems and other mutations at this position conferred higher resistance to all β-lactams.[69] This observation supports the proposal that a broader understanding of the structural and kinetic properties is of importance in the development of effective broad spectrum inhibitors against MBLs.[27]

VIM-2 is the most commonly found member of the VIM family, being endemic in some parts of the world.[50] VIM-2 was first discovered in France, soon after the initial discovery of VIM-1 in *P. aeruginosa* in Verona, Italy and soon appeared in several other strains of bacteria such as *Acinetobacter baumannii* in Korea.[82] VIM-2 is one of the best characterised members of the VIM family with several crystal structures and in-solution kinetic studies having been described.[80,83] Due to its clinical relevance,[48,84,85] and relatively high stability VIM-2 is a useful model to learn new and exciting information about the reaction mechanism of MBLs, having been used in the study and development of many MBL inhibitors, including bicyclic boronates. However, before this thesis, few structural studies have been performed on the interaction between VIM-2 and its carbapenem substrates.

Inhibitors of β-lactamases

Potent, clinically useful inhibitors of SBLs have been developed, the first being clavulanic acid, sulbactam and tazobactam, all of which have a β-lactam ring.[86,87] Whilst ineffective on their own, when combined with penicillins these inhibitors greatly help the antibiotic overcome the resistance mechanisms produced by Class A β-lactamases.[88] Clavulanic acid, the adjuvant in Augmentin, is described as a suicide inhibitor, as it becomes inactivated in order to inactivate the enzyme when it forms the acyl-enzyme complex.[89] Other clinically useful β-lactam based inhibitors have also been developed, including sulbactam and tazobactam.[90] Like clavulanic acid, sulbactam and tazobactam need to be taken in combination with β-lactam antibiotics in what is described as combination therapy.[91]

The development, of avibactam, the first β-lactamase inhibitor containing a γ-lactam type ring instead of a β-lactam, was important (**Figure 13**).[92] Avibactam behaves in a similar way to β-lactams as it forms an acyl-enzyme complex with the enzyme.[93] Unlike, most β-lactam inhibitors, this complex is reversibly formed.[93,94] This might increase the efficiency of avibactam's role as a "protector" for the antibiotic it is being taken with. Avibactam inhibits a broader range of SBLs compared to clavulanic

acid, including KPCs (Class A), AmpC (Class C) and some OXAs (Class D) and unlike clavulanic acid and similar inhibitors, it is not entirely degraded. However, Avibactam is a weak inhibitor of MBLs.[95]

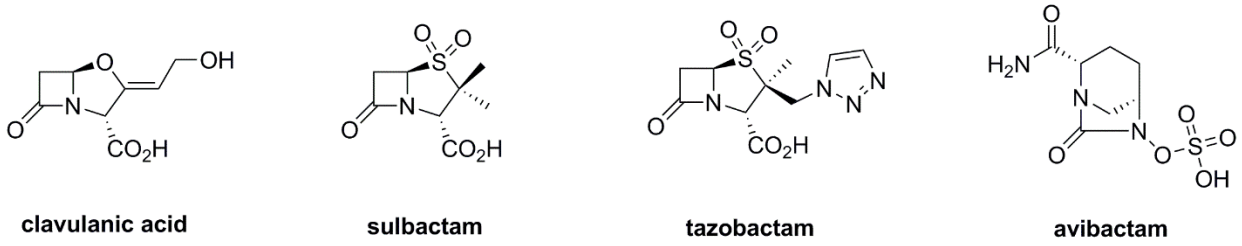


Figure 13: Examples of SBL inhibitors that are available in the clinic. All of them apart from avibactam contain a β-lactam ring: note that these inhibitors are not effective against all SBLs making the development of avibactam, a broad spectrum SBL inhibitor, an important advance. Avibactam also forms an acyl-enzyme complex with enzymes such as the Class D SBLs, however, it binds reversibly.[93] Despite the effective combination therapies in the clinic against SBLs, these have proven ineffective against all MBLs and many extended spectrum SBLs (ESBLs).[46,96] The ineffectiveness is due to the lack of similarity both structurally and mechanistically between MBLs and SBLs. This is a huge problem, as many β-lactamase enzymes are co-expressed in the same bacteria, making these therapy combinations redundant against some infections.[97]

Various studies of MBL inhibitors have been reported. Captopril inhibits MBLs by chelating the zinc ions in the active site using its thiolate, which displaces the hydrolytic water that acts as a bridge between the two zinc ions.[66] Captopril stereoisomers have been shown to inhibit a wide range of MBLs, including VIM-2, with different potencies (**Figure 14**).[66] Other MBL inhibitors have been developed, including ME1071.[98] This is a maleic acid derivative that has been shown to increase the susceptibility of carbapenems, such as meropenem and biapenem in MBL producing *P. aeruginosa* (**Figure 14**). However, ME1071 had little effect on the non MBL producing *P. aeruginosa*[98] indicating a lack of SBL inhibition.

Colloidal bismuth subcitrate (CBS) is also an effective inhibitor against B1 MBLs with strong evidence that it restores meropenem activity to NDM-1 producing Gram-positive bacteria, possibly *via* zinc ion chelation.[99] So far, no studies have been done to see how effective CBS is against SBLs. It is clear that development of a broad-spectrum inhibitor for SBLs, MBLs and PBPs is not a simple challenge as these enzymes are structurally diverse.

One focus of drug development for SBLs and MBLs instead moved to looking at inhibitors that mimic reaction intermediates. Both SBLs and MBLs form tetrahedral intermediates during the hydrolysis mechanism (**Figure 9**), which is sp^3 hybridised. Bicyclic boronates have been proposed to mimic both β-lactam containing substrates in their sp^2 form and the tetrahedral intermediates in their sp^3 form.[94,100,101]

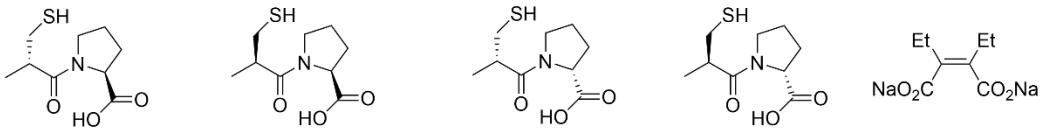


Figure 14: Structures of selected MBL inhibitors. Captopril has a similar structure to penicillinoic acid.[67] ME1071 was shown to increase the activity of some carbapenems in cells.[99]

The Development of Bicyclic Boronates

Recent studies have shown the potential of boron-based compounds for the development of MBL/SBL inhibitors.[101] Worries about the acute toxicity of boron were disproved, with boron being present in many everyday products such as vaginal creams as well as various food products.[102] Boron also has several useful properties, making it an ideal atom to have in potential inhibitors.[102] Not only does it act as a Lewis acid but also has an empty *p*-orbital and is thus electrophilic.[102] Boronic acids can inhibit serine proteases, as they form a covalent bond between the active serine and the boronate moiety,

producing a tetrahedral intermediate similar to the ones in β-lactam hydrolysis.[103] Following the initial work on the inhibition of SBLs *via* boronates,[104] when chemists started adding the acylamino side chain seen in penicillins and cephalosporins, the inhibition potency of boronic acids increased against SBLs such as CTX-M-9 and KPCs.[105–107]

Hecker *et al.,* have reported the first clinically approved cyclic boronate β-lactamase inhibitor known as vaborbactam (**Figure 15**).[108,109] This compound was developed because previous studies have shown that stable complex formation was more likely to happen with cyclised boronate esters; possibly because cyclic boronates may manifest better selectivity for SBLs compared to other serine proteases.[110] Vaborbactam is a monocyclic boronate inhibits a range of SBLs, but not MBLs. Bicyclic boronates have shown promise as inhibitors of β-lactamases; in their sp^3 form they mimic both the tetrahedral intermediate, and they can mimic the substrate in their sp^2 form (**Figure 15**). [110] The development of the bicyclic boronates taniborbactam (formerly known as VNRX-5133)[111,112] and bicyclic boronate **2**[27] (**Figure 15**) which showed inhibition for many SBLs and MBLs, indicates the potential for bicyclic boronates as broad spectrum β-lactamase inhibitors.

It is unlikely, however, that bicyclic boronates will ever fully replace β-lactam antibiotics, as they are significantly less potent against transpeptidases compared to β-lactams.[113] Thus, combination therapies involving cyclic boronate mediated inhibition SBLs and MBLs whilst targeting transpeptidases with a β-lactam will likely be pursued.[113]

Both taniborbactam and compound **2** have a standard acylamino type side chain also found in some cephalosporins and penicillins (**Figure 15**).[27,111,112] However, little research has been done into what effect altering the side chain would have on inhibition. In collaboration with the Latvian Institute of Organic Synthesis, the Schofield group have been working on the development on novel bicyclic

boronates to how altering the side chain alters the behaviour of the molecule. This has been done using a combination of kinetic, microbiology and crystallographic studies.

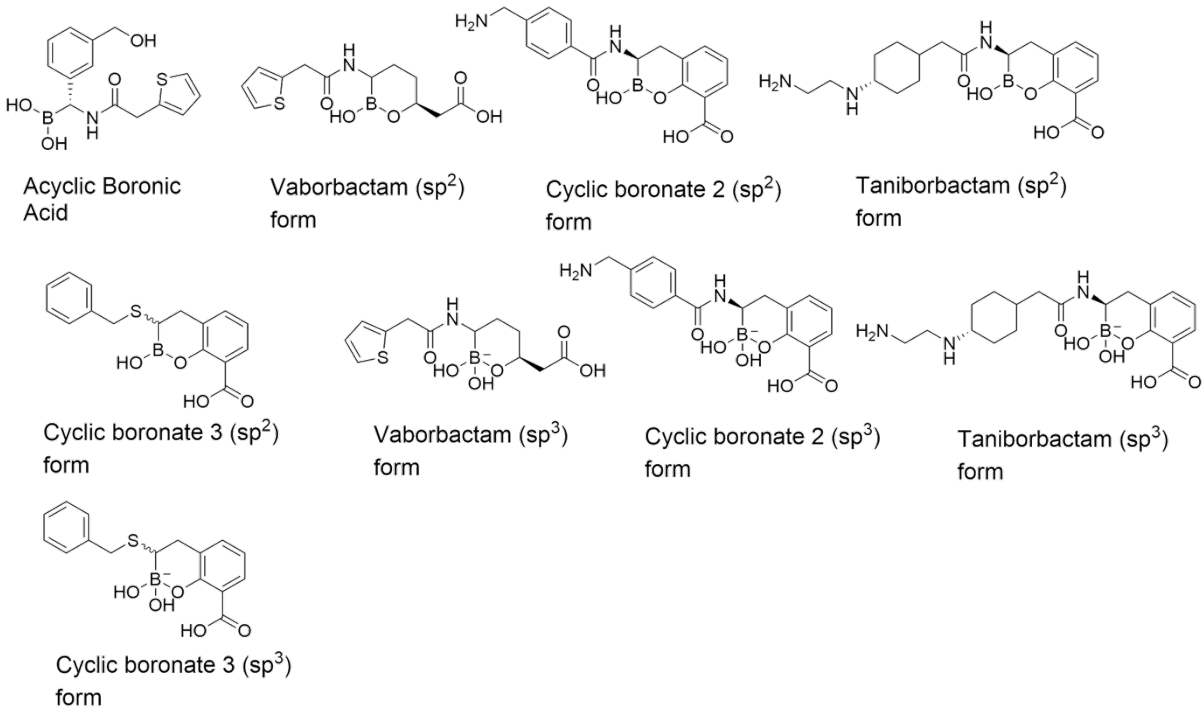


Figure 15: **Examples of acyclic Boronic acid**, **mono- and bicyclic-boronate inhibitors of SBLs and MBLs in sp^2 and sp^3 forms**. This acyclic boronic acid showed some activity against the class C SBL AmpC.[104] Vaborbactam was the first cyclic boronate to be clinically developed, but it has limited inhibition against MBLs.[109] The bicyclic boronates, taniborbactam, **2** and **3** have broader spectrum MBL and SBL inhibition.[27,112] Note that both of these have the acylamino side chain found in cephalosporins and penicillins.

Several crystal structures have been produced of bicyclic boronates with PBPs and β-lactamases; these indicate that a tetrahedral boronate complex is formed in all these cases (**Figure 16**).[27] However, it is difficult to compare this with intermediates formed in the reaction, since there are currently no structures of β-lactamases complexed with an intermediate are available. This is due to the fast turnover rate of most β-lactamases, making it difficult to capture intermediates using conventional data collection at a synchrotron.

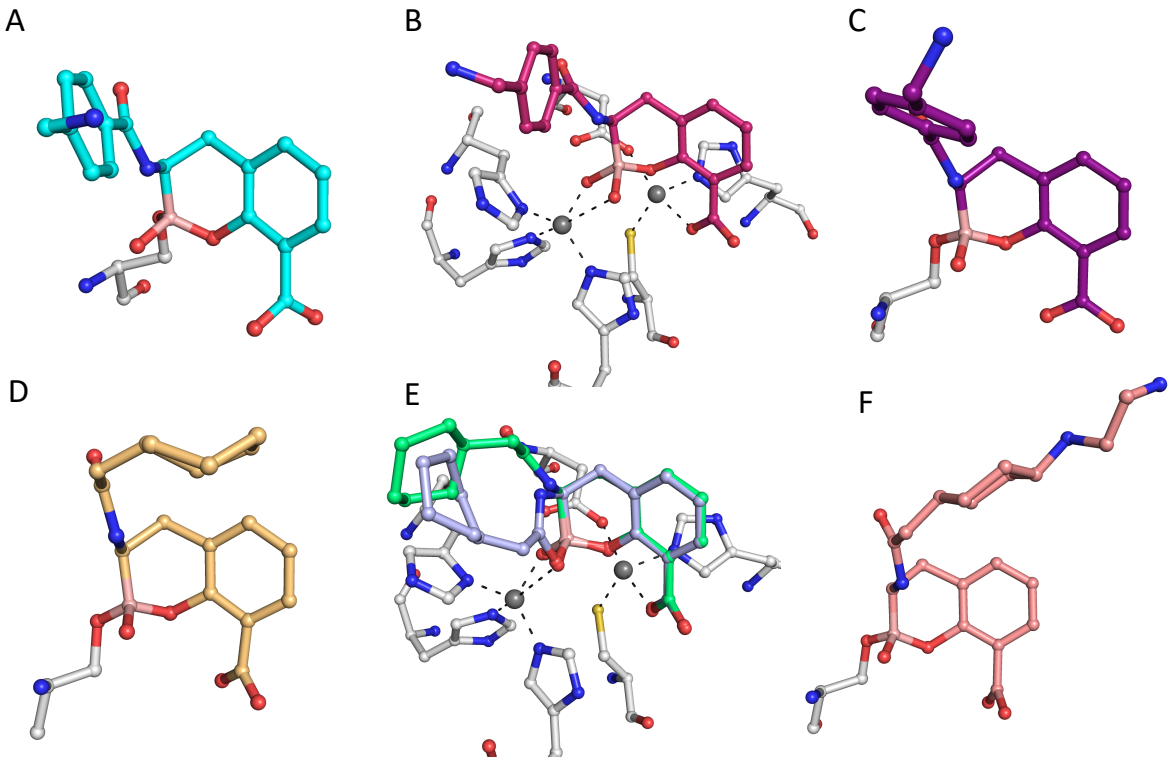


Figure 16: Views from previous reported structures of PBPs and β-lactamases with the cyclic boronate 2 and taniborbactam. A shows PBP5 from *E. coli* in complex with **2** (PDB 5J8X[27]). B shows VIM-2 in complex with **2** (5FQC[27]) and C shows **2** complexed with the Class C SBL AmpC (PDB 6YEO[54]). D depicts the active site of AmpC with taniborbactam bound to the nucleophilic serine in the active site of AmpC (PDB 6YEN[54]). NDM-1 in complex with both the tricyclic (light blue) and bicyclic form (green) of taniborbactam is shown in E (PDB 6RMF[111]) and F shows taniborbactam bound to the class D SBL OXA-10 (PDB 6RTN[111]). Note that both bicyclic boronates have an aminoacyl side chain as is often seen in penicillins and cephalosporins.

It is of interest to visualise these structural intermediates in order to understand the structural changes occurring during the reaction mechanism in order to help produce more effective, broad spectrum β-lactamase inhibitors.

Serial Crystallography and XFELs

Protein crystallography has been used to study protein structure since the 1950s.[114] To date, the vast majority of structures in the Protein Data Bank (PDB) have been acquired using X-Ray crystallography.[115] Technology for data collection at synchrotrons has changed dramatically since the early days of crystallography, with structural biologists being able to collect data on crystals as small as 10 μm^3 at micro focus beamlines in less than a minute. Whilst conventional crystallographic methods provide a large amount of information in the static form, there is still relatively little information about the dynamic changes that occur during either protein-protein interactions or enzyme reactions since conventional crystallographic methods only provide snapshots of chemical reactions at 100K.[116] Moreover, macromolecular crystallography is still an inefficient process overall, with some proteins requiring months of optimisation before a viable crystal is produced. Rather than using a single crystal that is 10 μm^3 or greater in size, for data collection at 100K, serial crystallography involves the use of a slurry of microcrystals for data collection, often at ambient temperature.[117] These microcrystals can be smaller than 5 μm^3, meaning that, in most cases, they would not be useful for cryo data collection at a synchrotron. During a serial data collection, one "image" of crystal lattice diffraction would be collected from each crystal and these images are merged together to form a single complete data set.[118]

Time resolved crystallography involves triggering a reaction inside a crystal during serial data collection.[119] This can be done either by soaking in the substrate or exposing it to gases or certain wavelengths of light. It is significantly easier to perform time resolved experiments using serial crystallography as you can trigger the reaction using the same microcrystal slurry. However, because microcrystals are much smaller, they tend not to diffract as well as larger crystals. This, alongside the issue of radiation damage in datasets and the natural limitations (such as capturing intermediates of fast reactions) of even third generation synchrotrons makes performing time resolved crystallography difficult.[117]

Studies have shown that using short X-ray pulses (in the femtosecond time range), along with an increase in the beam intensity, can drastically reduce radiation damage present in the final dataset.[120] Until the first experimental X-Ray Free Electron Lasers (XFELs) dataset was collected it was not certain whether a dataset could be collected from a crystal before it got destroyed.[121] Since then, the "diffraction before destruction" principle has been successfully applied using multiple XFELs; XFELs employ long lasers that generate incredibly intense, bright and short pulses at only a few femtoseconds.[117] XFELs have so far been used to help understand several protein reactions, broadening the scope of dynamic structural biology.[122] Micro-/nano-crystals are commonly used for data collection at an XFEL. Micro-/nanocrystals commonly used to refer to crystals that are less than 10 μm^3. Using microcrystals for serial femtosecond crystallography significantly reduces the amount of optimisation that needs to be done to produce suitable crystals of proteins that are often more difficult to crystallise such as membrane proteins. An advantage of using these smaller crystals is that they do not suffer from long range disorder to the same extent that many macrocrystals do, meaning that they can produce reliable data.[121]

Currently there are five XFELs operating around the world suitable for structural biology studies: Linac Coherent Light Source (LCLS), Spring-8 Angstrom Compact Free Electron Laser (SACLA), European XFEL (EuXFEL), Pohang Accelerator Laboratory XFEL (PAL-FEL) and Swiss XFEL (SWISSFEL) (**Figure 17, Table 1**). Each XFEL is slightly different, using different pulse frequencies and patterns, number of undulators and detectors. The limited number of XFELs makes XFEL beam time access significantly limited with few beamlines operating at the same time. This creates large push for both the development of more XFELs and for the advancement of what can also be achieved at synchrotrons, which are much more accessible. Serial data collection at XFELs and synchrotrons involves data produced from tens of thousands of images, each one from a different crystal at a different angle relative to the XFEL beam.



Figure 17: Map of the currently available XFELs around the world. Since there are only five currently available for beam time, XFEL experiments are not readily available to the entire crystallography community; there are also plans to upgrade LCLS.[123]

	LCLS	PAL-FEL	SACLA	Eu-XFEL	SwissFEL
Pulse rate (Hz)	120	60	60	27 000	60
Maximum electron energy (GeV)	14.3	10	8.5	17.5	5.8
Peak Brilliance	2×10^{33}	1.3×10^{33}	1×10^{33}	5×10^{33}	1×10^{33}
Photons/pulse ($x10^{11}$)	8.7	1-10	1.8	25	0.36
Maximum power (W)	300	100	100	500,000	100
Minimum wavelength of the laser (nm)	0.15	0.06	0.08	0.05	0.1

Table 1: **Comparison of different XFELs**. The main difference between current XFEL facilities is the number of flashes per second (or the pulse rate). Because Eu-XFEL uses super conducting technology for the accelerator rather than normal conducting technology, this the frequency of the pulse compared to other XFELs is significantly increased. The Shanghai High Repetition Rate XFEL and Extreme Light Facility (SHINE), will also use super conducting technology and should have a pulse frequency of 1,000,000 Hz.[124] New detectors, such as the Adaptive Gain Integrating Pixel Detector (AGIPD), will be developed to cope with such frequencies as the standard detectors cannot collect images at such a fast rate.[125]

How do XFELs work?

XFELs use a principle known as Self Amplified Spontaneous Emission (SASE) to produce their high energy pulses.[124] An electron gun releases the electrons into a superconducting accelerator; the electrons then fly through a group of alternating polarity magnets bunched together, known as undulators, close to the speed of light.[126] Electron guns contains a metal cathode that is heated up to emit electrons *via* a thermionic emission, electrodes in the electron gun focus the electron beam and anodes that which further focuses the beam and moves the electron away from the cathode.[127] Moving through the undulator, the oscillating electrons emit photons characteristic of the undulator at a certain energy bandwidth (**Figure 18**).

At each undulator, the photons and electrons interact with one another, causing the electrons to gain or lose energy allowing the slower electrons to catch up to the faster ones.[128] This leads to the modulation of the electron bunching known as micro-bunching, helping amplify certain photo energies. The process of SASE helps make the beam much more intense.[128] Compared to the undulators at third generation synchrotrons, those at XFELs are significantly larger, being up to 60 m long compared to the standard 2-4m at synchrotrons.[129] The intense femtosecond pulse beams produced present scientists with the opportunity to capture a "frozen" diffraction image of what is happening during enzyme reactions at the millisecond timescale; something that is impossible at a third generation synchrotron.[130] This helps scientists generate a "molecular movie" of a protein-protein interaction or of a chemical reaction occurring between an enzyme and substrate using slurries of very concentrated microcrystals.[131]

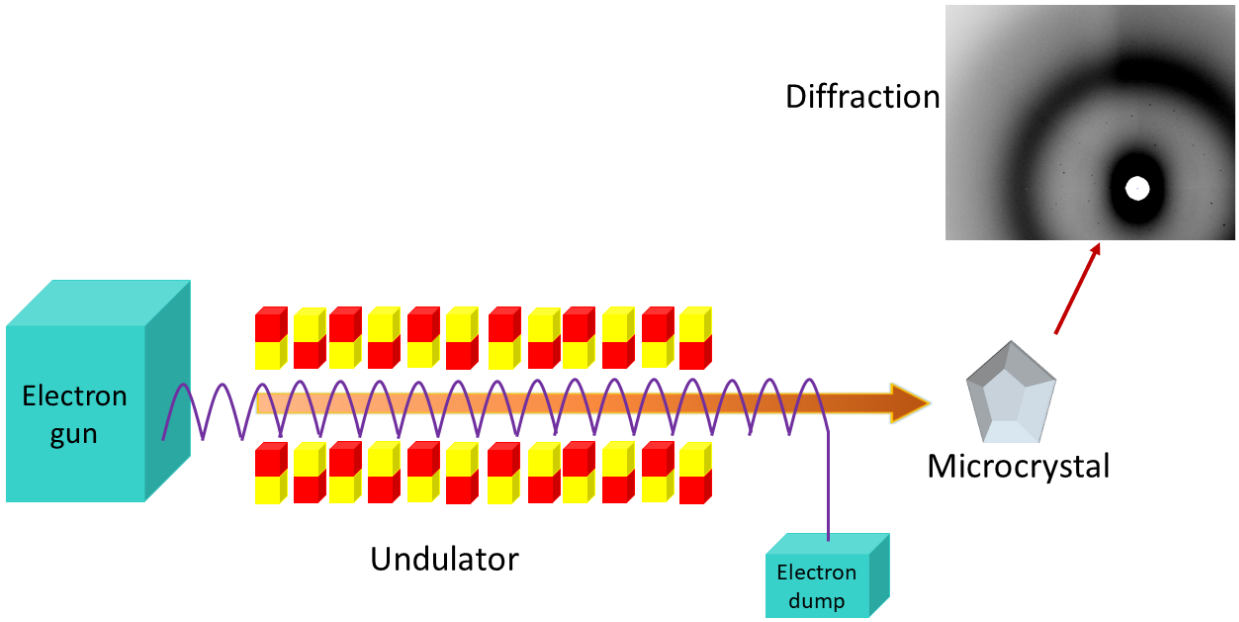


Figure 18: Simplified diagram showing the mechanism by which SASE works. Electrons are emitted from the electron gun and pass through multiple undulators. Once in the undulators they release X-ray photons (represented with the orange arrow) creating the micro bunching process. The remaining electrons go into the electron dump; X-ray photons reach the hutch where they interact with microcrystals resulting in a diffraction pattern collected by a detector. Different XFELs have a different number of undulators; these undulators are conceptually similar to the ones at synchrotrons except for the fact that they are much longer. The diffraction image shown is from a crystal of PBP5 that was collected at LCLS.

Reaction Initiation

Several issues must be considered when discussing the triggering of chemical reactions; the first being the method by which the reaction is triggered. The microcrystal slurry can often be soaked with a large excess of the substrate in order to start a reaction. Other methods can be used if the chemical reaction is triggered by environmental factors such as oxygen or certain wavelengths of light. A crystal complex

can be created in anaerobic or dark conditions then triggering the reaction by exposure to oxygen or light.

The time it takes for a substrate to diffuse through a crystal and into the active site must also be accounted for during time resolved work; different crystallisation conditions can drastically alter the diffusion time of a molecule along with the size and solubility of the substrate.[132] Crystal packing can also be a detriment to diffusion, with tightly packed crystals potentially making the active site significantly less accessible.[132] To prevent the presence of multiple intermediates in the active site, the crystals in the microcrystal slurry must be homogenous.[129] Having crystals with the same dimensions and space group influences the homogeneity of the final dataset as it makes it easier for substrates and other co-factors to diffuse into the crystal at similar rates.[117] The viscosity of the mother liquor as well as the solvent content of the crystals can also influence the behaviour how a substrate travels to the active site.

Sample Delivery Methods at XFELs

One of the main problems facing scientists working at XFELs is that crystals exposed to the X-ray pulse are destroyed very soon after the diffraction pattern is collected. Because of this, samples need to be continuously replenished during data collection.[122] This requires a sample delivery method that is capable of providing this replenishment but also does not waste a lot of sample. There are several different sample delivery methods used for serial data collection, each with benefits and drawbacks (**Figure 19**).

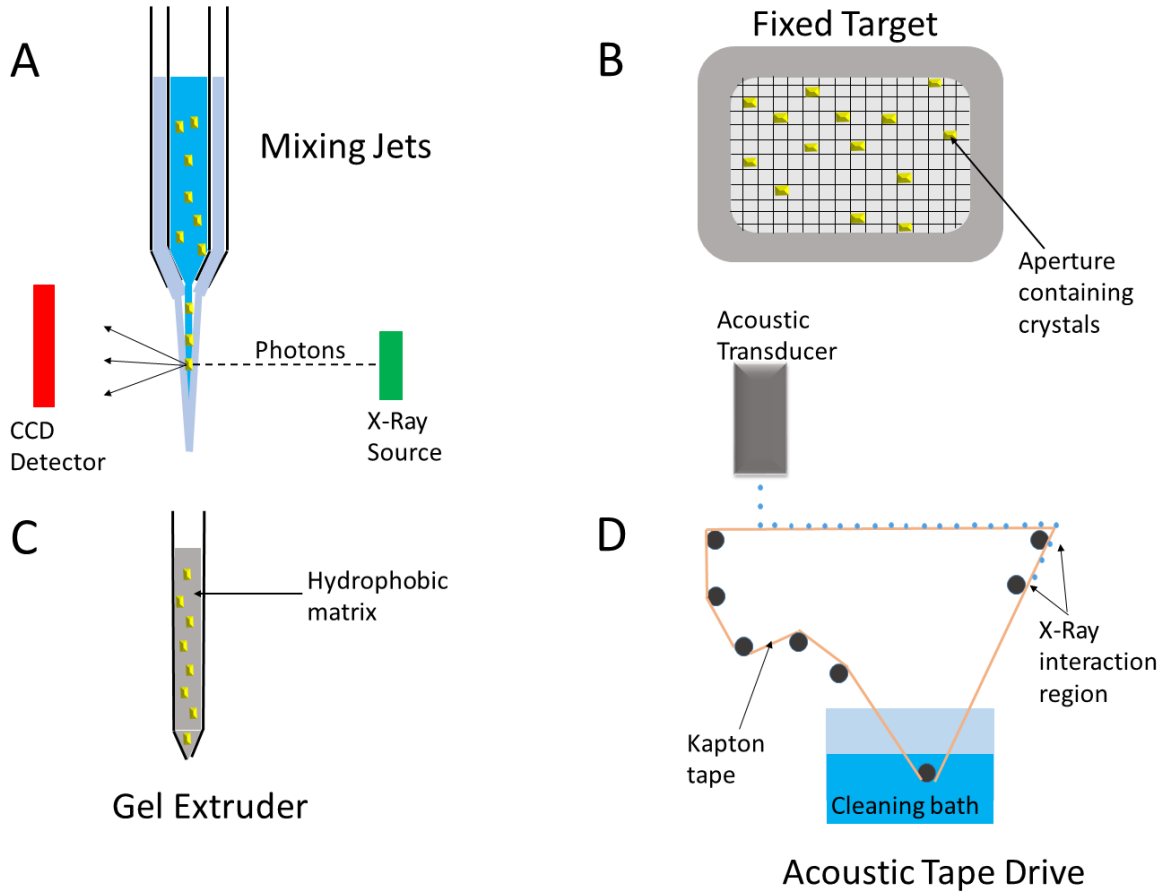


Figure 19: Four sample delivery methods used at XFELs and Serial synchrotron crystallography in this thesis. Four sample delivery methods are used at XFELs. Crystals shown in yellow cubic shapes. A) Shows a simplified version of the mixing jets method,[133] B) the fixed target method locates the crystals in the apertures,[134]C) the gel extruder method with the hydrophobic matrix shown in grey[135,136] and D) the acoustic tape drive method.[137]

Acoustic Drop Ejection (ADE) Method

The acoustic droplet ejection (ADE), or the acoustic tape drive, method is a unique sample delivery method, as it uses very little protein, an important factor when the sample is precious. In the ADE method, droplets are ejected from a sample reservoir using an acoustic transducer onto a polyimide tape (**Figure 19D**).[137] A "conveyor belt" made of Kapton tape can deliver droplets to the beam time at a fast rate (120 Hz).[137] A small reaction chamber can be attached to the belt to allow gases to diffuse through which may be used to trigger reaction. ADE has also been used to facilitate the pump/probe

method of triggering enzyme reactions such as photosystem II.[137,138] Pump/probe systems involve the use of lasers to trigger a light sensitive reaction. Although there has not been much work on using ADE to soak substrates into protein crystals, there is a lot of ground-breaking work being done on this, including in this thesis.

Gel Extruder Method

The gel extruder method involves leaving the microcrystal slurry to settle; a small volume of the microcrystal pellet (~10 µL) is then mixed with a hydrophobic "gel" such as grease or lipid cubic phase (LCP)(**Figure 19C**).[135,136] The mixture is then pulled from the syringe into the beam line using a high viscosity extruder and data is then collected. Pump/probe experiments have been performed using this method with Photosystem II,[139] however, it is not possible to do mixing experiments with substrates or gases.

Mixing Jets and GDVN Methods

The Gas Dynamic Virtual Nozzle (GDVN) method, which is the basis for the mixing jets method, is the most commonly used form of liquid jets used for XFEL data collection.[140] This involves the use of a helium stream to compress the diameter of a liquid jet during data collection to as small as 0.1 µm. The high gas and liquid pressure lead to a continuous micro thread stream of liquid in a process known as jetting (**Figure 19A**). The pressure of both the gas and the liquid play a very important role in the microfluidics of the liquid jet, as low gas and liquid pressure can lead to the formation of large singular droplets.[140]

Mixing jets allow for easy mixing of substrate solutions into enzyme crystals. However, one of the main downsides to this method is that it requires hundreds of milligrams to gram quantities of both the enzyme and substrate.[141] The jets used consist of two main parts, an inner and an outer jet. The microcrystal slurry flows through the inner jet and the substrate flows through the outer jet; the

substrate should be at a very high concentration (hundreds of mM) for the experiment to work as best as possible.[133] These then reach the mixing section where the substrate can soak into, and hopefully saturate, the protein crystals. There is a time delay before the crystals interact with the X-Ray beam after mixing; this time delay is the reaction time point that is captured in the diffraction pattern. The time delay can be altered by using a different nozzle on the jet, changing how long the substrates soak into the crystal before data collection.

Co-MESH Method

The Co-MESH, or the Concentric Flow electrokinetic injector method, has also been used for XFEL studies on various different proteins such as thermolysin and photosystem II.[142] A microfluidic electrokinetic sample holder (MESH) uses voltage rather than pressure (as in the case of GDVN) to control the flow rate of the microcrystal slurry. The inner capillary contains the microcrystal slurry and introduces the sample to the XFEL beam. There is also an outer capillary that contains a sister liquor, which prevents the sample from freezing and dehydrating when it enters the vacuum environment.[143] One main benefit of these systems is that Co-MESH experiments use significantly less sample in comparison to GDVN jets since a voltage controlled flow allows for a lower average flow rate.[142] This method was not used for our data collection studies.

Fixed Target Method

Fixed target sample delivery systems are a quick and easy way to collect serial crystallographic data sets. The method requires very little protein as there is little waste. A slurry of concentrated microcrystals (x10^8 crystals/mL) is loaded onto a silicon grid or chip in a high humidity chamber which contains thousands of tiny apertures (**Figure 19B**).[144] The grid has to be flow charged to allow for the even spread of the microcrystal slurry. A vacuum is applied to the grid, removing the moisture from the crystal slurry and allowing the crystals to sit in the apertures. The grid is then sealed with Mylar

film to prevent the crystals from drying out and is attached to the beam line, ready for data collection.[145,146]

Several other fixed target methods have been used previously for data collection at XFELs. These use similar principles to one another with some variations in the mounting techniques and materials between the different chips. Roedig *et al,* used single crystallised silicon with micropores with excess mother liquor being soaked off in the micropores.[147] Anaerobic fixed target sample delivery methods have also been developed in order to obtain room temperature structures of oxygen dependent enzymes.[148]

Aims

The overall aim of the work described in this thesis was to improve our knowledge of how the B1 MBL VIM-2, and by implication other B1 MBLs, catalyse the hydrolysis of carbapenem and penems to help in the development of new MBL inhibitors. Chapter 2 describes crystallographic and solution studies on VIM-2 catalysed carbapenem and penem hydrolysis. Chapters 3 compares and contrasts the different sample delivery methods used for serial and time resolved crystallography, both at synchrotrons and XFELs, using PBP5 as the sample. Chapter 4 discusses the results of time resolved experiments with VIM-2 and Chapter 5 describes studies on multiple bicyclic boronates with VIM-2.

References

(1) Gelpi, A.; Gilbertson, A.; Tucker, J. D. Magic bullet: Paul Ehrlich, Salvarsan and the birth of venereology. *Sex. Transm. Infect.*, **2015,** *91*, 68-69.

(2) OTTEN, H. Domagk and the development of the sulphonamides. *J. Antimicrob. Chemother.* **1986**, *17*, 689–690.

(3) Fleming, A. On the Antibacterial Action of Cultures of a Penicillium, with Special Reference to

their Use in the Isolation of B. influenzæ. *Br. J. Exp. Pathol.* , **1929**, *10*.

(4) Abraham, E. P.; Chain, E.; Fletcher, C. M.; Gardener, A. D.; Heatley, N. G.; Jennings; M. A.; Florey, H. W. FURTHER OBSERVATIONS ON PENICILLIN. *Lancet*, **1941,** *238,* 177–189.

(5) Hutchings, M. I.; Truman, A. W. Antibiotics: past, present and future. *Curr. Opin. Microbiol.* **2019,** *51*, 72–80.

(6) Singh, G. S. Beta-lactams in the new millennium. Part-I: monobactams and carbapenems. *Mini Rev. Med. Chem.*, **2004***, 4*, 69–92.

(7) Macheboeuf, P. Contreras-Martel, C.; Job, V.; Dideberg, O.; Dessen, A. Penicillin Binding Proteins: key players in bacterial cell cycle and drug resistance processes. *FEMS Microbiol. Rev.*, **2006***, 30*, 673–691.

(8) Papp-Wallace, K. M.; Endimiani, A.; Taracila, M. A.; Bonomo, R. A. Carbapenems: Past, Present, and Future. *Antimicrob. Agents Chemother.,* **2011,** *55*, 4943.

(9) Tahlan, K.; Jensen, S. E. Origins of the β-lactam rings in natural products. *J. Antibiot. (Tokyo).*, **2013**, *66*, 401–410.

(10) Singh, G. S. β-Lactams in the New Millennium. Part-II: Cephems, Oxacephems, Penams and Sulbactam. *Mini-Reviews Med. Chem.*, **2004**, *4*, 93–109.

(11) Slama, T. G. Clinical review: balancing the therapeutic, safety, and economic issues underlying effective antipseudomonal carbapenem use. *Critical care (London, England)*, **2008**, *12*.

(12) Dalhoff, A.; Janjic, N. Echols, R.; Redefining penems. *Biochem. Pharmacol.,* **2006**, *71*, 1085–1095.

(13) Ernest, I.; Gosteli, J.; Greengrass, C. W.; Holick, W.; Jackman, D. E.; Pfeandler, H. R.; Woodward, R. B. The penems, a new class of .beta.-lactam antibiotics: 6-acylaminopenem-3-carboxylic acids. *J. Am. Chem. Soc.*, **1978**, *100*, 8214–8222.

(14) Hamilton-Miller, J. M. T. Chemical and Microbiologic Aspects of Penems, a Distinct Class of β-Lactams: Focus on Faropenem. *Pharmacotherapy,* **2003***, 23*, 1497–1507.

(15) Curtiss, R.; Charamella, L. J.; Berg, C. M.; Harris, P. E. Kinetic and Genetic Analyses of d-

Cycloserine Inhibition and Resistance in *Escherichia coli*. *J. Bacteriol.*, **1965**, *90*, 1238–1250.

(16) Abraham, E. P.; Chain, E. An enzyme from bacteria able to destroy penicillin. *Nature*, **1940,** *146.*

(17) Coico, R. Gram Staining. in *Current Protocols in Microbiology* **00**, A.3C.1-A.3C.2 (John Wiley & Sons, Inc., 2005).

(18) Nangia, A.; Biradha, K.; Desiraju, G. R. Correlation of biological activity in β-lactam antibiotics with Woodward and Cohen structural parameters - A Cambridge database study. *J. Chem. Soc. Perkin Trans.,* **1996***, 5*, 943–953.

(19) SPRATT, B. G. Properties of the Penicillin-Binding Proteins of *Escherichia coli* K12. *Eur. J. Biochem.*, **1977**, *72*, 341–352.

(20) Patru, M. M.; Pavelka, M. S. A role for the class a penicillin-binding protein PonA2 in the survival of *Mycobacterium smegmatis* under conditions of nonreplication. *J. Bacteriol,* **2010** *192,* 3043–3054.

(21) Cordillot, M.; Dubée, V.; Triboulet, S.; Dubost, L.; Marie, A.; Hugonnet, J-E.; Arthur, M.; Mainardi, J-L. In vitro cross-linking of *Mycobacterium tuberculosis* peptidoglycan by L,D-transpeptidases and inactivation of these enzymes by carbapenems. *Antimicrob. Agents Chemother.,* **2013***, 57*, 5940–5945.

(22) Sütterlin, L.; Edoo, Z.; Hugonnet, J.-E.; Mainardi, J.-L.; Arthur, M. Peptidoglycan Cross-Linking Activity of l,d-Transpeptidases from *Clostridium difficile* and Inactivation of These Enzymes by β-Lactams. *Antimicrob. Agents Chemother.*, **2018**, *62.*

(23) Sauvage, E.; Kerff, F.; Terrak, M.; Ayala, J. A.; Charlier, P. The penicillin-binding proteins: structure and role in peptidoglycan biosynthesis. *FEMS Microbiol. Rev.,* **2008***, 32,* 234–258.

(24) Waxman, D. J.; Lindgren, D. M.; Strominger, J. L. High-molecular-weight penicillin-binding proteins from membranes of bacilli. *J. Bacteriol.*, **1981**, *148*, 950–5.

(25) Nelson, D. E.; Young, K. D. Penicillin binding protein 5 affects cell diameter, contour, and morphology of *Escherichia coli*. *J. Bacteriol.*, **2000**, *182*, 1714–1721.

(26) Sauvage, E.; Kerff, F.; Terrak, M.; Ayala, J. A.; Charlier, P. The penicillin-binding proteins: Structure and role in peptidoglycan biosynthesis. *FEMS Microbiology Reviews*, **2008**, *32*, 234–258.

(27) Brem, J.; Cain, R.; Cahill, S.; McDonough, M. A.; Clifton, I. J.; Jimenez-Castellanos, J-C.; Avison, M. B.; Spencer, J.; Fishwick, C. W. G.; Schofield, C. J. Structural basis of metallo-β-lactamase, serine-β-lactamase and penicillin-binding protein inhibition by cyclic boronates. *Nat. Commun.*, **2016**, *7*.

(28) Levy, N.; Bruneau, J-M.; Le Rouzic, E.; Bonnard, D.; Le Strat, F.; Caravano, A.; Chevreuil, F.; Barbion, J.; Chasset, S.; Ledoussal, B. et al. Structural Basis for *E. coli* Penicillin Binding Protein (PBP) 2 Inhibition, a Platform for Drug Design. *J. Med. Chem.*, **2019**, *62*, 4742–4754.

(29) DeLano, W. L. The PyMOL Molecular Graphics System. *Schrödinger LLC www.pymol.org* http://www.pymol.org, **2008**. doi:citeulike-article-id:240061

(30) Yamada, M.; Watanabe, T.; Baba, N.; Takeuchi, Y.; Ohsawa, F.; Gomi, S. Crystal structures of biapenem and tebipenem complexed with penicillin-binding proteins 2X and 1A from *Streptococcus pneumoniae*. *Antimicrob. Agents Chemother.* **2008**, *52*, 2053–2060.

(31) Zhang, W.; Shi, Q.; Meroueh, S. O.; Vakulenko, S. B.; Mobashery, S. Catalytic Mechanism of Penicillin-Binding Protein 5 of *Escherichia coli.*

(32) Sarkar, S. K.; Chowdhury, C.; Ghosh, A. S. Deletion of penicillin-binding protein 5 (PBP5) sensitises *Escherichia coli* cells to β-lactam agents. *Int. J. Antimicrob. Agents*, **2010**, *35*, 244–249.

(33) Nordmann, P.; Naas, T.; Poirel, L. Global spread of carbapenemase producing *Enterobacteriaceae*. *Emerg. Infect. Dis.*, **2011**, *17*, 1791–1798.

(34) Rattan, A. Multidrug-Resistant Mycobacterium tuberculosis: Molecular Perspectives. *Emerg. Infect. Dis.*, **1998**, *4*, 195–209.

(35) Musser, J. M. Antimicrobial agent resistance in mycobacteria: molecular genetic insights. *Clin. Microbiol. Rev.*, **1995**, *8*, 496–514.

(36) *WHO Report on Surveillance of Antibiotic Consumption*. **2016**.

(37) J.O. Neil. Home | AMR Review. Available at: https://amr-review.org/. (Accessed: 12th November 2020)

(38) Lambert, P. A. Mechanisms of antibiotic resistance in *Pseudomonas aeruginosa*. in *Journal of the Royal Society of Medicine, Supplement*, **2002**, *95*, 22–26.

(39) Webber, M. A. The importance of efflux pumps in bacterial antibiotic resistance. *J. Antimicrob. Chemother.*, **2003**, *51*, 9–11.

(40) Blair, J. M. A.; Webber, M. A.; Baylay, A. J.; Ogbolu, D. O.; Piddock, L. J. V. Molecular mechanisms of antibiotic resistance. *Nat. Rev. Microbiol.*, **2015**, *13*, 42–51.

(41) Hartman, B. J.; Tomasz, A. Low-affinity penicillin-binding protein associated with beta-lactam resistance in *Staphylococcus aureus*. *J. Bacteriol.*, **1984**, *158*, 513–6.

(42) Fontana, R.; Aldegheri, M.; Ligozzi, M.; Lopez, H.; Sucari, A.; Satta, G. Overproduction of a low-affinity penicillin-binding protein and high-level ampicillin resistance in *Enterococcus faecium*. *Antimicrob. Agents Chemother.*, **1994**, *38*, 1980–3.

(43) Fernández, L.; Hancock, R. E. W. Adaptive and mutational resistance: role of porins and efflux pumps in drug resistance. *Clin. Microbiol. Rev.*, **2012**, *25*, 661–81.

(44) Bush, K.; Jacoby, G. A. Updated functional classification of beta-lactamases. *Antimicrob. Agents Chemother.*, **2010**, *54*, 969–76.

(45) Hall, B. G.; Barlow, M. Evolution of the serine β-lactamases: Past, present and future. *Drug Resist. Updat.*, **2004**, *7*, 111–123.

(46) Paterson, D. L.; Bonomo, R. A. Extended-spectrum β-lactamases: A clinical update. *Clinical Microbiology Reviews*, **2005**, *18*, 657–686.

(47) Jovcic, B.; Lepsanovic, Z.; Suljagic, V.; Rackov, G.; Begovic, J.; Topisirovic, L.; Kojic, M. Emergence of NDM-1 metallo-β-lactamase in *Pseudomonas aeruginosa* clinical isolates from Serbia. *Antimicrob. Agents Chemother.*, **2011**, *55*, 3929–3931.

(48) Lagatolla, C.; Tonin, E. A.; Monti-Bragadin, C.; Dolzani, L.; Gombac., F.; Bearzi, C.; Edalucci, E.;

Gionechetti, F.; Rossolini, G. M. Endemic carbapenem-resistant *Pseudomonas aeruginosa* with acquired metallo-beta-lactamase determinants in European hospital. *Emerg. Infect. Dis.*, **2004**, *10*, 535–8.

(49) Bebrone, C. Metallo-β-lactamases (classification, activity, genetic organization, structure, zinc coordination) and their superfamily. *Biochem. Pharmacol.*, **2007**, *74*, 1686–1701.

(50) Walsh, T. R.; Toleman, M. A.; Poirel, L.; Nordmann, P. Metallo-beta-lactamases: the quiet before the storm? *Clin. Microbiol. Rev.*, **2005**, *18*, 306–25.

(51) Chen, Y.; McReynolds; A.; Shoichet, B. K. Re-examining the role of Lys67 in class C beta-lactamase catalysis. *Protein Sci.*, **2009**, *18*, 662–9.

(52) Tooke, C. L.; Hinchliffe, P.; Lang, P. A.; Mulholland, A. J.; Brem, J.; Schofield, C. J.; Spencer, J. Molecular Basis of Class A β-Lactamase Inhibition by Relebactam. *Antimicrob. Agents Chemother.*, **2019**, *63*.

(53) Golemi, D.; Maveyraud, L.; Vakulenko, S.; Tranier, S.; Ishiwata, A.; Kotra, L. P.; Samama, J-P.; Mobashery, S. The First Structural and Mechanistic Insights for Class D β-Lactamases: Evidence for a Novel Catalytic Process for Turnover of β-Lactam Antibiotics. *J. Am. Chem. Soc.*, **2000**, *122*, 6132–6133.

(54) Lang, P. A.; Parkova, A.; Leissing, T. M.; Calvopiña, K.; Cain, R.; Krajnc, A.; Panduawala, T.; Philippe, J.; Fishwick, C. W. G.; Trapencieris, P. et al. Bicyclic Boronates as Potent Inhibitors of AmpC, the Class C β-Lactamase from Escherichia coli. *Biomolecules*, **2020**, *10*.

(55) Golemi, D.; Maveyraud, L.; Vakulenko, S.; Samama, J. P.; Mobashery, S. Critical involvement of a carbamylated lysine in catalytic function of class D beta-lactamases. *Proc. Natl. Acad. Sci. U. S. A.*, **2001**, *98*, 14280–5.

(56) Hall, R. M.; Collis, C. M. Antibiotic resistance in gram-negative bacteria: the role of gene cassettes and integrons. *Drug Resist. Updat.*, **1998**, *1*, 109–119.

(57) Khosravi, Y.; Tay, S. T.; Vadivelu, J. Analysis of integrons and associated gene cassettes of metallo-β-lactamase-positive *Pseudomonas aeruginosa* in Malaysia. *J. Med. Microbiol.*, 2011,

60, 988–994.

(58) Pfeifer, Y.; Wilharm, G.; Zander, E.; Wichelhaus, T. A.; Göttig, S., Hunfeld, K-P., Seifert, H., Witte, W.; Higgins, P. G. Molecular characterization of blaNDM-1 in an *Acinetobacter baumannii* strain isolated in Germany in 2007. *J. Antimicrob. Chemother.*, **2011**, *66*, 1998–2001.

(59) Mazel, D. Integrons: agents of bacterial evolution. *Nat. Rev. Microbiol.*, **2006**, *4*, 608–620.

(60) Meini, M. R.; Llarrull, L. I.; Vila, A. J. Evolution of metallo-β-lactamases: Trends revealed by natural diversity and in vitro evolution. *Antibiotics*, **2014**, *3*, 285–316.

(61) Bush, K. Metallo-beta-lactamases: a class apart. *Clin. Infect. Dis.*, **1998**, *27 Suppl 1*, S48-53.

(62) Aitha, M.; Marts, A. R.; Bergstrom, A.; Møller, A. J.; Moritz, L.; Turner, L.; Nix, J. C.; Bonomo, R. A.; Page, R. C.; Tierney, D. L. et al. Biochemical, mechanistic, and spectroscopic characterization of metallo-β-lactamase VIM-2. *Biochemistry*, **2014**, *53*, 7321–31.

(63) Lassaux, P.; Traoré, D. A. K.; Loisel, E.; Favier, A.; Docquier, J. D.; Sohier, J. S.; Laurent, C.; Bebrone, C.; Frère, J. M.; Ferrer, J. L. et al. Biochemical and Structural Characterization of the Subclass B1 Metallo-Lactamase VIM-4. *Antimicrob. Agents Chemother.*, **2011**, *55*, 1248–1255.

(64) Garau, G.; Bebrone, C.; Anne, C.; Galleni, M.; Frère, J-M.; Dideberg, O. A metallo-beta-lactamase enzyme in action: crystal structures of the monozinc carbapenemase CphA and its complex with biapenem. *J. Mol. Biol.*, **2005**, *345*, 785–95.

(65) Bounaga, S.; Laws, A. P.; Galleni, M; Page, M. I. The mechanism of catalysis and the inhibition of the *Bacillus cereus* zinc-dependent β-lactamase. *Biochem. J*, **1998**, *331*, 703–711.

(66) Brem, J.; van Berkel, S. S.; Zollman, D.; Lee, S. Y.; Gileadi, O.; McHugh, P. J.; Walsh, T. R.; McDonough, M. A.; Schofield, C. J. Structural Basis of Metallo-β-Lactamase Inhibition by Captopril Stereoisomers. *Antimicrob. Agents Chemother.*, **2016**, *60*, 142–50.

(67) Crisp, J.; Connors, R.; Garrity, J. D.; Carenbauer, A. L.; Crowder, M. W.; Spencer, J. Structural basis for the role of Asp-120 in metallo-beta-lactamases. *Biochemistry*, **2007**, *46*, 10664–74.

(68) Bebrone, C.; Anne, C.; De Vriendt, K.; Devreese, B.; Rossolini, G. M.; Beeumen, J. V.; Frère, J-

M.; Galleni, M. Dramatic broadening of the substrate profile of the *Aeromonas hydrophila* CphA metallo-beta-lactamase by site-directed mutagenesis. *J. Biol. Chem.*, **2005**, *280*, 28195–202.

(69) Makena, A.; Düzgün, A. Ö.; Brem, J.; McDonough, M. A.; Rydzik, A. M.; Abboud, M. I.; Saral, A.; Çiçek, A. C.; Sandalli, C.; Schofield, C. J. Comparison of Verona Integron-Borne Metallo-Lactamase (VIM) Variants Reveals Differences in Stability and Inhibition Profiles. **2016**.

(70) Lisa, M.-N.; Palacios, A. R.; Aitha, M.; Gonzalez, M. M.; Moreno, D. M.; Crowder, M. W.; Bonomo, R. A.; Spencer, J.; Tierney, D. L.; Llarrull, L. I. et al. A general reaction mechanism for carbapenem hydrolysis by mononuclear and binuclear metallo-β-lactamases. *Nat. Commun.*, **2017**, *8*.

(71) Lohans, C. T.; Freeman, E. I.; Groesen, E.; Tooke, C. L.; Hinchliffe, P.; Spencer, J.; Brem, J.; Schofield, C. J. Mechanistic Insights into β-Lactamase-Catalysed Carbapenem Degradation Through Product Characterisation. *Sci. Rep.*, **2019,** *9*.

(72) Lohans, C. T.; Groesen, E.; Kumar, K.; Tooke, C. L.; Spencer, J.; Paton, R. S.; Brem, J.; Schofield, C. J. A New Mechanism for β-Lactamases: Class D Enzymes Degrade 1β-Methyl Carbapenems through Lactone Formation. *Angew. Chemie Int. Ed.*, **2018**, *57*, 1282–1285.

(73) F. Mojica, M.; Bonomo, R. A.; Fast, W. B1-Metallo-β-Lactamases: Where Do We Stand?

(74) Yamamoto, N.; Asada, R.; Kawahara, R.; Hagiya, H.; Akeda, Y.; Shanmugakani, R. K.; Yoshida, H.; Yukawa, S.; Yamamoto, K.; Takayama, Y. et al. Prevalence of, and risk factors for, carriage of carbapenem-resistant *Enterobacteriaceae* among hospitalized patients in Japan. *J. Hosp. Infect.*, **2017**, *97*, 212–217.

(75) Trudic, A.; Jelesic, Z.; Mihajovic-Ukropina, M.; Medic, D.; Zivlak, B.; Gusman, V.; Djilas, M., Carbapenemase production in hospital isolates of multidrug-resistant *Klebsiella pneumoniae* and *Escherichia coli* in Serbia. *Vojnosanit. Pregl.*, **2017**, *74*, 715–721.

(76) Sedighi, M.; Halajzadeh, M.; Ramazanzadeh, R.; Amirmozafari, N.; Heidary, M.; Pirouzi, S. Molecular detection of β-lactamase and integron genes in clinical strains of *Klebsiella*

pneumoniae by multiplex polymerase chain reaction. *Rev. Soc. Bras. Med. Trop.*, **2017**, *50*, 321–328.

(77) Yong, D.; Toleman, M. A.; Giske, C. G.; Cho, H. S.; Sundman, K.; Lee, K.; Walsh, T. R. Characterization of a new metallo-β-lactamase gene, bla NDM-1, and a novel erythromycin esterase gene carried on a unique genetic structure in *Klebsiella pneumoniae* sequence type 14 from India. *Antimicrob. Agents Chemother.*, **2009**, *53*, 5046–5054.

(78) Mojica, M. F.; Mahler, S. G.; Bethel, C. R.; Taracila, M. A.; Kosmopoulou, M.; Papp-Wallace, K. M.; Llarrull, L. I.; Wilson, B. M.; Marshall, S. H.; Wallace, C. J. et al. Exploring the Role of Residue 228 in Substrate and Inhibitor Recognition by VIM Metallo-β-lactamases. *Biochemistry*, **2015**, *54*, 3183–3196.

(79) Raczynska, J. E.; Imiolczyk, B.; Komorowska, M.; Sliwiak, J.; Czyrko-Horcak, J.; Brzezinski, K.; Jaskolski, M. Flexible loops of New Delhi metallo-β-lactamase modulate its activity towards different substrates. *Int. J. Biol. Macromol.*, **2020**, *158*, 104–115.

(80) Poirel, L.; Naas, T.; Nicolas, D.; Collet, L.; Bellais, S.; Cavallo, J. D.; Nordmann, P. Characterization of VIM-2, a carbapenem-hydrolyzing metallo-beta-lactamase and its plasmid- and integron-borne gene from a *Pseudomonas aeruginosa* clinical isolate in France. *Antimicrob. Agents Chemother.*, **2000**, *44*, 891–7.

(81) Docquier, J.-D.; Lamotte-Brasseur, J.; Galleni, M.; Amicosante, G.; Frère, J. M.; Rossolini, G. M. On functional and structural heterogeneity of VIM-type metallo-beta-lactamases. *J. Antimicrob. Chemother.*, **2003**, *51*, 257–266.

(82) Yum, J. H.; Yi, K.; Lee, H.; Yong, D.; Lee, K.; Kim, J. M.; Rossolini, G. M.; Chong, Y. Molecular characterization of metallo-b-lactamase-producing *Acinetobacter baumannii* and *Acinetobacter* genomospecies 3 from Korea: identification of two new integrons carrying the blaVIM-2 gene cassettes. *J. Antimicrob. Chemother.*, **2002**, *49*, 837–840.

(83) Garcia-Saez, I.; Docquier, J.-D.; Rossolini, G. M.; Dideberg, O. The Three-Dimensional Structure of VIM-2, a Zn-β-Lactamase from *Pseudomonas aeruginosa* in Its Reduced and

Oxidised Form. *J. Mol. Biol.*, **2008**, *375*, 604–611.

(84) Mavroidi, A.; Tsakris, A.; Tzelepi, E.; Pournaras, S.; Loukova, V.; Tzouvelekis, L. S. Carbapenem-hydrolysing VIM-2 metallo- beta-lactamase in *Pseudomonas aeruginosa* from Greece. *J. Antimicrob. Chemother.*, **2000**, *46*, 1041–1043.

(85) Moyo, S.; Haldorsen, B.; Aboud, S.; Blomberg, B.; Maselle, S. Y.; Sundsfjord, A.; Langeland, N.; Samuelen, O. Identification of VIM-2-Producing *Pseudomonas aeruginosa* from Tanzania Is Associated with Sequence Types 244 and 640 and the Location of blaVIM-2 in a TniC Integron. *Antimicrob. Agents Chemother.*, **2015**, *59*, 682–685.

(86) Keating, G. M.; Perry, C. M. Ertapenem. *Drugs*, **2005**, *65*, 2151–2178.

(87) Bryson, H. M.; Brogden, R. N. Piperacillin/Tazobactam. *Drugs*, **1994**, *47*, 506–535.

(88) Imtiaz, U.; Billings, E.; Knox, J. R.; Manavathu, E. K.; Lerner, S. E.; Mobashery, S. Inactivation of class A .beta.-lactamases by clavulanic acid: the role of arginine-244 in a proposed nonconcerted sequence of events. *J. Am. Chem. Soc.*, **1993**, *115*, 4435–4442.

(89) Foulstone, M.; Reading, C. Assay of amoxicillin and clavulanic acid, the components of Augmentin, in biological fluids with high-performance liquid chromatography. *Antimicrob. Agents Chemother.*, **1982**, *22*, 753–62.

(90) Campoli-Richards, D. M.; Brogden, R. N. Sulbactam/Ampicillin. *Drugs*, **1987**, *33*, 577–609.

(91) Reading, C.; Cole, M. Clavulanic acid: a beta-lactamase-inhiting beta-lactam from Streptomyces clavuligerus. *Antimicrob. Agents Chemother.*, **1977**, *11*, 852–7.

(92) Ehmann, D. E.; Jahić, H.; Ross, P. L.; Gu, R. F.; Hu, J.; Kern, G.; Walkup, G. K.; Fisher, S. L. Avibactam is a covalent, reversible, non-β-lactam β-lactamase inhibitor. *PNAS*, **2012**, *109*, 11663–11668.

(93) Wang, D. Y.; Abboud, M. I.; Markoulides, M. S.; Brem, J.; Schofield, C. J. The road to avibactam: the first clinically useful non-β-lactam working somewhat like a β-lactam. *Future Med. Chem.*, **2016**, *8*, 1063–1084.

(94) Bush, K. A resurgence of β-lactamase inhibitor combinations effective against multidrug-

resistant Gram-negative pathogens. *Int. J. Antimicrob. Agents*, **2015**, *46*, 483–493.

(95) Abboud, M. I.; Damblon, C.; Brem, J.; Smargiasso, N.; Mercuri, P.; Gilbert, B.; Rydzik, A. M.; Claridge, T. D. W.; Schofield, C. J.; Frère, J. M. Interaction of Avibactam with Class B Metallo-β-Lactamases. *Antimicrob. Agents Chemother.*, **2016**, *60*, 5655–62.

(96) Schneider, I.; Queenan, A. M.; Markovska, R.; Markova, B.; Keuleyan, E.; Bauernfeind, A. New variant of CTX-M-type extended-spectrum beta-lactamases, CTX-M-71, with a Gly238Cys substitution in a *Klebsiella pneumoniae* isolate from Bulgaria. *Antimicrob. Agents Chemother.*, **2009**, *53*, 4518–21.

(97) Weldhagen, G. F. Integrons and β-lactamases—a novel perspective on resistance. *Int. J. Antimicrob. Agents*, **2004**, *23*, 556–562.

(98) Ishii, Y.; Eto, M.; Mano, Y.; Tateda, K.; Yamaguchi, K. In Vitro Potentiation of Carbapenems with ME1071, a Novel Metallo-Lactamase Inhibitor, against Metallo-Lactamase-Producing Pseudomonas aeruginosa Clinical Isolates. *Antimicrob. Agents Chemother.*, **2010**, *54*, 3625–3629.

(99) Wang, R.; Lai, T. P.; Gao, P.; Zhang, H.; Ho, P. L.; Woo, P. C. Y.; Ma, G.; Kao, R. Y. T.; Li, H.; Sun, H. Bismuth antimicrobial drugs serve as broad-spectrum metallo-β-lactamase inhibitors. *Nat. Commun.*, **2018**, *9*, 439.

(100) Parkova, A.; Lucic, A.; Krajnc, A.; Brem, J.; Calvopiña, K.; Langley, G. W.; McDonough, M. A.; Trapencieris, P.; Schofield, C. J. Broad Spectrum β-Lactamase Inhibition by a Thioether Substituted Bicyclic Boronate. *ACS Infect. Dis.*, **2020**.

(101) Cahill, S. T.; Cain, R.; Wang, D. Y.; Lohans, C. T.; Wareham, D. W.; Oswin, H. P.; Mohammed, J.; Spencer, J.; Fishwick, C. W. G.; McDonough, M. A. et al. Cyclic Boronates Inhibit All Classes of β-Lactamases. *Antimicrob. Agents Chemother.* **2017**, *61*.

(102) Baker, S. J.; Ding, C. Z.; Akama, K.; Zhang, Y. K.; Hernandez, V.; Xia, Y. Therapeutic potential of boron-containing compounds. *Future Medicinal Chemistry*, **2009**, *1*, 1275–1288.

(103) Krajnc, A.; Lang, P. A.; Panduwawala, T. D.; Brem, J.; Schofield, C. J. Will morphing boron-

based inhibitors beat the β-lactamases? *Curr. Opin. Chem. Biol.*, **2019**, *50*, 101–110.

(104) Morandi, F.; Caselli, E.; Morandi, S.; Focia, P. J.; Blázquez, J.; Shoichet, B. K.; Prati, F. Nanomolar inhibitors of AmpC beta-lactamase. *J. Am. Chem. Soc.*, **2003**, *125*, 685–95.

(105) Rojas, L. J.; Taracila, M. A.; Papp-Wallace, K. M.; Bethel, C. R.; Caselli, E.; Romagnoli, C.; Winkler, M. L.; Spellburg, B.; Prati, F.; Bonomo, R. A. Boronic Acid Transition State Inhibitors Active against KPC and Other Class A β-Lactamases: Structure-Activity Relationships as a Guide to Inhibitor Design. *Antimicrob. Agents Chemother.*, **2016**, *60*, 1751–9.

(106) Woon, E. C. Y.; Zervosen, A.; Sauvage, E.; Simmons, K. J.; Živec, M.; Inglis, S. R.; Fishwick, C. W. G.; Gobec, S.; Charlier, P.; Luxen, A. et al. Structure Guided Development of Potent Reversibly Binding Penicillin Binding Protein Inhibitors. *ACS Med. Chem. Lett.*, **2011**, *2*, 219–223.

(107) Neu, H. C. β-lactam antibiotics: Structural relationships affecting in vitro activity and pharmacologic properties. *Rev. Infect. Dis.*, **1986**, *8*, 237–259.

(108) Lomovskaya, O.; Sun, D.; Rubio-Aparicio, D.; Nelson, K.; Tsivkovski, R.; Griffith, D. C.; Dudley, M. N. Vaborbactam: Spectrum of Beta-Lactamase Inhibition and Impact of Resistance Mechanisms on Activity in *Enterobacteriaceae. Antimicrob. Agents Chemother.*, **2017**, *61*.

(109) Hecker, S. J.; Reddy, K. R.; Totrov, M.; Hirst, G. C.; Lomovskaya, O.; Griffith, D. C.; King, P.; Tsivkovski, R.; Sun, D.; Sabet, M. et al. Discovery of a Cyclic Boronic Acid β-Lactamase Inhibitor (RPX7009) with Utility vs Class A Serine Carbapenemases. *J. Med. Chem.*, **2015**, *58*, 3682–3692.

(110) Cahill, S. T.; Tyrrell, J. M.; Navratilova, I. H.; Calvopiña, K.; Robinson, S. W.; Lohans, C. T.; McDonough, M. A.; Cain, R.; Fishwick, C. W. G.; Avison, M. B. et al. Studies on the inhibition of AmpC and other β-lactamases by cyclic boronates. *Biochim. Biophys. Acta - Gen. Subj.*, **2019**, *1863*, 742–748.

(111) Krajnc, A.; Brem, J.; Hinchliffe, P.; Calvopiña, K.; Panduwawala, T. D.; Lang, P. A.; Kamps, J. J. A. G.; Tyrrell, J. M.; Widlake, E.; Saward, B. G. et al. Bicyclic Boronate VNRX-5133 Inhibits Metallo- and Serine-β-Lactamases. *J. Med. Chem.*, **2019**, *62*, 8544–8556.

(112) Liu, B., Trout, R. E. L., Chu, G. H., McGarry, D., Jackson, R. W., Hamrick, J. C., Daigle, D. M., Cusick, S. M., Pozzi, C., Luca, F. D. et al. Discovery of Taniborbactam (VNRX-5133): A Broad-Spectrum Serine- and Metallo-β-Lactamase Inhibitor for Carbapenem-Resistant Bacterial Infections. *J. Med. Chem.* **2019.**

(113) Macheboeuf, P.; Fischer, D. S.; Brown, T.; Zervosen, A.; Luxen, A.; Joris, B.; Dessen, A.; Schofield, C. J. Structural and mechanistic basis of penicillin-binding protein inhibition by lactivicins. *Nat. Chem. Biol.*, **2007**, *3,* 565–569.

(114) Dessau, M. A.; Modis, Y. Protein crystallization for X-ray crystallography. *J. Vis. Exp.* **2011**.

(115) RCSB PDB: Homepage. Available at: https://www.rcsb.org/. (Accessed: 12th November 2020)

(116) Fromme, P. XFELs open a new era in structural chemical biology. *Nature Chemical Biology*, **2015**, *11*, 895–899.

(117) Spence, J. C. H. XFELs for structure and dynamics in biology. *IUCrJ*, **2017**, *4*, 322–339.

(118) Brewster, A. S.; Young, I. D.; Lyubimov, A.; Bhowmick, A.; Sauter, N. K. *Processing serial crystallographic data from XFELs or synchrotrons using the cctbx.xfel GUI*. *Computational Crystallography Newsletter* **2019**, *10*.

(119) Levantino, M.; Yorke, B. A.; Monteiro, D. C.; Cammarata, M.; Pearson, A. R. Using synchrotrons and XFELs for time-resolved X-ray crystallography and solution scattering experiments on biomolecules. *Curr. Opin. Struct. Biol.*, **2015**, *35*, 41–48.

(120) Hirata, K.; Shinzawa-Itoh, K.; Yano, N.; Takemura, S.; Kato, K.; Hatanaka, M.; Muramoto, K.; Kawahara, T.; Tsukihara, T.; Yamashita, E. et al. Determination of damage-free crystal structure of an X-ray–sensitive protein using an XFEL. *Nat. Methods*, **2014**, *11*, 734–736.

(121) Neutze, R.; Moffat, K. Time-resolved structural studies at synchrotrons and X-ray free electron lasers: Opportunities and challenges. *Current Opinion in Structural Biology*, **2012**, *22*, 651–659.

(122) Johansson, L. C.; Stauch, B.; Ishchenko, A.; Cherezov, V. A. Bright Future for Serial Femtosecond Crystallography with XFELs. *Trends Biochem. Sci.*, **2017**, *42*, 749–762.

(123) Emma, P.; Frisch, J.; Huang, Z.; Marinelli, A.; Maxwell, T.; Loos, H.; Nosochkov, Y.; Raubenheimer, T.; Welch, J.; Wang, L.; Woodley, M. *LINEAR ACCELERATOR DESIGN FOR THE LCLS-II FEL FACILITY * LINEAR ACCELERATOR DESIGN FOR THE LCLS-II FEL FACILITY*. , **2019**.

(124) Zhao, Z. *XFEL Projects in China*. *29 th Linear Accelerator Conference,* **2018**.

(125) Henrich, B.; Becker, J.; Dinnapoli, R.; Goetticher, P.; Graafsma, H.; Hirsemann, H.; Klanner, R.; Krueger, H.; Mazzocco, R.; Mozzanica, A. et al*.* The adaptive gain integrating pixel detector AGIPD a detector for the European XFEL. *Nucl. Instruments Methods Phys. Res. Sect. A Accel. Spectrometers, Detect. Assoc. Equip.*, **2011**, *633*, S11–S14.

(126) Margaritondo, G.; Rebernik Ribic, P. A simplified description of X-ray free-electron lasers. *J. Synchrotron Radiat.*, **2011**, *18,* 101–108.

(127) Baturin, A. S.; Yeskin, I. N.; Trufanov, A. I.; Chadaev, N. N.; Sheshin, E. P.; Tschesov, R. G. Electron gun with field emission cathode of carbon fiber bundle. *J. Vac. Sci. Technol. B Microelectron. Nanom. Struct.*, **2003**, *21*, 354.

(128) Pellegrini, C. High power femtosecond pulses from an X-ray SASE-FEL. *Nucl. Instruments Methods Phys. Res. Sect. A Accel. Spectrometers, Detect. Assoc. Equip.*, **2000**, *445*, 124–127 (2000).

(129) Liu, H.; Lee, W. The XFEL Protein Crystallography: Developments and Perspectives. *Int. J. Mol. Sci.*, **2019**, *20*.

(130) Limborg, C. Design considerations for the LCLS. in *Nuclear Instruments and Methods in Physics Research, Section A: Accelerators, Spectrometers, Detectors and Associated Equipment*, **2003**, *507*, 378–381.

(131) Hattne, J.;, Echols, N.; Tran, R.; Kern, J.; Gildea, R.J.; Brewster, A. S.; Alonso-Mori, R.; Glöckner, C.; Hellmich, J.; Yaksmono, H. et al. Accurate macromolecular structures using minimal measurements from X-ray free-electron lasers. *Nat. Methods*, **2014**, *11*, 545–548.

(132) Hassell, A. M.; Ann, G.; Bledsoe, R. K.; Bynum, J. M.; Carter, H. L.; Deng, S. J. J.; Gampe, R. T.; Grisard, T. E.; Madauss, K. P.; Nolte, R. T. et al. Crystallization of protein–ligand complexes.

Acta Crystallogr. Sect. D Biol. Crystallogr., **2007**, *63*.

(133) Calvey, G. D.; Katz, A. M.; Schaffer, C. B.; Pollack, L. Mixing injector enables time-resolved crystallography with high hit rate at X-ray free electron lasers. *Struct. Dyn.*, **2016**, *3*.

(134) Oghbaey, S.; Sarracini, A.; Ginn, H. M.; Pare-Lebrosse, O.; Kuo, A.; Marx, A.; Epp, S. W.; Sherrell, D. A.; Eger, B. T.; Zhong, Y. et al. Fixed target combined with spectral mapping: approaching 100% hit rates for serial crystallography. *Acta Crystallogr. Sect. D Struct. Biol.*, **2016**, *72*, 944–955.

(135) Kovácsová, G.; Grünbein, M. L.; Kloos, M.; Barends, T. R. M.; Schlesinger, R.; Heberle, J.; Kabsch, W.; Shoeman, R.; Doak, R.B. et al. Viscous hydrophilic injection matrices for serial crystallography. *IUCrJ*, **2017**, *4*, 400–410.

(136) Nogly, P.; James, D.; Wang, D.; White, T. A.; Zatsepin, N.; Shilhova, A.; Nelson, G.; Liu, H.; Johansson, L.; Heymann, M. et al. Lipidic cubic phase serial millisecond crystallography using synchrotron radiation. *IUCrJ*, **2015**, *2*, 168–176.

(137) Fuller, F. D.; Gul, S.; Chatterjee, R.; Burgie, E. S.;, Young, I. D.; Lebrette, H.;, Srinivas, V.; Brewster, A. S.; Michel-Clark, T.; Clinger, J. A. et al. Drop-on-demand sample delivery for studying biocatalysts in action at X-ray free-electron lasers. *Nat. Methods*, **2017**, *14*, 443–449.

(138) Mukherjee, S.; Stull, J. A.; Yano, J.; Stamatatos, T. C.; Pringouri, K.; Stich, T. A.; Abboud, K. A.; Britt, R. D.; Yachandra, V. K.; Christou, G. Synthetic model of the asymmetric [Mn 3CaO 4] cubane core of the oxygen-evolving complex of photosystem II. *Proc. Natl. Acad. Sci. U. S. A.*, **2012**, *109*, 2257–2262.

(139) Suga, M.; Akita, F.; Sugahara, M.; Kubo, M.; Nakajima, Y.; Nakane, T.; Yamashita, K.; Umena, Y.; Nakabayashi, M.; Yamane, T. et al. Light-induced structural changes and the site of O=O bond formation in PSII caught by XFEL. *Nature*, **2017**, *543*, 131–135.

(140) DePonte, D. P.; Weierstall, U.; Schmidt, K.; Warner, J.; Starodub, D., Spence, J. C. H.; Doak, R.B. Gas dynamic virtual nozzle for generation of microscopic droplet streams. *J. Phys. D. Appl. Phys.*, **2008**, *41*.

(141) Olmos, J. L.; Pandey, S.; Martin-Garcia, J. M.; Calvey, G.; Katz, A.; Knoska, J.; Kupitz, C.; Hunter, M. S.; Liang, M.; Oberthuer, D. et al. Enzyme intermediates captured “on the fly” by mix-and-inject serial crystallography. *BMC Biol.*, **2018**, *16*.

(142) Sierra, R. G.; Gati, C.; Laksmono, H.; Dao, E. H.; Gul, S.; Fuller, F.; Kern, J.; Chatterjee, R.; Ibrahim, M.; Brewster, A. S. et al. Concentric-flow electrokinetic injector enables serial crystallography of ribosome and photosystem II. *Nat. Methods*, **2016**, *13*, 59–62.

(143) O’Sullivan, M. E.; Poitevin, F.; Sierra, R. G.; Gati, C.; Dao, E. H.; Rao, Y.; Aksit, F.; Ciftci, H.; Corsepius, N.; Greenhouse, R. et al. Aminoglycoside ribosome interactions reveal novel conformational states at ambient temperature. *Nucleic Acids Res.*, **2018**, *46*, 9793–9804.

(144) Owen, R. L.; Axford, D. N.; Sherrell, D. A.; Kuo, A.; Ernst, O. P.; Schulz, E. C.; Miller, R. J. D.; Mueller-Werkmeister, H. M. Low-dose fixed-target serial synchrotron crystallography. *Acta Crystallogr. Sect. D, Struct. Biol.*, **2017**, *73*, 373–378.

(145) Hunter, M. S.; Segelke, B.; Messerschmidt, M.; Williams, G. J.; Zatsepin, N. A.; Barty, A.; Benner, W. H.; Carlson, D. B.; Coleman, M.; Graf, A. et al. Fixed-target protein serial microcrystallography with an X-ray free electron laser. *Sci. Rep.*, **2014**, *4*, 1–5.

(146) Davy, B.; Axford, D. N.; Beale, J. H.; Butryn, A.; Docker, P.; Ebrahim, A.; Leen, G.; Orville, A. M.; Owen, R. L.; Aller, P. Reducing sample consumption for serial crystallography using acoustic drop ejection. *J. Synchrotron Radiat.*, **2019**, *26*, 1820–1825.

(147) Roedig, P.; Vartiainen, I.; Duman, R.; Panneerselvam, S.; Stübe, N.; Lorbeer, O.; Warmer, M.; Sutton, G.; Stuart, D. I.; Weckert, E. et al. A micro-patterned silicon chip as sample holder for macromolecular crystallography experiments with minimal background scattering. *Sci. Rep.*, **2015**, *5*.

(148) Rabe, P.; Beale, J. H.; Butryn, A.; Aller, P.; Dirr, A.; Lang, P. A.; Axford, D. N.; Carr, S. B.; Leissing, T. M.; McDonough, M. A. et al. Anaerobic fixed-target serial crystallography. *IUCrJ*, **2020**, *7*, 901–912.

Chapter 2 – Biophysical and biochemical studies on the β-lactamase catalysed hydrolysis of Faropenem and Biapenem

Abstract

Both penems and carbapenems have been used clinically as antibacterials and β-lactamase inhibitors, with carbapenems being of particular clinical importance. However, their efficacy is increasingly being limited, as they can be hydrolysed by MBLs and SBLs. This chapter reports studies on faropenem, an orally active penem with a C2 tetrahydrofuran (THF) ring, and biapenem, a carbapenem antibiotic that is taken intravenously. The studies focused on VIM-1 and VIM-2 (both B1 MBLs), L1 (a B3 MBL), and KPC-2 (a class A SBL). The results of the kinetics studies show that all the tested enzymes have some hydrolytic activity against faropenem and biapenem. This conclusion was supported by NMR spectroscopic studies, which showed the presence of multiple products with both faropenem and biapenem. Imine and enamine products were seen in all cases at varying levels. In the case of faropenem, an imine product in which the THF ring was opened was observed in all cases. Imines with a closed THF ring were only observed with VIM-1 and VIM-2. Crystallographic analyses with faropenem showed an imine THF ring open product present at the active site of KPC-2 and VIM-2, and an imine THF ring closed product in the active site of L1. Crystallographic analyses with biapenem and VIM-2 show both the enamine and imine β-lactam ring opened derived products present in the active site

Introduction

VIM-2 is one of the most widespread MBLs in the world (see Chapter 1 - Introduction).[1,2] VIM-2 originated in *P. aeruginosa,* but is commonly found in other Gram-negative bacteria, where it is produced alongside other β-lactamases.[3] VIM-2 is a broad spectrum β-lactamase, hydrolysing penicillins, cephalosporins and carbapenems but not monobactams (**Figure 1**). Like with other B1 subfamily MBLs, VIM-2 has two zinc ions at its active site (**Figure 2**).[2,3]

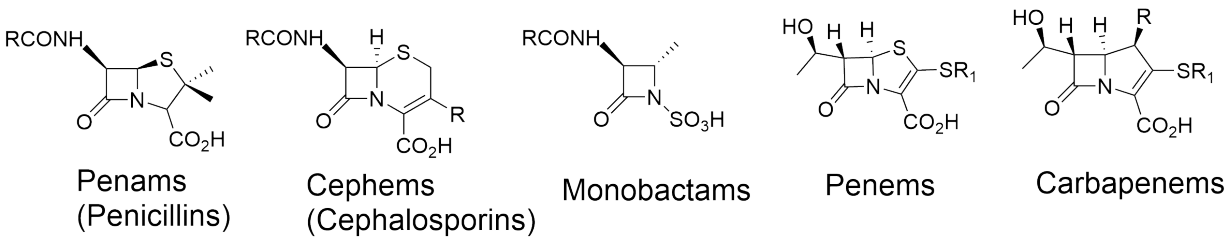


Figure 1: The different classes of clinically used β-lactams. This chapter mainly focuses on penems and carbapenems which have a thiazoline and pyrroline ring fused to the β-lactam ring.

As mentioned in the Introduction, the B1 MBL active site zinc ions are each bound by three residues, with Zn1 interacting with three histidine residues (His116, His118 and His196), and Zn2 with Asp120, Cys221 and His263 (**Figure 2**).[4] The zinc ions are bridged by a water molecule, as seen in resting state structures. The zinc ions can then act as Lewis acids, making the water/hydroxide a stronger nucleophile.[4] Studies have shown that the cysteine interacting with Zn2 can become oxidised in VIM-2, preventing Zn2 binding and rendering the enzyme inactive.[5] The cysteine oxidation alters the shelf life of VIM-2 crystals when performing structural studies on enzyme substrate interactions.[6]

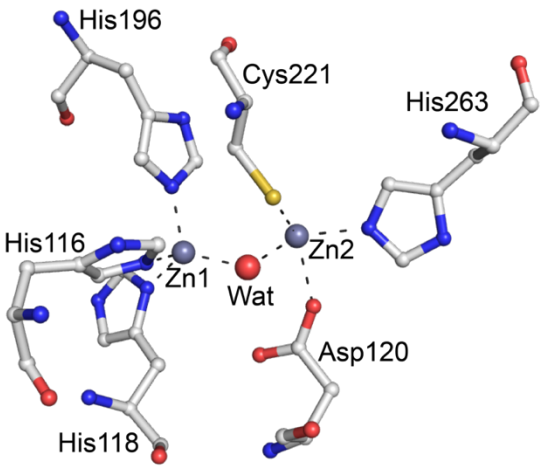


Figure 2: Views from a crystal structure of the active site of VIM-2. The nucleophilic water (Wat) interacts with the carbonyl in the β-lactam ring and is proposed to hydrolyse the ring (PDB 4BZ3).[7]

Carbapenem hydrolysis: what we know

Previous studies on carbapenem hydrolysis performed by Dr. Christopher Lohans (Schofield group, Oxford University) have shown that carbapenems can form several different product types following degradation by β-lactamases.[8,9] Figure 3 shows the formation of two different hydrolysis product types, i.e., an enamine form, which is proposed to be the nascent enzymatic product, and an imine form. The existence of two separate product types is due to the pyrroline ring which can exist in enamine and imine forms. The enamine form can tautomerise non-enzymatically to form the imine products.[8,9] Class D SBLs (oxacillinases) can form lactone products as well as the established hydrolysis products, which can exist as enamine or imine product forms (**Figure 3**). Both the enamines and imines are formed by all SBLs and MBLs that have carbapenemase activity, with the imine existing as (*S*)- and (*R*)- C2 stereoisomers, resulting from epimerisation of the chiral centre at the C2 position (**Figure 3**).

All three tautomeric enamine/imine forms have been observed in crystallographic analyses.[3,10,11] The tautomerisation between the imine and enamine products appears to be time dependent and to vary with different β-lactamases.[8] It is thought that the tautomerisation between the enamine and imine products has the potential to result in the inhibition of β-lactamase catalysis.[12] For example, studies on sulfhydryl variable β-lactamase 1 (SHV-1), a class A SBL, have led to the proposal that the acyl-enzyme complex is hydrolysed when the pyrroline ring is in the imine form, but not in the enamine form.[12] It has been proposed that the β-lactones are formed through the nucleophilic attack of the carbapenem-derived hydroxyethyl side chain onto the ester carbonyl in the acyl-enzyme complex although this is not certain.[9] These findings led me to study the interactions of faropenem and biapenem with both SBLs and MBLs, which would provide a better understanding of the tautomerisation and epimerisation that may occur during hydrolysis.

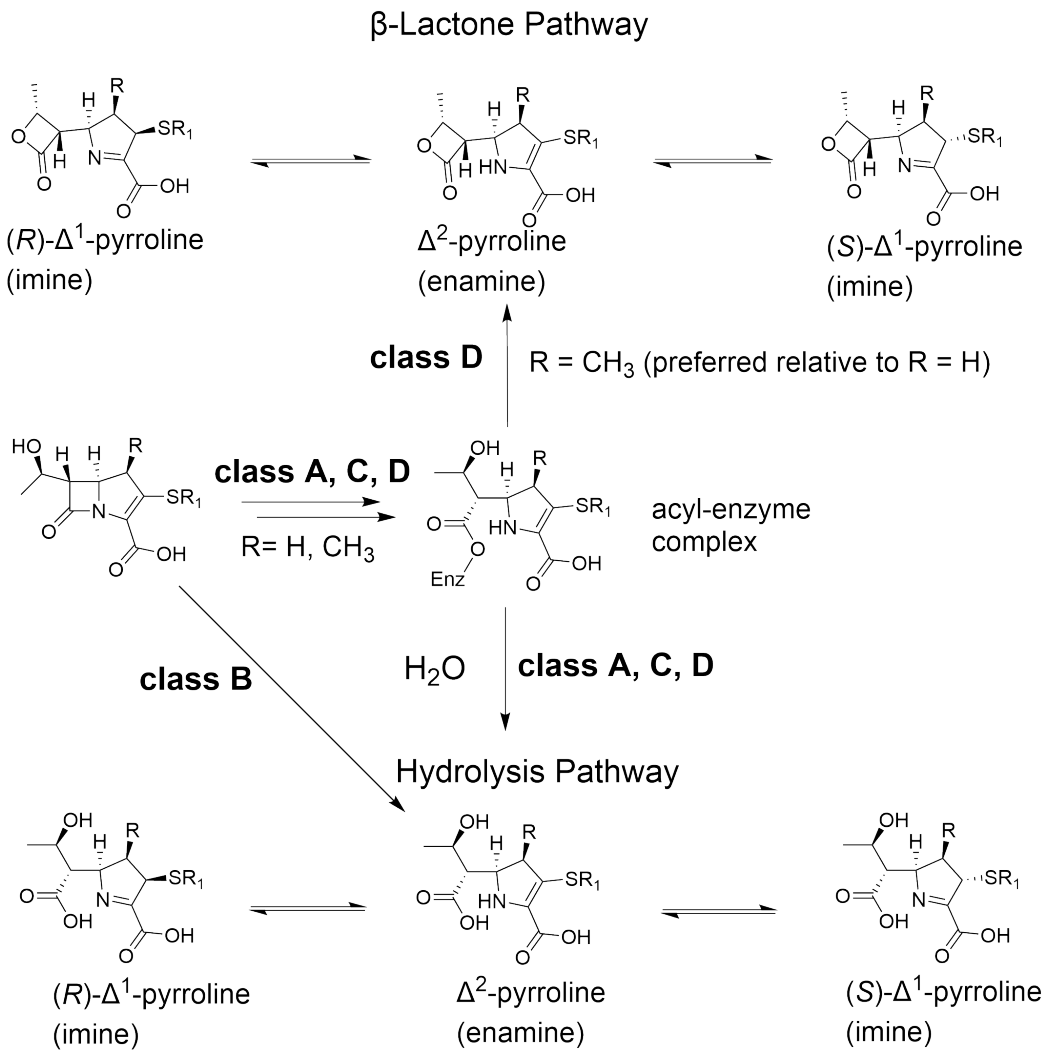


Figure 3: Products of carbapenem degradation formed by different classes of β-lactamases. To date, only the OXAs (Class D SBLs) have been shown to produce the lactone products. It is proposed that enamines are the major initial products. Whereas all SBLs use a nucleophilic serine to hydrolyse β-lactams, MBLs (Class B) use one or two zinc ions to activate a water molecule for nucleophilic attack.[9]

Biapenem

Biapenem was approved in 2001 for clinical use for the treatment of serious bacterial infections, such as lower respiratory infections and complicated urinary tract infections (UTIs).[13] Biapenem is a highly effective carbapenem, with strong coverage against Gram-negative and Gram-positive bacteria as well as both anaerobic and aerobic bacteria.[14] Biapenem is commonly used in East Asia to treat more serious infections such as respiratory diseases and UTIs.[13] Moreover, recent studies have revealed that

biapenem, in combination with the antibiotic rifampicin, may have some activity against *Mycobacterium tuberculosis,* inhibiting the activity of BlaC and Ldt enzymes.[15]

Biapenem belongs to the second generation of carbapenems and is given to patients intravenously twice daily. In addition, it has fewer adverse side effects in comparison to previously developed carbapenems since it is more stable against human renal dihydropeptidase 1 (DHP-1) meaning it does not need to be administered with DHP-1 inhibitors such as Cilastatin.[13,14] Biapenem has been proven be a potent SBL inhibitor against enzymes such as Temoniera β-Lactamase (TEMs). However, biapenem is hydrolysed by all three subclasses of MBLs.

Penems and faropenem

Penems, like the clinically tested carbapenems, are purely synthetic antibiotics that are often used to treat serious microbial infections. Instead of the pyrroline ring found in the carbapenems, the penems have a thiazoline ring attached to the β-lactam ring (**Figure 1**). Penems may be viewed as hybrids of the penicillins, cephalosporins, and carbapenems.[16] Penems show inhibitory activity against SBLs as shown by BRL 42715, which displayed potent inhibition of SBLs belonging to the OXA, SHV, and TEM subfamilies.[17] BRL 42715, like related SBL inhibitors, reacts to form an acyl-enzyme complex; however unusually, the acyl-enzyme complex rearranges to form a cyclic aminoacrylate derivative (**Figure 4**).[17,18]

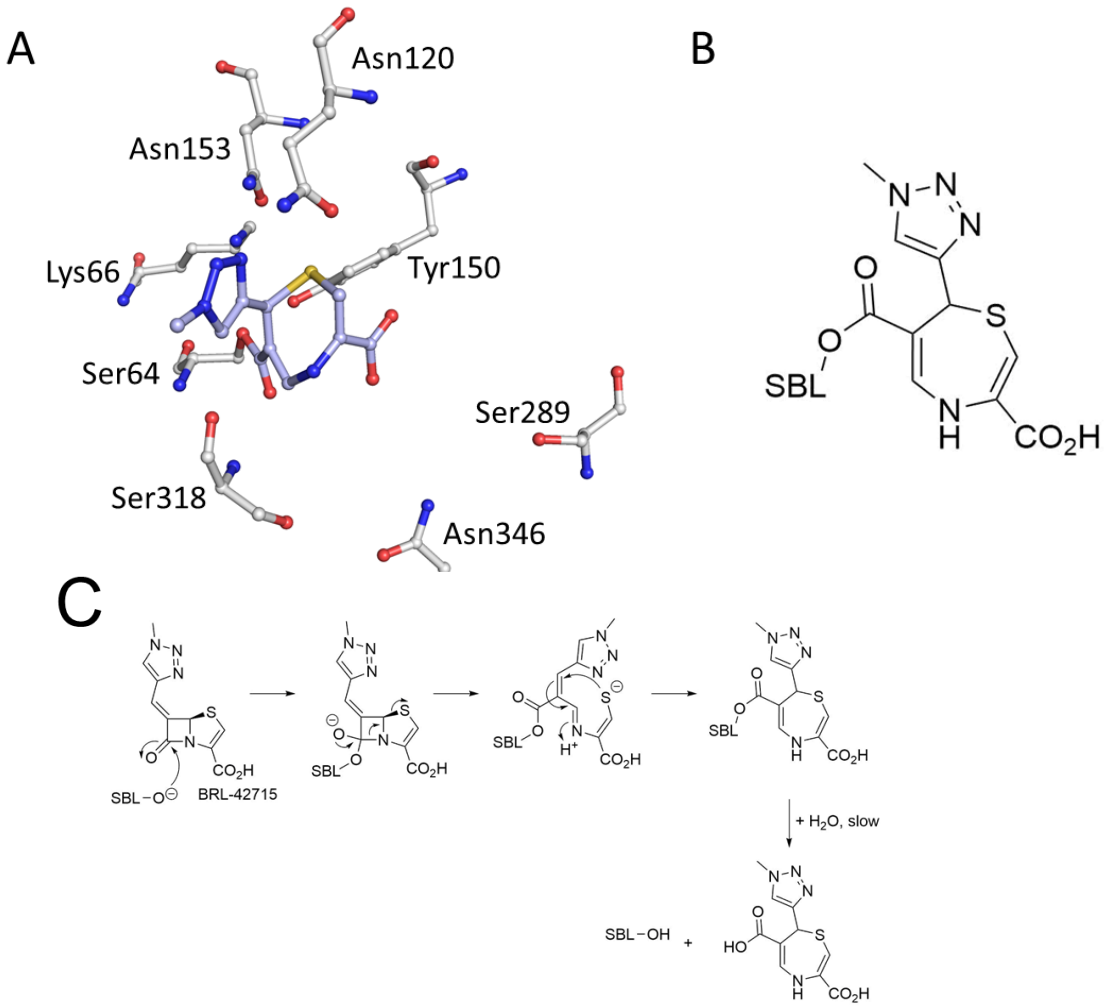


Figure 4: Mechanism of action for BRL 42715 with the SBL 908R. A) View from a structure of the aminoacrylate derivative of BRL 42715 in the active site of the 908R SBL (PDB 1Y54[17]). B) is a structure of the covalent complex derived from BRL 42715 with an SBL serine residue; C) A mechanism showing the cyclisation of BRL 42715 following reaction with the nucleophilic serine of 908R.[7]

Faropenem is an orally active penem antibiotic,[19] that has a C2 THF ring, it is currently the only clinically approved penem (although sulopenem is currently in clinically trials).[20] Faropenem is a commonly used medication in Asia for respiratory and UTIs.[21] Faropenem, like the carbapenems, inhibits certain SBLs including the class C SBL AmpC and even certain extended spectrum SBLs such as CTX-M.[22] However, faropenem and other carbapenems are susceptible to hydrolysis by B1 MBLs such as NDM-1.[23] Previous structural studies have been done on faropenem with SBLs and PBPs, although most of these structures are at a fairly low resolution.[24–26]

Recent studies with faropenem and β-lactamases have demonstrated the formation of several additional products.[25,27] One of these is the formation of two separate fragments due to C5-C6 fragmentation, yielding 3-hydroxybutyrate and a thiazole product (**Figure 6**).[27] These products were observed using NMR when faropenem was mixed with certain β-lactamases such as the S70C variants of the SBLs KPC-2 (class A) and OXA-48 (class D) and the transpeptidase Ldt_{Mt2}, while fragmentation was not seen for wild-type KPC-2 and OXA-48 (**Figure 5**).[27]

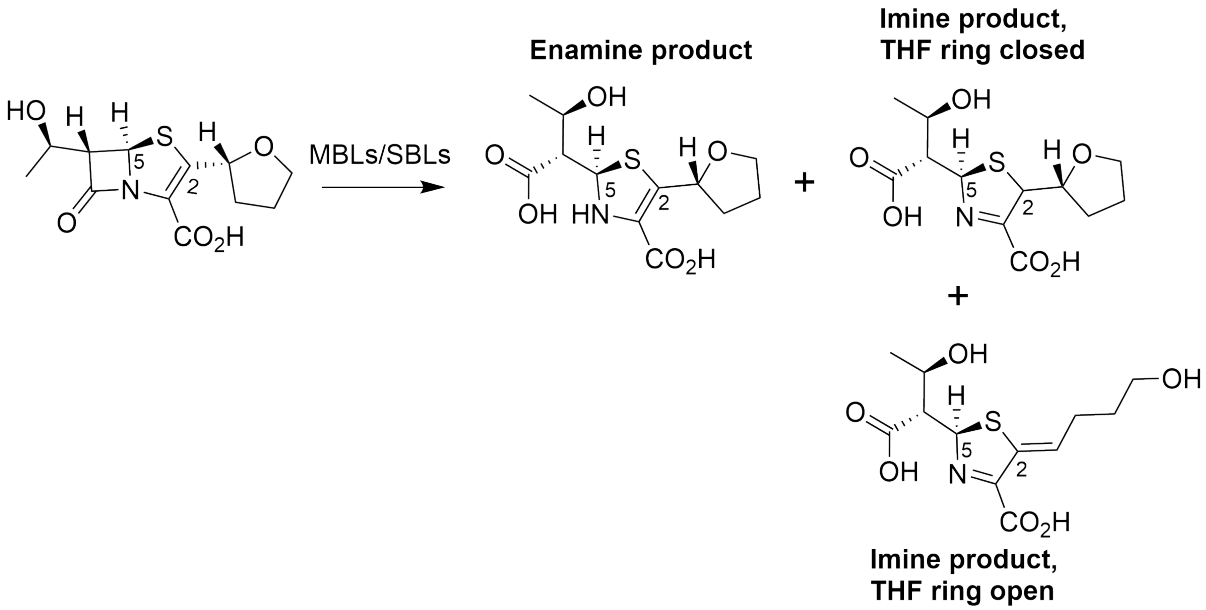


Figure 5: Potential products from faropenem hydrolysis. Faropenem hydrolysis leads to multiple products, including potential C2 stereoisomers for the ring closed imine product.

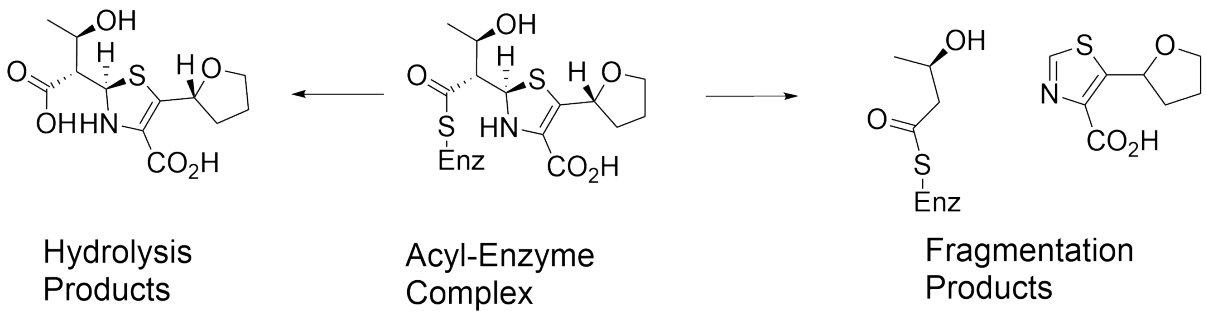


Figure 6: Faropenem fragmentation as observed in Ldt_{mt2}. Hydrolysis products are formed alongside the fragmentation products produced.

In order to better understand the mechanism of carbapenems and penems, it was decided to perform crystallographic studies on VIM-2 with a carbapenem and a penem, i.e., biapenem and faropenem. Crystallographic studies were also attempted with some cephamycin antibiotics and imipenem, as our knowledge of their hydrolysis *via* MBLs is limited; however, these experiments were unsuccessful, with no density corresponding to substrates or products observed in the active site. To compare the enzyme behaviour in crystals and in solution, solution studies were carried out with both biapenem and faropenem. Faropenem solution studies were performed by Ms. Tika Malla and Dr. Philip Hinchliffe. NMR studies were performed in order to compare and contrast what was observed in the crystal structures, whereas kinetic assays provided a clear understanding of kinetic constants. Solution studies were conducted with both MBLs and SBLs, i.e., VIM-1, VIM-2, KPC-2, OXA-10, OXA-23, OXA-48, L1 and NDM-1.

In collaboration with the University of Bristol, crystallographic analyses were conducted on faropenem complexed with KPC-2 and L1. KPC-2 is a class A serine-β-lactamase that has carbapenemase activity. It was originally found in *Klebsiella pneumoniae,* but has now been found in several other Gram-negative pathogens including *Escherichia coli* and *Acinetobacter spp*.[28,29] This makes KPC-2 one of the leading causes of β-lactam failure in clinical infections.[30,31]

L1 is a subclass B3 MBL that is chromosomally encoded in *Stenotrophomonas maltophilia*, which may also produce several different SBLs, and is consequently extremely difficult to treat in a clinical setting.[32] Though there is little sequence homology between VIM-2 and L1, they both have the conserved MBL αβ/βα fold and use two zinc ions for β-lactam hydrolysis.[33,34] L1 is a broad spectrum β-lactamase which is able to hydrolyse all classes of β-lactams except monobactams.[32,33] All experiments relating to L1 and KPC-2 were done by Dr. Philip Hinchliffe and Dr. Catherine Tooke. A variant version of KPC-2 (KPC-2^{E166Q}) was used to prevent deacylation.

Despite the fast turnover rate of VIM-2 and other MBLs, which makes it difficult to observe reaction intermediates by crystallography, conventional cryo crystallography can still offer a wide range of information about the structural changes and interactions that may occur during enzymatic catalysis, making it a useful, if limited, tool. Furthermore, in comparison to XFELs, synchrotrons are still more accessible for data collection on a large number of crystals with different substrates and ligands. High resolution datasets of VIM-2 with hydrolysed faropenem and biapenem were obtained. NMR solution studies indicated the formation of multiple products upon the hydrolysis of both faropenem and biapenem. The major products observed in NMR were in some cases different, demonstrating that the crystallographic observations do not always align with what is seen in solution.

Materials and Methods

Transformation and Starter Culture

The VIM-2 gene (bla_{VIM-2}) was expressed using a pOPINF plasmid which contains chloramphenicol and ampicillin resistance genes and a T7 promoter/lac operator as previously described.[34] The plasmid also codes for a hexahistidine tag at the N-terminus of VIM-2, which is used for nickel affinity purification.[35] The pOPINF vector was initially transformed into *E. coli* BL21 (DE3) pLysS cells. However, the strain was changed to *E. coli* Lemo21 (DE3) cells due to technical issues. 50 ng of DNA plasmid was added to an aliquot of competent cells and incubated on ice for 30 minutes.[36] The mixture of cells and plasmid DNA were heat shocked at 42°C for 30 seconds in order allow the plasmid to enter the competent cells. Super Optimal broth with Cabolite repression (SOC) media (from ThermoFisher) was next added, and the cells were incubated on ice for two minutes. The cells were incubated for 1 hour at 37°C in a water bath to enable cell growth. After incubation, the cells were spread onto a lysogeny broth (LB) agar plate containing 50 μg/mL ampicillin, and the plate was incubated overnight at 37°C.[37]

In order to create a starter culture, a single colony transformed with the pOPINF plasmid was used to inoculate 100 mL of LB media containing 50 μg/mL ampicillin. The media was incubated overnight at

37°C whilst being shaken at 150 rpm, ensuring aeration and nutrient availability for the bacteria.[37] All experiments were done under sterile conditions using a Bunsen burner or a sterile biosafety cabinet.

VIM-2 Protein Production

VIM-2 was produced using a large culture of *E. coli* (7.2 - 12 L) that was transformed with the pOPINF plasmid. After switching to Lemo21 (DE3) cells, several expression trials were carried out by Dr. Gareth Langley and Dr. Karina Calvopiña to identify the optimal conditions for VIM-2 protein production. The concentrations of isopropyl-β-D-thiogalactopyranoside (IPTG), temperatures, and incubation periods were all varied during these expression trials. Starter culture (10 mL) was added to 600 mL of 2TY media containing 50 μg/mL ampicillin. The cells were incubated at 37°C, shaking at 150 rpm; the optical density at 600 nm was measured every 30 minutes to determine when the *E. coli* cells reached the log, or exponential phase of growth (OD_{600} 0.6-0.7).[37,38]

Once the cell culture had reached an OD of 0.6-0.7, the temperature of the culture was lowered to 30°C, 0.5 mM of IPTG was added, and the cell culture was incubated for another 4 hours shaking at 150 rpm. IPTG mimics allolactose, which triggers the expression of the *lac* operon and any genes regulated by it.[39] Unlike allolactose however, IPTG is not degraded by the cell, allowing for consistent expression throughout incubation.[39] The culture was then centrifuged at 8,000 rpm for 10 minutes to remove the growth media, and the cell pellet was frozen and stored at -80°C.

VIM-2 Nickel Affinity Purification

The frozen bacterial cells were resuspended in 50 mL - 100 mL of Lysis buffer (50 mM Tris pH 7.5, 500 mM NaCl, 5 mM imidazole and 0.2% v/v Tween) at 4°C. DNAse and protease inhibitor (ThermoFisher) were also added to the mixture to prevent the degradation of VIM-2 upon cell lysis and to digest any DNA contaminants respectively. Once the cells were resuspended, they were sonicated on ice for 10 minutes at 60% amplitude (9.9 seconds pulse with 9.9 seconds break) then centrifuged at 20,000 rpm

for 30 min. The supernatant was clarified using an 0.22 µm filter, then loaded onto a 5 mL His Trap column (Sigma Aldrich) for Immobilised Metal Affinity Chromatography (IMAC). The column was washed extensively with Wash buffer (50 mM Tris pH 7.5, 500 mM NaCl and 5 mM imidazole) after which the concentration of Elution buffer (50 mM Tris pH 7.5, 500 mM NaCl, and 500 mM imidazole) was increased to 4% for 10 column volumes after which the concentration of the Elution buffer was increased in a gradient. The low imidazole concentration helps remove any impurities that might be non-specifically binding to the nickel resin. The protein was then eluted using a gradient of the Elution buffer; the concentration of the Elution buffer was increased since imidazole has a similar structure to the side chain of histidine, and therefore out competes the His tag for binding to the nickel resin, causing the protein to be eluted into the appropriate fractions.[35]

Fractions that corresponded to the elution peak (visualised using UV/vis) were analysed on a Sodium Dodecyl Sulfate Polyacrylamide electrophoresis gel (SDS-PAGE) to identify fractions containing VIM-2. For SDS-PAGE analysis, 5 µL of the loading dye (4% v/v SDS) was added to 15 µL samples of the fractions.[37] Samples of the original cell lysates were also used to ascertain the extent of VIM-2 production. Samples were heated at 95°C for three minutes, then loaded onto a NuPAGE gel with 4-12% (v/v) polyacrylamide (ThermoFisher) and electrophoresed for 55 minutes at 200 V. The gel was stained with Instant Blue Coomassie stain (Merck) to analyse the fraction samples.[37] Once it was clear which samples contained VIM-2, these fractions were pooled and concentrated for gel filtration using a protein concentrator with 10 kDa cut off (Merck).

VIM-2 Gel Filtration Purification

VIM-2 was concentrated to 2 mL, and then loaded onto a 300 mL Superdex S200 gel filtration column 16/600 (SigmaAldrich) pre-equilibrated in 20 mM Tris pH 7.5 and 200 mM NaCl. Gel filtration, or Size Exclusion Chromatography (SEC) is a method of protein purification that separates proteins by size. The method involves the use of different sized columns and resins.[40,41] Fractions observed using

UV/Vis spectrophotometry in the elution peak were analysed by SDS PAGE to confirm the presence and purity of VIM-2, and those with purified VIM-2 were pooled.

His tag Cleavage and Reverse IMAC purification

For crystallographic purposes, the His tag of VIM-2 was removed, as it can potentially impact protein structure, as well as its ability to crystallise.[42] The His tag was cleaved using the 3C protease produced by Dr. Jürgen Brem (50 mg/mL), utilising the 3C cleavage site encoded for by the pOPINF plasmid. 50 µL of 3C protease was added to the VIM-2 fractions from the gel filtration and incubated overnight at 4°C whilst gently shaking. Once the incubation was complete, the concentration of imidazole in the protein solution was increased to 20 mM (to prevent non-specific binding of VIM-2), and the mixture was loaded onto a 5 mL His Trap column (GE Healthcare).[37,43]

The cleaved protein was eluted using 50 mM Tris pH 7.5, 500 mM NaCl and 20 mM imidazole; any uncleaved protein was eluted using 500 mM imidazole. Fractions were analysed by SDS-PAGE to check if the His tag had been cleaved. The cleaved protein was concentrated, and buffer exchanged into crystallography buffer (50 mM HEPES pH 7.5, 100 mM NaCl, 1 mM TCEP and 100 µM $ZnCl_2$) to a final concentration of 8.5 mg/mL. Buffer exchange was done by concentrating the protein to 1 mL with a protein spin concentrator (Merck), then diluted it by a factor of 10 with crystallisation buffer, the dilution process was repeated 3 times.

Crystallisation of VIM-2

A previously developed VIM-2 crystallisation screen created by Dr. Jürgen Brem was initially used to see if the new batch of VIM-2 would crystallise (**Table 1**). This optimisation plate used a range of concentrations of magnesium formate and polyethylene glycol 3350 (PEG 3350) in a 96 well plate (Art Robbins low profile INTELLI plates, US).[34] Plates were set up at room temperature using a PhoenixRE robot (Art Robbins, US) three different protein: reservoir ratios were set up for each condition 2:1, 1:1

and 1:2 using sitting drop vapour diffusion. Another crystallography optimisation plate was created by Dr. Gareth Langley with magnesium chloride, PEG 8000 at different concentration and Tris at varying pH values (**Table 2**).[43] All plates were set up and incubated at ambient temperature. Plates were monitored once a day, and any conditions with crystals were marked for soaking and harvesting. All crystals were approximately 100 x 50 x 20 µm in size.

Magnesium formate (M)	**PEG 3350 (%)**											
	15	**16**	**17**	**18**	**19**	**20**	**21**	**22**	**23**	**24**	**25**	**26**
0												
0.05												
0.1				**X**								
0.15					**X**	**X**	**X**					
0.2												
0.25	**X**				**X**	**X**						
0.3												
0.35					**X**	**X**			**X**			

Table 1: The optimisation plate created by Dr. Jürgen Brem. X marks conditions where crystals appeared.

Tris buffer (pH)	PEG 8000 (%)											
	7.5	10	12.5	15	17.5	20	22.5	25	27.5	30	32.5	35
7.0									X		X	X
7.25								X		X	X	X
7.5												X
7.75											X	
8.0									X			
8.25												
8.5												
8.75												

Table 2: The optimisation block created by Dr. Gareth Langley. The concentration of Tris buffer was constant throughout the plate (0.1 M) along with the concentration of magnesium chloride (0.2 M). X marks conditions where crystals appeared.

Vapour diffusion is the most common method of protein crystallisation and is done using sitting drop or hanging drop methods.[44] Small droplets that contain protein and precipitant solution equilibrate with the well solution in the crystallisation plate over a period of time.[44] During the equilibration process, the concentration of protein and precipitant in the drop increases compared to the well solution, causing the protein to enter the nucleation phase for crystallisation (**Figure 7**).[45]

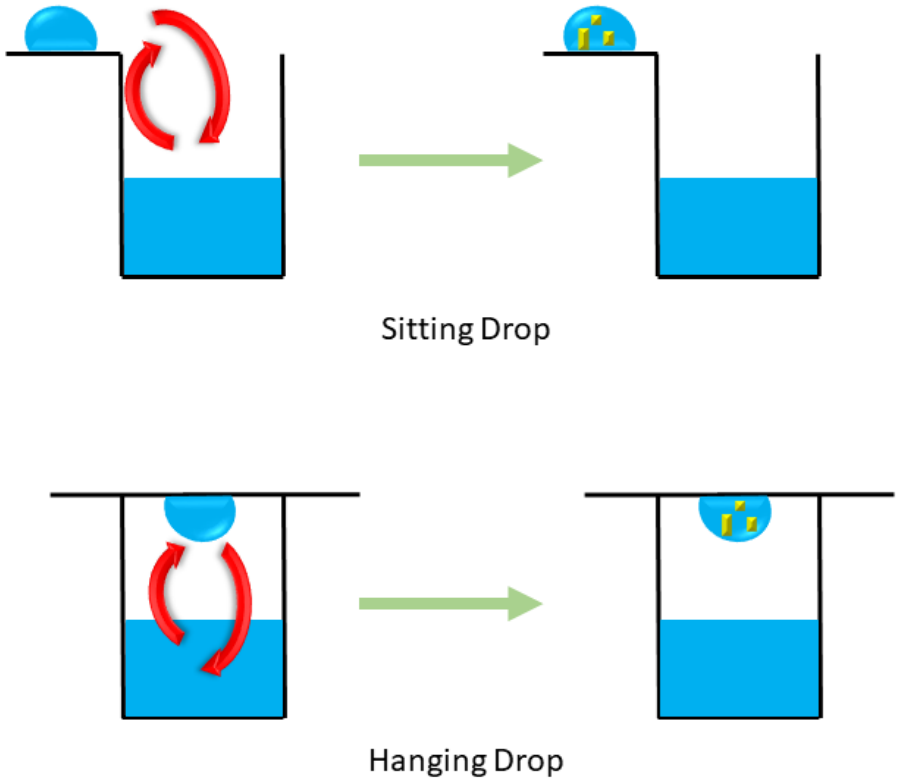


Figure 7: Diagram illustrating the sitting drop and hanging drop methods. The well solution at the bottom causes the evaporation of the well solution in the crystallisation drop. Evaporation causes the protein concentration to increase in the drop, causing the protein to nucleate and crystallise. If the protein concentration is too high, then the protein may precipitate.

Data Collections at Synchrotrons

Synchrotrons are circular particle accelerators that are used to produce X-ray radiation.[46] They produce X-rays with a million time more photons compared to in house sources.[46] The most commonly used method to compare X-ray sources is brilliance, which takes into consideration several different aspects of the X-ray source including the cross-sectional area of the beam, the number of photons produced, the angular divergence of the photons, and the photons that fall within a 0.1% bandwidth

of the central wavelength.[47] The greater the brilliance, the more photons in a given wavelength and the more the direction of the beam is concentrated on a spot per unit of time. All synchrotrons work on the same principle, where electrons are released by an electron gun and accelerated into the storage ring (**Figure 8**). Whilst in the storage ring, the electrons circulate at high speed and produce radiation, although they do not gain extra energy (**Figure 8**). The radiation produced is captured by various beamlines that start at bending magnets or dipole magnets.[47]

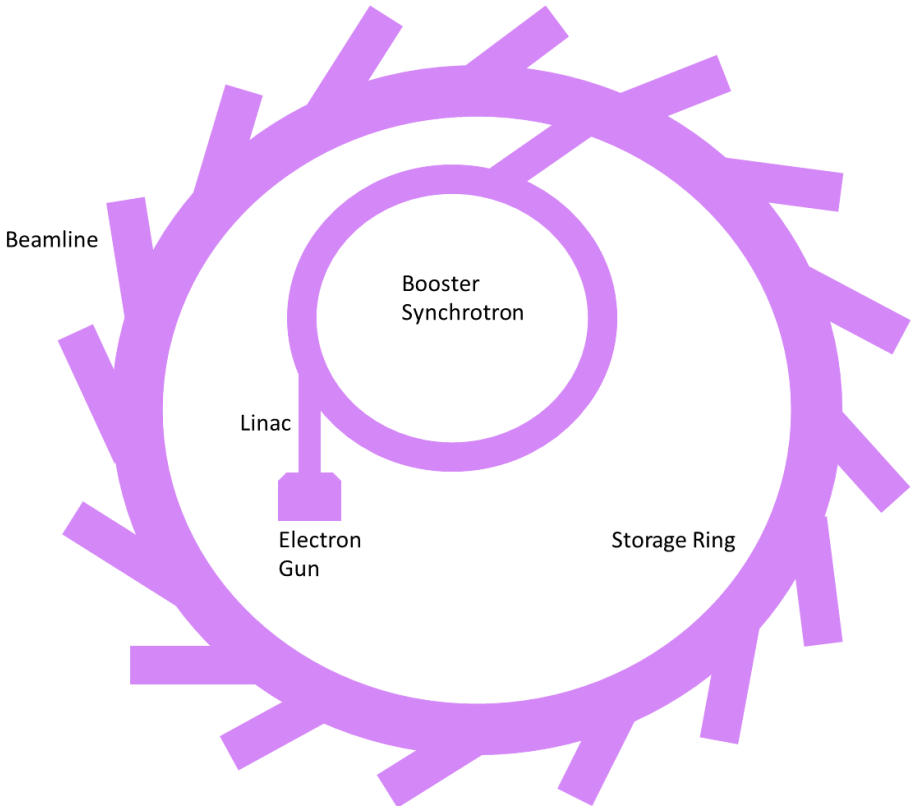


Figure 8: Outline of a synchrotron source. Electrons are released from the electron gun, a high voltage cathode is heated in a vacuum environment, which allows the electrons to escape by giving them a large amount of thermal energy. The electrons are accelerated using earthed anodes. The linac further accelerates the particles to 100 MeV. The electrons are then accelerated in the straight sections of the booster ring using a radio frequency voltage source. Once the electrons enter the storage ring, the kinetic energy of the electrons is kept constant. The electrons pass through undulators that are found throughout the storage ring to produce photons. The photons are then directed to individual beamlines for experiments.

Synchrotrons have been used as a radiation source for over 40 years.[48] The Diamond Light Source was the synchrotron used to collect the data described in this thesis. It is a third-generation synchrotron that contains an array of magnets known as insertion devices or undulators.[47] Undulators are placed in the linear sections of the ring and contain a structure of dipole magnets which produces a magnetic field that alternates along the undulator. When the electrons pass through the undulator, the magnetic structure causes the electrons to undergo oscillations and to produce photons.[49]

Soaking Compounds into Crystals and Data Collection

To gain a structural understanding of antibiotic binding to VIM-2, several different carbapenems, penems, cephalosporins and cephamycins were soaked into VIM-2 macrocrystals (crystals >20 μm^3) at various time points (**Figure 9**). All the antibiotics were dissolved in water at a concentration of 50 mM. The crystals produced from the optimisation block mentioned previously were soaked with ~300 nL of each antibiotic at 1 minute, 5 minutes, 10 minutes and 30 minutes. By soaking the crystals in an excess solution of the substrate, the substrate can enter the crystal through the solvent channels and bind to the protein in the active site.[50] Crystals of VIM-2 were cryoprotected with 20% (v/v) glycerol and cryocooled in liquid nitrogen and sorted into pucks for data collection at Diamond Light Source. KPC-2 and L1 crystals were soaked at the University of Bristol using 20 mM faropenem for 2.5 hours and 8 hours, respectively. 1800 images of all crystals were collected at the I04-1 beamline at Diamond Light Source at 100 K with 50 ms exposure at a wavelength of 0.9159 Å with an energy of 12.8 keV and 75% transmission. Diffraction patterns produced by the crystals were then used to solve the structure.

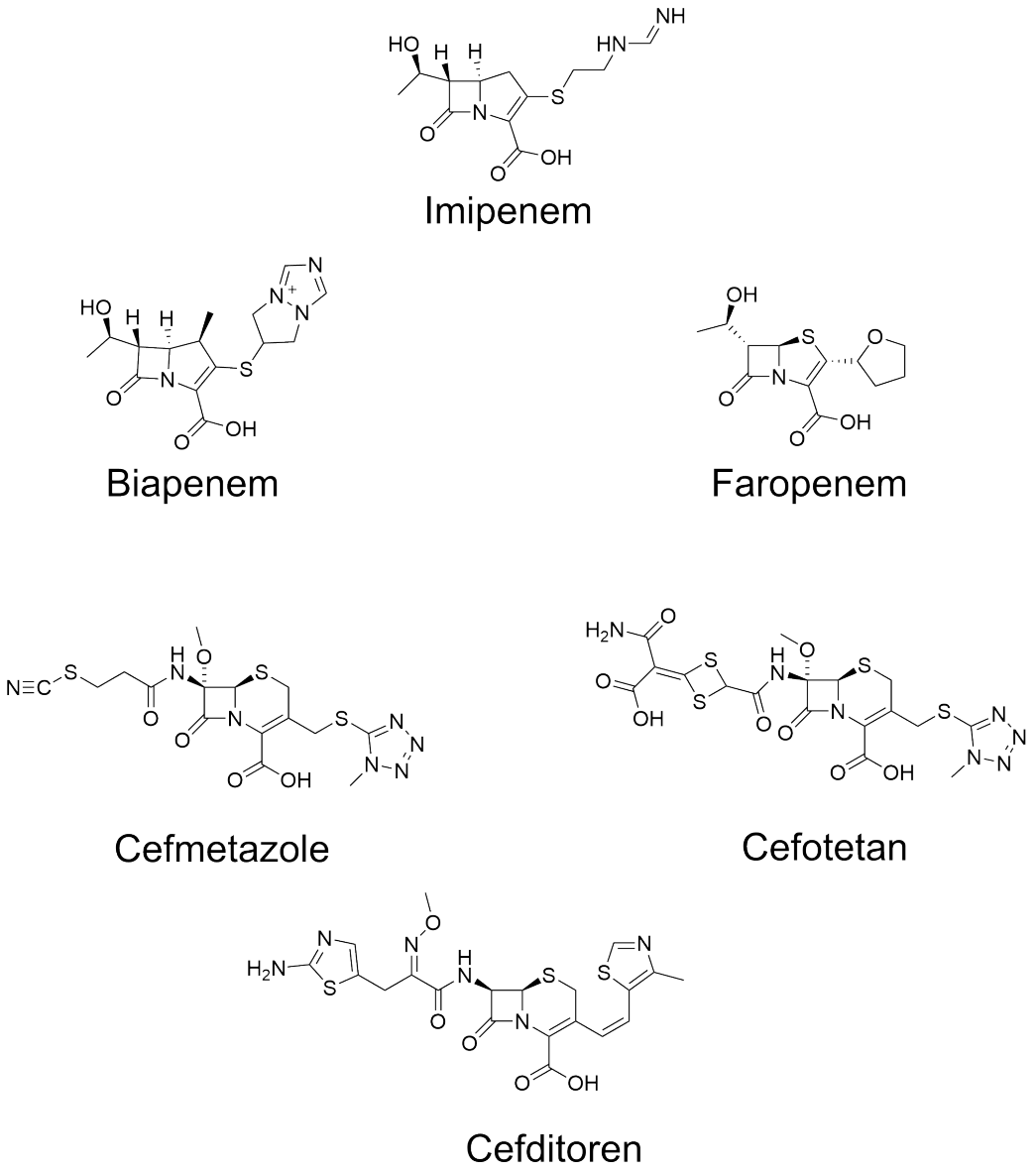


Figure 9: Diagram showing the antibiotics that were soaked into VIM-2 crystals. A variety of β-lactams were used, including penems, carbapenems, cephamycins and cephalosporins. Each antibiotic was soaked into different crystals at several time points: 1, 5, 10 and 30 minutes.

Data Processing and Refinement

Diffraction data from all crystals were processed automatically using Diamond Light Source data processing software, i.e. FastDP, Xia2 and DIALS.[51–53] The first step of data processing is indexing the images, which involves finding spots reflections, and assigning a space group and unit cell dimensions to the dataset.[54,55] The spot positions are first mapped by projecting the coordinates on the detector to vectors in the Ewald Sphere. Next, the unit cells are fitted to a primitive triclinic cell, the initial cell

is then compared to 44 crystallographic lattices. The next step is integration, which measures the diffracted intensities of the images, where the value of every pixel in a spot is added together.[55] Strong, well measured reflections can then be scaled and merged.

Scaling the data involves placing all the data on the same scale and produces several values such as R_{merge}, I/σI and CC1/2 which give crystallographers an idea of the quality of the dataset.[54] The R_{merge} value indicates the level of agreement between multiple measurements of the same reflection in a single dataset. There are other variations on the R_{merge} value such as R_{meas}, which are less sensitive at high multiplicity. I/σI describes the signal to noise ratio in the dataset whereas the CC1/2 value is the correlation coefficient between half datasets.[54]

The mtz files were then used for molecular replacement with Phaser as part of the PHENIX software package[56,57] using the PDB identifiers 4BZ3 (VIM-2)[34], 1SML (L1)[33] and 5UL8 (KPC-2)[26]. The refinements for KPC-2 and L1 were done by Dr. Philip Hinchliffe and Dr. Catherine Tooke. Molecular replacement is done in order to solve the phase of the dataset as the phase is not measured during data collection.[56] Molecular replacement is the most commonly used approach to solve the phase, and operates by using the phase of a known structure, which can be of the same protein, or a closely related one since they have the same or similar phase.

Two different parameters can be used to inform the user of how successful the molecular replacement was: the Log Likelihood Gain (LLG) score and the Translation Function Z (TFZ) score.[56] The minimum value for these has to be 120 and 8 respectively to have definitively solved the phase. There are seven steps to molecular replacement. Anisotropic correction is the first step that involves computationally removing any anisotropic variations.[56] Afterwards, a model is generated by estimating Root Means Squared Deviation (RMSD) from between the new structure and the model and the most likely rotation of the model is calculated using maximum-likelihood rotation function (MLRF).[56] The

translation and packing and functions help assess any clashes between the asymmetric unit, only solutions below a certain threshold are able to proceed to the next step. The structure is then refined using rigid body refinement to find the best orientation for the model. Finally the solutions with the highest LLG and TFZ scores are picked.[58]

Once the molecular replacement was complete, the datasets were refined using phenix refine,[59] the pdbs from the refinements was analysed on COOT to see if anything was bound in the active site.[60] The structures were further refined until the R factors were unchanging. The R_{work} shows the measure of agreement between the experimental crystallographic data and the crystallographic model produced during the refinement process. The R_{free} is used to measure overfitting, it also calculates the agreement between the model and experimental data, but it does this on a small sample of the data that is not included in the refinement process.

Refinement involves modifying the current parameters of the model to the point where they describe the experimental data as accurately as possible. Phenix uses three main steps, the first being initialisation, which processes the parameters of the input files, along with an analysis of the refinement strategy.[59] The second step is the macrocycle of refinement. This involves the optimisation of several model parameters including bond vibrations and bulk solvent parameters such as k_{sol} and B_{sol}. Translation Liberation Screw parameters (TLS) can also be refined during the refinement process, this divides the model into separate sections for rigid body refinement.[61] The R factors are used to assess how successful the refinement is.

COOT[62] is used to do manual model building after a round of refinement and to fix any rotamer outliers and Ramachandran outliers, along with modelling ligands and metals in the active site. If there was any un-modelled density in the active site, the appropriate hydrolysed ligand would be modelled into the active site by producing a CIF file using Grade Web Server and eLBOW.[62,63] CIF files contain

information about the angle and bond restraints in the ligand. Refinement and model building were continued in alternate cycles until the R factors could longer dropped.

PDB Deposition

Before any structures could be deposited in the PDB, the coordinates and structure factors were validated using the PDB Validation programme.[64] The Validation programme identifies issues such as clashes and a comparison of RMSD angle and bond restraints to other structures of a similar resolution. Any issues identified were fixed in COOT using real space refinement and the structure was put through further rounds of refinement.

NMR Studies

NMR studies were carried out to compare the behaviour of VIM-2 with faropenem and biapenem in solution and in crystals. It was also important to see how faropenem was hydrolysed by other groups of β-lactamases, therefore NMR experiments were performed using KPC-2 and L1 provided by Dr. Philip Hinchliffe (University of Bristol). The NMR studies with faropenem were carried out by Ms. Tika Malla.

All enzymes were buffer exchanged using a protein concentrator as described previously into 50 mM sodium phosphate pH 7.5 at a stock concentration of approximately 50 µM. The enzymes were diluted tenfold, 1 mM of the necessary substrate was added and a total of 10% (v/v) D_2O was also added to the solution. NMR data were collected for 30 minutes with an AVIIIHD 600 MHz or AVIII 700 MHz machine using ^1H NMR. Pre saturation or excitation sculpting with perfect echo was used for water suppression. Controls with just the antibiotic were also tested in order to ensure that the antibiotics had not degraded naturally and to get a comparison of behaviour of the antibiotic in the presence of enzyme. The data were analysed using MestRe Nova.[65]

Kinetics Experiments

Kinetics experiments were performed in order to determine the Michaelis Menten constants of the enzymes with faropenem and biapenem. Experiments with faropenem were performed by Dr. Philip Hinchliffe (University of Bristol) using steady state kinetics, which involved measuring the rate of faropenem hydrolysis at 360 nm. Experiments were performed using Greiner half area 96-well plates and a Tecan Infinite 200 Pro microplate reader. As faropenem is hydrolysed, the absorbance at 360 nm decreases. 10 nM VIM-2, L1 and KPC-2 was used in these experiments. 10 mM HEPES pH 7.5 and 150 mM NaCl were used for KPC-2, and 10 mM HEPES pH 7.5, 150 mM NaCl and 0.02 mM $ZnSO_4$ for VIM-2 and L1. The Beer Lambert Law (**Equation 1**) was used to calculate the concentration of faropenem derived product using the extinction coefficient $\Delta\varepsilon_{306}$ = 3,445 M^{-1} cm^{-1}.[66]

Once the concentration values had been plotted, the slope could be calculated to give a rate of reaction. Biapenem kinetic assays were done using the same principle but absorbance was measured at 293 nm and the $\Delta\varepsilon_{293}$ = -3,630 M^{-1} cm^{-1} with 100 nM VIM-1 and VIM-2.[67] Slopes were first calculated in Microsoft Excel, then processed in the programme Prism[68] to get important kinetic values such as the K_m and the k_{cat}.

$$A = \varepsilon c l$$

Equation 1: Beer Lambert Law. A is the absorbance value, c is the concentration, l is the length of the pathway the light has to travel and ε is the extinction coefficient. This value is different for every substrate.

Results

Protein Production and Purification

Recombinant VIM-2 protein production and purification was successful with dense bands being clearly seen at approximately 25 kDa, as the molecular weight of VIM-2 is 25 kDa, this indicated that VIM-2 had been successfully produced and purified using nickel affinity purification (**Figure 10**).

The successful IMAC purification method allowed the process to proceed to the next step of the purification, i.e., gel filtration chromatography. Fractions 20-25 from the IMAC column were collected and analysed on an SDS PAGE gel. Once again clear bands were present at approx. 25 kDa (**Figure 11**) with significantly less impurities present than after the IMAC purification step. These fractions were pooled together for His tag cleavage, which was also successful, with the VIM-2 protein eluting early (**Figure 12**).

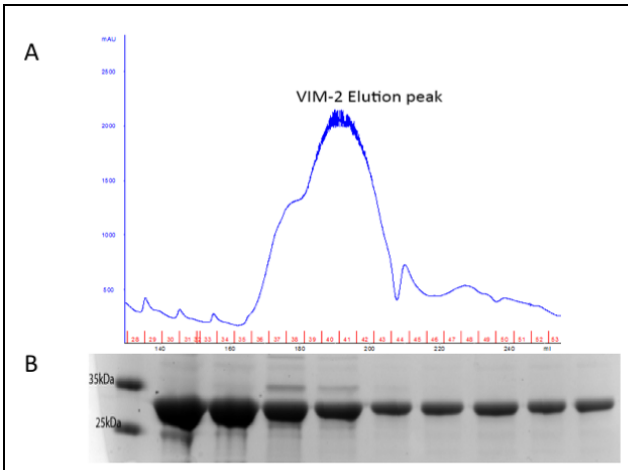


Figure 10: SDS PAGE analysis after IMAC purification and part of the elution profile. There is clearly a protein present at the 25 kDa mark suggesting that VIM-2 is present in these fractions. Gel shows fractions 48 to 56 were pooled together and concentrated.

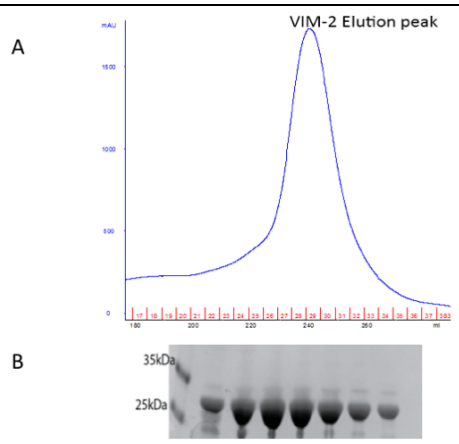


Figure 11: SDS PAGE analysis and elution profile after gel filtration chromatography. Fractions appear to have less contaminants present than previously indicating that the purification was successful. The gel shows fractions 27-33 were pooled and concentrated.

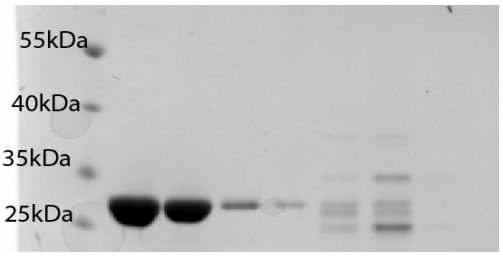


Figure 12: showing SDS PAGE gel of fractions from a reverse IMAC. Note the thick bands in the first fractions indicating the early elution of VIM-2

Crystallisation of VIM-2

Next, crystallisation trials were carried out using optimisation plates produced by Dr. Gareth Langley and Dr. Jürgen Brem. VIM-2 crystals appeared in several different conditions in both plates as described in the Material and Methods section (**Tables 1** and **2**). These crystals were approximately 100 x 50 x 20 µm in size, although there was variation from within the drops and the different conditions (**Figure 13**). The crystals were mostly rectangular, with some rhombohedral crystals present as well. Crystal conditions in the new plate (**Table 2**) were soaked with a range of antibiotics.

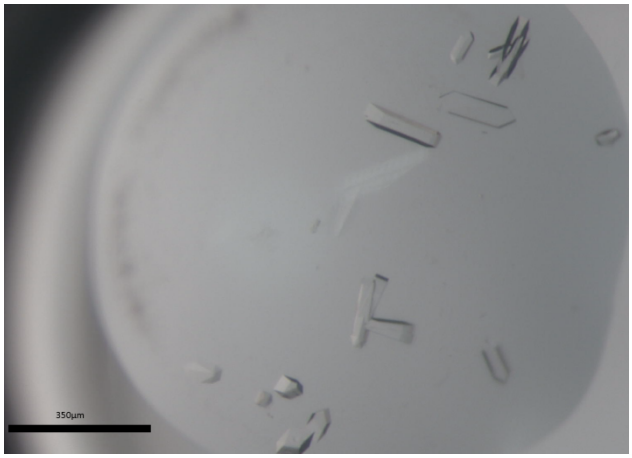


Figure 13: Crystals of VIM-2 from the optimisation plate in Table 2. These crystals appeared between 24-48 hours after setting up the plate.

Data Collection and Soaking

Faropenem, biapenem, imipenem, cefmetazole, cefotetan and cefditoren were soaked into the crystals at various different time points at a concentration of 50 mM. Most the crystals were in good condition after the soaking process, but some did appear slightly damaged, with cracks observed. Minor damage is not unusual using high concentrations of ligands and substrates, as they can alter the morphology of the protein inside the crystal which leads to damage.

At the indicated time points (1 min, 5 min, 10 min, and 30 min), the crystals were harvested using nylon loops and cryocooled with liquid nitrogen for data collection. All crystals that were successfully harvested diffracted to high resolution. Crystals within the same plate appeared to occur in several different space groups, with most being in the standard *C* 1 2 1 or *I* 2 2 2 but some also showing up in *P* 2_1 2_1 2_1. It is expected that there would be some differences in space group as the crystals were grown in different conditions. Most crystals in the *P* 2_1 2_1 2_1 space group appeared in conditions where there was a lower PEG concentration (<15% w/v).

Data processing and molecular replacement revealed that in a majority of cases, no antibiotics were bound at the active site. A factor that could have impacted on this is the crystal packing; if the protein is tightly packed together in the crystal, it can make it very difficult for the substrate to reach the enzyme active site.[69] Binding was seen in the cases of faropenem and biapenem. Density corresponding to a faropenem derived product appeared in crystals that had been soaked at 5 minutes and 30 minutes and biapenem appeared in the data set with a 10-minute soak (**Figure 14**). Faropenem density was also observed in the KPC-2 and L1 structures produced by Dr. Philip Hinchliffe and Dr. Catherine Tooke.

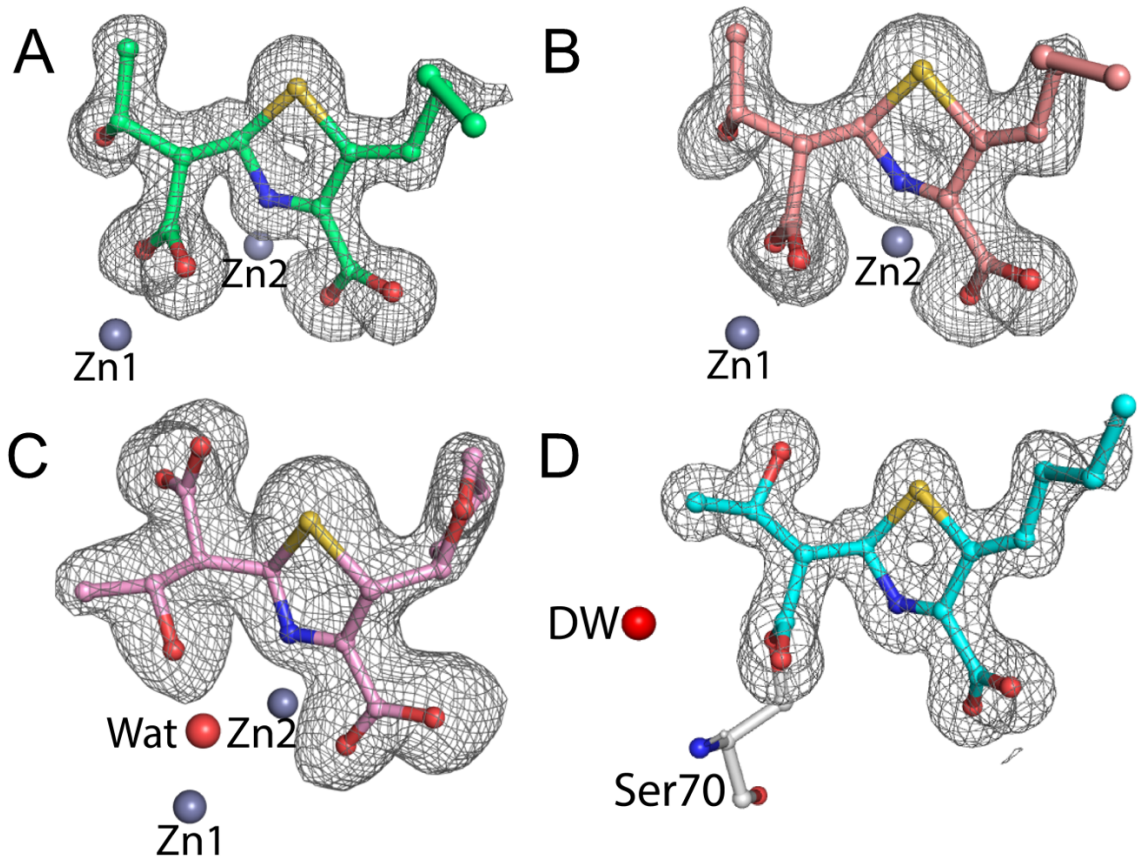


Figure 14: View of faropenem derived complexes in the β-lactamase active sites as defined by mF_o-DF_c electron density maps contoured to 3σ. A) VIM-2 *I* 2 2 2 structure (green, PDB 7A5Z), B) VIM-2 *C* 1 2 1 structure (light red, PDB 7A60), C) L1 (pink, PDB 7A63) and D) KPC-2 (cyan, PDB 7A61). Note the different positions of the hydroxyethyl group compared to the other three structures, and the presence of the zinc bridging water in L1, but not in VIM-2. No density corresponding to the oxygen was observed for the hydrolysed THF ring, so it was omitted from the final models. DW stands for Deacylating water and Wat for nucleophilic water.

Faropenem Kinetic Assays

Like carbapenems, faropenem is poorly hydrolysed by, and can inhibit, certain β-lactamases, including the class C SBL AmpC and extended spectrum β-lactamases such as BlaC and CTX-M.[70,71] However faropenem is susceptible to hydrolysis by carbapenemases such as class B enzymes, e.g. NDM-1.[72] The steady state kinetic parameters of faropenem hydrolysis by the carbapenemases KPC-2, VIM-2 and L1

(belonging to classes A, B1 MBL and B3 MBL, respectively) were initially determined. The three enzymes degrade faropenem with varying degrees of efficiency (**Table 3**).

Comparison of turnover numbers (k_{cat}) reveals the MBLs VIM-2 and L1 both hydrolyse faropenem at a maximal rate ~15 times greater than KPC-2, although the K_M with L1 is substantially higher than either KPC-2 or VIM-2. The catalytic efficiency of KPC-2 with faropenem, as judged by k_{cat}/K_M, is therefore 6 or 35 times poorer than for L1 or VIM-2, respectively. The K_M of VIM-2 is the lowest, indicating that VIM-2 has the highest affinity for faropenem. The much lower k_{cat} of KPC-2 largely explains the poorer KPC-2 efficiency, although the weak substrate inhibition (44 μM) we observed for KPC-2, but not the other MBLs, may also contribute.

Enzyme	Type	Class	k_{cat} (s^{-1})	K_M (μM)	k_{cat}/K_M (s^{-1} μM^{-1})	K_i (μM)
KPC-2	SBL	A	2.59 (1.26)	12.2 (7.44)	0.21	44.1 (25.0)
VIM-2	MBL	B1	36.7 (1.03)	5.11 (0.63)	7.17	-
L1	MBL	B3	43.7 (2.70)	36.3 (8.80)	1.20	-
BlaC[73]	SBL	A	0.91 (0.03)	23 (3)	0.040	
NDM-1[72]	MBL	B1	14.7 (0.08)	99 (0.16)	0.15	
BJP-1[74]	MBL	B3	2 (<0.1)	245 (<0.1)	0.008	

Standard errors of the mean in parenthesis (n = 3). See Experimental Section for KPC-2, VIM-2 and L1 assay details.

Table 3: Kinetic values for faropenem degradation by VIM-2, L1 and KPC-2 by Dr. Philip Hinchliffe. Reported values for other enzymes are presented for comparison.

Faropenem Datasets and Crystallography

Crystallographic studies were performed to better understand the binding of faropenem with β-lactamases. Once the datasets had been collected, they underwent molecular replacement to solve the phase and to refine the structures. After the first round of refinement, it was clear that several of the datasets contained a faropenem derived product bound in the active site (**Figure 14**). This was seen in two datasets of VIM-2, one of which was obtained after 30 minutes of soaking, and the other, from the University of Bristol, was soaked for 5 hours. Two other datasets of L1 and a KPC-2 mutant

(KPC-2^{E166Q}) from the University of Bristol also contained density for faropenem hydrolysis products. L1 was soaked in a faropenem solution overnight, while KPC-2^{E166Q} was soaked with faropenem for 2.5 hours (**Figures 14 and 15, Table 4**). In all four datasets, the β-lactam ring in the faropenem structure had been hydrolysed but there were differences regarding the THF ring and the C2 stereochemistry.[7]

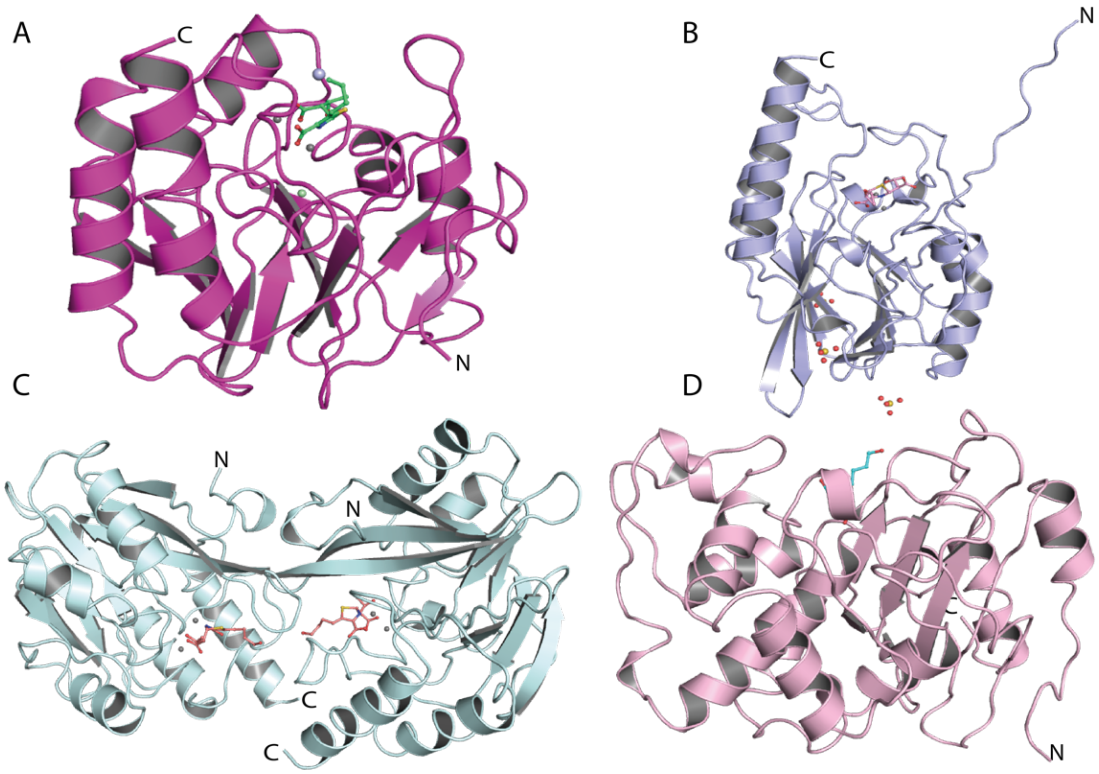


Figure 15: Overall fold of the β-lactamase: faropenem complex structures. A) VIM-2: faropenem dataset, collected at the University of Oxford, in the *I* 2 2 2 space group (PDB: 7A5Z). B) Overall fold of L1 (*Stenotrophomonas maltophilia*) complexed with a faropenem derived product (space group *P* 6_4 2 2; PDB: 7A63). C) VIM-2 in the space group *C* 1 2 1 (PDB 7A60). D) KPC-2 (from *Klebsiella pneumoniae*) in the *P* 2_1 2_1 2 space group (PDB 7A61). Faropenem was soaked into the crystals for varying lengths of time (30 minutes, 2 hours, 5 hours, and overnight). Zinc ions are shown in light grey, sodium ions in lilac, chloride in green and sulfate ions in red and yellow.[7]

	KPC-2: faropenem	VIM-2: faropenem	VIM-2: faropenem	L1: faropenem
PDB accession	7A61	7A5Z	7A60	7A63
Data collection				
Space group	*P* 2_1 2_1 2	*I* 2 2 2	*C* 2	*P* 6_4 2 2
Molecules/ASU	1	1	2	1
Cell dimensions				
a, *b*, *c* (Å)	60.53, 80.03, 56.00	64.65,74.68,78.77	102.18, 79.38, 67.33	105.30, 105.30, 98.10
α, β, γ (°)	90.0, 90.0, 90.0	90.0, 90.0, 90.0	90.0, 130.38, 90.0	90.0, 90.0, 120.0
Wavelength	0.90	0.9159	0.88	0.97951
Resolution (Å)	48.28 – 1.25 (1.27 – 1.25)	49.97-1.29 (1.31-1.29)	51.34 – 1.47 (1.50 – 1.47)	52.65 – 1.57 (1.60 – 1.57)
R_{pim}	0.046 (0.823)	0.032 (0.629)	0.039 (0.699)	0.012 (0.552)
CC 1/2	0.999 (0.703)	1.0 (0.6)	0.991 (0.469)	0.911 (0.846)
$I/\sigma I$	9.2 (0.8)	13.8 (1.3)	9.2 (1.1)	32.3 (1.6)
Completeness (%)	100.0 (100.0)	100 (99.5)	98.1 (94.3)	100.0 (99.9)
Redundancy	13.2 (13.2)	12.8 (12.8)	7.0 (7.2)	72.9 (54.6)
Refinement				
Resolution (Å)	48.28 – 1.25	49.97-1.29	51.34 – 1.47	52.65 – 1.57
No. reflections	75789	48222	68096	45194
R_{work} / R_{free}	13.25 / 15.95	13.09 / 16.31	16.26 / 18.87	16.92 / 19.28
No. non-H atoms				
Protein	2149	1839	3679	2054
Solvent	375	190	398	230
Zn	N/A	3	4	2
Faropenem	18	17	38	20
B-factors				
Protein	15.9	17.3	24.7	35.7
Solvent	37.6	30.7	36.1	42.4
Zn	N/A	11.9	19.5	26.4
Faropenem	17.0	15.8	25.2	35.1
R.m.s. deviations				
Bond lengths (Å)	0.008	0.009	0.010	0.009
Bond angles (°)	1.040	1.10	1.105	1.071
Ramachandran (%)				
Outliers	0.00	0.44	0.22	0.00
Favoured	98.88	98.25	98.47	95.45

Table 4: Data collection and refinement statistics of the different enzyme: faropenem structures. All structures are to a high resolution. Values in brackets are for the high-resolution shells.

VIM-2 Structures

The interactions observed with the faropenem derived β-lactam hydrolysis product were equivalent in the two VIM-2 structures. It was clear that faropenem reacted with VIM-2 to give a Z-imine alkene product with the THF ring opened (**Figures 14 and 16**). The density around the THF ring atoms is poorly defined, making it difficult to define its precise interactions (if any). The VIM-2 structures indicated

that the zinc bridging water was displaced by one of the oxygens on the β-lactam derived C7 carboxylate, as an increased distance between the two zinc ions was observed in both structures (4.2 Å) compared to the resting state structure 4BZ3 (3.5 Å) (**Figures 17 and 24**). The zinc ion movement is consistent with what has previously been observed with inhibitors of VIM-2 e.g. bicyclic boronates.[43,75] Several hydrogen bonds are involved in stabilising the faropenem derived complex. The C7 carboxylate hydrogen bonds with the amide group of the Asn233 side chain whereas the C6 hydroxyethyl oxygen interacts with the Asp120 (**Figure 16**). Hydrophobic interactions further stabilise the intermediate, through Phe61 and Tyr67 on the L3 loop, as well as Trp87.

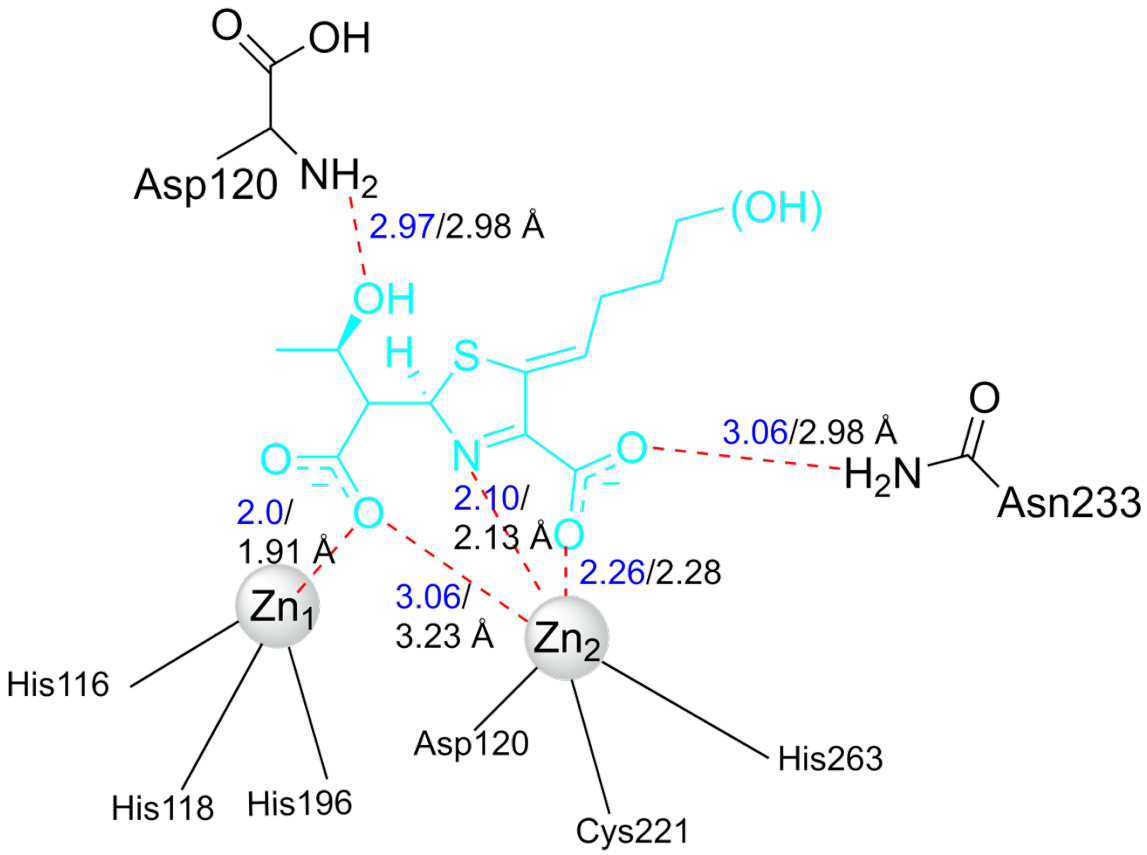


Figure 16: Polar interactions seen between VIM-2 and the faropenem derived imine alkene product. Interactions and distances from both VIM-2 structures are shown (black for *I* 2 2 2 structure, PDB 7A5Z and blue for *C*2 structure, PDB 7A60). Distances are in Å. The (OH) group resulting from opening of the tetrahydrofuran ring was not modelled due to a lack of apparent electron density.

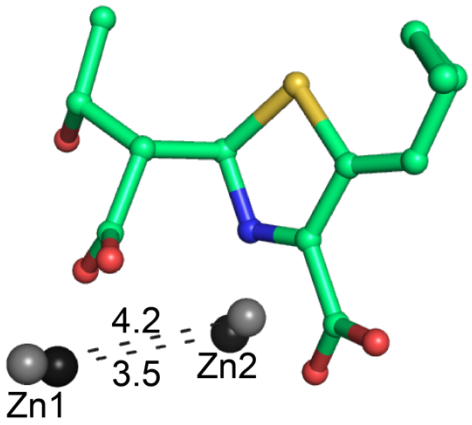


Figure 17: Comparison of active site zinc positions in VIM-2 complexed with a faropenem derivative versus VIM-2 alone. Note the longer distance between the two zinc ions upon faropenem binding (PDB 7A5Z, zinc ions shown in grey) compared to VIM-2 in its resting state (PDB 4BZ3, zinc ions in black[34]). The zinc ion movement is consistent with what has been previously observed when some other inhibitors interact with VIM-2.[7]

Structural comparison

In contrast with the VIM-2: faropenem derived product, a structure of NDM-1: meropenem (5YPN[76]) shows the presence of a Δ^2-pyrroline (enamine) product form at 2.1 Å resolution (C2 is sp^2 hybridised). Furthermore, there are differences in the positioning of the C6 hydroxyethyl group in the NDM-1: meropenem structure (PDB: 5YPN[76]), which is likely caused by interactions with active site residues. A structure with VIM-1 complexed with meropenem (5N5I[10]) showed that the zinc bridging water was not displaced (**Figure 18**).

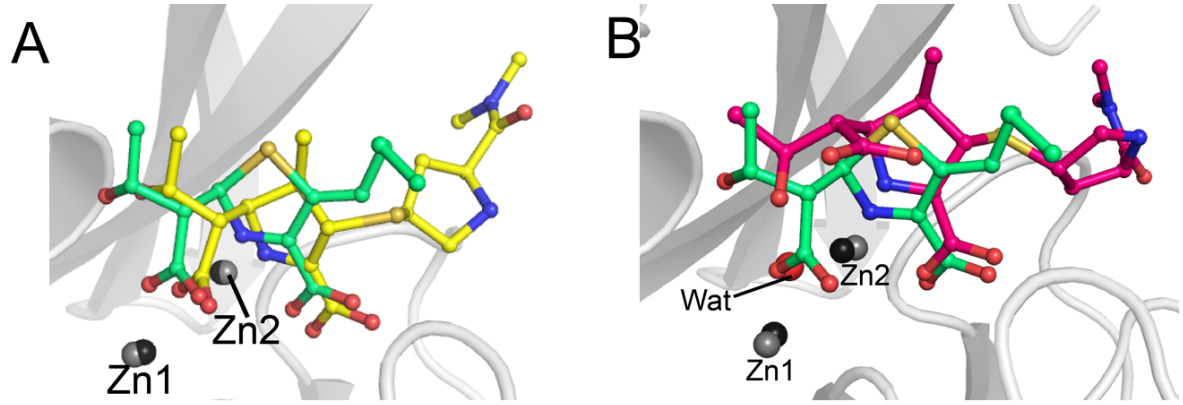


Figure 18: Comparison of the VIM-2: faropenem complex (pale green, PDB 7A5Z) with the NDM-1: meropenem (yellow, PDB 5YPN, RMSD 3.352[76]) derived complexed (A) and VIM-1: meropenem derived complex (pink, PDB 5N5I, RMSD 0.895[10]). Note the difference in hydroxyethyl and carboxylate positioning in the VIM-1: meropenem derived structure compared to the VIM-2: faropenem structure (zinc ions in charcoal grey) and the presence of the zinc bridging water. The zinc bridging water is not seen in the NDM-1: meropenem derived structure (zinc ions shown in charcoal grey).[7]

L1 Structure

An L1: faropenem structure was obtained by Dr. Philip Hinchliffe. Crystallographic analysis of the complex structure derived from L1 and faropenem reveals that faropenem reacts with L1 to form an imine product with a closed THF ring. This is expected to occur *via* protonation at the C2 position, which, from the electron density, appears to be sp^3 hybridised and in the (*S*)-configuration (**Figure 14**). Moreover, the C7 carboxylate and the hydroxyethyl chain are rotated when compared to the VIM-2 and KPC-2 structures, and the zinc bridging water is still present in the active site (**Figures 19 and 24**).

Unlike what has previously been reported with regard to MBL: carbapenem interactions, the C7 carboxylate does not interact with Zn1 but instead with Tyr32. Therefore, all interactions between the faropenem derived product and the metal centre of L1 are exclusively with Zn2, which is ligated by interactions *via* the nitrogen and carboxylate of the thiazoline ring. The β-lactam derived C7

carboxylate further interacts with L1 through the side chains of Ser221 (3.1 Å) and Ser223 (2.7 Å), which were previously observed to be involved in L1 substrate and inhibitor binding.

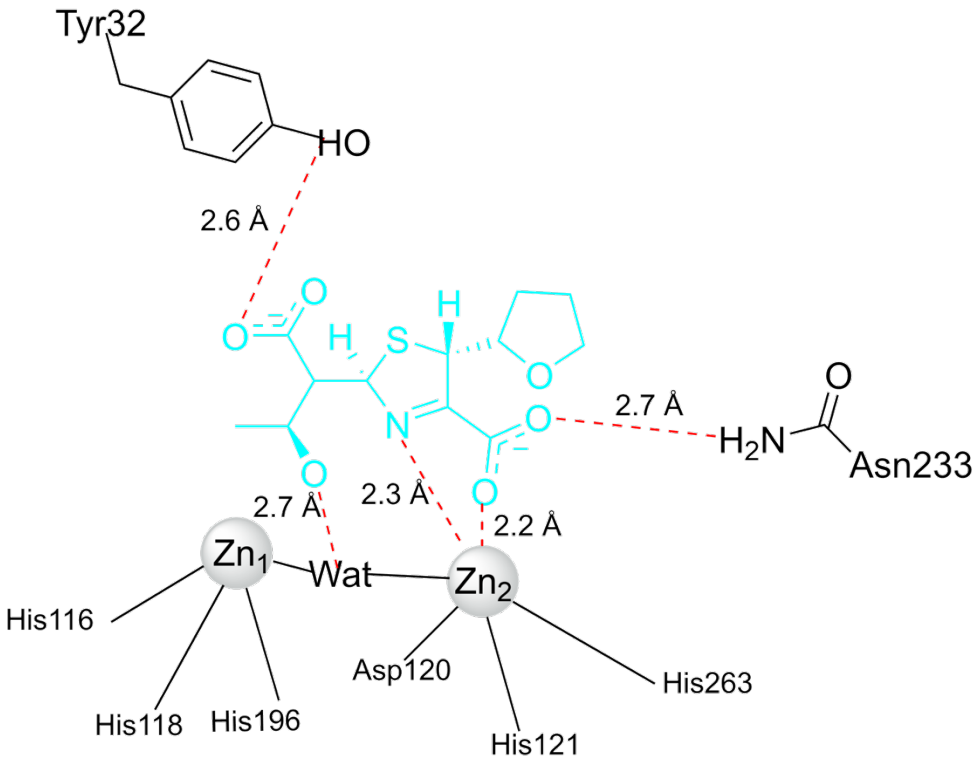


Figure 19: Hydrogen bond interactions between the faropenem-derived imine product and L1 (PDB 7A63). Measured distances are shown as red dashed lines and are in Å. Note the C2 stereocentre in the imine product is observed in the (*S*)-configuration.

Structural comparison

Upon comparison of the L1: faropenem structure and previously reported structures, it is clear that the faropenem binding mode is similar to that observed between L1: faropenem structure and a structure of imipenem with the B3 MBL Serratia metallo-β-lactamase 1 (SMB-1) (PDB 5B1U[77]), in which the hydrolysed carbapenem substrate is observed in the imine form (C2 is sp^3 hybridised) and the C7 carboxylate does not displace the zinc bridging water. Moreover, the imine derived products are observed with the C2 (*S*)-configuration (**Figure 20**).[77]

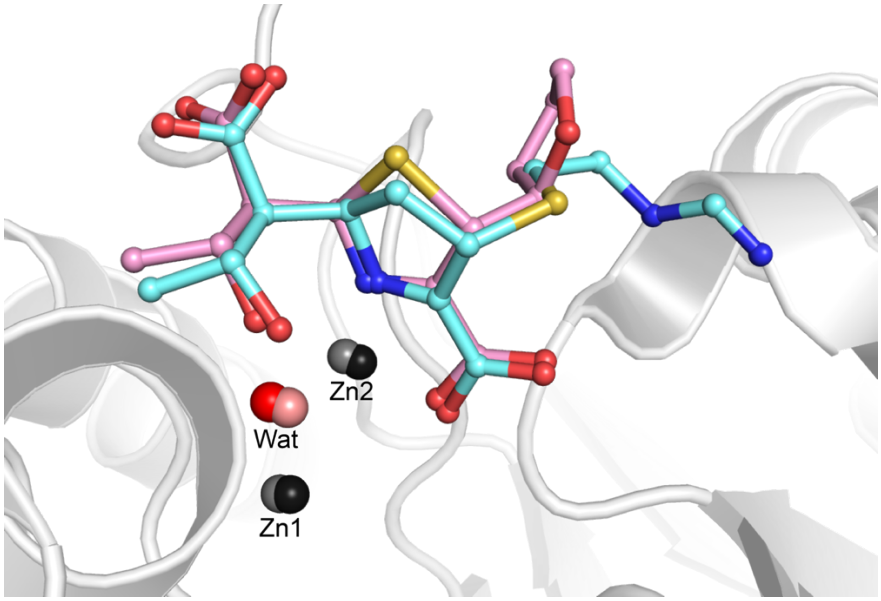


Figure 20: Comparison between the L1: faropenem derived structure (magenta, PDB 7A63) and a SMB-1: imipenem derived structure (cyan, PDB 5B1U[77]). The zinc ions are either light grey (L1) or charcoal grey (SMB-1) and the zinc bridging water is either dark red (L1) or light red (SMB-1) and is labelled as Wat. Both products have the (*S*)-configuration. The RMSD from the alignment is 2.974.[7]

KPC-2^{E166Q} Structure

In the KPC-2^{E166Q} structure, the faropenem derived species is covalently bound to the nucleophilic Ser70. The product observed in the active site is an imine alkene, with the C2 sp^2 hybridised and the THF ring opened (**Figure 14**). The exocyclic alkene (C2-C11) is in the Z-isomer, something that was not assigned in the NMR studies (Section NMR studies with Faropenem). This is analogous to the product observed in both VIM-2 structures, except the density around the THF derived atoms was poor, making it difficult to accurately define protein: ligand interactions. In comparison, a previous structure of KPC-2 with a faropenem derived product shows a non-covalently bound enamine product present in the active site with the THF ring intact.[78] However, the electron density for the ligand was relatively poor, and so the precise nature of this faropenem-derived product is unknown.[78]

The carbonyl oxygen derived from the β-lactam ring is positioned in the oxyanion hole, allowing the carbonyl to form interactions with Ser70 and Thr237, which is consistent with previous observations of acyl-enzyme complexes in SBLs.[79,80] Further polar interactions are observed between the C10 carboxylate and Thr235, and between the hydroxyethyl oxygen with Asn132 (**Figure 21**). Hydrophobic interactions between the fragmented THF ring and Trp105 are also seen, and Trp105 is known to be involved in interactions with SBL inhibitors such as relebactam (**Figure 21**).[79]

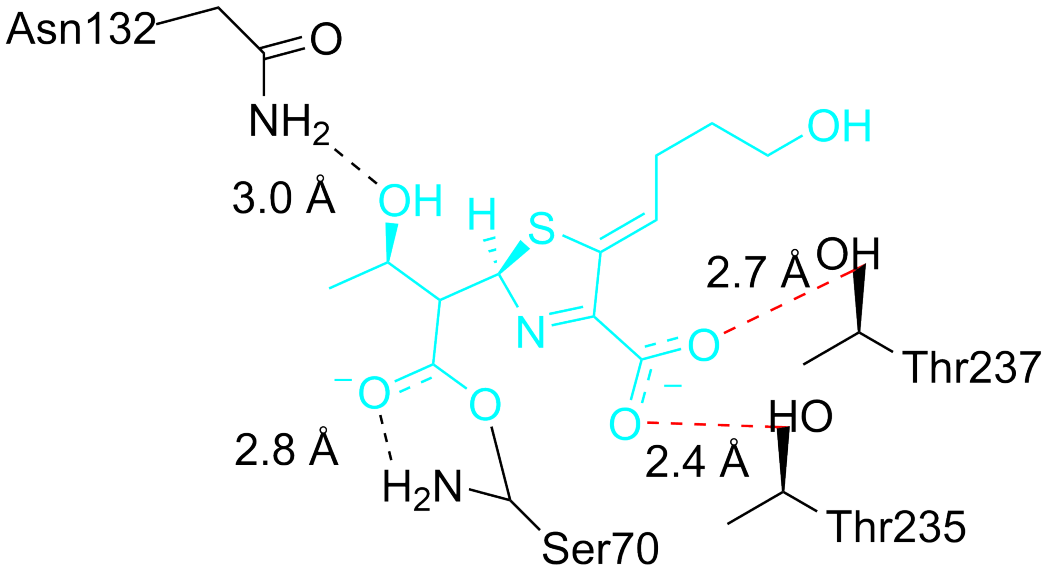


Figure 21: Hydrogen bond interactions between KPC-2^{E166Q} and the faropenem-derived imine alkene product (PDB 7A63). Hydrogen bonds are shown as red dashed lines with distances labelled. Due to poorly defined density, the OH group from the opened THF ring was not modelled.

Structural comparison of KPC-2^{E166Q} and SFC-1

Similar interactions are seen in the KPC-2^{E166Q}: faropenem structure as those reported in an SFC-1: meropenem structure (PDB 4EV4).[81] *Serratia fonticala* Carbapenemase (SFC-1) is another class A SBL that has shown carbapenemase activity. In both structures, the hydroxyethyl chain is orientated away from the deacylating water and forms a hydrogen bond with Asn132 (**Figures 22 and 24**). It is proposed

that the interaction with Asn132 allows for carbapenemase activity, since interactions with the deacylating water inhibit hydrolysis.[81]

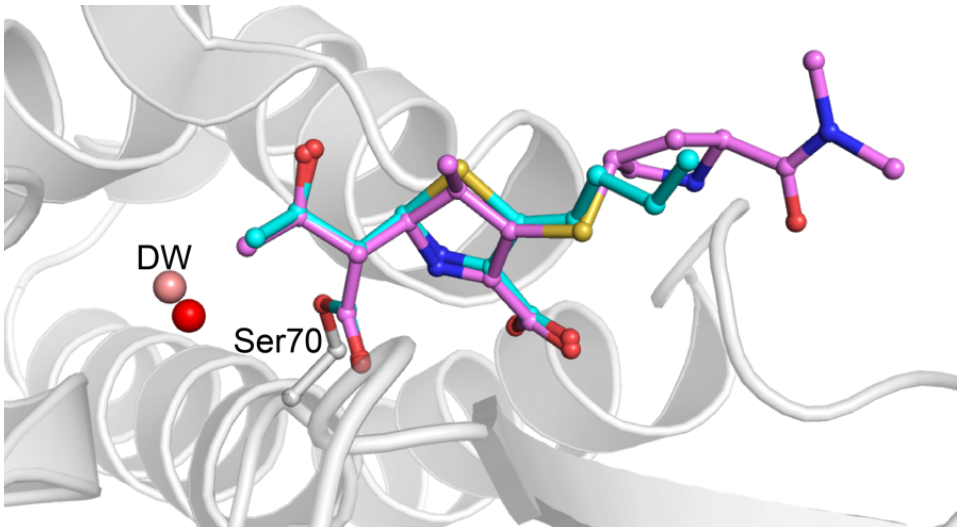


Figure 22: Comparison of KPC-2^{E166Q}: faropenem derived product structure (cyan, PDB 7A61) and SFC-1: meropenem derived product structure (violet, PDB 4EV4[81]). The proposed deacylating water molecules are shown in dark red (KPC-2) or light red (SFC-1). Note the similar binding position and stereochemistry between the two products. The RMSD from the alignment is 1.37.[7]

Loop variations

In the KPC-2^{E166Q}: faropenem derived structure, two conformations of Gln166 are observed due to a conformational change in the Ω-loop (**Figure 23**). The wildtype Glu166 plays an important role in acting as a base in the deacylating step. In one conformation, Gln166 is directed towards the active site, allowing it to interact with the deacylating water. In the other, Gln166 is positioned away from the active site. These multiple conformations may contribute to slow turnover rate observed in our kinetic studies (**Table 3**).

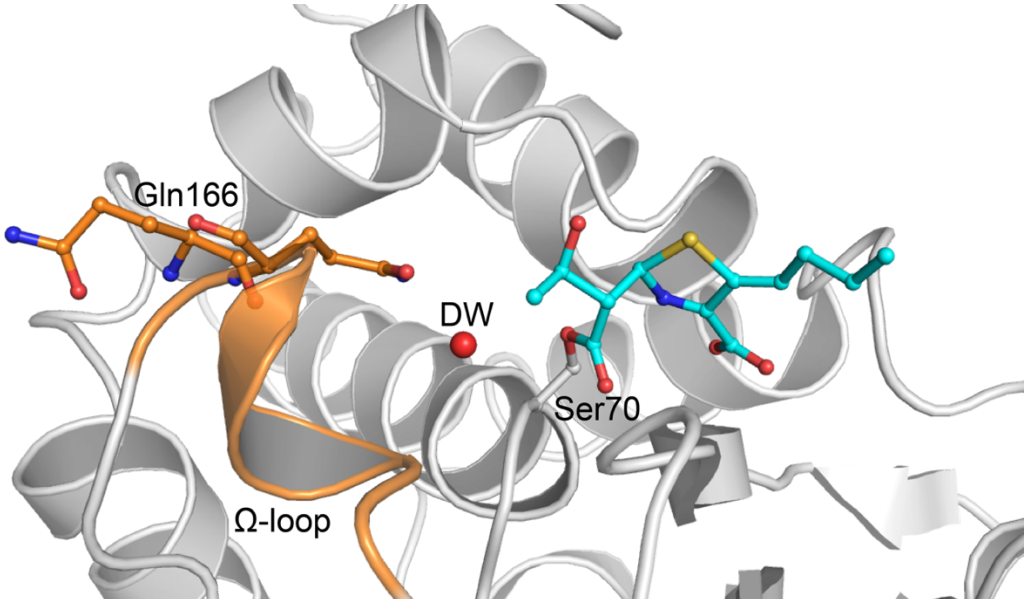


Figure 23: Different conformations of the Ω-loop (orange) observed in the KPC-2^{E166Q}: faropenem derived structure (PDB 7A61). The Gln166 residue of the Ω-loop is observed in two different conformations, one directly pointing towards the active site and therefore interacting with the deacylating water (shown in red) and the other pointing away from the active site.[7]

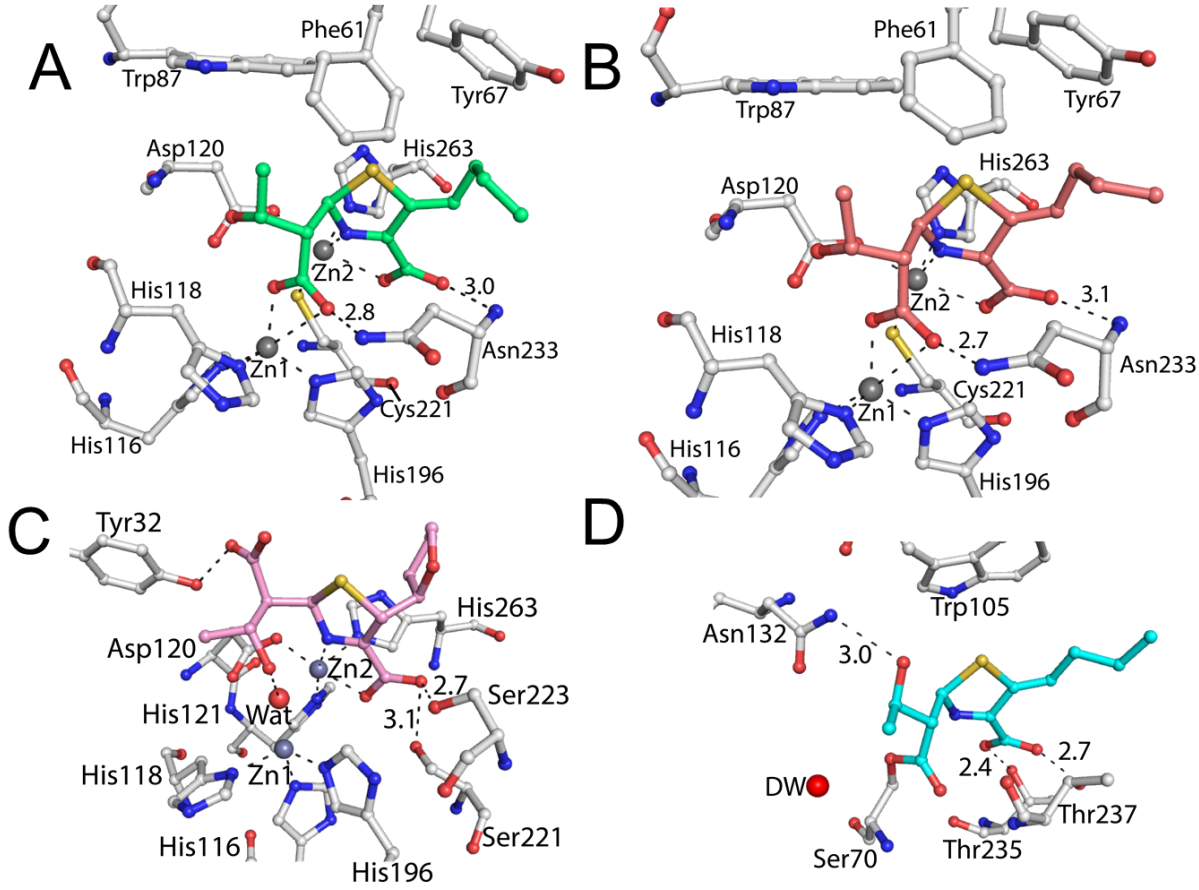


Figure 24: Views of the active sites from the faropenem derived crystal structures solved in this study. A) View from the structure of the VIM-2 crystal produced by the University of Bristol in magnesium formate and PEG 3350. B) Structure of the VIM-2 crystal produced by the new optimisation plate (**Table 2**). Apart from the difference in space group, the active sites of these structures are similar, with the Z-imine alkene product form observed in the active site in both cases. C) Active site of L1 in complex with faropenem. Note the intact faropenem side chain ring, as compared to the other structures, as well as the flipped position of C6. D) Structure of the active site of KPC-2^{E166Q} in complex with faropenem. Distances are in Å.[7]

NMR Experiments with Faropenem

The next step was to investigate the relevance of the crystallographically observed structures using 1D and 2D NMR spectroscopic methods. Initial studies focused on VIM-2, KPC-2 and L1, while other MBLs and SBLs (i.e., class D SBLs OXA-10, OXA-23 and OXA-48 and the B1 MBLs NDM-1 and VIM-1) were tested for comparison. Full spectra for each enzyme are in the Appendix (**Figures S1-S16**). Five

distinct faropenem derived products were observed and assigned in these studies, and several unassigned products were also observed at low levels (**Figure 25**). Compounds **1** and **2** (major and minor respectively) were observed with all enzymes and were assigned based on previous studies as the C5-epimeric enamine products in which the THF ring was closed.[8] The 5(*R*) minor product (**2**) arises from the epimerisation of the major 5(*S*) product (**1**) (**Figure 26**). **1** appears to be the initially formed major enzymatic product for all SBLs and MBLs, although the levels of **1** and **2** decrease over time, likely due to their conversion to imine alkenes in which the THF ring is open (**3** and **4**).

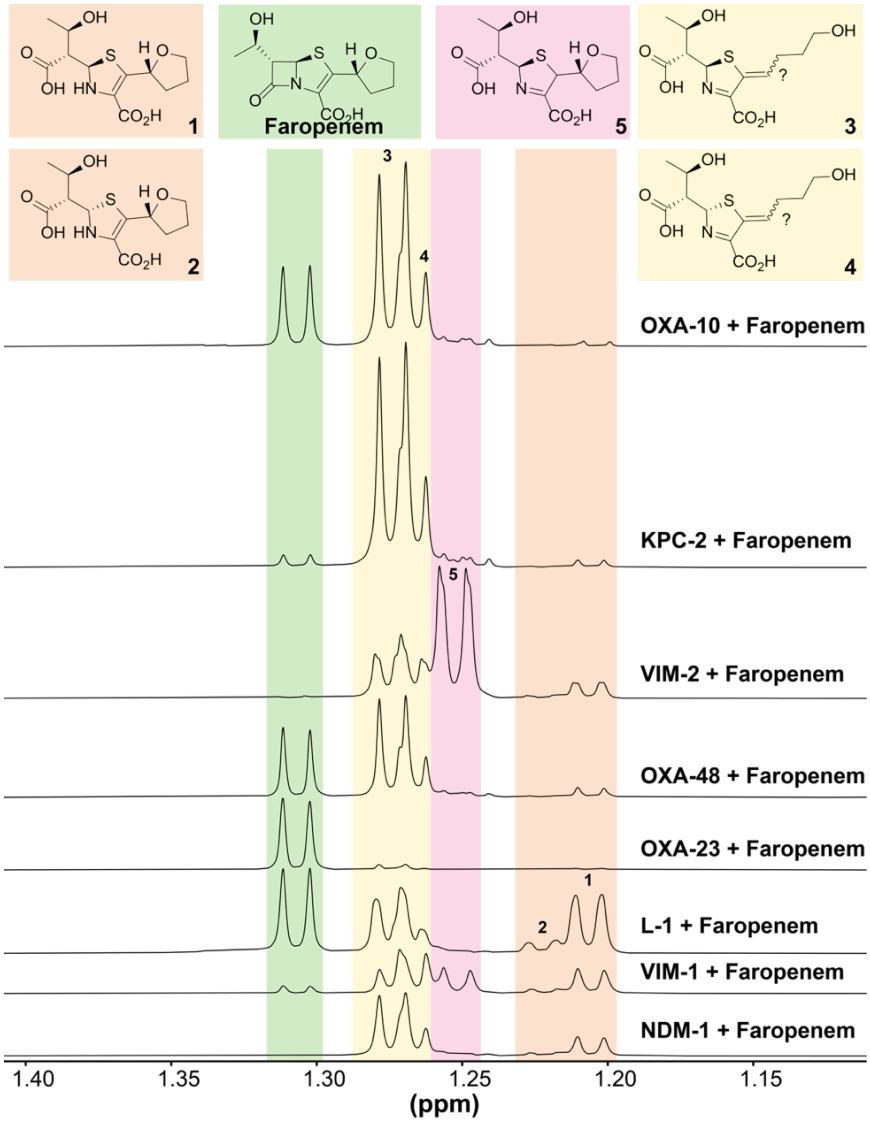


Figure 25: ^{1}H NMR (AVIII700 MHz) spectra displaying methyl group resonances of the faropenem derived products. Enamines **1** and **2** (THF ring closed products, orange), THF ring opened imines **3** and **4** (yellow) and the THF ring closed imine **5** (pink) products were formed after incubating faropenem (green) with OXA-10 (5 µM, 16 h), OXA-23 (5 µM, 15 min), OXA-48 (5 µM, 55 min), VIM-1 (280 nM, 5 min), VIM-2 (280 nM, 5 min), NDM-1 (5 µM, 5 min), KPC-2 (125 nM, 72 min), L1 (125 nM, 5 min). The products were observed to varying levels with the different enzymes. All enzymes were incubated with 5 mM faropenem apart from OXA-23, which was incubated with 2 mM faropenem. Reactions were carried out in in 50 mM sodium phosphate, pH 7.5, 10% (v/v) D_2O in H_2O. Note **5** was only observed with VIM-1 and VIM-2. Colour coding corresponds to the structures shown and the resonances.

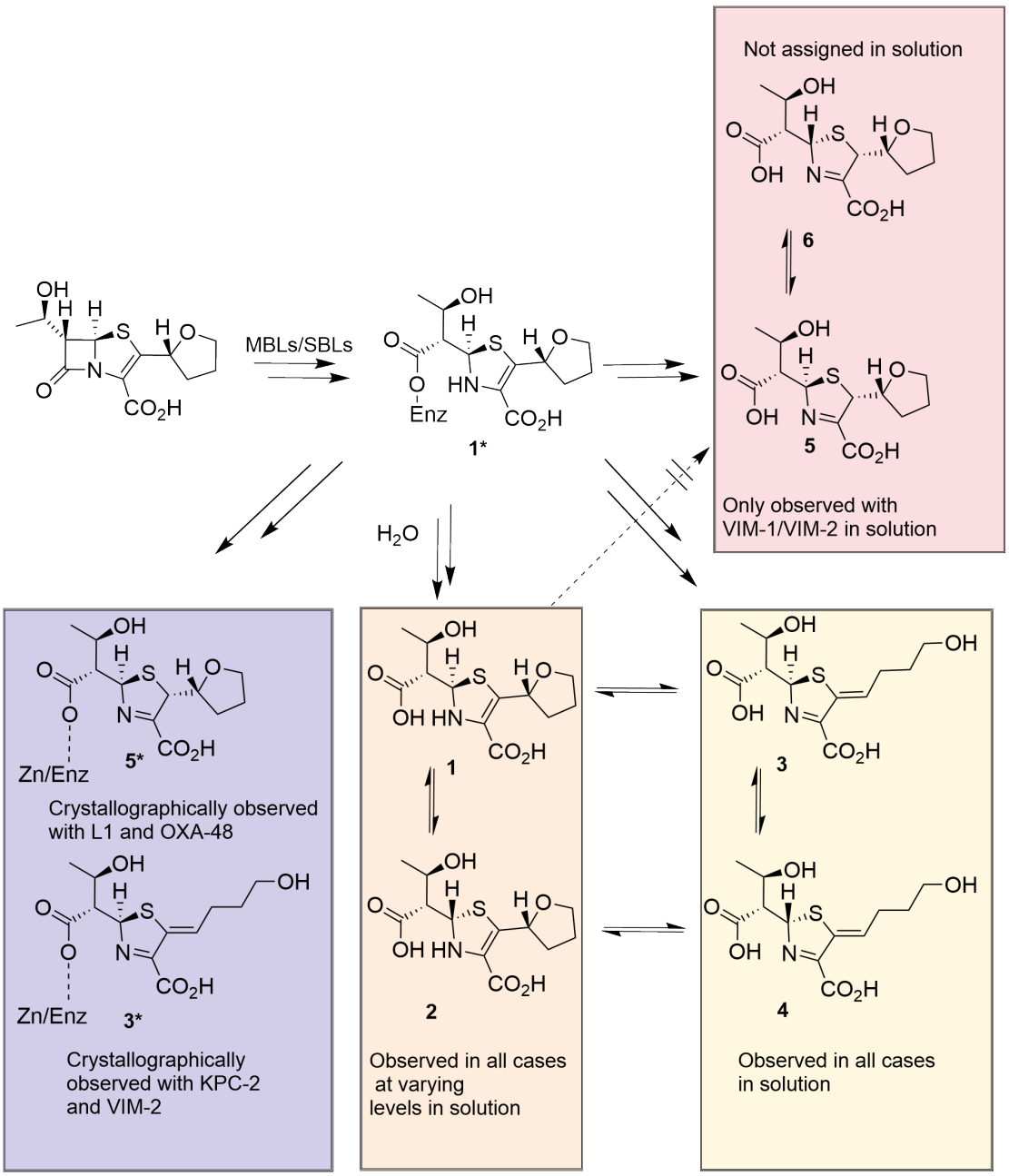


Figure 26: Summary of faropenem hydrolysis products formed by SBLs and MBLs based on solution studies and observed crystal structure complexes. *Denotes crystallographically observed enzyme-bound complexes. Note that **5** and **6** were only observed during solution studies with VIM-1 and VIM-2. Complex **5*** was previously modelled based on crystallographic data with OXA-48 (PDB 6PSG[25]).

Imines **3** and **4** with open THF rings were observed in all cases with 5(*R*)-**3** and 5(*S*)-**4** stereochemistry (**Figures 25 and 26**). The Z-alkene geometry was assigned solely based on the crystallographic analyses discussed above; however, it is likely that this geometry also occurs in solution. **3** and **4** also appear to

be formed non-enzymatically from **1** and **2** based on the NMR experiments; however, **3**, at least in part, could be a direct enzyme product. Compound **5** i.e., the imine with the close THF ring was only observed in VIM-1 and VIM-2, as a minor and major product respectively (**Figures 25, S4 and S5**). The stereochemistry of C2 was not assigned in solution studies but was observed to be 2(*S*) based on the crystallographic studies with L1 (**Figure 26**). There was no evidence for the formation of the C5 epimer of **5** (i.e., compound **6**), although **6** cannot be ruled out as a minor product. There was also no evidence of conversion from **1**/**2** to **5**/**6.** Experiments analysing the turnover of faropenem *via* VIM-2 showed that **1** and **2** are initially the dominant product but that these slowly tautomerise to give 3 and **4** respectively along with **5** (**Figure S16**).

Overall, the solution studies provide important additional information to the crystallographic observations, although some differences were observed between the two. In the case of L1, for instance, the imine with the closed THF ring (**5***) was observed crystallographically. However, compound **5** was not seen in the solution studies with L1 (**Figures 25 and S1**). A possible explanation is that, in the case of L1, tautomerisation of the complexed enamine (**1***) leads to the formation of protein bound **5*** under crystallographic conditions (**Figure 26**). Moreover, in the L1: faropenem crystal structure, **5*** was characterised in the (*S*) configuration which could not be defined in our NMR studies. This contrasts with what was recently observed in a structure of OXA-48 with a faropenem derived product, in which C2 was modelled in the (*R*)-configuration.[25] However, it is important to note that the relatively poor resolution of the other structure (i.e., 2.1 Å vs 1.57 Å) makes it unclear whether the C2 configuration in this faropenem derived product was modelled accurately.

The same 5(*S*)-**5*** product was observed in a crystal structure of BlaC (PDB: 4EBL),[24] but the electron density around the THF derived side chain was poor and may indicate that the C2 atom is in the sp^2 hybridised form, which would rule out the **5*** complex. The crystal structures of VIM-2 and KPC-2 described here showed no evidence of the THF ring closed product (**Figures 14 and 25**). Instead, the

imine alkene **3*** was modelled in the crystal structure and was also observed in solution. However, whilst **3** could be produced as a direct enzyme product arising from **3***, the combined results indicate that it is more likely that **3** is, at least predominantly, produced from enamine **1** *via* **1*.** One method which could be used for further studies is to perform a chemical hydrolysis on products **1** to **5** and compare the results using NMR.

Biapenem Kinetic Assays

Like faropenem, biapenem is also capable of inhibiting several SBLs but has been shown to be susceptible to MBL hydrolysis and some SBLs.[9,27] Steady state kinetics was used to measure kinetic parameters for biapenem turnover by VIM-1 and VIM-2. The biapenem absorbance was measured at 293 nm for 30 minutes, with the absorbance decreasing over time upon biapenem hydrolysis.[69] Both VIM-1 and VIM-2 appeared to degrade biapenem at similar levels. The K_M and k_{cat} values show that VIM-1 had a higher affinity and higher turnover rate compared to VIM-2. However, initial K_M and k_{cat} values were significantly higher than those reported.[82] The K_M of VIM-4 is lower by a factor of 10, indicating a much higher affinity.[82]

Moreover, the turnover rate for VIM-4 is higher, with the k_{cat} for VIM-4 being several magnitudes higher than k_{cat} VIM-1 and VIM-2 (**Table 5**, **Figures 27 and 28**). The k_{cat}/K_M values for the experimental values are promising however, showing that the VIM-1 and VIM-2 used for the experiments in this chapter are less active. The kinetic experiments should be repeated in different conditions with different enzyme batches, to investigate differences with the reported values in K_M and k_{cat}.

Enzyme	Type	Class	k_{cat} (s^{-1})	K_M (μM)	k_{cat}/K_M (s^{-1} $μM^{-1}$)
VIM-1	MBL	B1	0.0002/**8.5**[88] ($1x10^{-5}$)	579.6/**7.5**[88] (0.13)	$3.4x10^{-7}$/**1100**[88]
VIM-2	MBL	B1	0.00013/**8.5**[88] ($1x10^{-5}$)	783/**15**[88] (0.14)	$1.7x10^{-8}$/**550**[88]
VIM-4[82]	MBL	B1	**15**	**66**	**230**

Standard deviations of the mean in parenthesis (n=3). See Experimental Section for VIM-1 and VIM-2 assay details. Reported values are in bold

Table 5: Reported and observed kinetic values for VIM-1, VIM-2 and VIM-4 with biapenem. Values in bold are reported values for VIM-1 and VIM-2, and standard deviation values for my experimental values are in parantheses.[83] Note the difference between my experimental results and those reported, which requires further investigation.

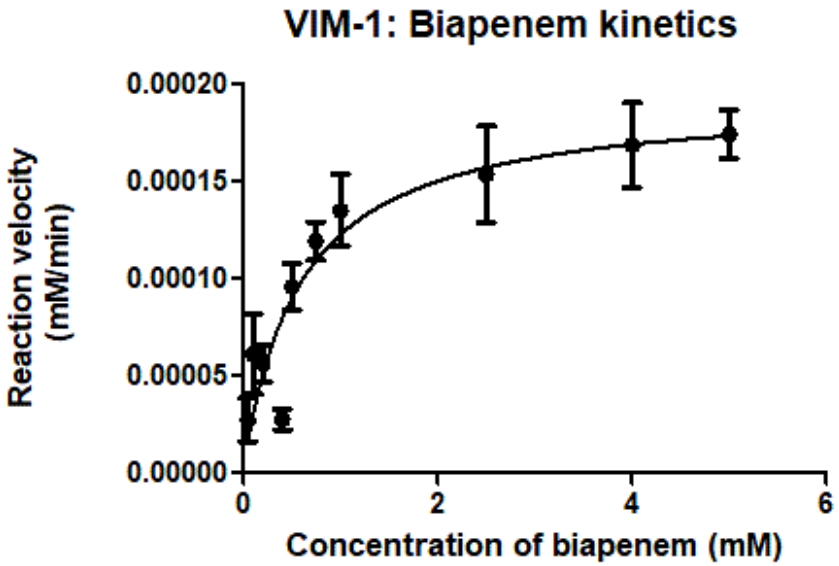


Figure 27: Michaelis Menten curve for VIM-1 and biapenem. Kinetics data were obtained from initial experiments performed with 1 μM VIM-1. Error bars indicate the standard error mean for each plotted value. These values were observed to give the best curve compared to the experiments at 100 nM, even though the kinetics parameters were high compared to those previously reported (**Table 5**).

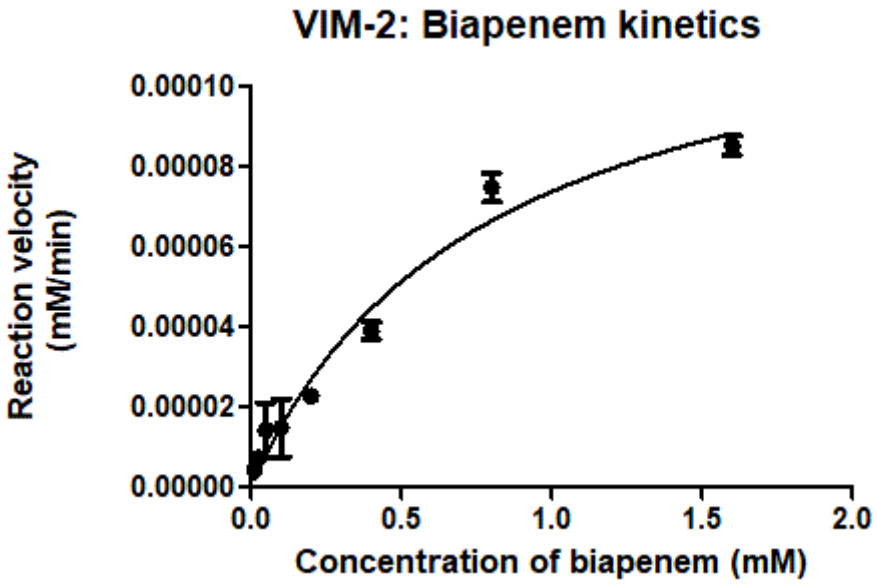


Figure 28: Michaelis Menten curve for VIM-2 and biapenem. The curve was produced using 100 nM VIM-2, since this gave more consistent values for lower concentrations of biapenem compared to the experiments performed with 1 µM VIM-2. Higher concentrations of biapenem would be needed in order to reach a plateau. Error bars indicate the standard error mean for each plotted value.

Biapenem Crystallography Dataset

Crystallographic studies were performed to understand how the products derived from biapenem interact with the active site of VIM-2. To obtain a crystal structure, VIM-2 was crystallised as previously described (Section Methods and Materials), and 50 mM biapenem was soaked into the crystal at various time points.[43] A dataset was obtained to 1.3 Å at Diamond Light Source in the space group *I* 2 2 2 (**Table 6**).

The dataset was of high resolution (1.3 Å); however, the resolution was cut off to 1.5 Å to improve the completeness of the dataset. Once molecular replacement (using PDB identifier 4BZ3[34]) was complete,

it was clear that there was more than one biapenem-derived product (enamine or imine) at the active site, and that there was one molecule in the asymmetric unit (**Figures 29 and 30**).

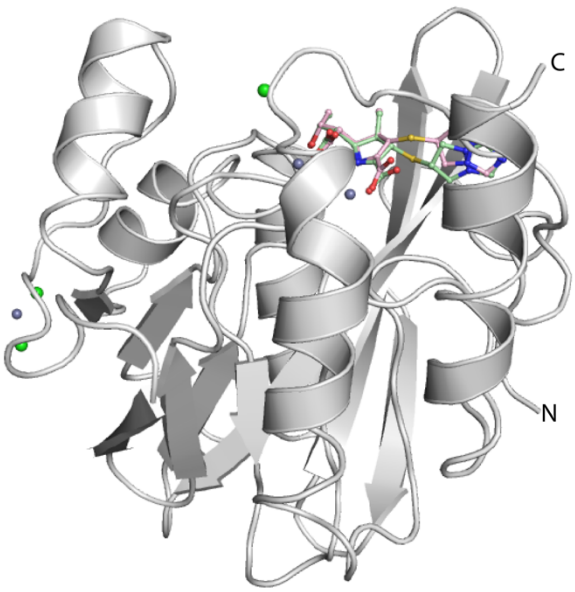


Figure 29: View from a structure of VIM-2: biapenem derived product complex in the asymmetric unit of an *I* 2 2 2 crystal. Zinc ions are in grey, chloride ions in green (PDB 6Y6J).[7]

	VIM-2: biapenem
PDB accession	6Y6J
Data collection	
Facility/Beamline	Diamond I04-1
Space group	*I* 2 2 2
Molecules/ASU	1
Cell dimensions	
a, *b*, *c* (Å)	64.324, 74.02, 78.354
α, β, γ (°)	90.0, 90.0, 90.0
Wavelength	0.9159
Resolution (Å)	27.61-1.5 (1.554-1.50)
R_{pim}	0.030 (0.205)
CC 1/2	0.998 (0.872)
I / σI	14.6 (3.0)
Completeness (%)	99.56 (98.96)
Multiplicity	13.3 (12.6)
Refinement	
Resolution (Å)	27.61-1.5
No. reflections	30179
R_{work} / R_{free}	0.1287 / 0.1573
No. non-H atoms	2048
Protein	1792
Solvent	200
Zn	3
Ligands	56
B-factors	
Protein	17.40
Solvent	31.03
Ligands	16.49
R.m.s. deviations	
Bond lengths (Å)	0.009
Bond angles (°)	1.15
Ramachandran (%)	
Outliers	0.00
Favoured	98.25

Table 6: Data collection and refinement statistics for the VIM-2: biapenem structure. Numbers in brackets are for the highest-resolution shell.

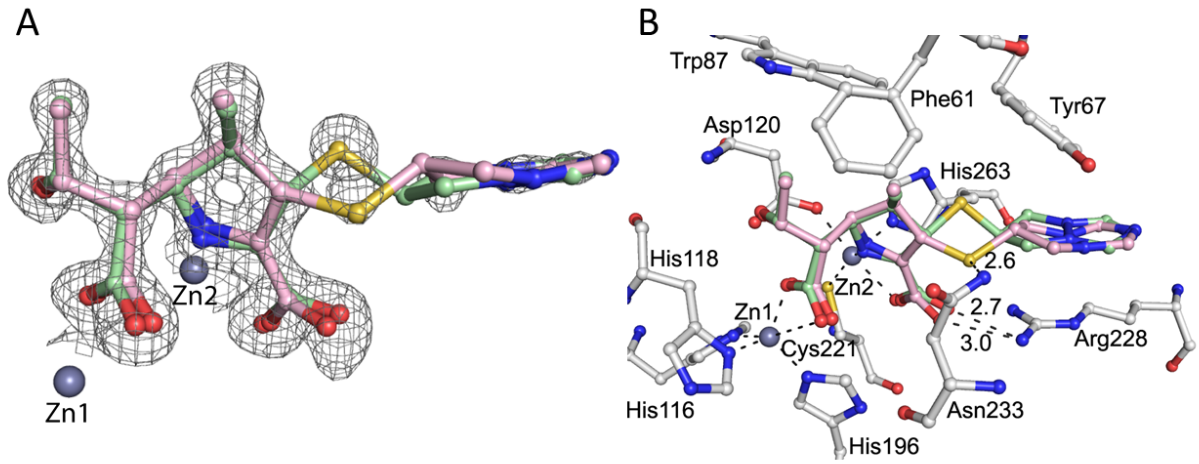


Figure 30: Structure of biapenem derived products with VIM-2. PDB: 6Y6J. A) The $mF_o - DF_c$ map is shown as a grey mesh contoured at 3σ. The enamine is shown in light pink and the imine in light green. Note the poor density around the biapenem side chain, likely caused by the multiple conformations of the side chain. B) Interactions occurring between the imine and enamine forms of the biapenem hydrolysis product and the VIM-2 active site**.** Both products interact with Arg228, and only the enamine interacts with Asn233 via the thioether sidechain. Distances are in Å. PDB: 6Y6J.[7]

Further refinement indicated the presence of both imine and enamine products with the imine being in the (*R*)-configuration at C2. The imine and the enamine were modelled to an occupancy of 50% (**Figure 30**). The electron density around the C2 side chain is significantly weaker than for the main structure, most likely due to multiple conformations of the side chain in the different products. The imine product was modelled in the (*R*)-configuration at the C2 position.

The interactions observed in this structure are consistent with previous VIM-2: carbapenem derived substrate/inhibitor structures,[34,43,75] with the newly formed carboxylate displacing the zinc bridging water and the same hydrophobic interactions being observed (**Figures 30 and 31**). Both the imine and enamine C7 carboxylate interact with Arg228, while Asn233 interacts with the sulfur on the side chain of the enamine (2.6 Å) but not the enamine product (**Figures 30-32**). This is consistent with previous VIM-2: substrate/ inhibitor structures.[43]

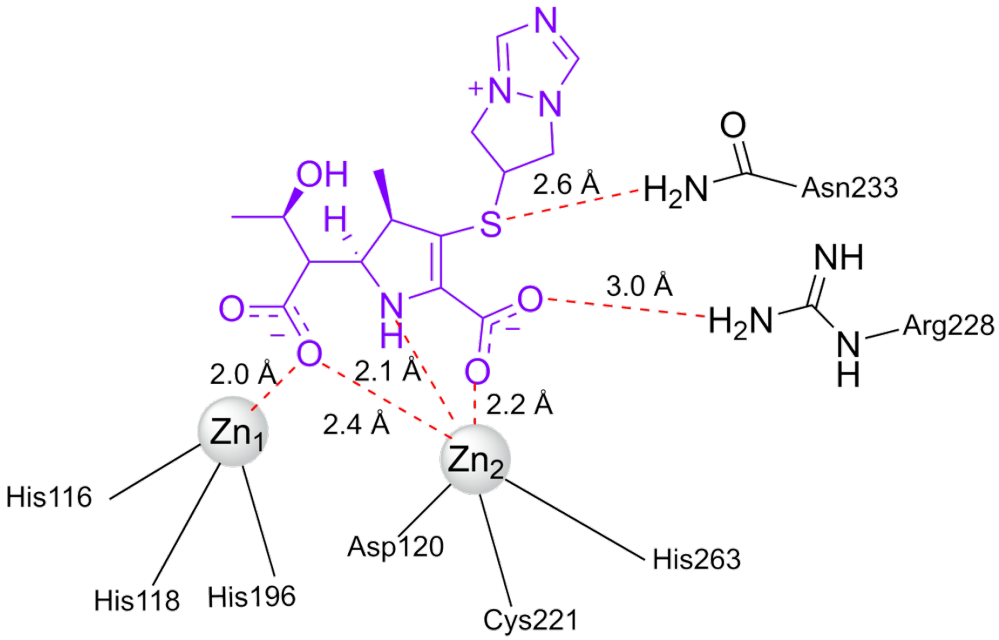


Figure 31: Hydrogen bond interactions between the enamine biapenem-derived product and VIM-2 (PDB 6Y6J). Interactions are shown as red dashed lines with the distances labelled.

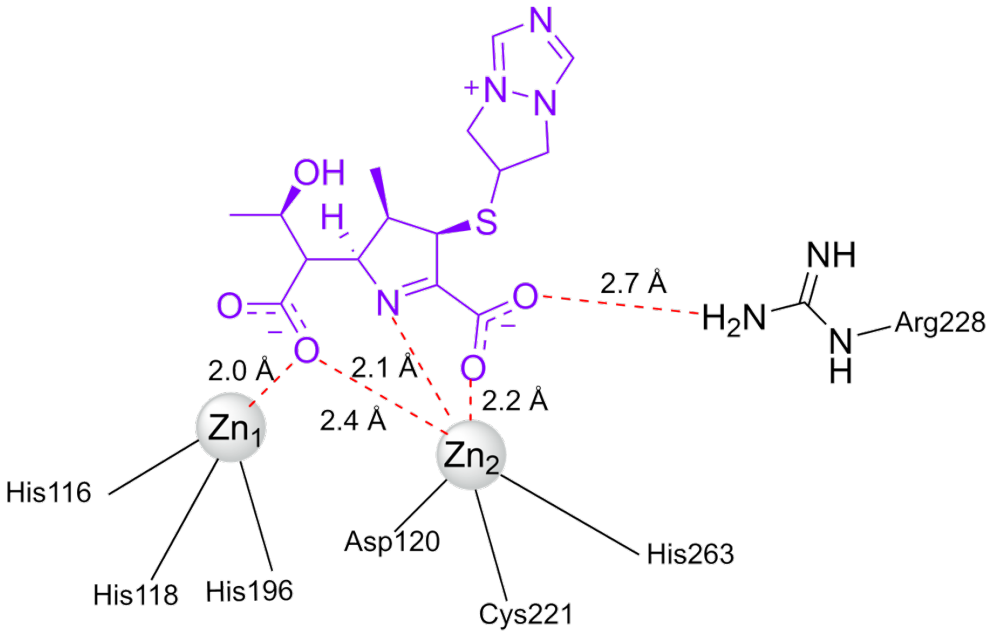


Figure 32: Hydrogen bond interactions between the imine derived biapenem product and VIM-2 (PDB 6Y6J). Interactions are shown as red dashed lines with distances labelled. Note the lack of interactions between the imine product and Asn233 compared to the enamine product and compared to faropenem products (**Figures 16 and 31**).

The binding modes between VIM-2 the biapenem derived structure and the VIM-1: meropenem derived structure (5N5I[10]) show some differences. The newly formed carboxylate and hydroxyethyl group in the meropenem imine product have a different orientation compared to both biapenem products. The binding modes between the biapenem derived products and the faropenem imine are more similar with regard to the positioning of the carboxylate (**Figure 33**).

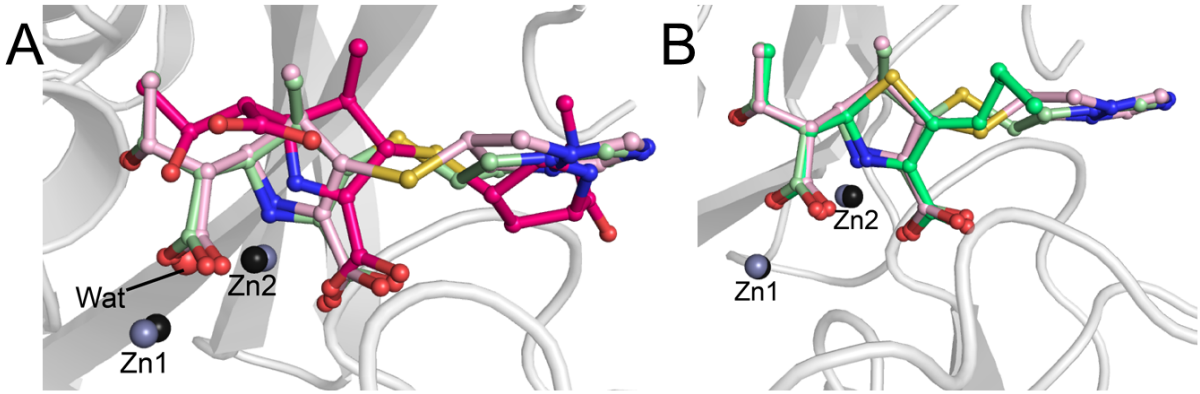


Figure 33: Comparisons between the VIM-2: biapenem derived product structure (pink and green, PDB 6Y6J) with (A) VIM-1: meropenem (light purple, PDB 5N5I, RMSD 0.966[10]) and (B) VIM2: faropenem (purple, PDB 7A5Z, RMSD 1.016). The hydroxyethyl position in the VIM-1: meropenem derived product structure is significantly different compared to the VIM-2: faropenem derived product structure.[7]

Biapenem NMR Data

In order to compare the crystallographic observations with the reaction in solution, I investigated β-lactamase catalysed hydrolysis of biapenem using ^{1}H NMR. This was initially done just with VIM-2, but later was done with VIM-1 and KPC-2 to compare the products formed. All individual spectra are given in the Appendix (**Figures S17-S19**). The findings are consistent with those observed for other SBLs and Class B1 MBLs.[8,9] A minor enamine product (**7**) was formed with all three enzymes, albeit at varying levels. The imine products (**8** and **9**) were also seen with VIM-1, VIM-2 and KPC-2, and no lactone products were seen (**Figure 34**).

This observation is consistent with what was observed crystallographically observed, although the ratios of products varied between the solution and crystallography studies, indicating that **7** tautomerises to give **8** and **9** (**Figure 35**).[9] ^{1}H NMR showed that after 30 minutes, most of the **7** was converted to **8** (**Figure 34**). Further NMR experiments should be performed to verify the stereochemistry at C2, and to assign some of the minor peaks that were observed.

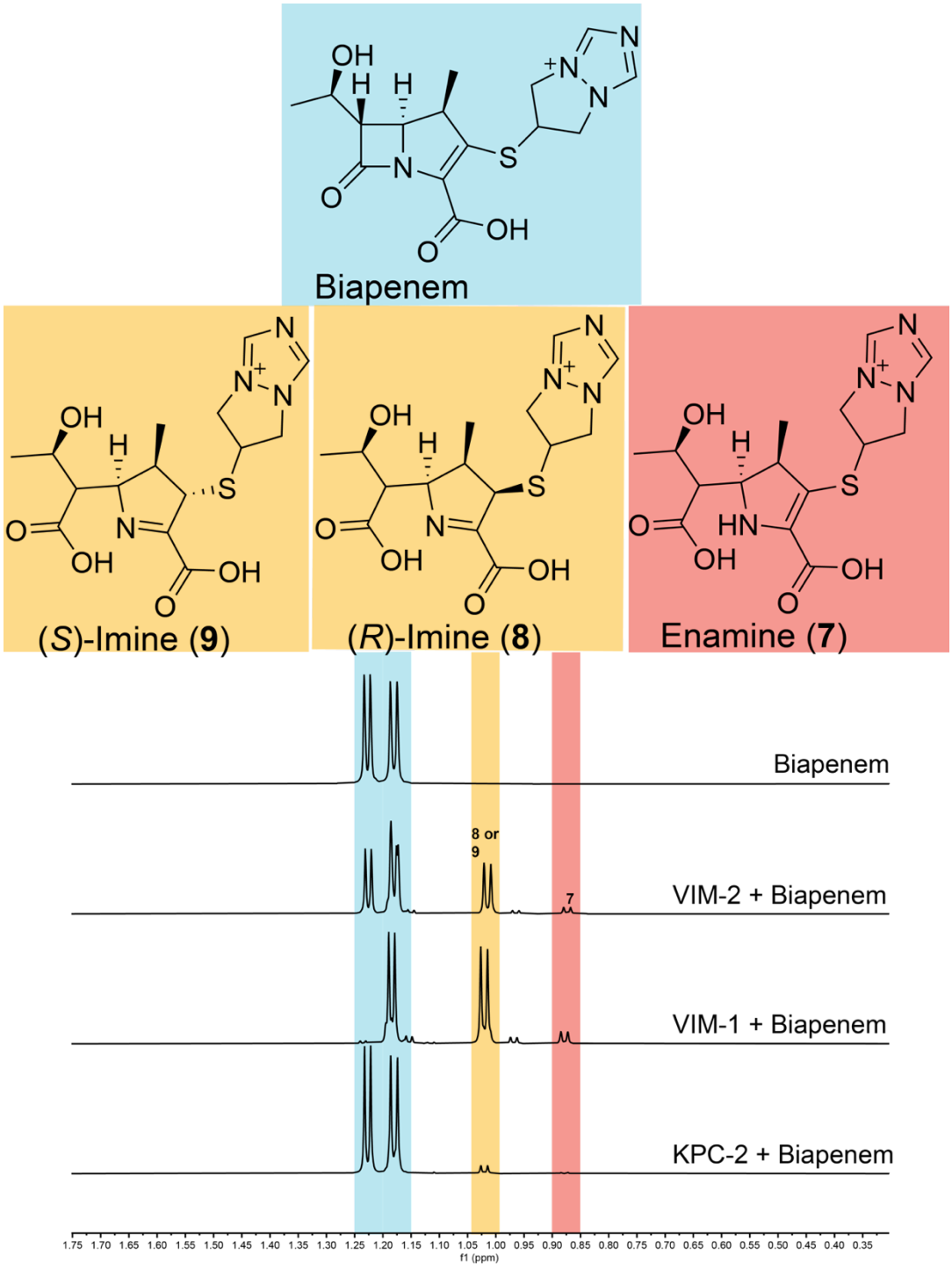


Figure 34: ^{1}H NMR (AVIII600HD MHz) spectra displaying methyl group resonances of the biapenem-derived products. As in the crystal structure, both the enamine and imine products are visible in the NMR spectra for VIM-2 and biapenem after 30 minutes. Both products were also observed with VIM-1 and KPC-2, although to varying levels. Concentrations were 280 nM VIM-1, VIM-2 and 125 nM KPC-2).

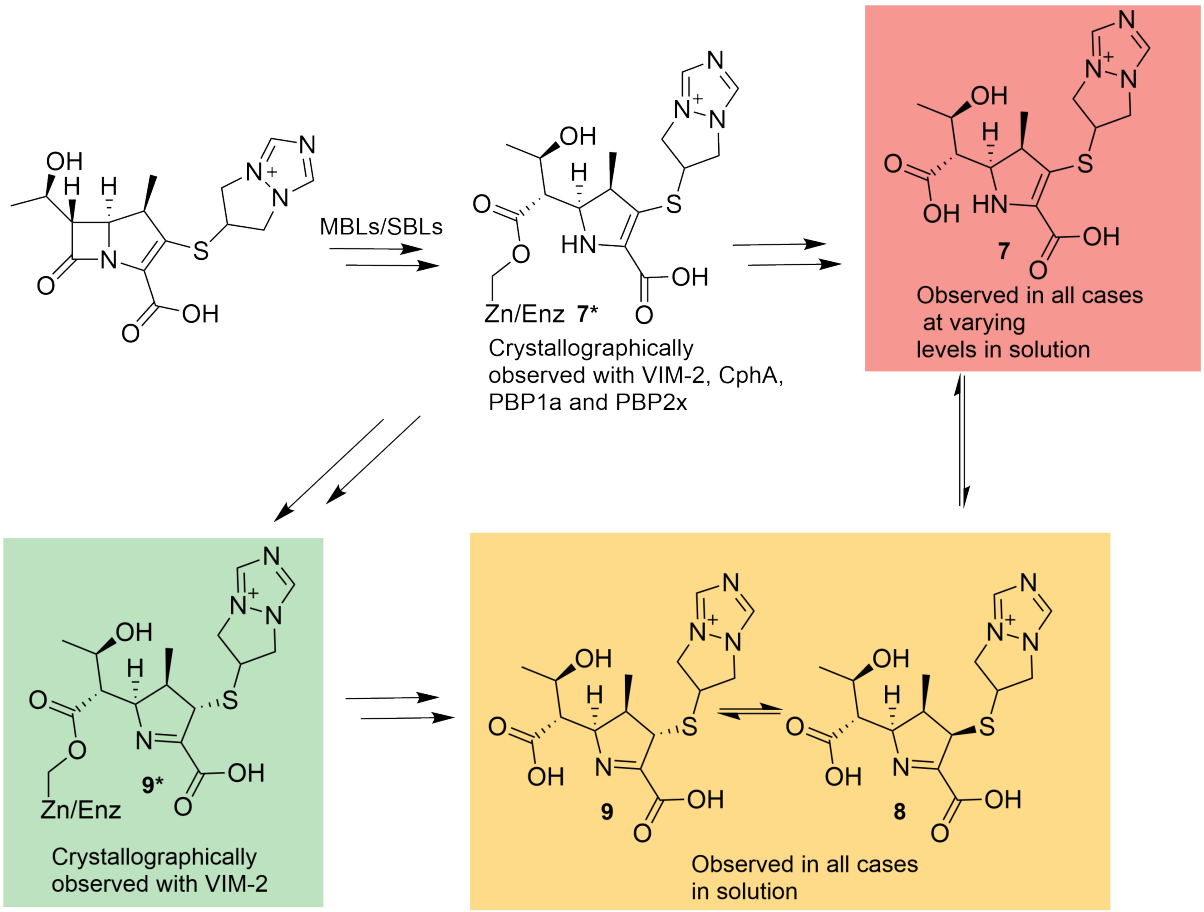


Figure 35: Summary of faropenem hydrolysis by SBLs/MBLs based on NMR solution studies and observed crystal structure complexes. * Denotes complexes observed in crystals. All three product forms were seen in solution with all enzymes. Note that **7*** has been observed in several previous crystal structures such as PBP2x (PDB 2ZC3[83]), PBP1A (PDB 2ZC5[83]) and CphA (PDB 1X8I[84]).

Conclusions

Whilst studying the MBLs and SBLs in this chapter, it was apparent that VIM-2 can be successfully expressed and crystallised in several conditions. However, crystallisation conditions to be further optimised as the protein production levels for VIM-2 were still relatively poor, with respect to the amounts required for XFEL. Moreover, it is clear that the crystal forms used for these experiments are not the optimal for soaking experiments. This could be because the solvent content is not high enough, or because the crystal packing made it difficult for the substrate to enter the active site of the protein.

Even though KPC-2 reacts interacts covalently with the nucleophilic serine at the active site, several polar interactions are necessary for stabilising the complex derived from faropenem in the active site. These observations are consistent with what has previously been seen for KPC-2 with other antibiotics and inhibitors, such as relebactam and avibactam.[43,76,79] Moreover, there are similarities observed with the binding modes of faropenem with KPC-2 and VIM-2, since these enzymes both have the Z-imine alkene hydrolysis product in their active site and the THF ring is opened, leading to the formation of a double bond between C2 and C11 (**Figure 36**).

Through the studies reported here contribute to an understanding of how both serine and metallo-β-lactamases hydrolyse penems and carbapenem antibiotics. It is clear that in the case of penems, the imine intermediate seems to preferably bind to L1, VIM-2 and KPC-2, at least as observed by crystallography. Both KPC-2 and VIM-2 had the Z alkene imine form of the product bound in the active site, whereas L1 seemed to have the (*S*)-imine product in the active site (**Figure 26**). In addition, the product in the L1: faropenem structure did not have the THF side chain ring fragmented, where the other two structures did. The opening of the THF ring observed in VIM-2 and KPC-2 was confirmed through NMR spectroscopy (compounds **3** and **4**), as was the conversion of the enamine product to the imine (**Figures 25 and 26**). This is consistent with previously reported solution studies with faropenem.[8,9] The kinetics data produced by the University of Bristol (Dr. Catherine Tooke and Dr. Hinchliffe) shows that all three enzymes are capable of hydrolysing faropenem, although KPC-2 clearly has a much slower turnover rate when compared to the VIM-2 and L1.

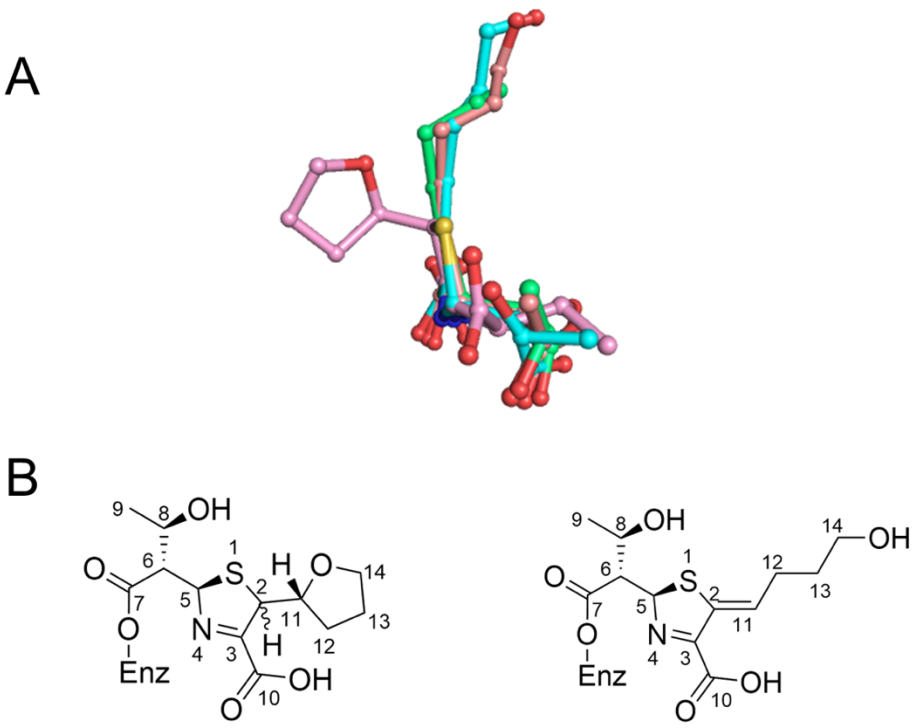


Figure 36: Comparison of the faropenem derived product complex conformations in the crystal structures solved here. Note that the conformations for the two VIM-2 crystal forms (green for the *I* 2 2 2 and salmon for the *C* 1 2 1 forms) are most similar. These conformations are similar to that observed for the faropenem derived product with KPC-2 (cyan), with the exception of an approximate 90° rotation of the hydroxyethyl group about C8. Note that, the C2 side chain conformation observed with L1 (pink) is different from that observed with the ring opened THF complexes in the other structures (PDB codes: 7A5Z, 7A60, 7A61 and 7A63). **B)** Structures of hydrolysed faropenem products as observed crystallographically. Left, the faropenem-derived product obtained on reaction with the L1 MBL. Note the (*S*)-configuration at C2. Right, the faropenem-derived product obtained on reaction with VIM-2 and KPC-2 (note in the case of KPC-2^{E166Q} the β-lactam derived carbonyl is linked to the enzyme via an ester). The stereochemistry of the exocyclic double bond was assigned based on crystallography as the *Z*-isomer.[7]

The crystal structure obtained for VIM-2 with the biapenem-derived product shows a different story compared to the faropenem structures. A clear mixture of enamine and imine products was observed

in the active site of VIM-2 with faropenem. A potential explanation is that the tautomerisation between the imine and enamine can still happen in the active site. NMR studies with biapenem shows the production of both imine and enamine products (compounds **7**, **8** and **9**) by VIM-1, VIM-2 and wildtype KPC-2, confirming what was observed crystallographically in the VIM-2 structure. Previous studies with biapenem all showed only the enamine in the active site, with no imine products having been observed crystallographically previously (**Figure 37**).[83,84]

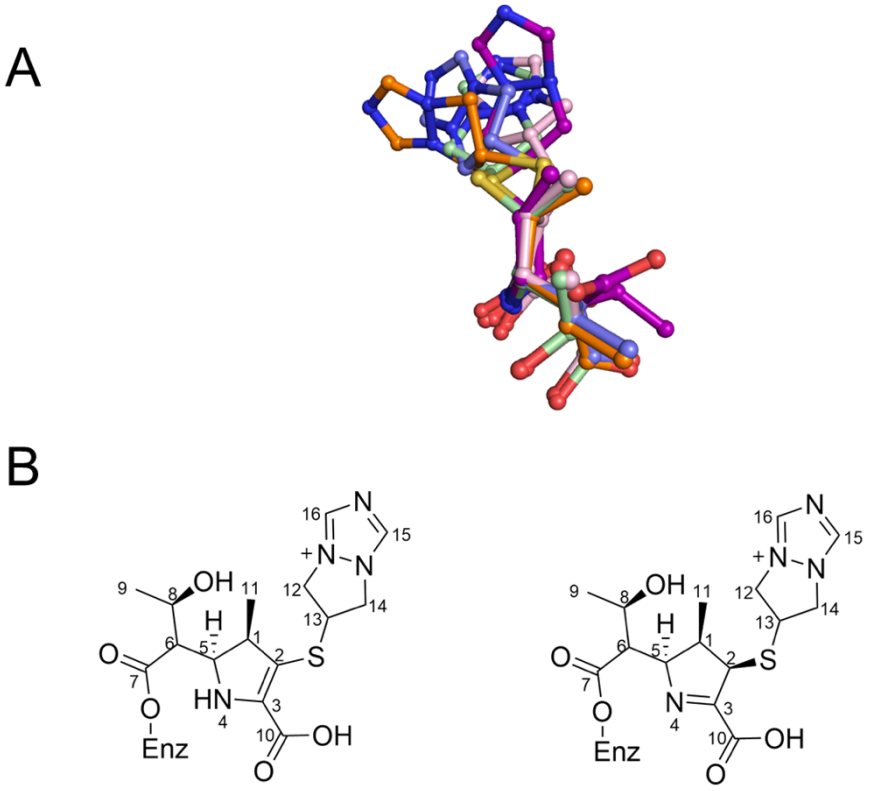


Figure 37: Overlay of crystallographically-observed biapenem structures. A) Superimposition of the biapenem derived products in crystals. The enamine is shown in light pink and the imine in light green (PDB 6Y6J). Similar binding is seen between the enamine and the acyl enamine from the PBP2x: biapenem complex (PDB 2ZC3, slate blue[83]), PBP1A: Biapenem (PDB 2ZC5, orange[83]) and CphA (PDB 1X8I, purple[84]). B) schematic representation of the biapenem derived products.[7]

Kinetics assays with VIM-1 and VIM-2 against biapenem revealed low activity, with unusually high K_m values for B1 enzymes and carbapenem substrates (**Table 5**). This is unusual, as the curves for both

enzymes looked as expected, with a steep slope and a gradual plateau with the high enzyme concentrations. One possible problem is that the enzyme concentration was too high (100 nM). High concentrations mean that the enzyme turns over the substrate too quickly to get an accurate slope. Future work would involve experiments with a lower enzyme concentrations and fresh batches of enzymes to see how these affect the Michaelis Menten constants that are determined.

Both the solution and crystallographic studies gave further insight into how β-lactamases behave with penems and carbapenems, with the imine product being the predominant product upon equilibrium with the penems. Further studies should be done with a range of SBLs and MBLs along with different penems such as sulopenem. This would allow for a more in-depth comparison of different binding modes for the hydrolysed products along with having an in depth understanding of the solution kinetics.

Gaining structural information about the intermediates that are produced would also be beneficial in gaining more precise knowledge about the hydrolysis mechanism for penems and carbapenems. For this, time resolved crystallography would need to be performed to have the slightest chance of seeing an intermediate structure. In addition, it would enable a better understanding of the tautomerisation process between the imine and the enamine products i.e., what triggers the tautomerisation and do any products have inhibitory properties. Being able to visualise the conversion between these two species would be a step forward in understanding the mechanism of carbapenem hydrolysis, which, eventually, could lead to the creation of better antimicrobial therapeutics.

References

(1) Makena, A.; Düzgün, A. O. ¨; Brem, J.; Mcdonough, M. A.; Rydzik, A. M.; Abboud, M. I.; Saral, A. A.; Ays¸egül, A.; Çiçek, Ç.; Sandalli, C.; et al. Comparison of Verona Integron-Borne Metallo-Lactamase (VIM) Variants Reveals Differences in Stability and Inhibition Profiles. **2016**.

(2) Walsh, T. R.; Toleman, M. A.; Poirel, L.; Nordmann, P. Metallo-Beta-Lactamases: The Quiet before the Storm? *Clin. Microbiol. Rev.* **2005**, *18* , 306–325.

(3) Poirel, L.; Naas, T.; Nicolas, D.; Collet, L.; Bellais, S.; Cavallo, J. D.; Nordmann, P. Characterization of VIM-2, a Carbapenem-Hydrolyzing Metallo-Beta-Lactamase and Its Plasmid- and Integron-Borne Gene from a *Pseudomonas Aeruginosa* Clinical Isolate in France. *Antimicrob. Agents Chemother.* **2000**, *44*, 891–897.

(4) Lisa, M.-N.; Palacios, A. R.; Aitha, M.; González, M. M.; Moreno, D. M.; Crowder, M. W.; Bonomo, R. A.; Spencer, J.; Tierney, D. L.; Llarrull, L. I.; et al. A General Reaction Mechanism for Carbapenem Hydrolysis by Mononuclear and Binuclear Metallo-β-Lactamases. *Nat. Commun.* **2017**, *8*, 538.

(5) Docquier, J.-D.; Lamotte-Brasseur, J.; Galleni, M.; Amicosante, G.; Frère, J.-M.; Rossolini, G. M. On Functional and Structural Heterogeneity of VIM-Type Metallo-Beta-Lactamases. *J. Antimicrob. Chemother.* **2003**, *51*, 257–266.

(6) Garcia-Saez, I.; Docquier, J.-D.; Rossolini, G. M.; Dideberg, O. The Three-Dimensional Structure of VIM-2, a Zn-β-Lactamase from *Pseudomonas Aeruginosa* in Its Reduced and Oxidised Form. *J. Mol. Biol.* **2008**, *375*, 604–611.

(7) DeLano, W. L. The PyMOL Molecular Graphics System. *Schrödinger LLC www.pymol.org* **2008**, http://www.pymol.org.

(8) Lohans, C. T.; Freeman, E. I.; Groesen, E. van; Tooke, C. L.; Hinchliffe, P.; Spencer, J.; Brem, J.; Schofield, C. J. Mechanistic Insights into β-Lactamase-Catalysed Carbapenem Degradation Through Product Characterisation. *Sci. Rep.* **2019**, *9*, 13608.

(9) Lohans, C. T.; van Groesen, E.; Kumar, K.; Tooke, C. L.; Spencer, J.; Paton, R. S.; Brem, J.; Schofield, C. J. A New Mechanism for β-Lactamases: Class D Enzymes Degrade 1β-Methyl Carbapenems through Lactone Formation. *Angew. Chemie Int. Ed.* **2018**, *57*, 1282–1285.

(10) Salimraj, R.; Hinchliffe, P.; Kosmopoulou, M.; Tyrrell, J. M.; Brem, J.; van Berkel, S. S.; Verma, A.; Owens, R. J.; McDonough, M. A.; Walsh, T. R.; et al. Crystal Structures of VIM-1 Complexes Explain Active Site Heterogeneity in VIM-Class Metallo-β-Lactamases. *FEBS J.* **2019**, *286*,

(11) Everett, M.; Sprynski, N.; Coelho, A.; Castandet, J.; Bayet, M.; Bougnon, J.; Lozano, C.; Davies, D. T.; Leiris, S.; Zalacain, M.; et al. Discovery of a Novel Metallo-β-Lactamase Inhibitor That Potentiates Meropenem Activity against Carbapenem-Resistant *Enterobacteriaceae*. *Antimicrob. Agents Chemother.* **2018**, *62*, e00074-18.

(12) Kalp, M.; Carey, P. R. Carbapenems and SHV-1 β-Lactamase Form Different Acyl-Enzyme Populations in Crystals and Solution †. *Biochemistry* **2008**, *47*, 11830–11837..

(13) Perry, C. M.; Ibbotson, T. Biapenem. *Drugs*. Adis International Ltd October 10, 2002, 2221–2234.

(14) Bonfiglio, G.; Maccarone, G.; Mezzatesta, M. L.; Privitera, A.; Carciotto, V.; Santagati, M.; Stefani, S.; Nicoletti, G. In Vitro Activity of Biapenem against Recent Gram-Negative and Gram-Positive Clinical Isolates. *Chemotherapy* **1997**, *43*, 393–399.

(15) Kaushik, A.; Ammerman, N. C.; Tasneen, R.; Story-Roller, E.; Dooley, K. E.; Dorman, S. E.; Nuermberger, E. L.; Lamichhane, G. In Vitro and in Vivo Activity of Biapenem against Drug-Susceptible and Rifampicin-Resistant *Mycobacterium Tuberculosis*. *J. Antimicrob. Chemother.* **2017**, *72*, 2320–2325.

(16) Ernest, I.; Gosteli, J.; Greengrass, C. W.; Holick, W.; Pfaendler, H. R.; Woodward, R. B. The Penems, a New Class of .Beta.-Lactam Antibiotics: 6-Acylaminopenem-3-Carboxylic Acids. *J. Am. Chem. Soc.* **1978**, *100*, 8214–8222.

(17) Michaux, C.†; Charlier, P. ‡; Frère, J-M. ‡ and; Wouters*, J.†. Crystal Structure of BRL 42715, C6-(N1-Methyl-1,2,3-Triazolylmethylene)Penem, in Complex with Enterobacter

Cloacae 908R β-Lactamase: Evidence for a Stereoselective Mechanism from Docking Studies. **2005**.

(18) Coleman, K.; Griffin, D. R.; Page, J. W.; Upshon, P. A. In Vitro Evaluation of BRL 42715, a Novel Beta-Lactamase Inhibitor. *Antimicrob. Agents Chemother.* **1989**, *33*, 1580–1587.

(19) Schurek, K. N.; Wiebe, R.; Karlowsky, J. A.; Rubinstein, E.; Hoban, D. J.; Zhanel, G. G. Faropenem: Review of a New Oral Penem. *Expert Rev. Anti. Infect. Ther.* **2007**, *5*, 185–198.

(20) Dalhoff, A.; Janjic, N.; Echols, R. Redefining Penems. *Biochem. Pharmacol.* **2006**, *71*, 1085–1095.

(21) Gandra, S.; Klein, E. Y.; Pant, S.; Malhotra-Kumar, S.; Laxminarayan, R. Faropenem Consumption Is Increasing in India. *Clin. Infect. Dis.* **2016**, *62*, 1050.2-1052.

(22) Mushtaq, S.; Hope, R.; Warner, M.; Livermore, D. M. Activity of Faropenem against Cephalosporin-Resistant *Enterobacteriaceae*. *J. Antimicrob. Chemother.* **2007**, *59*, 1025–1030.

(23) Samuelsen, Ø.; Thilesen, C. M.; Heggelund, L.; Vada, A. N.; Kümmel, A.; Sundsfjord, A. Identification of NDM-1-Producing *Enterobacteriaceae* in Norway. *J. Antimicrob. Chemother.* **2011**, *66*, 670–672.

(24) RCSB PDB - 4EBL: BlaC E166A Faropenem Acyl-Intermediate Complex.

(25) Akhtar, A.; Pemberton, O. A.; Chen, Y. Structural Basis for Substrate Specificity and Carbapenemase Activity of OXA-48 Class D β-Lactamase. *ACS Infect. Dis.* **2020**, *6*, 261–271.

(26) Pemberton, O. A.; Zhang, X.; Chen, Y. Molecular Basis of Substrate Recognition and Product Release by the *Klebsiella Pneumoniae* Carbapenemase (KPC-2). *J. Med. Chem.* **2017**, *60*,

(27) Lohans, C. T.; Chan, H. T. H.; Malla, T. R.; Kumar, K.; Kamps, J. J. A. G.; McArdle, D. J. B.; van Groesen, E.; de Munnik, M.; Tooke, C. L.; Spencer, J.; et al. Non-Hydrolytic β-Lactam Antibiotic Fragmentation by l,d -Transpeptidases and Serine β-Lactamase Cysteine Variants. *Angew. Chemie Int. Ed.* **2019**, *58*, 1990–1994.

(28) Leavitt, A.; Navon-Venezia, S.; Chmelnitsky, I.; Schwaber, M. J.; Carmeli, Y. Emergence of KPC-2 and KPC-3 in Carbapenem-Resistant *Klebsiella Pneumoniae* Strains in an Israeli Hospital.

Antimicrob. Agents Chemother. **2007**, *51*, 3026–3029.

(29) Lomovskaya, O.; Sun, D.; Rubio-Aparicio, D.; Nelson, K.; Tsivkovski, R.; Griffith, D. C.; Dudley, M. N. Vaborbactam: Spectrum of Beta-Lactamase Inhibition and Impact of Resistance Mechanisms on Activity in *Enterobacteriaceae*. *Antimicrob. Agents Chemother.* **2017**, *61*.

(30) Tooke, C. L.; Hinchliffe, P.; Bragginton, E. C.; Colenso, C. K.; Hirvonen, V. H. A.; Takebayashi, Y. β-Lactamases and β-Lactamase Inhibitors in the 21st Century. *J. Mol. Biol.* **2019**, *431*, 3472–3500.

(31) Shen, P.; Wei, Z.; Jiang, Y.; Du, X.; Ji, S.; Yu, Y.; Li, L. Novel Genetic Environment of the Carbapenem-Hydrolyzing Beta-Lactamase KPC-2 among *Enterobacteriaceae* in China. *Antimicrob. Agents Chemother.* **2009**, *53*, 4333–4338.

(32) Simm, A. M.; Higgins, C. S.; Carenbauer, A. L.; Crowder, M. W.; Bateson, J. H.; Bennett, P. M.; Clarke, A. R.; Halford, S. E.; Walsh, T. R. Characterization of Monomeric L1 Metallo-Beta - Lactamase and the Role of the N-Terminal Extension in Negative Cooperativity and Antibiotic Hydrolysis. *J. Biol. Chem.* **2002**, *277*, 24744–24752.

(33) Ullah, J. H.; Walsh, T. R.; Taylor, I. A.; Emery, D. C.; Verma, C. S.; Gamblin, S. J.; Spencer, J. The Crystal Structure of the L1 Metallo-β-Lactamase from *Stenotrophomonas Maltophilia* at 1.7 å Resolution 1 1Edited by K. Nagai. *J. Mol. Biol.* **1998**, *284*, 125–136.

(34) Brem, J.; van Berkel, S. S.; Zollman, D.; Lee, S. Y.; Gileadi, O.; McHugh, P. J.; Walsh, T. R.; McDonough, M. A.; Schofield, C. J. Structural Basis of Metallo-β-Lactamase Inhibition by Captopril Stereoisomers. *Antimicrob. Agents Chemother.* **2016**, *60*, 142–150.

(35) Hengen, P. Purification of His-Tag Fusion Proteins from Escherichia Coli. *Trends Biochem. Sci.* **1995**, *20*, 285–286.

(36) Van Die, I. M.; Bergmans, H. E. N.; Hoekstra, W. P. M. Transformation In *Escherichia Coli:* Studies On The Role Of The Heat Shock In Induction Of Competence. *Microbiology* **1983**, *129*, 663–670.

(37) Cahill, S. T.; Tarhonskaya, H.; Rydzik, A. M.; Flashman, E.; McDonough, M. A.; Schofield, C. J.;

Brem, J. Use of Ferrous Iron by Metallo-β-Lactamases. *J. Inorg. Biochem.* **2016**, *163*, 185–193.

(38) Baneyx, F. Recombinant Protein Expression in *Escherichia Coli*. *Curr. Opin. Biotechnol.* **1999**, *10*, 411–421.

(39) Malakar, P.; Venkatesh, K. V. Effect of Substrate and IPTG Concentrations on the Burden to Growth of *Escherichia Coli* on Glycerol Due to the Expression of Lac Proteins. *Appl. Microbiol. Biotechnol.* **2012**, *93*, 2543–2549.

(40) Barth, H. G.; Jackson, C.; Boyes, B. E. Size Exclusion Chromatography. *Anal. Chem.* **1994**, *66*, 595–620.

(41) Laurent, T. C.; Killander, J. A Theory of Gel Filtration and Its Exeperimental Verification. *J. Chromatogr. A* **1964**, *14*, 317–330.

(42) Carson, M.; Johnson, D. H.; McDonald, H.; Brouillette, C.; DeLucas, L. J.; IUCr. His-Tag Impact on Structure. *Acta Crystallogr. Sect. D Biol. Crystallogr.* **2007**, *63*, 295–301.

(43) Parkova, A.; Lucic, A.; Krajnc, A.; Brem, J.; Calvopiña, K.; Langley, G. W.; McDonough, M. A.; Trapencieris, P.; Schofield, C. J. Broad Spectrum β-Lactamase Inhibition by a Thioether Substituted Bicyclic Boronate. *ACS Infect. Dis.* **2020**.

(44) Dessau, M. A.; Modis, Y. Protein Crystallization for X-Ray Crystallography. *J. Vis. Exp.* **2011**,

(45) Asherie, N. Protein Crystallization and Phase Diagrams. *Methods* **2004**, *34*, 266–272.

(46) Phillips, J. C.; Wlodawer, A.; Yevitz, M. M.; Hodgson, K. O. Applications of Synchrotron Radiation to Protein Crystallography: Preliminary Results. *Proc. Natl. Acad. Sci. U. S. A.* **1976**, *73*, 128–132.

(47) Materlik, G.; Rayment, T.; Stuart, D. I. Diamond Light Source: Status and Perspectives. *Philos. Trans. R. Soc. A Math. Phys. Eng. Sci.* **2015**, *373*,

(48) Kunz, C. Synchrotron Radiation. **1974**.

(49) Roux, D.; Safinya, C. R. A Synchrotron X-Ray Study of Competing Undulation and Electrostatic Interlayer Interactions in Fluid Multimembrane Lyotropic Phases. *J. Phys.* **1988**, *49*, 307–318.

(50) McNae, I. W.; Kan, D.; Kontopidis, G.; Patterson, A.; Taylor, P.; Worrall, L.; Walkinshaw, M. D.

Studying Protein–Ligand Interactions Using Protein Crystallography. *Crystallogr. Rev.* **2005**, *11*, 61–71.

(51) Ginn, H. M.; Mostefaoui, G. K.; Levik, K. E.; Grimes, J. M.; Walsh, M. A.; Ashton, A. W.; Stuart, D. I. *SynchLink* : An IOS App for ISPyB. *J. Appl. Crystallogr.* **2014**, *47*, 1781–1783. h

(52) Winter, G. *Xia2* : An Expert System for Macromolecular Crystallography Data Reduction. *J. Appl. Crystallogr.* **2010**, *43*, 186–190.

(53) Winter, G.; Waterman, D. G.; Parkhurst, J. M.; Brewster, A. S.; Gildea, R. J.; Gerstel, M.; Fuentes-Montero, L.; Vollmar, M.; Michels-Clark, T.; Young, I. D.; et al. *DIALS* : Implementation and Evaluation of a New Integration Package. *Acta Crystallogr. Sect. D Struct. Biol.* **2018**, *74*, 85–97.

(54) Evans, P. R.; Murshudov, G. N.; IUCr. How Good Are My Data and What Is the Resolution? *Acta Crystallogr. Sect. D Biol. Crystallogr.* **2013**, *69*, 1204–1214.

(55) Leslie, A. G. W.; IUCr. The Integration of Macromolecular Diffraction Data. *Acta Crystallogr. Sect. D Biol. Crystallogr.* **2006**, *62*, 48–57.

(56) McCoy, A. J.; Grosse-Kunstleve, R. W.; Adams, P. D.; Winn, M. D.; Storoni, L. C.; Read, R. J.; IUCr. *Phaser* Crystallographic Software. *J. Appl. Crystallogr.* **2007**, *40*, 658–674.

(57) Adams, P. D.; Afonine, P. V.; Bunkóczi, G.; Chen, V. B.; Davis, I. W.; Echols, N.; Headd, J. J.; Hung, L.-W.; Kapral, G. J.; Grosse-Kunstleve, R. W.; et al. *PHENIX* : A Comprehensive Python-Based System for Macromolecular Structure Solution. *Acta Crystallogr. Sect. D Biol. Crystallogr.* **2010**, *66*, 213–221.

(58) Rossmann, M. G.; IUCr. The Molecular Replacement Method. *Acta Crystallogr. Sect. A Found. Crystallogr.* **1990**, *46*, 73–82.

(59) Afonine, P. V.; Grosse-Kunstleve, R. W.; Echols, N.; Headd, J. J.; Moriarty, N. W.; Mustyakimov, M.; Terwilliger, T. C.; Urzhumtsev, A.; Zwart, P. H.; Adams, P. D. Towards Automated Crystallographic Structure Refinement with *Phenix.Refine*. *Acta Crystallogr. Sect. D Biol. Crystallogr.* **2012**, *68*, 352–367.

(60) Emsley, P.; Cowtan, K.; IUCr. *Coot* : Model-Building Tools for Molecular Graphics. *Acta Crystallogr. Sect. D Biol. Crystallogr.* **2004**, *60*, 2126–2132.

(61) Winn, M. D.; Isupov, M. N.; Murshudov, G. N. Use of TLS Parameters to Model Anisotropic Displacements in Macromolecular Refinement. *Acta Crystallogr. Sect. D Biol. Crystallogr.* **2001**, *57*, 122–133.

(62) Grade Web Server http://grade.globalphasing.org/cgi-bin/grade/server.cgi (accessed Jan 3, 2021).

(63) Moriarty, N. W.; Grosse-Kunstleve, R. W.; Adams, P. D.; IUCr. *Electronic Ligand Builder and Optimization Workbench* (*ELBOW*): A Tool for Ligand Coordinate and Restraint Generation. *Acta Crystallogr. Sect. D Biol. Crystallogr.* **2009**, *65*, 1074–1080.

(64) Young, J. Y.; Westbrook, J. D.; Feng, Z.; Sala, R.; Peisach, E.; Oldfield, T. J.; Sen, S.; Gutmanas, A.; Armstrong, D. R.; Berrisford, J. M.; et al. OneDep: Unified WwPDB System for Deposition, Biocuration, and Validation of Macromolecular Structures in the PDB Archive. *Structure* **2017**, *25*, 536–545.

(65) Willcott, M. R. MestRe Nova MestRe Nova . Mestrelab Research S.L. Feliciano Barrera 9B, Bajo, 15706 Santiago de Compostela, Spain. Http://Www.Mestrelab.Com . See Web Site for Pricing Information. *J. Am. Chem. Soc.* **2009**, *131*, 13180–13180.

(66) Tremblay, L. W.; Fan, F.; Blanchard, J. S. Biochemical and Structural Characterization of *Mycobacterium Tuberculosis* Beta-Lactamase with the Carbapenems Ertapenem and Doripenem. *Biochemistry* **2010**, *49*, 3766–3773.

(67) Crowder, M. W.; Walsh, T. R.; Banovic, L.; Pettit, M.; Spencer, J. Overexpression, Purification, and Characterization of the Cloned Metallo-Beta-Lactamase L1 from *Stenotrophomonas Maltophilia*. *Antimicrob. Agents Chemother.* **1998**, *42*, 921–926.

(68) Prism - GraphPad https://www.graphpad.com/scientific-software/prism/ (accessed Dec 26, 2020).

(69) Vera, L.; Stura, E. A. Strategies for Protein Cryocrystallography. *Cryst. Growth Des.* **2014**, *14*,

427–435.

(70) Dhar, N.; Dubée, V.; Ballell, L.; Cuinet, G.; Hugonnet, J.-E.; Signorino-Gelo, F.; Barros, D.; Arthur, M.; McKinney, J. D. Rapid Cytolysis of *Mycobacterium Tuberculosis* by Faropenem, an Orally Bioavailable β-Lactam Antibiotic. *Antimicrob. Agents Chemother.* **2015**, *59*, 1308–1319.

(71) Schneider, I.; Queenan, A. M.; Markovska, R.; Markova, B.; Keuleyan, E.; Bauernfeind, A. New Variant of CTX-M-Type Extended-Spectrum Beta-Lactamases, CTX-M-71, with a Gly238Cys Substitution in a *Klebsiella Pneumoniae* Isolate from Bulgaria. *Antimicrob. Agents Chemother.* **2009**, *53*, 4518–4521.

(72) Kim, Y.; Tesar, C.; Mire, J.; Jedrzejczak, R.; Binkowski, A.; Babnigg, G.; Sacchettini, J.; Joachimiak, A. Structure of Apo- and Monometalated Forms of NDM-1--a Highly Potent Carbapenem-Hydrolyzing Metallo-β-Lactamase. *PLoS One* **2011**, *6*, e24621.

(73) Dhar, N.; Dubée, V.; Ballell, L.; Cuinet, G.; Hugonnet, J.-E.; Signorino-Gelo, F.; Barros, D.; Arthur, M.; McKinney, J. D. Rapid Cytolysis of *Mycobacterium Tuberculosis* by Faropenem, an Orally Bioavailable β-Lactam Antibiotic. *Antimicrob. Agents Chemother.* **2015**, *59*, 1308–1319.

(74) Stoczko, M.; Frère, J.-M.; Rossolini, G. M.; Docquier, J.-D. Postgenomic Scan of Metallo-Beta-Lactamase Homologues in Rhizobacteria: Identification and Characterization of BJP-1, a Subclass B3 Ortholog from Bradyrhizobium Japonicum. *Antimicrob. Agents Chemother.* **2006**, *50*, 1973–1981.

(75) Brem, J.; Cain, R.; Cahill, S.; McDonough, M. A.; Clifton, I. J.; Jiménez-Castellanos, J.-C.; Avison, M. B.; Spencer, J.; Fishwick, C. W. G.; Schofield, C. J. Structural Basis of Metallo-β-Lactamase, Serine-β-Lactamase and Penicillin-Binding Protein Inhibition by Cyclic Boronates. *Nat. Commun.* **2016**, *7*, 12406.

(76) Feng, H.; Liu, X.; Wang, S.; Fleming, J.; Wang, D.-C.; Liu, W. The Mechanism of NDM-1-Catalyzed Carbapenem Hydrolysis Is Distinct from That of Penicillin or Cephalosporin Hydrolysis. *Nat. Commun.* **2017**, *8*, 2242.

(77) RCSB PDB - 5B1U: Crystal Structure of Metallo-beta-Lactamase SMB-1 Bound to Hydrolyzed

Imipenem https://www.rcsb.org/structure/5B1U (accessed Nov 3, 2020).

(78) OA, P.; X, Z.; Y, C. Molecular Basis of Substrate Recognition and Product Release by the Klebsiella Pneumoniae Carbapenemase (KPC-2). *J. Med. Chem.* **2017**, *60* (8).

(79) Tooke, C. L.; Hinchliffe, P.; Lang, P. A.; Mulholland, A. J.; Brem, J.; Schofield, C. J.; Spencer, J. Molecular Basis of Class A β-Lactamase Inhibition by Relebactam. *Antimicrob. Agents Chemother.* **2019**, *63*.

(80) RCSB PDB - 4EBL: BlaC E166A Faropenem Acyl-Intermediate Complex https://www.rcsb.org/structure/4EBL (accessed Nov 9, 2020).

(81) Fonseca, F.; Chudyk, E. I.; Van Der Kamp, M. W.; Correia, A.; Mulholland, A. J.; Spencer, J. The Basis for Carbapenem Hydrolysis by Class a β-Lactamases: A Combined Investigation Using Crystallography and Simulations. *J. Am. Chem. Soc.* **2012**, *134*, 18275–18285.

(82) Lassaux, P.; Traoré, D. A. K.; Loisel, E.; Favier, A.; Docquier, J.-D.; Sohier, J. S.; Laurent, C.; Bebrone, C.; Frè, J.-M.; Ferrer, J.-L.; et al. Biochemical and Structural Characterization of the Subclass B1 Metallo-Lactamase VIM-4. *Antimicrob. Agents Chemother.* **2011**, *55*, 1248–1255.

(83) Yamada, M.; Watanabe, T.; Baba, N.; Takeuchi, Y.; Ohsawa, F.; Gomi, S. Crystal Structures of Biapenem and Tebipenem Complexed with Penicillin-Binding Proteins 2X and 1A from Streptococcus Pneumoniae. *Antimicrob. Agents Chemother.* **2008**, *52*, 2053–2060.

(84) Garau, G.; Bebrone, C.; Anne, C.; Galleni, M.; Frère, J.-M.; Dideberg, O. A Metallo-Beta-Lactamase Enzyme in Action: Crystal Structures of the Monozinc Carbapenemase CphA and Its Complex with Biapenem. *J. Mol. Biol.* **2005**, *345*, 785–795.

Chapter 3 – Testing XFEL sample delivery methods with PBP5

Abstract

X-Ray free electron lasers are very promising tools for determining the structures of transient reaction intermediates, as shown by work on monitoring the reaction of photosystem II and BlaC. Several different sample delivery methods are currently available to use at XFEL beamlines, each with their own advantages and disadvantages. Here, studies on the protein Penicillin Binding Protein 5 (PBP5) were carried out to compare and contrast different sample delivery methods. The main questions that were assessed in determining adequacy of the samples delivery system were: how much protein is needed to produce a full dataset? can mixing experiments be performed? and how easy the method is to use? It was clear that all three sample delivery methods tested required relatively little protein (20 – 80mg) to obtain a dataset, however, there were issues with performing mixing experiments with the different methods that are discussed.

Introduction

To date, X-ray crystallography is the most prevalent method used to determine macromolecular structures, with the vast majority (151233) of the 170968 PDB's biological macromolecular structures being determined using X-ray diffraction.[1] This technique continues to be developed, with third and fourth generation synchrotrons allowing for micro focused beamlines that can produce a diffraction pattern from crystals as small as 10 μm. Datasets collected at synchrotrons typically result in static structures, and, due to the lack of fast pulses, it is very difficult to capture snapshots of transient reaction intermediates. Because of this, visualising intermediates for reactions with fast turnover rates (fs-ms) remains a challenge. Time resolved crystallography aims to obtain structures at several different time points along a reaction pathway to create the frames of a molecular movie.[2,3] New instruments providing bright X-Rays with a fast pulse rate enable a new time resolved method for

investigating dynamic structural biology, which has been a real challenge using standard synchrotron sources.

X-Ray Free Electron Lasers (XFELS) are linear X-Ray sources with a high peak brilliance and an X-Ray pulse in the femtosecond range.[4] Rather than accelerating electrons in a ring, as in synchrotrons, XFELs are linear and use Spontaneous Self Amplified Emission (SASE) to accelerate electrons and emit bunches of photons.[5] Because of the high flux X-ray pulses produced, XFELs typically generate high resolution structures from crystals smaller than 5 μm^3. Due to the very high number of photons in pulses of tens of femtoseconds, intense diffraction occurs for a very short period of time (ps-fs) before all of the electrons are stripped away from the atoms in the beam path leaving behind a plasma, so the crystal is near instantly vaporised, this is known as the "diffraction before destruction" principle in time resolved Serial Femtosecond Crystallography (trSFX) (**Table 1**).[4] Since the XFEL pulse duration is only 10-50 fs, the diffraction pattern of the crystal is already collected long before the crystal is destroyed.[3,6,7] The existence of XFELs therefore enables observations of fast enzyme reactions at atomic resolution.[2] Since one crystal produces only one diffraction image, tens of thousands of crystals are needed to accumulate a complete data set representing a single reaction time point.

Due the high number of images/crystals required for an XFEL structure; millilitre quantities of a microcrystal slurry are produced using highly optimised batch crystallisation methods.[7,8] Batch crystallisation requires large amounts of protein for each structure and since a number of time point structures are needed to complete a molecular movie; robust protein production methods are needed. Therefore, not all proteins, especially those that cannot be easily produced, can be easily studied using XFELs. However, it is early days for time resolved serial femtosecond crystallography (trSFX) and more efficient methods of sample delivery are constantly being developed. It is hoped that one day many more proteins can be investigated by trSFX using drastically less material and requiring less of the highly expensive beamtime.

Several different sample delivery methods have been developed to carry out XFEL experiments, each with its own advantages and disadvantages.[7] The methods discussed here are: (1) the acoustic droplet ejection method (ADE), (2) The fixed target method and (3) The gel extrusion method. Penicillin Binding Protein 5 (PBP5) was tested using each of these sample delivery methods to see which was most suitable for XFEL data collection. The fixed target and gel extrusion sample delivery methods were tested at Diamond Light Source. Serial data collection and time resolved crystallography for slow reactions has shown potential at synchrotrons.[9–13] If structures can be obtained by these sample delivery methods at the easily accessible Diamond Light Source, they would provide proof of principle that trSFX might be possible at the less accessible XFEL. *E. coli* PBP5 (DacA) was selected for sample delivery method analysis as it crystallises easily and can be produced in high yield. PBP5 is a clinically relevant enzyme being a target protein for many β-lactam antibiotics. Thus, PBP5 is potentially useful for purposes as a model XFEL enzymes, and the results may be medically relevant.[14,15]

The sample delivery methods can be tested at synchrotrons first during serial synchrotron crystallography (SSX). Several different sample delivery systems are currently being developed at Diamond Light Source including fixed target and gel extrusion methods.[8,16–19] In this work, five different datasets of PBP5 at room temperature were obtained: (1) A structure of an acyl-enzyme complex of PBP5 with the β-lactam antibiotic ertapenem, (2) A PBP5 structure from the MFX beamline at the Stanford Linac Coherent Light Source (LCLS), (3) A PBP5 structure from the I24 beamline using fixed target method, (4) A PBP5 structure from the I24 beamline using a gel extruder and (5) A PBP5 structure from the VMXi beamline using a gel extruder.

	SFX	SSX	MX Cryo Synchrotron
Temperature performed (K)	Ambient temperature	Ambient temperature	100
Advantages	Bright femtosecond pulses allow for observation of intermediates at defined reaction time points. Samples are destroyed almost instantaneously – very little radiation damage on diffraction patterns. Can use very small crystals.	Allows for room temperature studies at synchrotrons which are more readily available. Less protein is needed (less than 1 mL of crystal slurry needed). Can use very small crystals.	Cryo cooling of sample reduces radiation damage of samples. Less protein is needed than in comparison with XFEL studies.
Disadvantages	Very few XFELs are available for beam time. Large amounts of protein are needed.	Weaker, slower pulses prevent studies of intermediates for fast reactions. More radiation damage in diffraction patterns.	Cannot perform mixing experiments with cryo. This prevents studies of reaction intermediates in crystals. Radiation damage is still a common issue. Macro crystals are needed for most cryo data collection.

Table 1 Table showing the advantages and disadvantages of each different method of data collection used for these studies.

Materials and Methods

Protein Production

Due to technical issues in the laboratory caused by a bacteriophage infection, recombinant PBP5 protein was initially produced and purified by Dr. Jürgen Brem and used for all experiments described in this chapter. Two separate variants of PBP5 were used, one wildtype PBP5 and an identical construct except for having a C-terminal cysteine. Genes encoding for both proteins were expressed using the pET28b plasmid in BL21 DE3 *E. coli* cells. A transformation was performed using a kanamycin resistant LB agar plate. Starter cultures were created by picking a single colony from the plate and adding it to 100 mL 2TY media which had been treated with 50 μg/mL kanamycin, this was then incubated overnight at 37°C. The cells were grown in 7.2 litres of 2TY media which had been treated

with 50 μg/mL kanamycin and incubated at 34°C until an OD_{600} of 0.5 was reached after which time 0.2 mM in full IPTG was added and the temperature was dropped to 28°C. The cells were incubated for a further 4.5 hours before being spun down using a centrifuge (Beckman Coulter Avanti J25) and stored at -80°C.

Protein Purification

For protein purification, the cell pellet was thawed and resuspended in a buffer composed of 50 mM HEPES and 300 mM NaCl pH 8.0. Once the lysed cells had been spun down (Beckman Coulter Avanti J25) , the lysates were loaded onto His trap column for IMAC eluting with a gradient of imidazole from 10 mM to 150 mM.[20] Once the protein had been eluted from the column, the resultant fractions on the column were analysed *via* an SDS PAGE gel and those containing protein of sufficient purity were pooled. The resultant protein solution was then buffer exchanged into 50 mM HEPES, 500 mM NaCl and 1 mM TCEP for the cysteine variant and 50 mM HEPES and 200 mM NaCl for the wildtype protein. Buffer exchange was done using a PD10 desalting column. The proteins were concentrated to 7.2 mg/mL for the cysteine variant and 4.2 mg/mL for the wildtype protein.

Broad Screen Crystallisation Trials

Crystallisation broad screens were set up to test crystallisation conditions for PBP5 in its resting state, as previous structures were of PBP5 co-crystallised with an inhibitor.[21] PBP5 crystals were set up using the Phoenix crystallisation robot in the same manner as described in Chapter 2. Plates used were JCSG+, PEG RX, PEG ION, PACT PREMIER, SALT RX and Index, as purchased form Molecular Dimensions and Hampton Research. Plates were incubated at room temperature and checked on a daily basis for a week. Data were collected on crystals that appeared in conditions common to both the wild type and the mutant. When it was clear that the crystals produced from the PBP5 cysteine variant generally seemed to diffract to a higher resolution compared to the wildtype PBP5 crystals, optimisation blocks were created based on the results from the broad screening.

Macrocrystal Optimisation

The conditions with the best crystals were in E3 (0.2 M sodium iodide and 20% (w/v) PEG 3350), E5 (0.2 M sodium nitrate and 20% (w/v) PEG 3350) and H3 (0.2 M sodium iodide, 0.1 M Bis tris propane pH 7.5 and 20% (w/v) PEG 3350) of the PACT PREMIER broad screen (Molecular Dimensions). Initially, 3 24-well sitting drop plates were set up (**Tables 2-4**). Optimisation plates for E3 and E5 had a gradient of PEG 3350 and a gradient of salt concentration (sodium iodide and sodium nitrate respectively). On the other hand, the optimisation plate for H3 had a pH gradient rather than a salt concentration gradient. The plates were incubated at room temperature and checked daily for a week. All drops had a 1:1 protein: precipitant ratio. 24 well sitting drop plates were purchased from Hampton Research.

Sodium Nitrate conc. (M)	**PEG 3350 (%)**					
	18	**19**	**20**	**21**	**22**	**23**
0.1						
0.15	**X**	**X**	**X**	**X**	**X**	**X**
0.2		**X**	**X**			
0.25		**X**		**X**	**X**	

Table 2. 24 well plate used for PBP5 optimisation based on the E5 condition from PACT PREMIER. Most of these crystals produced viable crystals - these are shown with an X.

Bis-Tris pH	PEG 3350 (%)					
	18	**19**	**20**	**21**	**22**	**23**
8.1	**X**					
8.3	**X**					
8.5	**X**					
8.7	**X**					

Table 3 24 well plate used for PBP5 optimisation based on the H1 condition from PACT PREMIER. Very few of these conditions produced crystals. Conditions with crystals are shown with an X. Concentrations of sodium iodide and Bis tris propane were consistent throughout (0.1 M).

Sodium Iodide conc. (M)	PEG 3350 (%)					
	18	**19**	**20**	**21**	**22**	**23**
0.1		**X**	**X**	**X**		
0.15	**X**	**X**	**X**	**X**	**X**	**X**
0.2						
0.25						

Table 4. 24 well plate used for PBP5 optimisation based on the condition E3 in PACT PREMIER. Several conditions produced crystals - these are shown with an X.

Sodium nitrate conc. (M)	**PEG 3350 (%)**											
	15	**16**	**17**	**18**	**19**	**20**	**21**	**22**	**23**	**24**	**25**	**26**
0.05												
0.1												
0.15												
0.2					**X**	**X**						
0.25												
0.3				**X**				**X**			**X**	
0.35												**X**
0.4								**X**	**X**		**X**	

Table 5. New PBP5 optimisation blocks created from the condition E5 in the PACT PREMIER screen. Boxes marked with X are other conditions which produced crystals that were used for later soaking experiments.

Since the E5 optimisation plate produced the most PBP5 crystals, a new 96-well optimisation plate was created with a broader range of PEG and sodium nitrate concentrations (**Table 5**) (plates were purchased from Molecular Dimensions). The plate was set up with the Phoenix robot machine as previously described in Chapter 2. Plates were set up with the wildtype and the PBP5 cysteine variant. A couple of images of the crystals that appeared were collected on our in-house diffractometer, a Rigaku FRE+ X-ray generator equipped with HF Varimax optics (300 µM collimator) and a Saturn 944+ CCD detector, to investigate which crystals diffracted to the highest resolution. Since the crystals in D5 (19% (w/v) PEG 3350 0.2 M sodium nitrate) behaved the best as judged by testing diffraction using the in house Rigaku diffractometer, this condition was used for batch optimisation. The crystals in the other conditions were harvested for use as seeds.

Seeding Crystals

Crystals that appeared in the E5 24-well and 96-well optimisation plate were harvested and mixed together in an Eppendorf vial containing a standard seed bead purchased from Hampton Research. The crystals were vortexed for a total of 10 minutes with 30 seconds breaks on ice after every 30 seconds. This prevented the seeds from melting due to overheating from the vortexing process. Seeding is a technique that is often used to encourage crystallisation of proteins as they aid protein nucleation. Whilst setting up crystals for the LCLS data collection, seeds were added to the 24-well optimisation conditions. This was done to compare the shape and size of the crystals against those produced with no seeds as well as batch method crystals.

Batch Crystallisation Trials

Batch crystallisation is often used to produce large volumes of crystal slurry.[22,23] Rather than relying on the diffusion of the solution like vapour diffusion does, batch crystallisation methods involve mixing a large volume of the protein with a precipitant solution.[22] This forces the super saturation of the protein, causing it to crystallise.[22]

Since serial crystallography requires a highly concentrated microcrystal slurry, batch crystallisation trials were performed with PBP5 along with the addition of seeds. Both the wildtype and mutant conditions were tested using a precipitant solution of 19% (w/v) PEG 3350 and 0.2 M sodium nitrate at room temperature. Protein and well solutions were set up for crystallisation in 96-well Clariostar plates. Several different protein: precipitant ratios were initially tried for both the mutant and wildtype protein. 1:1, 1:2, 1:3, 1:4, 1:5 and 1:10 were all tested at room temperature to see which condition was the best, this turned out to be the 1:4. To prevent the crystals from growing too large (>50 μm^3), the plates in which the batch solutions were set up were initially shaken at 1000 rpm then at 700 rpm using a microplate shaker purchased from SciQuip. Shaking the crystals disrupts crystal growth and nucleation, making them smaller than if they were left over several days.[24]

In Oxford, the best condition was the 1:4 precipitant: protein (60 µL well solution, 15 µL protein) with the PBP5 cysteine variant and 3 µL of seeds whilst being shaken at approximately 700 rpm at ambient temperature. This was scaled up for serial experiments at Diamond Light Source.

Gel Extruder Data Collection at I24

The first serial dataset of PBP5 was collected at the I24 beamline in Diamond Light Source using the gel extruder delivery system.[17,18] This is a sample delivery method that uses very little protein, although it is incredibly difficult to perform any time resolved experiments with it unless the reactions are triggered by light.[17] In the gel extruder method, the microcrystal slurry in solution must be pooled together and allowed to settle. Afterwards, crystals from the pellet are removed using a pipette and mixed with a hydrophobic matrix.[18] The latter can be several different hydrophobic materials such as grease, lipid cubic phase (LCP) or hydroxycellulose (**Figure 1**). A multipurpose grease was purchased from SuperLube.[18] Once crystal pellet and the hydrophobic matrix were mixed, the solution is loaded into an injector, which releases the crystal/matrix mixture where it can interact with the beam. The residual sample is then collected by a nozzle using a vacuum.[17] This is a method frequently used in XFEL data collection, particularly for membrane proteins as they tend to crystallise in other hydrophobic matrices.

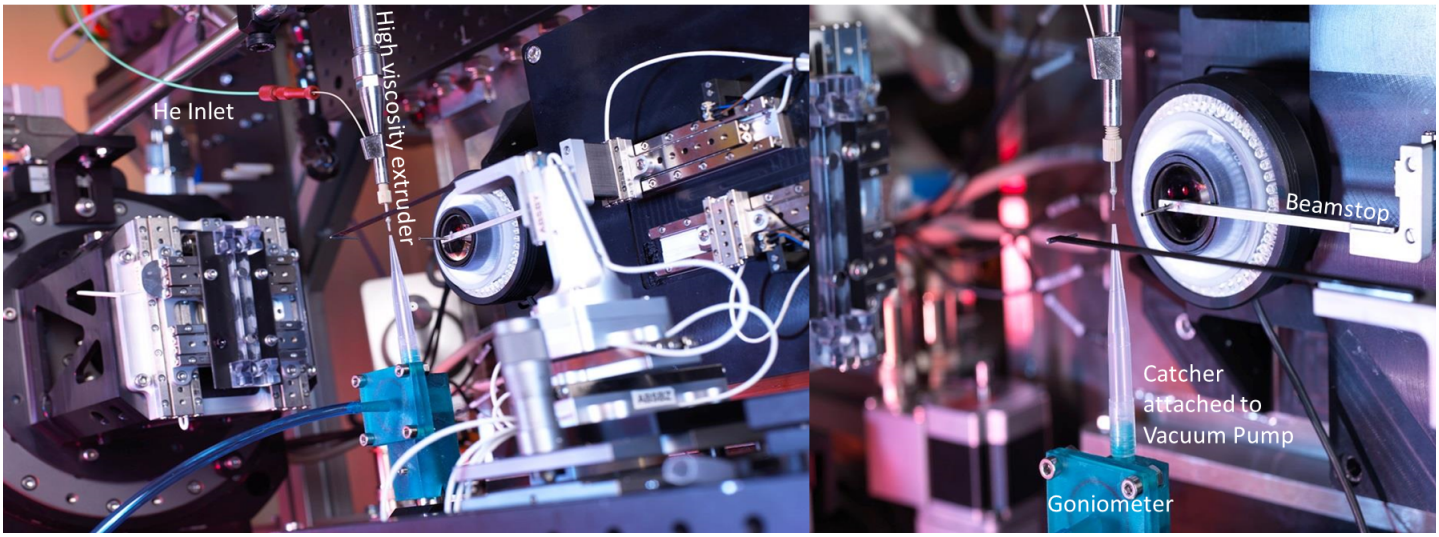


Figure 1: Photographs taken at Diamond Light Source showing the setup of the gel extruder method at the I24 beamline. A viscous jet is attached to the beamline and the sample is injected through the high viscosity extruder. The flow rate for these experiments is very low (below 0.01 mL/min). A vacuum is created below the jet to remove the matrix: crystal mixture from the beamline.

Initially, 8 µL of PBP5 cysteine variant crystal pellet was added to 32 µL of grease from Super Lube. The pellet was produced after leaving the microcrystals to settle at the bottom of the Eppendorf vial. Data were collected at room temperature (298K) with 100% transmission and 80 milliseconds exposure time. The photon energy was 12.8 keV with a flux of $4x1^{-12}$ ph/s. The flow rate for the sample was 0.003 mL/min and the detector distance was 600 mm. Data collection was also done using Lipid Cubic Phase (LCP) as the matrix instead of grease, as the crystals seemed to survive longer in compared to grease (2 hours compared to less than an hour). The sample was prepared with the same 1:4 dilution of crystals to matrix as was previously used. The same data collection variables were used for LCP data collection as they were for grease.

Crystallisation of PBP5 Cysteine C- Terminal Variant at LCLS

Several 24-well sitting drop plates were then set up at SLAC using the PBP5 cysteine variant using the 19% PEG 3350 and 0.2 M sodium nitrate with a 1:1 protein: precipitant ratio. The same protein to precipitant ratios were used as with the optimisation attempts in Oxford, with the samples being shaken at 700 rpm at ambient temperature. Conditions with a 1:1 protein: precipitant ratio produced the best crystals, so this method was scaled up for data collection with crystals being approximately 5 μm^3. Several 24 well plates were also set using 19% (w/v) PEG 3350 and 0.2 M sodium nitrate, with a 1:1 protein reservoir ratio (2 µL protein, 0.5 µL seeds and 2 µL well solution) and left overnight.

Data Collection at LCLS

LCLS was the first XFEL opened for public use in 2009; located at the University of Stanford, it has a linac 3 km long where bunches of electrons are injected and accelerated through 100 m long undulators. LCLS produces photons using SASE at a repetition rate of 120 Hz, with each pulse containing 10^{12}-10^{13} photons and having a duration of 100 fs. Beryllium refractive lenses are used to focus the beam to 5 µm, allowing for the analysis of incredibly small crystals. These photons can have an energy of up to 8.25 keV. All experiments were performed at the MFX beamline at LCLS. MFX has a standard configuration for its goniometer, allowing for several different sample delivery methods and for data collection at cryogenic and room temperature and humidity-controlled environments.[25] The goniometer (also known as the micro-diffractometer), allows for the rapid positioning of the crystals into the interaction region for data collection.

All XFEL data in this chapter were collected at the Linac Coherent Light Source at ambient temperature for the P110 screening time which was part of the LS00 beam time (A.M. Orville, *et al*, 3/05/18-6/05/18).[26] The Rayonix MX340-XFEL detector (4x4 pixel binning mode) was used for data collection with a photon energy of 9.5 keV and a 40 fs pulse rate. The detector distance was first calibrated with Silver Behanate.

Sample Delivery at LCLS

During data collection, the acoustic droplet ejection (ADE) technique was used to collect a resting state structure of the PBP5 cysteine variant.[27] This method is ideal for collecting resting state structures, as it requires smaller quantities of protein in comparison with the liquid jets methods.[28] ADE is a validated sample delivery method, as it has been used in several experiments such as those studying Photosystem II at the LCLS beamline.[27,29] Droplets are ejected onto a Kapton belt using an ADE.[27] This uses an ultrasonic pulse to dispense small droplets (10 nL) of microcrystal slurry onto the belt, which moves at a defined speed (~300 mm/s), transporting the droplets to the X-Ray interaction region for data collection. This allows for various perturbations to the crystal, such as exposure to oxygen or a pump probe system, where the droplets are exposed to laser light.

The PBP5 crystals were harvested and pooled together separately. The total crystal concentrations of the batch method and sitting drop crystal methods were $7.2x10^8$ crystals/mL and $5.7x10^7$ crystals/mL respectively. The detector distance was first calibrated with silver behenate in order to ensure the detector was behaving as expected with various detector distances. Silver behenate is often used as a calibration standard, both at XFELs and with other X-ray scattering experiments since it has a number of well positioned rings upon diffraction whose positions are well known. The energy used for data collection was 9.5 keV with a detector distance of 93.67 mm and a 3 μm beam. All data were collected using a Rayonix MX340-XFEL detector (4x4 pixel binning mode) at 10Hz with a belt speed of 300mm/s.

Gel Extruder Data Collection of PBP5 wildtype at VMXi

A new beamline has recently been developed at the Diamond Light Source. This is a beam line that is highly automated and designed for room data collection as well as using a Double Multilayer Monochromator (DMM), which helps provide a broader energy bandwidth with a beam that has 60x more photons compared to other monochromatic beamlines at Diamond Light Source. The Versatile Macromolecular Xtallography *in-situ* (VMXi) can also use something known as a “pink beam”, a slightly

polychromatic beamline that allows for a two-fold increase of photon flux without the high scattering background seen in Laue diffraction.[12,13,30]

These factors combined makes VMXi ideal for replicating serial experiments that occur in XFELs. Since the PBP5 cysteine variant sample was not available at the time due to beam time overlaps with LCLS, the PBP5 wildtype sample at a stock concentration of 4.2 mg/mL was used instead for serial room temperature data collection at VMXi. Crystals were set up using batch methods experiments optimised by myself and by Dr. Agata Butryn and data collection was done by Dr. Agata Butryn and Dr. Pierre Aller using the same gel extruder method as described for I24.

Fixed Target Data Collection of PBP5 Cysteine Variant at I24

To compare the quality of data collected from several sample delivery methods, data were collected on PBP5 cysteine variant crystals using the fixed target method. Several methods of fixed target data collection have previously been described,[31] however, this data collection used the method described by Owen *et al.*[32] The crystals are loaded onto a silicon chip which has thousands of small apertures for the crystals to sit in. The loading of the chip happens in a humidity-controlled environment to prevent the crystals from dehydrating. A vacuum is applied to the chip to remove any excess moisture and the chip is covered with a very thin transparent cellophane material, known as Mylar film (6 µm thick),[16] then mounted onto the beamline for data collection (**Figure 2**). To help position the chip in the beam line, the chip has a fiducial system in place to allow for easy chip alignment for data collection. This, in combination with the small volume of microcrystal slurry needed for data collection, gives the fixed target approach the chance to be a vital method of data collection. During our data collections it was

not possible to perform mixing experiments, however new methods are being developed to allow for substrate mixing.[8,16,19]

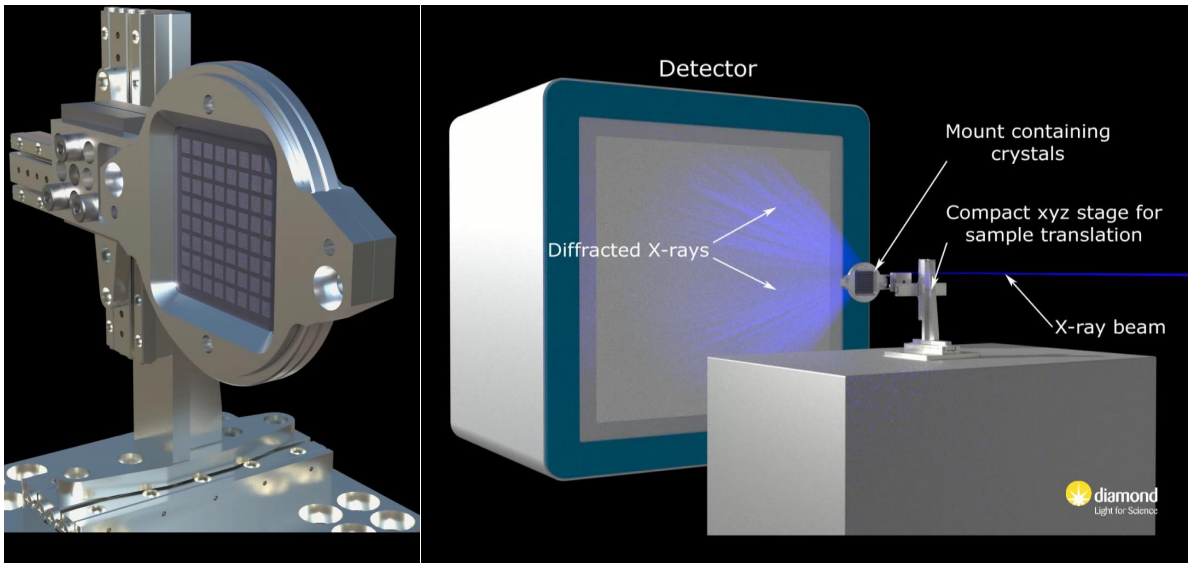


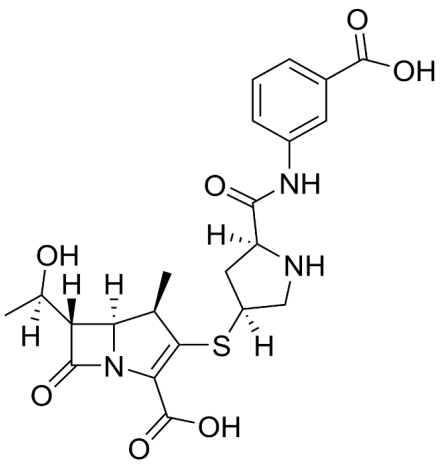
Figure 2: Diagrams from Diamond Light Source showing the setup of the fixed target system used for serial crystallography at the I24 beamline. The data collection is done by first aligning the chip using fiducials on the corner of the grids. The chip is then moved along the grid to allow all apertures to be exposed to X-rays.[52]

Batch method microcrystals of the PBP5 cysteine variant were prepared for the data collection (10 x 5 x 2 µm) and were loaded onto the silicon chips with the apertures of 7 µm. Once the chips were loaded, data were collected at I24 with a detector distance of 240 mm, 100% transmission, 20 ms exposure time at 12.5 keV and an average of 14440 images per chip. Since I24 is a micro focus beam line, the beam size is very small (7x7 µm) making it easier to collect data on very small microcrystals.[8,16,19,32] However, the PBP5 cysteine variant microcrystals initially used proved to be too small in width and depth, causing them to fall through the apertures. For the next beam time, the microcrystal slurry was prepared without any shaking, allowing the crystals to grow to a more adequate size (20 x 10 x 10 µm). The same crystal condition used by Dr. Agata Butryn was also used to generate a crystal slurry in order to obtain a comparison.

Macrocrystallisation of PBP5 with Ertapenem

After collecting several datasets of the resting state PBP5 structure, the next step was to produce a structure of PBP5 in complex with a β-lactam. Ertapenem (**Figure 3**) was chosen for this due to its availability at reasonable cost, high solubility and clinical relevance. Initially, a 96-well plate of the original optimisation (**Table 6**) was set up at ambient temperature with the PBP5 cysteine variant, at a stock concentration of 7.2 mg/mL. 50 mM ertapenem was soaked into the macro crystals (~50 x 10 x 5 µm) at various time points (30 minutes, 2 hours and overnight). All the crystals were harvested and cryocooled by plunging in liquid nitrogen. 50% (v/v) glycerol was used as a cryo protectant and data were collected at Diamond Light Source.

Since the density for the ertapenem in the active site was poor or non-existent, co-crystallisation was attempted instead. Several broad screens were set up. 6 µL of 100mM ertapenem was added to 60 µL of the mutant PBP5 and was incubated on ice for 20 minutes before the broad screens were set up as previously described. Crystals appeared in conditions across several different broad screens such as Index, PEG RX and PACT PREMIER. All crystals were harvested and cryo cooled for data collection. A new 96-well optimisation plate was designed based on the H3 condition in the PEGRx broad screen (10% (w/v) PEG 200, 18% (w/v) PEG 8000 and 0.1 M Bis Tris Propane pH 9.0). The new optimisation block produced several more crystals which were harvested and cryocooled for data collection.



Ertapenem

Figure 3: Structure of the carbapenem ertapenem. Ertapenem is one of the most soluble carbapenems (20 mg/mL), which is why it was used for all serial experiments. It is also one of the most clinically relevant carbapenems.[33]

PEG 8000 (%)	**PEG 200 (%)**											
	2	**4**	**6**	**8**	**10**	**12**	**14**	**16**	**18**	**20**	**22**	**24**
8	**X**									**X**		
9.5												
11												
12.5						**X**						
14												
15.5						**X**						
17												
18.5			**X**	**X**	**X**							

Table 6: PBP5 optimisation blocks created from the condition H3 in the PEGRX screen (10% PEG 200, 0.1 M Bis Tris Propane, 18% PEG 8000. Boxes marked with X are other conditions which produced crystals that were used for later soaking experiments. 0.1 M Bis Tris propane pH 9.0 was used throughout the plate.

Data Collection and Processing of PBP5 Macrocrystals with Ertapenem

Data were collected on PBP5 ertapenem crystals at Diamond Light Source at the I03 beamline. Beamline. 1800 images were collected in total using an Eiger2 XE 16M Detector. A dataset was collected to 1.9 Å in the space group *C* 1 2 1 from a crystal in condition H3 of the PEG RX broad screen (**Table 7**). The data processing and refinement was done as previously described in Chapter 2. The rest of the crystals showed no diffraction.

Batch Method Optimisation of PBP5: Ertapenem Microcrystals

Several 96-well plates of the PBP5: ertapenem optimisation block were set up in order to produce a large quantity of seeds. Batch method crystals were set up with several protein: precipitant ratios, 1:1, 1:2, 1:3, 1:4, 1:5 and 1:10, with the precipitant being 6% (w/v) PEG 200, 0.1 M Bis Tris propane pH 9.0, 18.5% (w/v) PEG 8000 at ambient temperature. A condition was chosen with the smallest amount of PEG possible, to reduce the viscosity of the solution. These conditions were tested with and without any shaking. It became clear that the concentration of crystals was not high enough, with very few crystals observed in solution, so PBP5 was crystallised in the same conditions used for previous fixed target data collection, with the fixed target and 100 mM ertapenem added to the crystals in a 1:10 dilution and soaked for 4-6 hours before data collection.

Data Processing of Serial Crystallographic Data

Since one crystal produces one image during serial data collection, the data processing is significantly different in comparison to traditional crystallographic methods. There are two different programmes that are used for serial data processing in this thesis, i.e. cctbx and CRYSTFEL.[34,35] Other data processing pipelines have been developed at SACLA.[13,36] All data discussed in this chapter were processed using cctbx and was performed by Dr. Aaron Brewster from Berkley and Drs Pierre Aller and Agata Butryn from Diamond Light Source. The individual images are indexed and integrated

separately, then merged. cctbx can identify the unit cell dimensions by searching for the directional vectors which describe the Bragg Spots, three of these are then chosen to form the unit cell.[37,38] Because the crystals are destroyed after one image, it is impossible to shoot any of the crystals from multiple different directions. To compensate, a target unit cell is given either from a previous dataset of the protein or from an isomorphous crystal form.[39]

There is also the problem of multiple lattices that needs to be considered. There are two potential methods that can be used for XFEL data.[34,37] The first is to filter any multiple lattices away by making it a requirement that 80% of observed sports appear in a single model. The second is to create two separate lattices, whereby bright spots are used for the first lattice and other candidate spots are used for the second lattice. This makes overlaps between the spots rare, reducing the inaccuracies in integration.[34,37]

The final resolution of the dataset is determined during the merging process; this can be a challenge for serial data as each crystal lattice will have a different diffraction limiting angle.[34,37,40] To determine the resolution limit of each separate lattice, Wilson plots were constructed (integrated Bragg spot intensity vs diffraction angle bin) to determine separate cut off angles for each lattice.[37,39] Once the data is merged, an iterative refinement technique is employed to decipher the highest resolution shell. When the data was merged and an mtz file produced, a molecular replacement was performed using Phaser and Coot for the molecular replacement and manual model building.[41,42] Since CCP4i2 suite and the Phenix package were used for data processing, Refmac and phenix refine were used for refinement.[43–46]

Results

PBP5 Crystallisation

To obtain an XFEL structure of PBP5, a crystallisation condition that was reliable and which could produce microcrystals which could diffract to a high resolution, was required. Crystals also need to appear in these conditions quickly, as XFEL beam time can be incredibly time sensitive, due to low availability throughout the year. Several crystals appeared in the PACT PREMIER broad screen, with the best ones being in conditions E3 (0.2 M sodium iodide and 20% (w/v) PEG 3350), E5 (0.2 M sodium nitrate and 20% (w/v) PEG 3350) (**Figure 4**) and H1 (0.2 M sodium iodide, 0.1 M Bis Tris propane pH 7.5 and 20% (w/v) PEG 3350) with crystals appearing overnight, both with the wildtype and mutant PBP5 protein. Based on these conditions, three 24-well sitting drop optimisation plates were designed to see which produced the most crystals. All three optimisation plates showed crystals after 12-14 hours room temperature incubation, with the E5 optimisation plate producing the most crystals as well as ones that appeared to diffract the best.

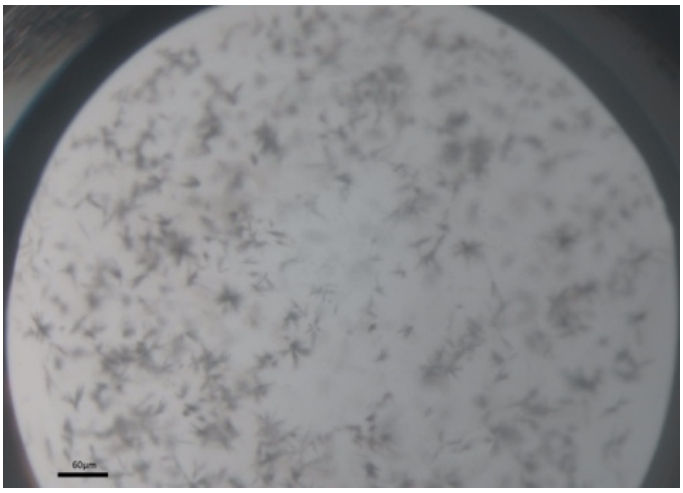


Figure 4: Crystals produced from the initial 24 well E5 optimisation plate. There is clearly a high concentration of needle shaped crystals that could be classified as microcrystals; however, the concentration is not high enough for XFEL experiments. The crystals also seemed to have formed in clusters, which could lead to the presence of multiple lattices when collecting data.

Seeds and Batch Crystallisation

A 96-well optimisation plate was created based on the E5 condition. Since the PBP5 cysteine variant appeared to crystallise the best, it was decided that this batch of protein should be used for all further trials. This produced crystals in a broad range of crystals overnight, with the highest quality one being in the condition with 19% (w/v) PEG 3350 and 0.2 M sodium nitrate (**Figure 4**). The plate was harvested for seeds and batch method conditions were developed as described in the Materials and Methods. After further optimisation and the production of more concentrated seeds, the condition which produced the best micro crystals in Oxford was found to be the 1:4 protein: precipitant ratio with 3 µL of concentrated seed stock being added to the solution and the plate being shaken at 700 rpm. This condition did not produce high quality crystals in LCLS however, so the protein: precipitant ratio was adjusted to 1:1.

Optimisation with the PBP5 cysteine variant: ertapenem complex proved to be less successful compared to crystallisation of PBP5 alone, with fewer crystals appearing the broad screens in the former case (**Table 6** and **Table 4**). This could be due to several different reasons, such as the protein being several years old at this point meaning it could have been degrading whilst being transported to XFEL beam lines across the world.

Another possible explanation is that the ertapenem solution could have degraded in the process of freeze thawing, affecting its ability to bind to PBP5 and thus making the protein substrate solution more disordered, which would reduce the chances of the complex crystallising. Some crystals did appear in condition H3 of the PEG ION broad screen, so a 96-well optimisation plate was based on this condition to produce more seeds for batch method crystallisation. The batch method trials had limited success, with some crystals appearing in the 1:3 protein: precipitant mixture. However, the crystal concentration for this was low, making it difficult to get a full data set. Instead, batch crystals of the PBP5 cysteine variant by itself were set up and a solution of ertapenem was soaked into the crystals.

PBP5 Resting State Serial Data Collection at Diamond Light Source

Two different sample delivery methods were used for serial, room temperature data collection, i.e. the gel extruder and fixed target methods.[8,16,32,47,48] A crystal concentration between $1x10^7$ – $1x10^8$ crystals/mL was used for all experiments. Upon starting the data collection using the gel extruder, it became clear that the microcrystal slurry did not cope well in the mixture with grease as there was little to no diffraction later on in the data collection. LCP was used as a matrix instead for the data collection. This produced a complete dataset of the PBP5 cysteine variant to a resolution of 3 Å, indicating that it is possible to use serial data collection methods at synchrotrons.

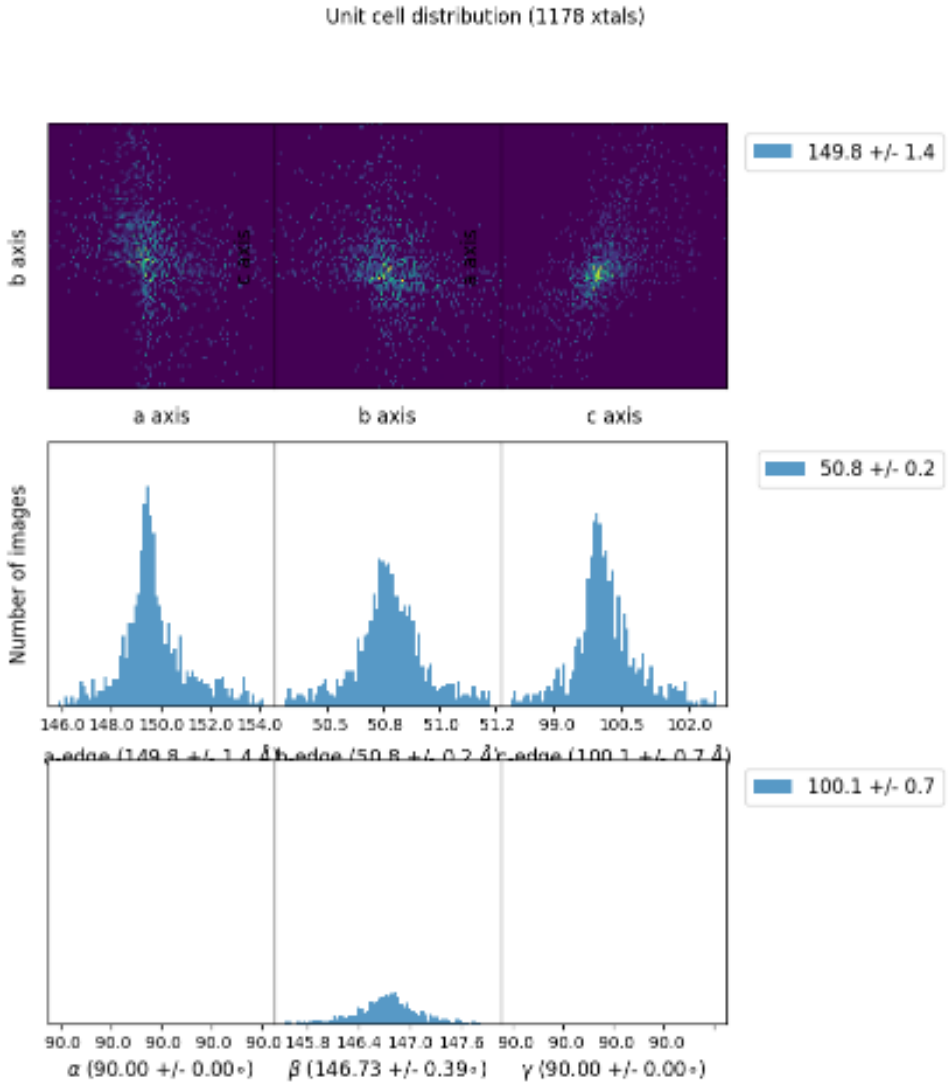


Figure 5: Unit cell dimensions for PBP5 fixed target data collection. Small variations in the unit cell dimensions can be seen between a, b and c. Average dimensions for a, b and c can be observed on the side of the image although they are obscured below the graphs for a, b and c.

Several chips were used for each fixed target data collection. The first one was not useful, as the crystals were too small and appeared to fall through the apertures of the chip. Although diffraction was observed, insufficient images were collected to produce a complete dataset. The next chip used for data collection was more successful. With larger crystals being used, a dataset of PBP5 cysteine variant in the resting state was collected to 2.7 Å resolution (**Figure 5**). At another beam time using a more concentrated solution of crystals, a dataset to 2.4 Å resolution was obtained. These results show

that diffraction data can be successfully collected on PBP5 microcrystals. The sequence of experiments supports the idea of doing preliminary serial data collection on micro crystals before an XFEL beam time. Use of fixed target data collection seemed to consistently produce higher resolution data compared to the gel extruder technique. The most likely explanation for this is that the quality of the crystals decreases upon being mixed with the matrices, leading to lower resolution datasets. Whilst this was the case for PBP5, it is not true for all crystals, with several high-resolution datasets having been collected using the gel extruder method at synchrotrons and at XFELs.

Only the gel extruder sample delivery method was used for data collection at VMXi due to lack of availability of fixed target chips at the time of the beam time. The results were similar with what was seen at I24, with a dataset being produced to 2.9 Å using grease as the matrix. This confirms the versatility of these sample delivery methods in that they can be used across several beamlines in a synchrotron.

LCLS Data Collection

During the P110 screening time at LCLS, data were collected on PBP5 cysteine variant crystals that were made using both sitting drop and batch methods. The hit and indexing rate with the batch method crystals was poor (**Figure 6**), most likely due to a low concentration of crystals (high hit rates = high crystal concentration). The sitting drop crystals were larger in all dimensions, so these were used for the rest of the data collection at LCLS. The hit rate improved significantly (**Figure 7**) as well as the indexing rate and a complete dataset was generated to 2.3 Å although the resolution was cut back later to 2.7 Å due to poor data quality. It is likely that higher resolution data could have been collected, however, there were technical issues regarding the beam power during the data collection that reduced the available beam time. The resolution is close to what was observed at Diamond Light Source for fixed target PBP5 serial data collection, proving that serial data collection at synchrotrons can give crystallographers a good grasp of how the crystals would behave at an XFEL source. These

results also show that the ADE method[27] is capable of producing data of decent quality whilst using little sample (0.5 mL) of microcrystal slurry, as was used for the entire data collection.

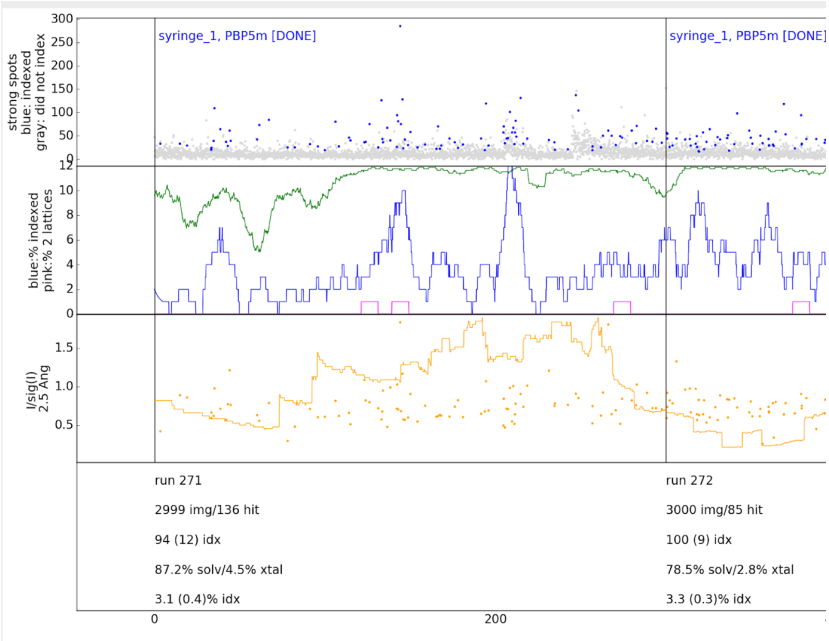


Figure 6: Data analysis of data collection on the first PBP5 syringe. Note the low hit rate (grey spots in top panel) and indexing rate of the spots (shown as blue spots in top panel). The crystals in the slurry were less than <5 µm, which could cause problems with indexing.

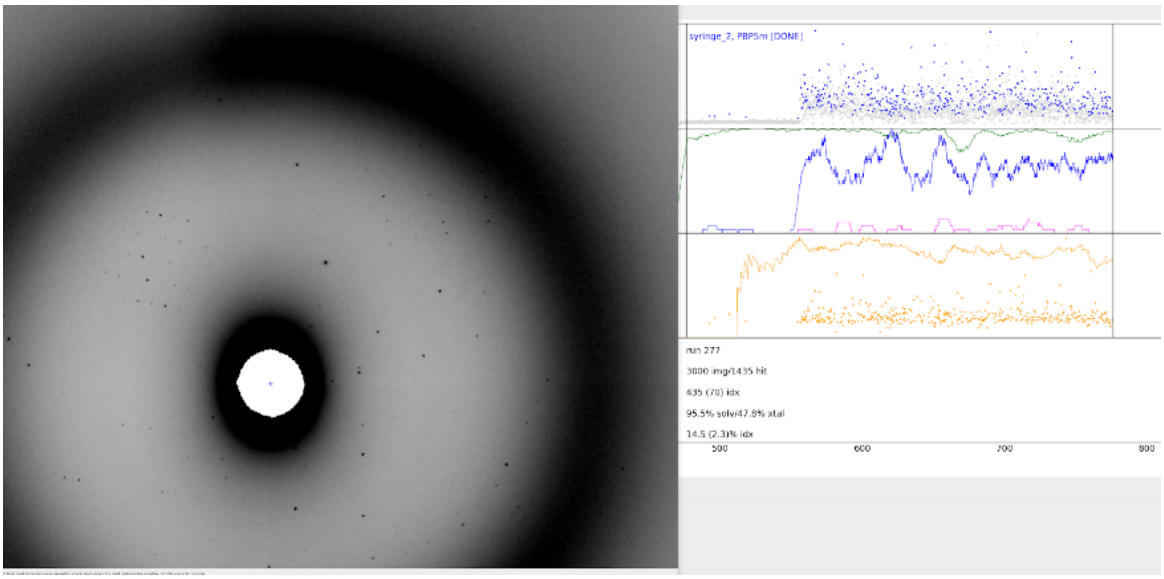


Figure 7: Data collection on the second batch of PBP5 microcrystals at LCLS. The second run used a different batch of crystals set up using the vapour diffusion method rather than batch crystallisation method which produced larger crystals. It is clear that this run had a significantly higher hit rate and indexing rate compared to the first run as shown by the grey and blue spots respectively in the top panel. This is potentially due to the comparatively larger crystals, making it easier for them to interact with the beam. The I/σI is also significantly higher on average compared to first run. Further data collection would have led to a higher resolution dataset.

Resting State Structure Comparison

Comparison of the room temperature resting state structures (fixed target dataset, gel extruder dataset from I24 and VMXi and the LCLS dataset) reveals relatively similar structures (**Table 7**). As seen in Table 7, there is little difference in the size of the unit cell between the structures or in the positioning of the two domains in the PBP5 room temperature structures (**Figure 8**). Little change is seen between the active sites of the different structures, with similar positionings of the SXXK residues (**Figure 8**). This confirms that having a batch crystallisation condition that is mostly consistent in producing high concentrations of microcrystal slurry, can lead to the production of comparable datasets using various different sample delivery methods.

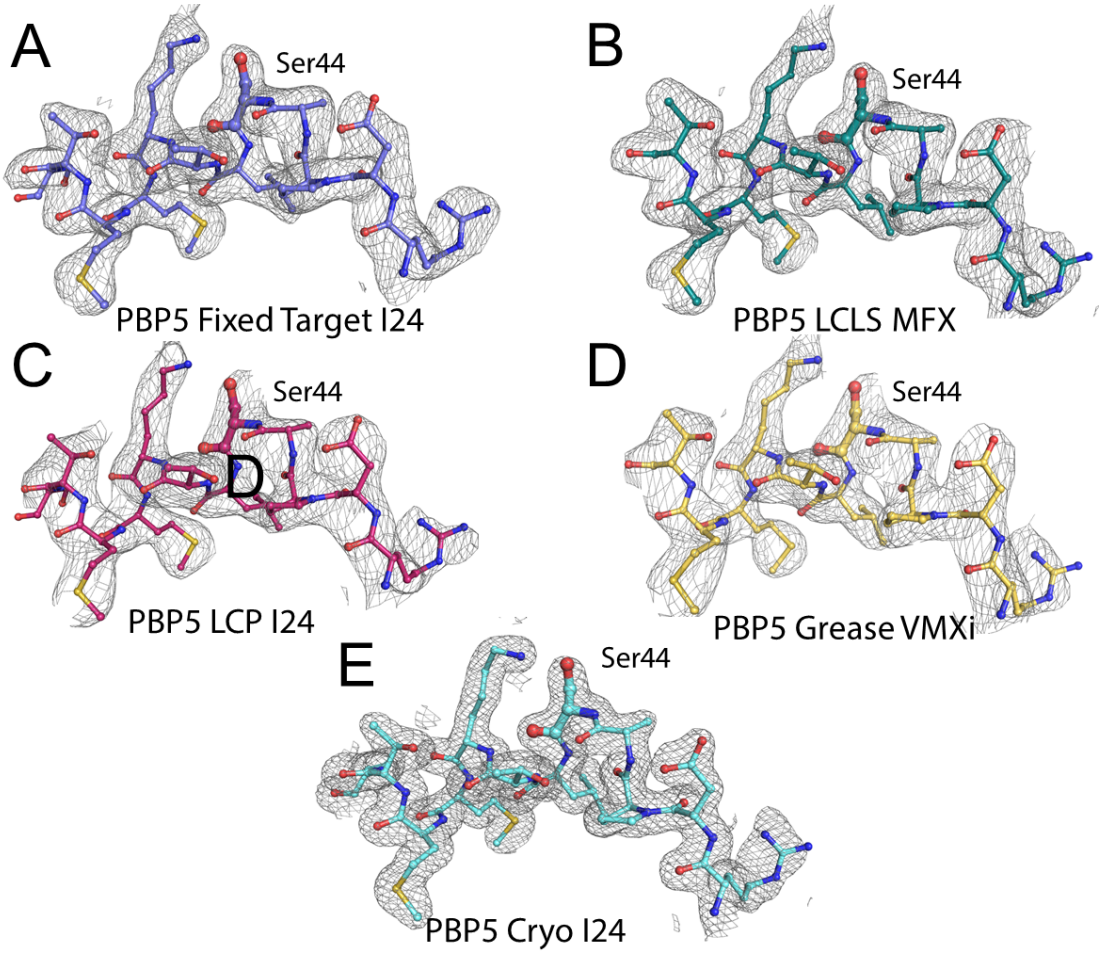


Figure 8: $2mF_o$-DF_c Electron density maps (contoured to 1σ) of resting state PBP5 room temperature datasets collected at various sources X-Ray sources. Resolutions are: 2.4 Å for fixed target dataset, 2.7 Å for LCLS dataset, 3.2 Å for LCP dataset, 3.0 Å for the grease dataset and 1.65 Å for the cryo dataset. All datasets were in the space group *C* 1 2 1.

	PBP5	PBP5 LCLS	PBP5 VMXi Grease	PBP5 I24 LCP	PBP5 Fixed Target
Beamline	I24	MFX	VMXi	I24	I24
Temperature (K)	100	298	298	298	298
Space group	*C2*	*C2*	*C2*	*C2*	*C2*
Molecules/ASU	1	1	1	1	1
Total Reflections	298419 (14544)	381900 (24430)	301960 (4359)	179822 (3243)	3937231 (16226)
Unique Reflections	46570 (2310)	18548 (1840)	8484 (438)	6979 (340)	15488 (1138)
a, *b*, *c* (Å)	108.40 50.02 84.09	149.75 50.80 100.35	149.86 50.79 100.45	150.11 50.80 100.42	149.51 50.65 100.24
α, β, γ (°)	90.00 120.97 90.00	90 146.88 90.00	90.00 146.61 90.00	90.00 146.88 90.00	90.00 146.88 90.00
Wavelength	0.9686	0.9686	0.9686	0.9686	0.9686
Resolution (Å)	32.23 - 1.65 (1.864 - 1.65)	24.03 - 2.7 (2.796 -2.7)	28.7 - 3.0 (3.107-3.0)	43.19 -3.2 (3.314-3.2)	54.77 - 2.4 (2.486 -2.4)
R_{pim} / R_{meas}	0.088 (1.891)	44.4 (70.0)	25.8 (54.5)	35.2 (54.9)	30.2 (79.9)
CC 1/2	1.0 (0.5)	57. 2 (1)	89. 3 (19.9)	82.6 (17.1)	88.6 (36.1)
I / σI	11.1 (1.1)	11.968 (1.172)	11.524 (1.611)	13.149 (2.711)	27.35 (3.03)
Completeness (%)	99.60 (99.89)	99.76 (99.83)	99.10 (95.28)	99.61 (98.56)	99.88 (99.13)
Multiplicity	6.40 (6.30)	20.57 (13.27)	35.50 (9.86)	25.74 (9.51)	50.10 (9.65)
Refinement					
Resolution (Å)	32.23 - 1.80	24.03 - 2.70	28.7 - 3.0	43.19 - 3.2	54.77 - 2.4
R_{work} / R_{free}	0.1782/0.1944	0.2122/0.2513	0.2080/0.2550	0.2122/0.2458	0.2216/0.2441
No. non-H atoms	2959	2637	2613	2615	2662
Protein	2682	2628	2613	2615	2619
Solvent	277	19			43
B-factors	35.68	40.18	60.23	49.46	41.40
Protein	35.00	40.23	60.23	49.46	41.43
Solvent	42.33	32.33			39.83
R.m.s. deviations					
Bond lengths (Å)	0.005	0.002	0.002	0.003	0.002
Bond angles (°)	0.79	0.51	0.48	0.58	0.47
Ramachandran Favoured (%)	98.86	97.71	96.85	95.38	97.71
Ramachandran outliers	0.28	0.00	0.86	0.00	0.29

Table 7 Data collection statistics for PBP5: Ertapenem datasets. High resolution shell values are in brackets. R_{meas} was used for the cryo dataset.

In the cryo- single crystal PBP5 resting state analyses, there was a substantial change in the unit cell parameters compared to those collected at room temperature, despite the crystals being in the same space group (**Figure 9**). The unit cells of the PBP5 room temperature appears to be larger in comparison. The difference is also manifest when comparing the structures, since the C-terminal domain is positioned differently in the cryo and room temperature datasets, with the loops being shifted by several Å.

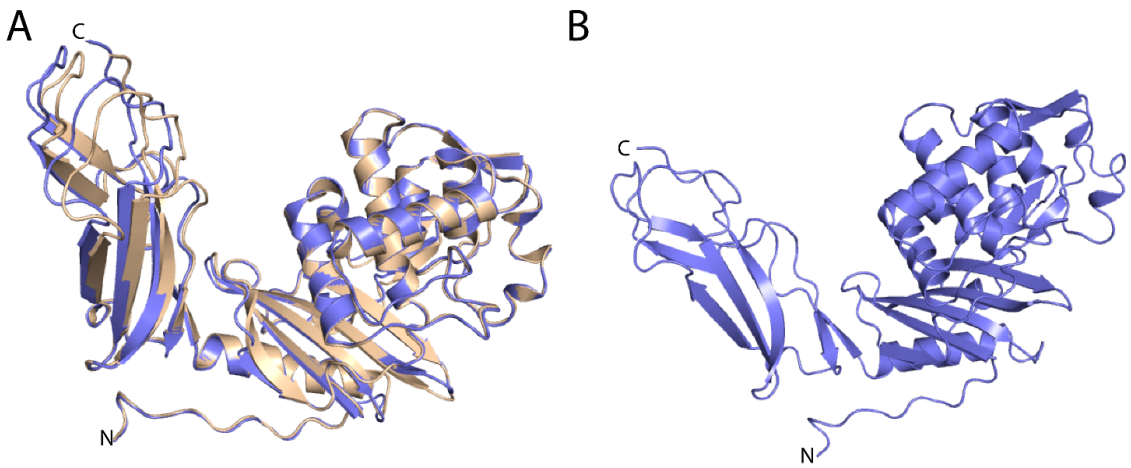


Figure 9: A) Comparison of molecules in the cryo-single crystal (with ertapenem) and room temperature structure (resting state). Note the repositioning of the define them loops in the C terminal domain. RMSD = 0.855. **B)** View from the asymmetric unit of PBP5 fixed target dataset. All room temperature structures had the same asymmetric unit.

It was initially thought the difference in the unit cell might be caused by the binding of ertapenem, but it is unlikely to be the sole cause since this shift in unit cell is seen between the PBP5 cryo and room temperature structures, even without ertapenem in the active site. Therefore, one likely explanation for this is that the process of cryocooling is what leads to this shift in unit cell.[49]

PBP5: Ertapenem Macrocrystal Datasets

A crystal structure of PBP5 in complex with ertapenem was considered an important goal to obtain towards gaining a better understanding of the structural changes that occur upon protein substrate binding. Initially, macrocrystals of mutant PBP5, obtained using the 96-well optimisation plate previously mentioned, were soaked with ertapenem for two hours. The crystal used was from the H3 condition (6% (w/v) PEG 200, 0.1 M Bis Tris propane pH 9.0, 18% (w/v) PEG 8000) and data were collected at the I03 beamline in Diamond Light Source to a resolution of 1.99 Å. The images were processed in the space group *C*2 with one protein molecule in the asymmetric unit (**Table 8 and Figure 10**). There is a large shift in the C-terminal domain loops (**Figure 9**), most likely due to the large changes in the unit cell dimensions.

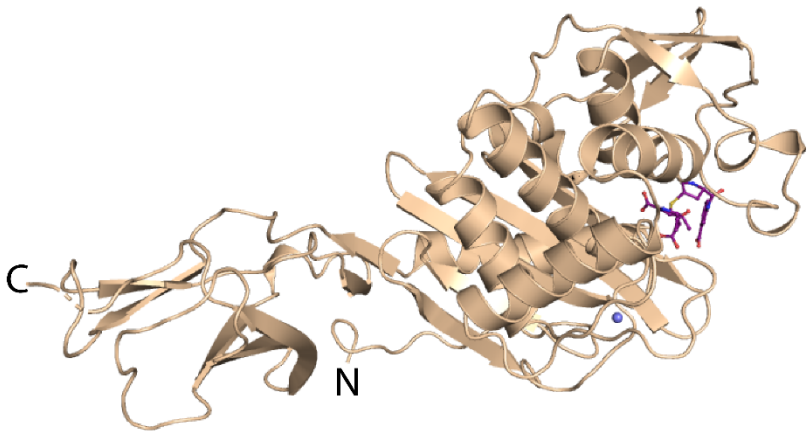


Figure 10: View of the overall structure of PBP5: ertapenem in the asymmetric unit collected at Diamond Light Source at the I03 beamline.

Upon molecular replacement and refinement, it was clear that electron density interpreted as ertapenem (1.9 Å) was in the active site near the nucleophilic serine (**Figure 11A**). The β-lactam ring had been opened forming an acyl-enzyme complex. Refinement analysis showed that it was the imine ertapenem derivative with stereochemistry (*R*) at the C2 position that was predominantly present in the active site. Several polar interactions were seen being formed between PBP5 and ertapenem, such as those between Tyr222 and the side chain carboxylate group interacting with the threonine and

arginine in the active site groove (**Figures 11B and 12**). These observations are consistent with what has been observed with other PBP/ β-lactam structures with a stable acyl-enzyme complex.

Similar conformations are seen between ertapenem and PBP5 as observed with meropenem and PBP5, i.e., in both cases an imine acyl-enzyme complex is observed, with the same (*R*)-C2 stereochemistry.[21,50] The binding modes between ertapenem and meropenem appear very similar, with some differences in the side chain conformation (though these should be treated with care because the electron density around the side chains in the PBP5: ertapenem structure was relatively weak). In the PBP5: ertapenem structure, the positioning of the newly formed carboxylate is also different. (**Figure 13**).

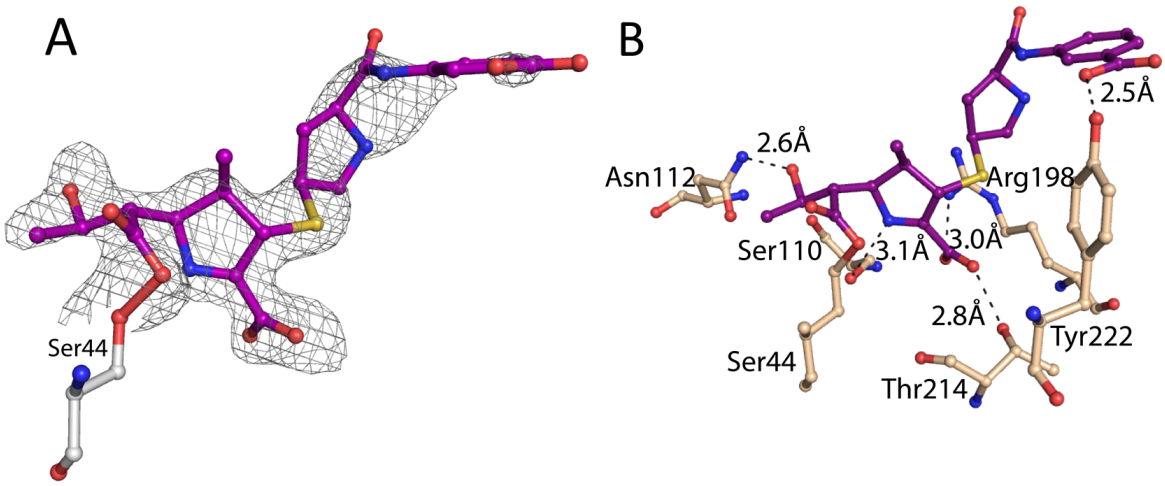


Figure 11: **A) Views of ertapenem derived complex binding in PBP5 active site as defined by the electron density map**. Views from the PBP5 active site, with the mF_o-DF_c density (grey mesh, contoured at 3σ) calculated from the final model after removal of the ligand (Shown in purple). B) Interactions between ertapenem and PBP5. Multiple polar interactions are observed that stabilise the complex.

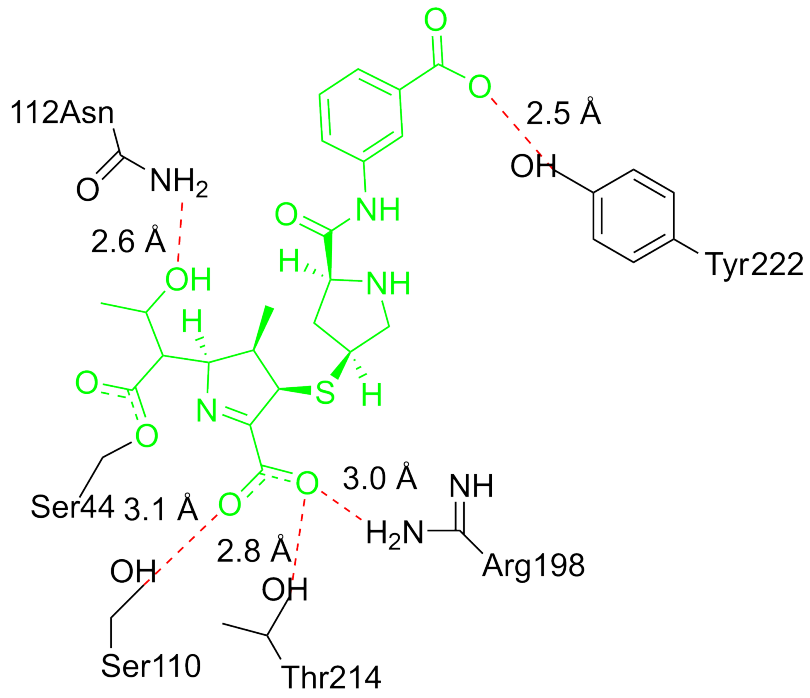


Figure 12: Schematic of interactions between ertapenem and PBP5. Polar interactions are shown as red dashed lines. The C2 stereochemistry is in the (*R*)-form.

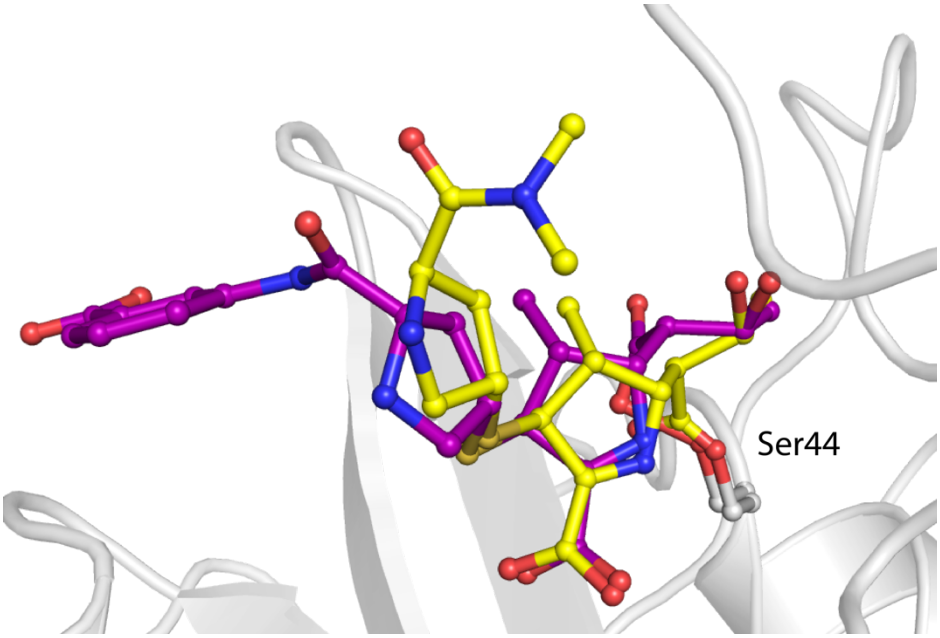


Figure 13: Binding mode comparison of the PBP5 complexes with ertapenem (purple) and meropenem (yellow, PDB 6NTZ[51]). The similar binding mode for meropenem and ertapenem is clearly very similar with some differences in the side chain. RMSD of protein alignment = 1.079.

PBP5: Ertapenem Microcrystal Datasets

Since co-crystallisation produced no usable data, soaking ertapenem into the PBP5 microcrystals was attempted. Due to issues with the seed stock, the concentration of the crystals was insufficient to produce a complete dataset during the initial data collection. Once a new batch of microcrystals was developed with a new seed stock however, the concentration of the microcrystals was high enough to produce a very high hit rate as seen by the high number of indexed spots (**Figure 14**).

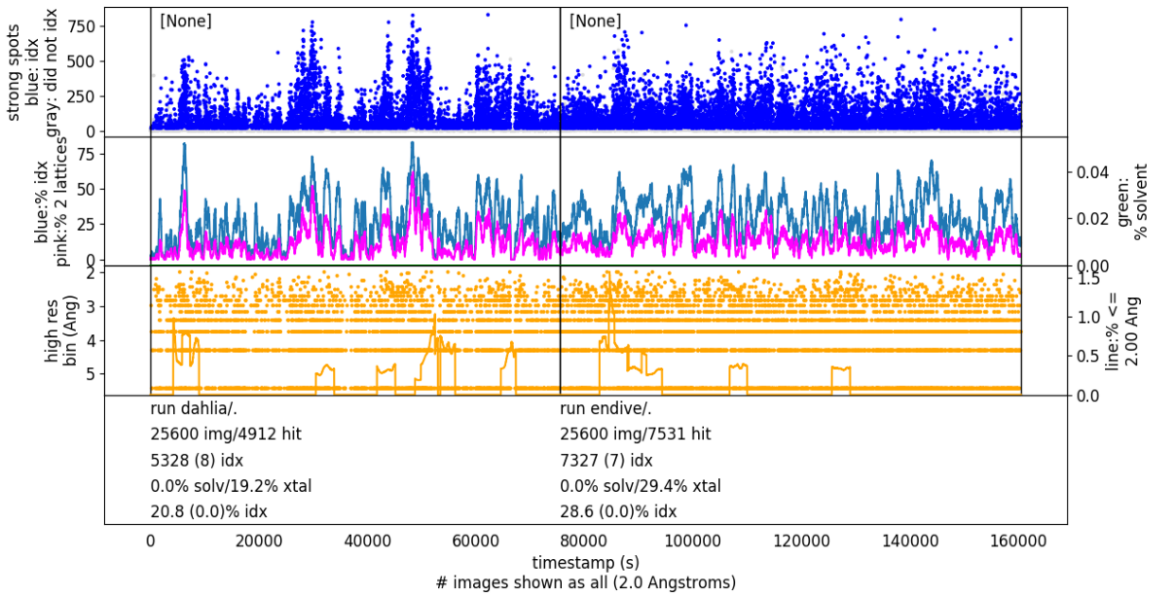


Figure 14: Analysis from PBP5: ertapenem serial data collection at I24 Diamond Light Source. The blue spots indicated the images that had been indexed. A large portion of the images are being indexed however there were difficulties merging the data due to the lack of homogeneity with the unit cells. Note the high number of multiple lattices as shown in pink in the middle panel.

However, there were issues with processing the PBP5: ertapenem data, due to large deviations between the actual unit cell and the target unit cell causing many of the images to be processed as outliers and consequently not integrated. Data processing issues could also be due to the high number of multiple lattices present (**Figure 14**). It should be noted that there was significant difference in the

unit cells between the PBP5: ertapenem macrocrystal data and the resting state datasets of PBP5 (**Figure 15**).

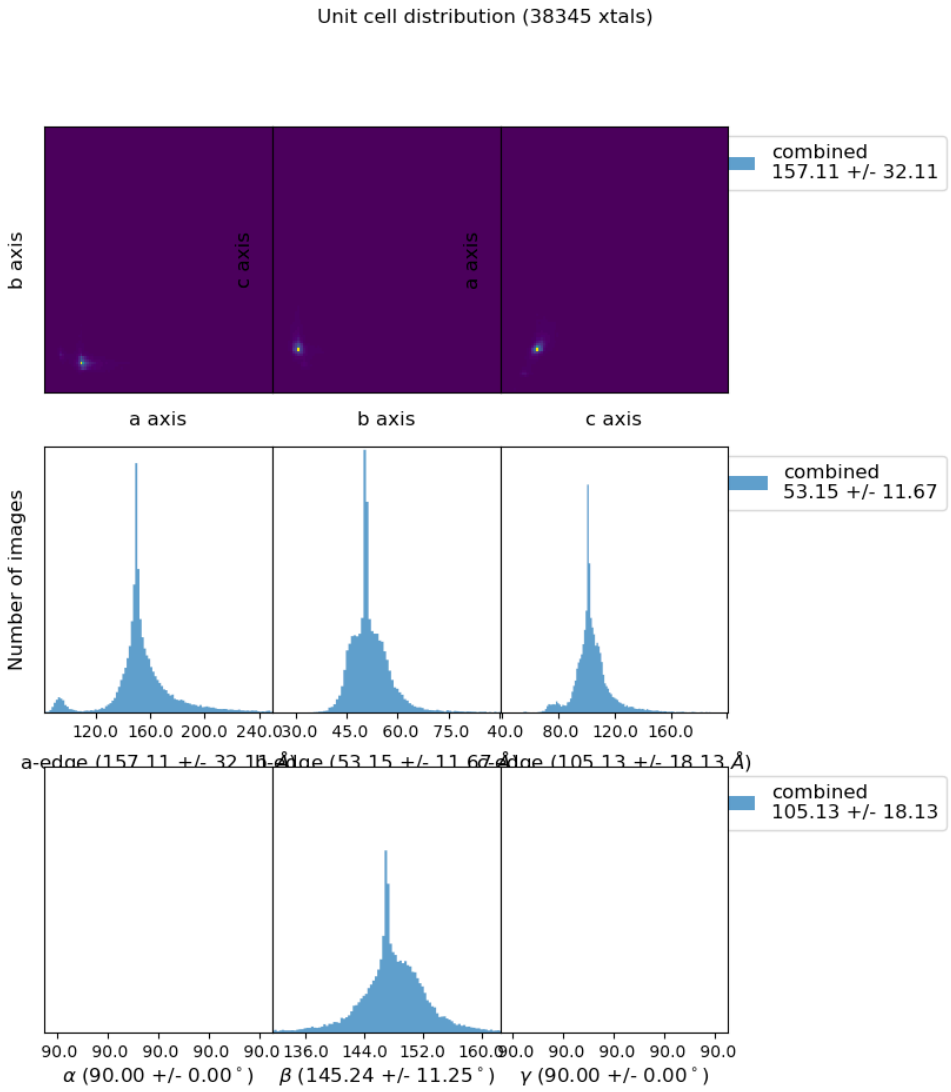


Figure 15: Unit cells in PBP5: ertapenem microcrystal slurry during serial data collection at Diamond Light Source. Note that rather than one single peak being present for each unit cell parameter, there appear to be multiple peaks present for nearly all unit cell dimensions except α and γ. It is clear from this that soaking the microcrystals with ertapenem for an extended period of time has a detrimental effect on the consistency of the unit cell. A condition where PBP5 can be reliably co-crystallised with ertapenem in large microcrystal slurries is needed to avoid this issue. Average dimensions for a, b and c can be observed on the side of the image although they are obscured below the graphs for a, b and c.

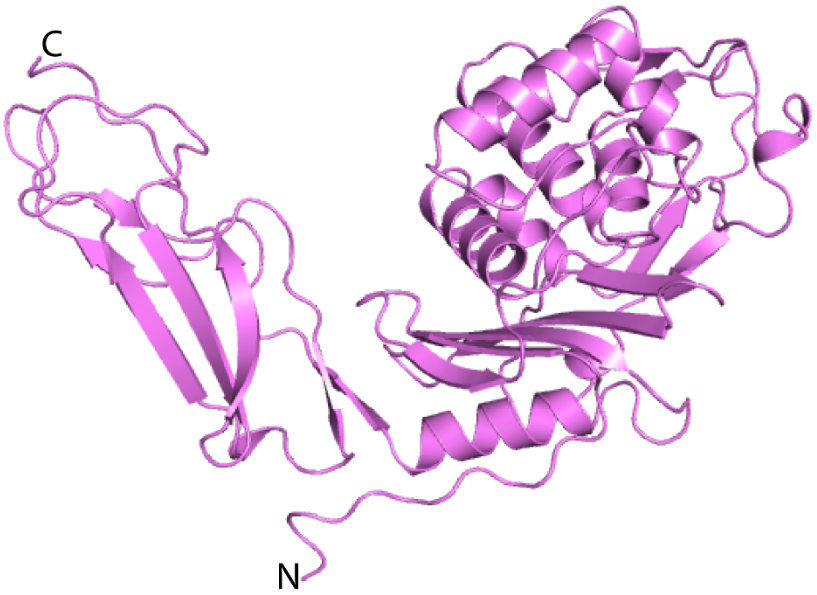


Figure 16: Overall fold of PBP5: Ertapenem structure in the asymmetric unit as observed using fixed target sample delivery methods at room temperature. The dataset was processed in the same unit cell as previously observed with room temperature data collection.

This initial processing of the PBP5: ertapenem data yielded a complete dataset to 2.9 Å (**Table 8**) and early refinements indicated that there was a ligand present in the active site (**Figures 16 and 17A**). However, this resolution was too low to see the side chain positioning accurately. Further data collection would be needed with a new crystal condition to minimise the appearance of multiple unit cells in a dataset. Finding a condition where PBP5 can be reliably co-crystallised with ertapenem is vital.

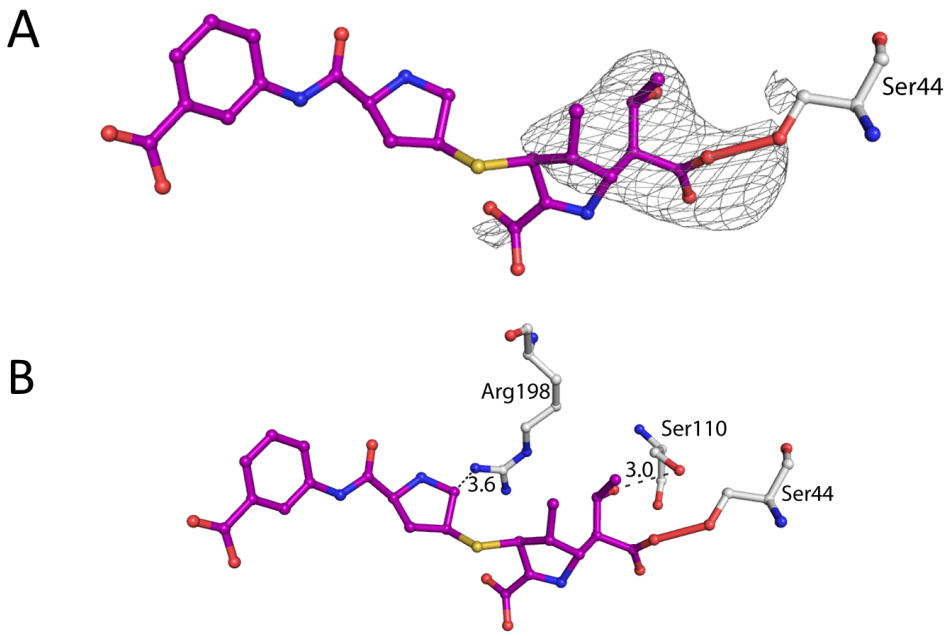


Figure 17: A) Ertapenem derived complex binding in PBP5 active site as defined by the electron density map. The mF_o-DF_c density map (grey mesh, contoured at 3σ) was calculated from the final model after removal of the ligand (Shown in purple). Note the poor density around the pyrrole ring and the total lack of density around the ertapenem C2 side chain. **B)** Polar interactions between PBP5 and ertapenem in the active site. Due to the relatively low resolution and poor density, the side chain could not be modelled accurately. Observations showed that a lot of the interactions observed in the cryo PBP5: ertapenem structure were not seen in this room temperature dataset. However, a higher resolution structure is absolutely necessary to get a good comparison.

Because of the very poor density from ertapenem described species it was difficult to model the C2 side chain with any accuracy and so all observations seen in this structure must be viewed through that lens. The C2 side chain appeared to be in a rather different conformation in comparison to the cryo structure, with very few of the interactions observed in the cryo dataset being replicated in the room temperature dataset. The hydroxyethyl appears to be forming polar interactions with Ser110 in

the active site and the nitrogen in the pyrrole ring interacts with Arg198, which was seen with the cryo PBP5: ertapenem structure. Unlike the cryo PBP5: ertapenem structure however, no interactions were observed with Tyr222 or with the neighbouring threonine residue (**Figures 17B and 18**). A higher resolution structure would be needed to validate these interactions so they can be properly considered.

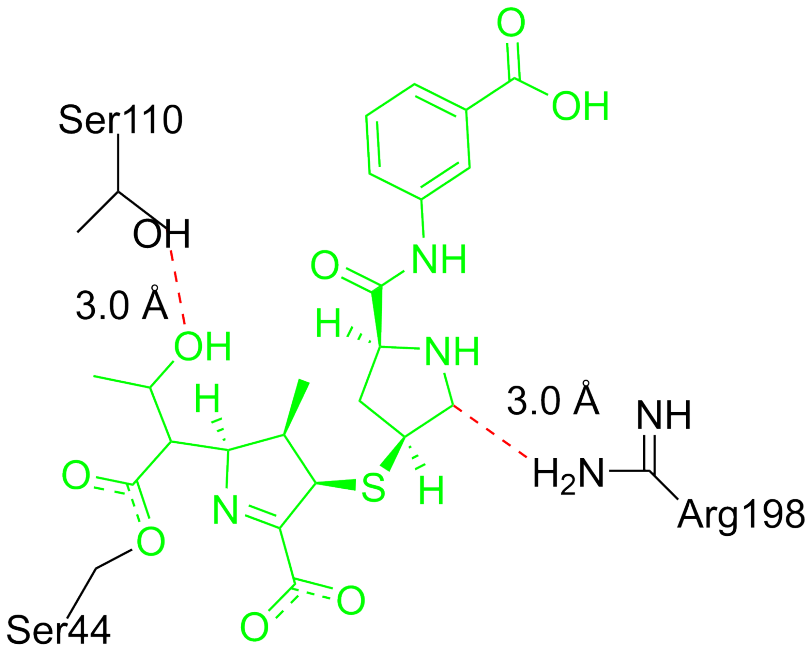


Figure 18: Schematic of interactions between PBP5 and ertapenem in the room temperature dataset. Polar interactions are represented as dashed lines. Ertapenem derived product is modelled in the (*R*)-form.

	PBP5: Ertapenem	PBP5: Ertapenem FT
Beamline	I03	I24
Temperature (K)	100	298
Space group	*C2*	*C2*
Molecules/ASU	1	1
Total reflections	180122	180542
Unique reflections	26449 (1325)	9424 (478)
a, *b*, *c* (Å)	106.91 50.16 83.86	150.588 50.5632 101.472
α, β, γ (°)	90 120.5 90	90 146.964 90
Wavelength	0.97622	
Resolution (Å)	39.92 - 1.99 (2.061 - 1.99)	33.62 - 2.9 (3.004 -2.9)
R_{pim}	0.104 (1.047)	0.267 (0.675)
CC 1/2	0.994	0.9698 (0.55)
I / σI	6.8 (1.2)	1.95 (0.54)
Completeness (%)	99.69 (99.51)	99.66 (98.49)
Multiplicity	6.8 (7.1)	18.79 (14.54)
Refinement		
Resolution (Å)	39.92 - 1.99	33.62 - 2.9
No. reflections		
R_{work} / R_{free}	0.1917/0.2193	0.2392/0.2831
No. non-H atoms	2874	2681
Protein	2670	2646
Solvent	169	
Ligand	35	35
B-factors	41.25	58.61
Protein	40.59	57.94
Solvent	40.59	
Ligand	71.79	110.75
R.m.s. deviations		
Bond lengths (Å)	0.005	0.002
Bond angles (°)	0.79	0.45
Ramachandran Favoured (%)	98.29	96.30
Ramachandran outliers	0.00	0.57

Table 8: Data collection statistics for PBP5: Ertapenem datasets. High resolution shell values are in brackets.

Conclusions

Serial data collection analyses on PBP5 demonstrates that when the right condition to grow microcrystals is found, useful datasets can be collected using different sample delivery methods i.e., fixed target, gel extruder and ADE. There are several requirements for a suitable microcrystal condition. First, the microcrystal slurry must be of sufficiently high concentration (~x10^8 crystals/mL would be the ideal) and the microcrystals have to be as homogenous as possible especially when soaking compounds in. This is to ensure that there are no differences between the crystals when it comes to the diffusion rate of the ligand into the solvent channels. The condition also needs to be able to produce microcrystals quickly (within a 48-hour period), particularly for any experiments that has to be done at an XFEL machine, as there is limited time available during the beam time when one set up crystallisation experiments.

Reliable conditions for batch crystallography have been found for the resting state PBP5 structure, as the microcrystals can be grown at room temperature and appear overnight. With the addition of seeds, the condition produces a highly concentrated slurry of microcrystals, though they can sometimes be too small in width and depth at times. The small size of the microcrystals in certain dimensions has led to problems in data collection, with certain dimensions being too small for the beam. Changes in the unit cell upon soaking ertapenem into the active site need to be considered, as there are multiple unit cell populations in the microcrystal slurry after the introduction of ertapenem. This problem, could be addressed by having a reliable batch method of co-crystallising PBP5 with ertapenem, reducing the need for soaking experiments. All of this confirmed that PBP5 was a good model enzyme for validating sample delivery methods, with its high yield and ability to crystallise overnight in high concentrations.

Despite the issues uncovered during data collection and sample preparation, four datasets at room temperature of comparable quality were produced of PBP5 in its resting state; while all were in the

same space group and had the same unit cell dimensions with variations in the resolution from 2.4 Å to 3.2 Å. It is likely that a higher resolution dataset could have been produced at LCLS, but this was not possible at the time due to technical issues during the beam time. The data collection using the fixed target sample delivery method produced the highest resolution dataset (2.4 Å), as the PBP5 crystals were not perturbed from their natural environment as they were when mixed with LCP or grease for gel extrusion. This observation shows that using the gel extruder method, although it has lower sample consumption, is riskier for data collection as the quality of crystals may be reduced in a hydrophobic environment. This would be a suitable method of data collection for membrane crystals for instance, as they are often crystallised in matrices like LCP and hydroxycellulose, meaning that they experience minimal disruption due to environmental changes.

The ADE and fixed target sample delivery systems have significant advantages over the gel extruder method (**Table 9**);[17,18] however, it is difficult to do mixing experiments with the fixed target system in its current format.[8,16] This makes studying reactions with fast turnover rates difficult, as the intermediates simply cannot be captured by co crystallising or soaking the substrate in before the beam time. Work on developing drop on drop methods for the acoustic tape drive using the PolyPico dispensing system is ongoing.[16] Because the hydrolysis of the acyl-enzyme complex described from ertapenem and PBP5 is an incredibly slow reaction, it may be possible to use these sample systems to study this apart of the PBP5 reaction. The acyl-enzyme PBP5: ertapenem complex was seen in both the cryo and serial datasets collected at Diamond Light Source. Despite the crystals being grown with a different mixture of precipitants, the space group and unit cell dimensions were similar between the two. Because the resolution of the serial dataset was significantly lower, it was difficult to see the precise interactions between the ertapenem side chains and PBP5. To obtain better resolution data, further optimisation of the batch crystallisation method is clearly needed. Ideally, crystals with a more 3D structure would be developed to make it less likely for the crystals to fall through the fixed target apertures.

Sample delivery method	Advantages	Disadvantages
ADE	Low sample consumption. Possible to do mixing experiments when you attach a PolyPico device.	Not user friendly, is complicated to maintain and set up.
Fixed Target	Low sample consumption. Easy to use and durable, any damaged chips can simply be replaced with a new one.	Currently not possible to do any enzyme: substrate mixing experiments.
Gel extruder	Low sample consumption. Relatively user friendly, easy to set up at both a Diamond and an XFEL beamline.	Currently not possible to do any enzyme: substrate mixing experiments. Hydrophobic matrices may affect the quality of crystals.

Table 9: Table discussing the advantages and disadvantages of each sample delivery method mentioned in this chapter.

All room temperature resting state structures of PBP5 in it resting state were comparable to one other with similarities in resolution, space group and unit cell as seen with the RMSD values. Furthermore, the loop from residues 73-89 that was missing previous structures of PBP5 from the Schofield group[21], was modelled in for all structures, both resting state and those of PBP5 complexed with ertapenem. The unit cell of PBP5 crystals appears to shift upon cryo cooling, with significant changes between what was observed at room and cryo temperatures for both resting state and complexed structures (**Tables 7 and 8, Figure 9**). This confirms that cryo cooling of PBP5 crystals can affect them structurally. Co-crystallisation of PBP5 with ertapenem produced crystals that diffracted to 1.99 Å with electron density confirming the presence of ertapenem in the active site (**Figure 11**). Further optimisation needs to be performed in order to get a room temperature structure of PBP5 complexed with ertapenem (**Figure 17**).

Overall, the results show serial crystallography of PBP5 is possible both at synchrotrons and at XFELs with structural results from the two being comparable. In addition to being applicable to both synchrotrons and XFELs, the sample delivery methods used at the synchrotron were user friendly and consumed little sample. Although the acoustic tape drive method is currently only used at XFELs, there are plans to adapt it for synchrotron use to make time resolved crystallography more accessible to the crystallographic community.

References

(1) RCSB PDB: Homepage https://www.rcsb.org/ (accessed Nov 12, 2020).

(2) Spence, J. C. H. XFELs for Structure and Dynamics in Biology. *IUCrJ* **2017**, *4*, 322–339.

(3) Fromme, P. XFELs Open a New Era in Structural Chemical Biology. *Nature Chemical Biology*. Nature Publishing Group December 1, 2015, pp 895–899.

(4) Johansson, L. C.; Stauch, B.; Ishchenko, A.; Cherezov, V. A Bright Future for Serial Femtosecond Crystallography with XFELs. *Trends Biochem. Sci.* **2017**, *42*, 749–762.

(5) Shintake, T.; Tanaka, T.; Hara, T.; Togawa, K.; Inagaki, T.; Kim, Y. J.; Ishikawa, T.; Kitamura, H.; Baba, H.; Matsumoto, H.; et al. Status of SPring-8 Compact SASE Source FEL Project. In *Nuclear Instruments and Methods in Physics Research, Section A: Accelerators, Spectrometers, Detectors and Associated Equipment*; North-Holland, 2003; *507*, pp 382–387.

(6) Wang, D.; Weierstall, U.; Pollack, L.; Spence, J. Double-Focusing Mixing Jet for XFEL Study of Chemical Kinetics. *J. Synchrotron Radiat.* **2014**, *21*, 1364–1366.

(7) Liu, H.; Lee, W. The XFEL Protein Crystallography: Developments and Perspectives. *International Journal of Molecular Sciences*. MDPI AG July 2, 2019.

(8) Rabe, P.; Beale, J. H.; Butryn, A.; Aller, P.; Dirr, A.; Lang, P. A.; Axford, D. N.; Carr, S. B.; Leissing, T. M.; McDonough, M. A.; et al. Anaerobic Fixed-Target Serial Crystallography. *IUCrJ* **2020**, *7*, 901–912.

(9) Levantino, M.; Yorke, B. A.; Monteiro, D. C.; Cammarata, M.; Pearson, A. R. Using Synchrotrons and XFELs for Time-Resolved X-Ray Crystallography and Solution Scattering Experiments on Biomolecules. *Curr. Opin. Struct. Biol.* **2015**, *35*, 41–48.

(10) Neutze, R.; Moffat, K. Time-Resolved Structural Studies at Synchrotrons and X-Ray Free Electron Lasers: Opportunities and Challenges. *Current Opinion in Structural Biology*. NIH Public Access October 2012, pp 651–659.

(11) Pearson, A. R.; Mehrabi, P. Serial Synchrotron Crystallography for Time-Resolved Structural Biology. *Curr. Opin. Struct. Biol.* **2020**, *65*, 168–174.

(12) Meents, A.; Wiedorn, M. O.; Srajer, V.; Henning, R.; Sarrou, I.; Bergtholdt, J.; Barthelmess, M.; Reinke, P. Y. A.; Dierksmeyer, D.; Tolstikova, A.; et al. Pink-Beam Serial Crystallography. *Nat. Commun.* **2017**, *8*, 1281.

(13) Moffat, K. Laue Diffraction and Time-Resolved Crystallography: A Personal History. *Philos. Trans. R. Soc. A Math. Phys. Eng. Sci.* **2019**, *377*, 20180243.

(14) Sarkar, S. K.; Chowdhury, C.; Ghosh, A. S. Deletion of Penicillin-Binding Protein 5 (PBP5) Sensitises Escherichia Coli Cells to β-Lactam Agents. *Int. J. Antimicrob. Agents* **2010**, *35*, 244–249.

(15) Georgopapadakou, N. H. Penicillin-Binding Proteins and Bacterial Resistance to Beta-Lactams. *Antimicrob. Agents Chemother.* **1993**, *37*, 2045–2053.

(16) Davy, B.; Axford, D.; Beale, J. H.; Butryn, A.; Docker, P.; Ebrahim, A.; Leen, G.; Orville, A. M.; Owen, R. L.; Aller, P. Reducing Sample Consumption for Serial Crystallography Using Acoustic Drop Ejection. *J. Synchrotron Radiat.* **2019**, *26*, 1820–1825.

(17) Kovácsová, G.; Grünbein, M. L.; Kloos, M.; Barends, T. R. M.; Schlesinger, R.; Heberle, J.; Kabsch, W.; Shoeman, R. L.; Doak, R. B.; Schlichting, I. Viscous Hydrophilic Injection Matrices for Serial Crystallography. *IUCrJ* **2017**, *4*, 400–410.

(18) Nogly, P.; James, D.; Wang, D.; White, T. A.; Zatsepin, N.; Shilova, A.; Nelson, G.; Liu, H.; Johansson, L.; Heymann, M.; et al. Lipidic Cubic Phase Serial Millisecond Crystallography

Using Synchrotron Radiation. *IUCrJ* **2015**, *2*, 168–176.

(19) Mehrabi, P.; Schulz, E. C.; Agthe, M.; Horrell, S.; Bourenkov, G.; von Stetten, D.; Leimkohl, J.-P.; Schikora, H.; Schneider, T. R.; Pearson, A. R.; et al. Liquid Application Method for Time-Resolved Analyses by Serial Synchrotron Crystallography. *Nat. Methods* **2019**, *16*, 979–982.

(20) Hengen, P. Purification of His-Tag Fusion Proteins from Escherichia Coli. *Trends Biochem. Sci.* **1995**, *20*, 285–286.

(21) Brem, J.; Cain, R.; Cahill, S.; McDonough, M. A.; Clifton, I. J.; Jiménez-Castellanos, J.-C.; Avison, M. B.; Spencer, J.; Fishwick, C. W. G.; Schofield, C. J. Structural Basis of Metallo-β-Lactamase, Serine-β-Lactamase and Penicillin-Binding Protein Inhibition by Cyclic Boronates. *Nat. Commun.* **2016**, *7*, 12406.

(22) Dessau, M. A.; Modis, Y. Protein Crystallization for X-Ray Crystallography. *J. Vis. Exp.* **2011**, No. 47.

(23) Mahon, B. P.; Kurian, J. J.; Lomelino, C. L.; Smith, I. R.; Socorro, L.; Bennett, A.; Hendon, A. M.; Chipman, P.; Savin, D. A.; Agbandje-McKenna, M.; et al. Microbatch Mixing: "Shaken Not Stirred", a Method for Macromolecular Microcrystal Production for Serial Crystallography. *Cryst. Growth Des.* **2016**, *16*, 6214–6221.

(24) Mahon, B. P.; Kurian, J. J.; Lomelino, C. L.; Smith, I. R.; Socorro, L.; Bennett, A.; Hendon, A. M.; Chipman, P.; Savin, D. A.; Agbandje-McKenna, M.; et al. Microbatch Mixing: "Shaken Not Stirred", a Method for Macromolecular Microcrystal Production for Serial Crystallography. *Cryst. Growth Des.* **2016**, *16*, 6214–6221.

(25) Boutet, S.; Cohen, A. E.; Wakatsuki, S. The New Macromolecular Femtosecond Crystallography (MFX) Instrument at LCLS. *Synchrotron Radiat. News* **2016**, *29*, 23–28.

(26) Sierra, R. G.; Batyuk, A.; Sun, Z.; Aquila, A.; Hunter, M. S.; Lane, T. J.; Liang, M.; Yoon, C. H.; Alonso-Mori, R.; Armenta, R.; et al. The Macromolecular Femtosecond Crystallography Instrument at the Linac Coherent Light Source. *J. Synchrotron Radiat.* **2019**, *26*, 346–357.

(27) Fuller, F. D.; Gul, S.; Chatterjee, R.; Burgie, E. S.; Young, I. D.; Lebrette, H.; Srinivas, V.;

Brewster, A. S.; Michels-Clark, T.; Clinger, J. A.; et al. Drop-on-Demand Sample Delivery for Studying Biocatalysts in Action at X-Ray Free-Electron Lasers. *Nat. Methods* **2017**, *14*, 443–449.

(28) Martiel, I.; Müller-Werkmeister, H. M.; Cohen, A. E.; IUCr. Strategies for Sample Delivery for Femtosecond Crystallography. *Acta Crystallogr. Sect. D Struct. Biol.* **2019**, *75*, 160–177.

(29) Burgie, E. S.; Clinger, J. A.; Miller, M. D.; Brewster, A. S.; Aller, P.; Butryn, A.; Fuller, F. D.; Gul, S.; Young, I. D.; Pham, C. C.; et al. Photoreversible Interconversion of a Phytochrome Photosensory Module in the Crystalline State. *Proc. Natl. Acad. Sci. U. S. A.* **2020**, *117*, 300–307.

(30) Sawhney, K. J. S.; Dolbnya, I. P.; Scott, S. M.; Tiwari, M. K.; Preece, G. M.; Alcock, S. G.; Malandain, A. W. A Double Multilayer Monochromator for the B16 Test Beamline at the Diamond Light Source; Morawe, C., Khounsary, A. M., Goto, S., Eds.; International Society for Optics and Photonics, **2011**; *8139*.

(31) Hunter, M. S.; Segelke, B.; Messerschmidt, M.; Williams, G. J.; Zatsepin, N. A.; Barty, A.; Henry Benner, W.; Carlson, D. B.; Coleman, M.; Graf, A.; et al. Fixed-Target Protein Serial Microcrystallography with an X-Ray Free Electron Laser. *Sci. Rep.* **2014**, *4*, 1–5.

(32) Ebrahim, A.; Appleby, M. V.; Axford, D.; Beale, J.; Moreno-Chicano, T.; Sherrell, D. A.; Strange, R. W.; Hough, M. A.; Owen, R. L.; IUCr. Resolving Polymorphs and Radiation-Driven Effects in Microcrystals Using Fixed-Target Serial Synchrotron Crystallography. *Acta Crystallogr. Sect. D Struct. Biol.* **2019**, *75*, 151–159.

(33) Keating, G. M.; Perry, C. M. Ertapenem. *Drugs* **2005**, *65*, 2151–2178.

(34) Sauter, N. K.; Hattne, J.; Grosse-Kunstleve, R. W.; Echols, N. New Python-Based Methods for Data Processing. *Acta Crystallogr. Sect. D Biol. Crystallogr.* **2013**, *69*, 1274–1282.

(35) White, T. A.; Kirian, R. A.; Martin, A. V.; Aquila, A.; Nass, K.; Barty, A.; Chapman, H. N.; IUCr. *CrystFEL* : A Software Suite for Snapshot Serial Crystallography. *J. Appl. Crystallogr.* **2012**, *45*, 335–341.

(36) Nakane, T.; Joti, Y.; Tono, K.; Yabashi, M.; Nango, E.; Iwata, S.; Ishitani, R.; Nureki, O. Data Processing Pipeline for Serial Femtosecond Crystallography at SACLA. *J. Appl. Crystallogr.* **2016**, *49*, 1035–1041.

(37) Brewster, A. S.; Young, I. D.; Lyubimov, A.; Bhowmick, A.; Sauter, N. K. *Processing Serial Crystallographic Data from XFELs or Synchrotrons Using the Cctbx.Xfel GUI*; 2019; Vol. 10.

(38) Winter, G.; Waterman, D. G.; Parkhurst, J. M.; Brewster, A. S.; Gildea, R. J.; Gerstel, M.; Fuentes-Montero, L.; Vollmar, M.; Michels-Clark, T.; Young, I. D.; et al. *DIALS* : Implementation and Evaluation of a New Integration Package. *Acta Crystallogr. Sect. D Struct. Biol.* **2018**, *74*, 85–97.

(39) Hattne, J.; Echols, N.; Tran, R.; Kern, J.; Gildea, R. J.; Brewster, A. S.; Alonso-Mori, R.; Glöckner, C.; Hellmich, J.; Laksmono, H.; et al. Accurate Macromolecular Structures Using Minimal Measurements from X-Ray Free-Electron Lasers. *Nat. Methods* **2014**, *11*, 545–548.

(40) Sauter, N. K. XFEL Diffraction: Developing Processing Methods to Optimize Data Quality. *J. Synchrotron Radiat.* **2015**, *22*, 239–248.

(41) McCoy, A. J.; Grosse-Kunstleve, R. W.; Adams, P. D.; Winn, M. D.; Storoni, L. C.; Read, R. J.; IUCr. *Phaser* Crystallographic Software. *J. Appl. Crystallogr.* **2007**, *40*, 658–674.

(42) Emsley, P.; Cowtan, K.; IUCr. *Coot* : Model-Building Tools for Molecular Graphics. *Acta Crystallogr. Sect. D Biol. Crystallogr.* **2004**, *60*, 2126–2132.

(43) Adams, P. D.; Afonine, P. V.; Bunkóczi, G.; Chen, V. B.; Davis, I. W.; Echols, N.; Headd, J. J.; Hung, L.-W.; Kapral, G. J.; Grosse-Kunstleve, R. W.; et al. *PHENIX* : A Comprehensive Python-Based System for Macromolecular Structure Solution. *Acta Crystallogr. Sect. D Biol. Crystallogr.* **2010**, *66*, 213–221.

(44) Potterton, L.; Agirre, J.; Ballard, C.; Cowtan, K.; Dodson, E.; Evans, P. R.; Jenkins, H. T.; Keegan, R.; Krissinel, E.; Stevenson, K.; et al. *CCP* 4 *i* 2: The New Graphical User Interface to the *CCP* 4 Program Suite. *Acta Crystallogr. Sect. D Struct. Biol.* **2018**, *74*, 68–84.

(45) Murshudov, G. N.; Skubák, P.; Lebedev, A. A.; Pannu, N. S.; Steiner, R. A.; Nicholls, R. A.;

Winn, M. D.; Long, F.; Vagin, A. A.; IUCr. *REFMAC* 5 for the Refinement of Macromolecular Crystal Structures. *Acta Crystallogr. Sect. D Biol. Crystallogr.* **2011**, *67*, 355–367.

(46) Afonine, P. V.; Grosse-Kunstleve, R. W.; Echols, N.; Headd, J. J.; Moriarty, N. W.; Mustyakimov, M.; Terwilliger, T. C.; Urzhumtsev, A.; Zwart, P. H.; Adams, P. D. Towards Automated Crystallographic Structure Refinement with *Phenix.Refine*. *Acta Crystallogr. Sect. D Biol. Crystallogr.* **2012**, *68*, 352–367.

(47) Oghbaey, S.; Sarracini, A.; Ginn, H. M.; Pare-Labrosse, O.; Kuo, A.; Marx, A.; Epp, S. W.; Sherrell, D. A.; Eger, B. T.; Zhong, Y.; et al. Fixed Target Combined with Spectral Mapping: Approaching 100% Hit Rates for Serial Crystallography. *Acta Crystallogr. Sect. D Struct. Biol.* **2016**, *72*, 944–955.

(48) Owen, R. L.; Axford, D.; Sherrell, D. A.; Kuo, A.; Ernst, O. P.; Schulz, E. C.; Miller, R. J. D.; Mueller-Werkmeister, H. M. Low-Dose Fixed-Target Serial Synchrotron Crystallography. *Acta Crystallogr. Sect. D, Struct. Biol.* **2017**, *73*, 373–378.

(49) Fraser, J. S.; van den Bedem, H.; Samelson, A. J.; Lang, P. T.; Holton, J. M.; Echols, N.; Alber, T. Accessing Protein Conformational Ensembles Using Room-Temperature X-Ray Crystallography. *Proc. Natl. Acad. Sci. U. S. A.* **2011**, *108*, 16247–16252.

(50) Caveney, N. A.; Caballero, G.; Voedts, H.; Niciforovic, A.; Worrall, L. J.; Vuckovic, M.; Fonvielle, M.; Hugonnet, J.-E.; Arthur, M.; Strynadka, N. C. J. Structural Insight into YcbB-Mediated Beta-Lactam Resistance in Escherichia Coli. *Nat. Commun.* **2019**, *10*, 1849.

(51) NA, C.; G, C.; H, V.; A, N.; LJ, W.; M, V.; M, F.; JE, H.; M, A.; NCJ, S. Structural Insight into YcbB-Mediated Beta-Lactam Resistance in Escherichia Coli. *Nat. Commun.* **2019**, *10*.

(52) SSX at I24 - - Diamond Light Source https://www.diamond.ac.uk/Instruments/Mx/I24/I24-serial.html (accessed Nov 21, 2020).

Chapter 4 – XFEL experiments using VIM-2

Abstract

VIM-2 is one of the most clinically relevant MBLs, being endemic in regions of Eastern Europe and Asia. VIM-2 is a broad spectrum β-lactamase, catalysing the hydrolysis of all clinically useful β-lactam antibiotics to date except monobactams. VIM-2 is found in various pathogenic bacteria such as *Pseudomonas aeruginosa*. Despite the high profile of VIM-2, little is known about the precise mechanism by which VIM-2 hydrolyses β-lactams. The work in this chapter aimed to help enable the creation of a "molecular movie" of the VIM-2 reaction. The "last resort" carbapenem ertapenem, a clinically relevant β-lactam was employed, together with the sample delivery systems tested in the previous chapter, along with a mixing jets procedure. Resting state XFEL datasets were obtained with these sample delivery methods: the resultant structures were of varying quality. To date, none of the mixing experiments have been successful, but the suitability of VIM-2 for XFEL studies has been established.

Introduction

The Verona integron metallo-β-lactamase 2 (VIM-2) is one of the most clinically relevant MBLs, being endemic in some regions across Eastern Europe.[1] Moreover, outbreaks of opportunistic bacteria expressing the VIM MBLs genes have been observed in intensive care units around the globe with cases in Mexico, Greece and France being notable examples.[1–3] VIM-2 was originally identified from a clinical isolate in *Pseudomonas aeruginosa* in 1997; it is a broad spectrum MBL that hydrolyses cephalosporins, penicillins and carbapenems, but not monobactams.[4] VIM-2 is often co-expressed with other MBLs and SBLs making treatment of these superbugs difficult.[4] To date, there are no clinically available drugs that can inhibit MBLs, although the bicyclic boronate taniborbactam (VNRX-5133) is in phase 3 clinical trials.[5]

The steady state kinetics of VIM-2 with its various substrates have been studied, including as discussed in this thesis. Overall, VIMs are fast-acting enzymes, with high turnover rates across all classes of β-lactams except monobactams with some variation depending on the substrate.[4] Because of its fast turnover, capturing reaction intermediates (or enzyme: substrate complexes) in crystal structures by classical techniques is thus likely to be difficult unless modifications are made to the enzyme-substrate combinations i.e., the metals in the active site are altered or photocaging is used. Understanding structural changes during catalysis could be important for the development of future MBL inhibitors. Applying time resolved crystallography to understand VIM-2 catalysis is therefore of interest. Two XFEL machines were employed in the work described in this chapter, the EuXFEL and the XFEL at SACLA. It was envisaged that XFELs could be used to study the structural changes that occur, at the VIM-2 active site as well as characterising the intermediates during the reaction, with the ultimate aim of producing a "molecular movie".[6,7] Whilst SACLA was the second XFEL opened in 2011 for experimental purposes, the EuXFEL was a relatively new facility during our beamtime in 2018. The EuXFEL is unique with its super cooling resonators and has the highest pulses per train out of the operating XFELs.

As was the case with PBP5, ertapenem was used as the substrate for all the XFEL experiments due to its high solubility, its availability at reasonable cost, and its clinical relevance. Ertapenem is a carbapenem that is widely used to treat secondary infections in several different countries.[8] Two different sample delivery methods were used during the work at XFELs, i.e., mixing jets and drop on drop mixing using ADE and PolyPico dispenser.[9] The results enable for comparisons between the different methods and XFELs, so providing information on which sample delivery method is best suited for the desired experiments. Fixed target experiments were also performed at the I24 beamline in Diamond Light Source to investigate how suitable the microcrystal solutions were for XFEL experiments.[9] Resting state structures of VIM-2 were collected at the Diamond Light Source and at

both XFELs. Attempts were made to collect data at various time points during the reaction of VIM-2 with ertapenem, but these proved to be unsuccessful for reasons that are discussed in this chapter.

Materials and Methods

Recombinant VIM-2 Production and Purification

Recombinant VIM-2 was expressed as described in Chapter 2. In brief, the supernatant from the recombinant cell lysate was loaded onto a His Trap column for purification. The protein was further purified using a gel filtration column as described in Chapter 2. The His tag was cleaved using 3C protease and the protein was the re-purified using the His Trap column. The eluted cleaved protein was concentrated, and buffer exchanged into the crystallisation buffer, as described in Chapter 2.[10,11]

VIM-2 Crystallisation

VIM-2 was first crystallised in a 96 well optimisation, previously developed by Dr. Jürgen Brem, as described in Chapter 2.[12] The plate was incubated at room temperature over one week and was observed on a daily basis. A single crystal was harvested and cryocooled for in house data collection. The plates were then harvested to make seeds for the batch crystallisation trials of VIM-2. The seeds were crushed using a vortex mixer for three minutes with 30 seconds pauses every 30 seconds to ensure that the crystals did not melt from overheating. The seeds were aliquoted and stored at -80°C.

VIM-2 was also crystallised in an optimisation plate created by Dr. Gareth Langley, with magnesium chloride, PEG 8000 and Tris buffer. Crystallisation was attempted at two different concentrations, i.e., the normal 8.5 mg/mL concentration and at 15 mg/mL; crystals from both conditions were harvested for data collection at Diamond Light Source at beamline I04. Data collection was performed at 100K with 1800 images collected for each crystal. Attempts were also made to crystallise VIM-2 in a Tris

based buffer compared to a HEPES one (50 mM Tris pH 7.5, 100 mM NaCl, 1 mM TCEP and 100 µM $ZnCl_2$).

Batch Crystallisation of VIM-2

Batch crystallisation methods of VIM-2 were developed by Dr. Thomas Leissing using a well solution of 26% (w/v) PEG 3350 and 0.2 M magnesium formate; a relatively high PEG concentration was initially chosen to increase the nucleation of the protein. Once a condition was chosen, the procedure described in Chapter 2 was used to for batch method crystallisation. All conditions were set up in 96 well Clariostar plates (BMG Labtech) and were incubated at room temperature with shaking (800 rpm); they were checked every day to see if new crystals had appeared.

Broad Screening VIM-2

Because high PEG concentrations are not optimal for mixing jet and drop-on-drop XFEL sample delivery methods,[13] it was decided that a new crystal condition should be determined for the XFEL experiments. Broad screens were set up at a protein concentration of 8.2 mg/mL with VIM-2 in the same crystallisation buffer as used in Chapter 2. Plates were set up at the Harwell Research Complex due to the large number of broad screens available there. Broad screens tested include Morpheus I, Morpheus II, Index, Wizard I and II, PEG ION, Structure 1&2, PACT Premier, Salt RX, PEG RX and JSCG+. Broad screens were purchased either from Molecular Dimensions or Hampton Research. Plates were set up using a Mosquito machine for the drops and a Hydra machine for the wells, they were stored at 18°C in incubation fridges. Trays were checked regularly for the first two weeks. Any crystals that appeared were harvested and cryocooled with liquid nitrogen to 100K for data collection at Diamond Light Source at I04 Beamline.

Fixed Target Data Collection

To test the quality of the VIM-2 crystals produced, the microcrystals were sent to the Diamond Light Source for serial data collection. 500 µL of the batch crystal slurry was harvested for data collection and stored at room temperature without anything being added to it. A smaller aliquot of the microcrystal slurry (~300 µL) was soaked with 30 µL of 150 mM ertapenem for 10 minutes. This was done to try and mimic the soaking experiments that would happen at an XFEL as best as possible (albeit with longer soaker times), to test if ligand soaking was a viable option for the VIM-2 microcrystals. On average 2 to 3 full chips were used to obtain each dataset; 40% transmission was used for data collection with a photon flux of 4 x 1^{-12} ph/s, an energy of 12.8 keV and an exposure time of 80 ms. All data collected was processed using cctbx software.

Data Collection at EuXFEL

The Schofield group, as part of the Orville *et al.,* proposal, was awarded User Assisted commissioning beam time at the European XFEL in Hamburg, Germany in October 2017. All data were collected at the SFX/SPB beam line. This involved a collaboration with over 100 people from across the globe. Because of issues that occurred during this beamtime, compensatory time was allotted in June 2018 which I was involved in (XFEL-2017b, Orville et al., 6/06/18-10/06/18). Data collection was done with the AGIPD detector (binning 8 x 8) at 10.5 keV.

Even though it has only three SASE undulators, the EuXFEL can produce 27,000 pulses per second.[14] What makes the European XFEL unique compared to previously developed XFELs is that it uses a superconducting system developed for a positron linear collider. The XFEL instrument is close to 2 km long and distributed the beam to two separate sets of undulators: SASE1 and SASE3 being the North Branch and SASE2 as the South Branch (**Figure 1**).[15] Each of these feed into a separate beamline. The EuXFEL also uses a technique known as microbunching; this is where the pulse sequence is made of bunch trains that have a repetition rate of 10 Hz at a length of 600 µs. Each of these trains consists of

27,000 bunches.[16] A single bunch consists of approximately 10^{12} photons with pulse durations of 30-50 fs.[15]

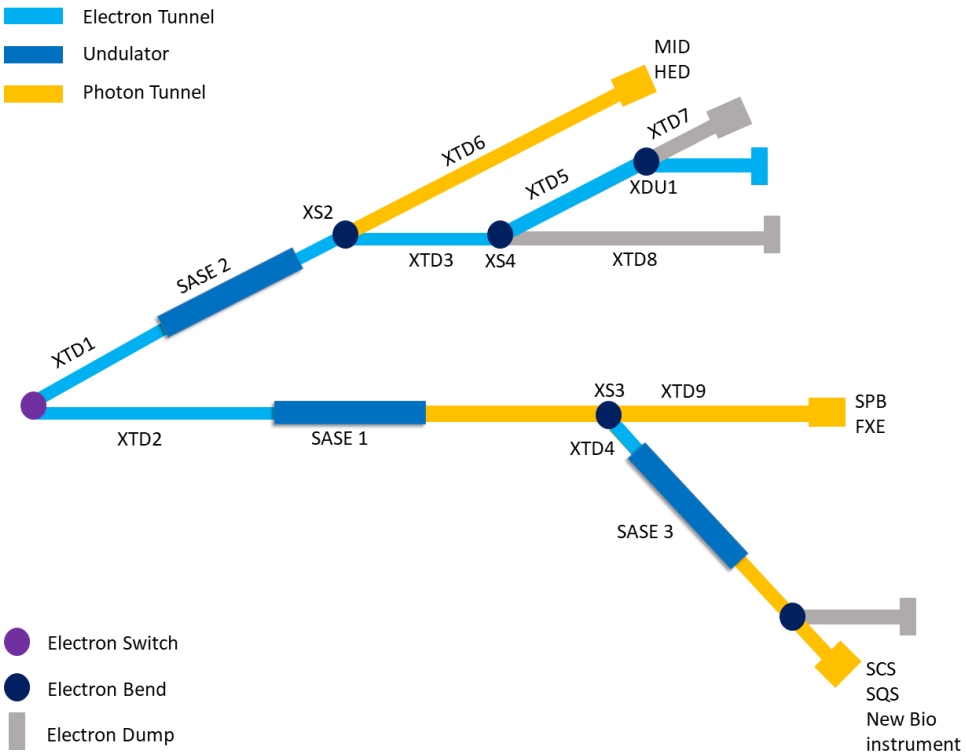


Figure 1: Simple schematic of EuXFEL set up. Three different SASE undulators are used to generate photons for XFEL experiments, each of these feed into separate beamlines.

As a result of the photo flux density of the beam, a standard detector cannot be used as these cannot keep up with the high number of photons being used.[14] The EuXFEL uses an Adaptive Gain Integrating Pixel Detector (AGIPD); this is a hybrid pixel detector. The detector consists of 16 AGIPD modules, with each module 8 x 2 chips joined together using a thick silicon sensor. Each of these chips has 64 x 64 pixels with a pixel size of 200 x 200 μm^2.[17] The AGIPD uses dynamic gains switching to be able to cope with the high dynamic range and to resolve single photons, allowing the detector to cope with these demands. There is a data analysis pipeline at the EuXFEL that allows for the storage of images at 5 MHz speed.[17]

Data Processing at EuXFEL using CrystFEL

Indexing and integrating

Unlike at LCLS (See Chapter 3), data processing at the EuXFEL was done using the programme CrystFEL, with ONDA (Online Data Analysis) for real time analysis of the data being produce.[18–20] Data processing was performed by Dr. Thomas White and Dr. Anton Barty. CrystFEL is specifically designed to take advantage of multi core processing in order to help with processing such large amounts of data. Several programmes are available in the CrystFEL suite, including indexamajig.[18] Indexamajig is the software used to help index and integrate a large number of images at high speed.[21] CrystFEL also uses MOSFLM and DirAx for data processing.[21,22] The initial input is a list of named images, peak detection is performed on each of these images and these peaks are sent to the selected autoindexing programme.[18,23] The selected module will then produce a unit cell which can be compared with a reference cell although this is not necessary, unlike with cctbx where a reference cell is incredibly important.

If it turns out that the unit cell matches the unit cell expected, the predicted peaks in the image are calculated and compared with the initial peak positions submitted to the autoindexing software. If <10% of the initial peaks match the predicted peaks the image is rejected. These lower percentages are more commonly seen in the smallest of nanocrystals (<1 μm^3) compared to larger microcrystals. Problems tend to arise when one of the unit cell axes is close to another making it difficult to tell the different unit cells apart; this can cause problems very similar to those witnessed with twinning.[23] The cell matching procedure can be refined until the predictions match the data observed.[18,23]

The next step is to ensure that the intensities are integrated using the predicted peaks. A summing of the pixel counts within a fixed radius is used for integration; this radius can be altered in the detector geometry file. The background that surrounds the peak is subtracted by measuring the intensity

surrounding the integration region. All of the information produced by indexamajig are written in a text file, including the initial peak search and the peak locations.

A large enough resolution range between two sets of intensities will exhibit a positive correlation, as low-resolution reflections are the strongest and the high-resolution reflections are the weakest. To make up for this, the correlation coefficients are calculated for a limited resolution which is set by the user. The programme cell explorer is used to determine the unit cell of the dataset and produces a list of unit cell parameters from each diffraction pattern. The programme allows you to visualise these unit cells using histograms.

Merging intensities- process hkl

The merging of intensities is done by the programme process_hkl, which is a part of the CrystFEL package, where the mean of all measurements for each reflection is taken.[18,23–25]As this tends to involve a large amount of data, Monte Carlo integration is used over the 3D reflection profiles which results in values that are proportional to the integrated intensity. Any variations in pulse intensity or crystal size will be integrated out and will become a constant factor instead. This means that it affects all intensities equally throughout the data set. This can prove a problem for XFELs as the spectrum, wavelength and incident beam intensity can vary for each pulse. When merging the data, process_hkl only considers the point symmetry and not systematic absences. The programme scales the data, to improve the results which is done by normalising the intensities in accordance with the mean intensity of the Brag peaks in each pattern.

Assessing data quality

Because the Monte Carlo merging takes samples from a number of different distributions these individual values will not share a high degree of similarity. It does not make sense in this case to use values such as the R_{merge} to measure the quality of the data. Instead, an alternative measure the R_{split}

is calculated, where the data is split into two sets that are merged independently. The level of agreement between these two sets of data is then measured using the R_{split}.[21] Other factors such as CC1/2 and I/σI can also be used as discussed in Chapter 2.

OnDA and Cheetah-Real Time Data Analysis

OnDA

OnDA or Online Data Analysis was used at EuXFEL for the real time analysis of the samples.[19] This programme is designed to process multi-dimensional and multi pixel data from various potential sources or any output from a digital sensor. The OnDA framework operates on data found from the data acquisition system (DAQ). The DAQ collects simultaneous readings from the instruments and then groups them into events with each event corresponding to a single instrument state or the measurements for a single pulse of an XFEL laser.

The worker nodes in the OnDA framework extract important information from the single event data and carry out the required processing.[19,26] All resulting data is then sent to the master node that carries out multi event processing and information can be sent to the Graphical User Interface (GUI). The worker nodes communicate amongst one another using MPI framework. OnDA is a very modular programme, with clearly separate functions for data retrieval, data extraction and node communication. These functions can be split into four different layers. The first layer is the instrument layer, which extracts data from a single instrument, sensor or detector.[19] After this comes the data extraction layer where the relevant information is extract from the event's data, in the case of XFELs this would be the recorded image from the detector. The parallelisation layer controls communication between the worker and the master nodes and allows worker nodes to recover data from the data source. Finally, the data processing layer carries out the relevant scientific data processing. The specific functions needed for performing data processing are implemented by OnDA using both the worker and the master nodes.

OnDA is able to provide three different real time monitors, one of which is an SFX monitor; this allows for monitoring of the hit rate by reading the data from the detector, applying the necessary data correction and searching for Bragg peaks in the image. This is done using the programme Cheetah.[27] Depending on the number of peaks found, the programme decides whether or not the image can be counted as a viable diffraction pattern. The data collected is sent to the GUI for visualisation afterwards. The GUI shows two main outputs from the detector, one is a virtual powder pattern of the data that builds up as SFX data accumulates and the other is a running average of the hit rate and saturation rate. New developments to OnDA aim to provide online indexing of crystallographic Bragg peaks, providing the users with information on the indexing rate in real time. The programme has been used for analysis in several experiments at the EuXFEL, including time resolved work on photoactive yellow protein (PYP).

Cheetah

Cheetah was originally developed for XFEL experiments and operates using a modular library that is independent of the facility where the data collection is occurring.[27] Cheetah's main purpose is to assess the quality of the data in each time frame in order to provide rapid feedback on the progress of the experiment. Frames that do not need further analysis are removed from the processing pipeline and data processing steps are performed on those that are seen to be viable.

The first step in this process is correction for any artefacts seen on the detector. Any pixels that appear saturated are identified and flagged by the programme. Next, any detector offsets determined from the dark frames are subtracted and estimates are made for the common mode offset on each module. "Bad" pixels are eliminated, and corrections are made for gain calibration. Because the AGIPD detector is made up of several modules, Cheetah treats each of these modules as a separate detector.[17,27] This means that background subtraction and peak finding are performed separately on each module.

The next step involves image analysis, where possible Bragg peaks are identified. If the pixel intensity is below a certain threshold the Cheetah will move onto the next pixel. If a pixel intensity is above a certain threshold, then all the connected pixels are located and assessed, if they fall between the minimum and maximum threshold then the connected region shall be counted as a peak. The background noise is then calculated, and the peak is only retained if the integrated intensity is sufficiently above the noise levels of the surroundings.[27]

Sample hits are identified by counting the individual number of peaks in an image; only if there is a certain number of peaks is the image to be counted as a hit. In nanocrystals that are often used in XFEL diffraction studies, n needs to be > 20 for any image to be classified as a hit, this is the minimum number required for autoindexing using CrystFEL.[23] Criteria can be adapted by getting the programme to discard any images that are below a certain resolution. Once all these steps have been completed, Cheetah provides stills of some of the image hits and information on the hit rate and resolution of the sample.

Sample Delivery at EuXFEL

The mixing jets method was the key sample delivery method used on VIM-2 crystals during the data collection at EuXFEL (Orville et al., 2017-b, SPB/SFX).[13] The mixing jet method was chosen as it allowed for the fast diffusion of substrate solution into crystals at high concentrations, provided the substrate was soluble, by soaking the large volumes of substrate into the microcrystal slurry.[13] The method by Lois Pollack's group was developed as part of a larger collaboration to trigger reactions without using light, where a mixing jet contains an inner and an outer capillary. During a data collection, the inner capillary contains the crystal slurry whereas the outer capillary contains the substrate (**Figure 2**). Further down the inner jet there is a mixing region where the substrate and slurry mix. This mixture is then released from the jet and the microcrystals can interact with the beam to produce a diffraction pattern. Helium is used to focus the jet into a thin stream.

Different nozzles have been developed by Calvey *et al.*, for the jets have been developed for different time points, enabling the microcrystals to interact with their substrate for various lengths of time. This was done by altering the length of the nozzle components of the mixing jet. The jets were tested before with the microcrystal slurry (**Figure 3**). A flow rate of 25 µl/min was used during data collection. Ertapenem was dissolved in water for these mixing experiments.

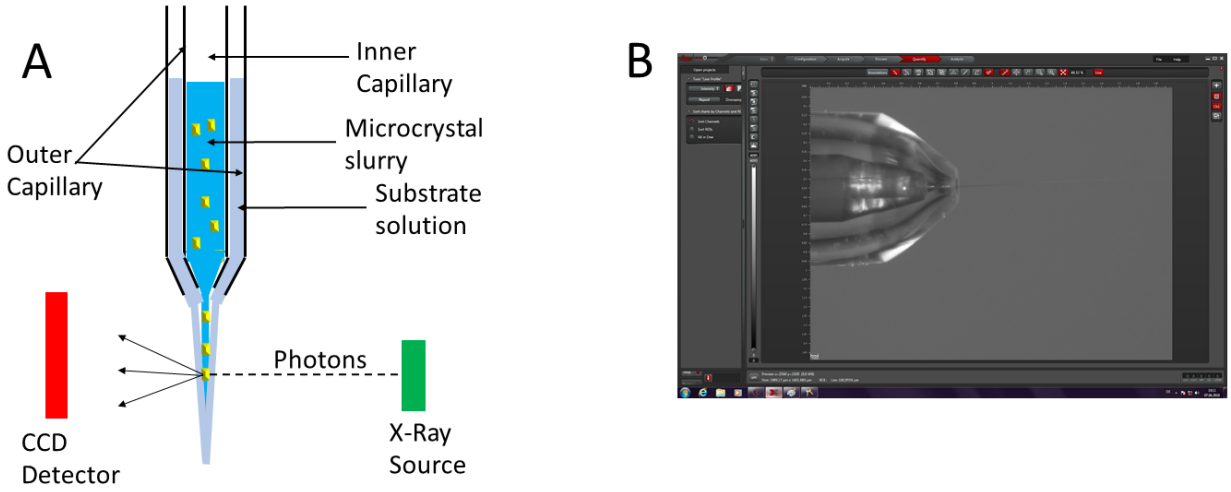


Figure 2: Diagram of mixing jets (A) and a jet containing the mother solution (0.2 M magnesium formate and 26% PEG 3350) during a flow test (B). This was done in order to making sure that the solution would cause the jet to clog during data collection which could lead to a delay of two to three hours.

Data Collection at SACLA

XFEL experiments on VIM-2 were performed as part of the Orville *et al.,* 2019B8088 proposal. Unlike EuXFEL, SACLA does not use a superconducting system for its data collection meaning that it can only reach a pulse frequency of 120 Hz.[28] Moreover, SACLA uses a thermionic gun with a caesium boride cathode to produce electrons compared to the laser driven photocathode.[29] Another major difference between SACLA and LCLS is that the X-rays are created in short periods in vacuum undulators compared to those in LCLS which are not in vacuum conditions. This vacuum technology allows for the creation of sub angstrom X-Ray wavelengths (0.6 Å) and a photon energy of 20 keV with an 8.5 GeV

electron beam.[28] The wavelength at SACLA can be changed by altering the gaps between the undulators at a fixed beam energy.

Sample Delivery at SACLA

Like LCLS, the acoustic tape drive was used for sample delivery at the SACLA data collection (See Chapter 3). However, since mixing experiments needed to be done, a PolyPico machine was attached to the system to allow for drop-on-drop mixing (**Figure 3**). The PolyPico uses high frequency acoustic waves to dispense small amounts of liquids (0.1 nL per drop was used for SACLA experiments), be it microcrystal slurry or substrate.[9] Unlike with the mixing jets, where one has to change jets every time a new time point needs to be tested, the PolyPico relies on cartridges that can be removed and replaced with new sample. Moreover, smaller quantities of protein and substrate are needed for these experiments. Altering the belt speed is used to change the mixing times of the substrate and the microcrystal slurries (**Figure 3**). Before arriving at SACLA the PolyPico had been tested at Diamond Light Source with the fixed target system. All solutions of ertapenem were dissolved in water.

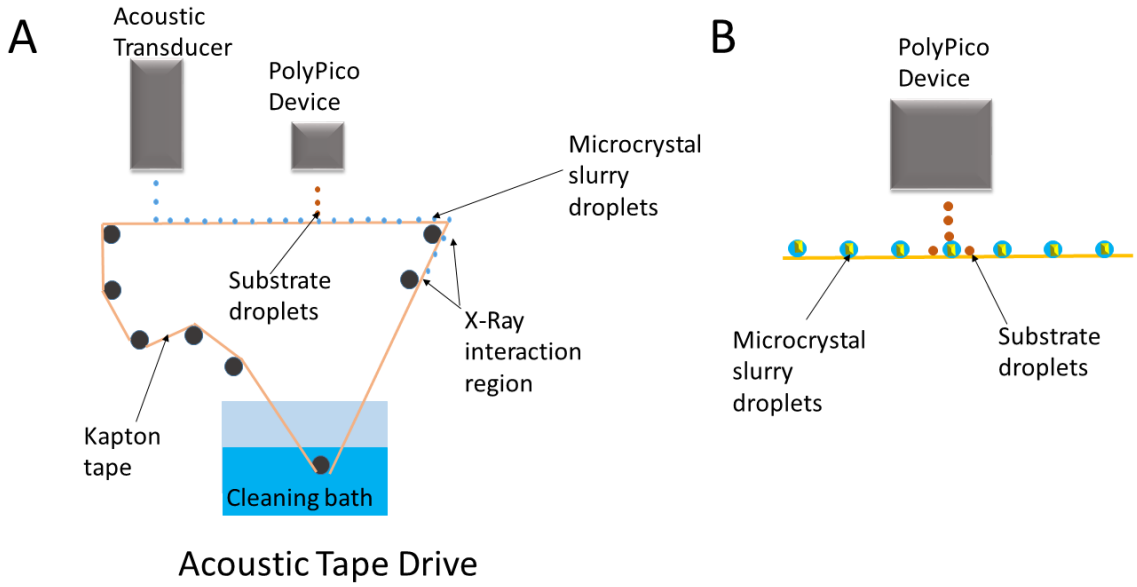


Figure 3: Diagram of acoustic tape drive/ acoustic droplet ejection with a drop-on-drop mechanism. A) shows the overall set up observed at an XFEL beamline and B) is a close of the drop-on-drop interaction region. Substrate droplets are represented in red and microcrystal slurry droplets in blue. Several droplets from the PolyPico device land on the microcrystal droplets with some landing on either side.

Data Collection and Processing at SACLA

Data collection at SACLA was performed using an 8 chip MPCCD-Phase III detector. Two beam stops were used, a front beam stop, which was 3 mm in diameter and another that was 6 mm in diameter, giving a low-resolution limit of 46 Å. Datasets for VIM-2 were collected for the resting state (no substrate added) and with ertapenem added to the crystal drops with two different belt speeds, 300 mm/s and 30 mm/s. All data processing was done using cctbx by Aaron Brewster and his team from the Lawrence Berkley National Laboratory.[30,31] Five Ertapenem drops of 100 pL were used for each microcrystal slurry drop dispensed onto the tape drive during the data collection however this might not be entirely accurate as it was difficult to measure drop size with the camera in the hutch. All data at SACLA was processed using cctbx, molecular replacements and refinements were carried out using Phaser and Phenix respectively.

Results

VIM-2 Purification and Crystallisation

Recombinant VIM-2 was successfully produced and purified using the methods described in Chapter 2. Once the purification was complete, the protein was crystallised using the optimisation block developed by Dr. Jürgen Brem (magnesium formate vs PEG3350) several crystals appeared in the higher PEG concentrations after 24 to 48 hours (**Figure 4**) and their quality was assessed using the in house Rigaku diffractometer with only a small number of images being collected. The crystals diffracted to a high resolution (~1.4 Å) in the space group *C* 1 2 1.

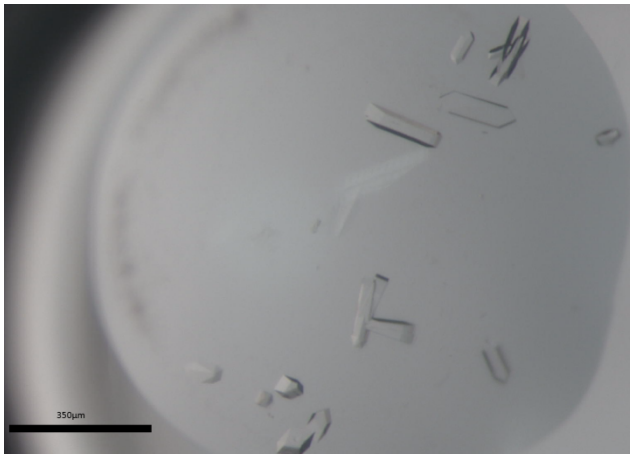


Figure 4: VIM-2 crystals produced using vapour diffusion methods. These came from the optimisation plate created by Dr. Gareth Langley. Those that were not used for data collection were crushed and turned into a seed stock for batch crystallisation methods.

Despite the success of producing macrocrystals in the 0.2 M magnesium formate 26% PEG 33350 condition, there were several problems with this condition. First the high PEG concentrations made dispensing with a PolyPico potentially difficult; high PEG concentrations could cause problems with the mixing jets, due to the high viscosity compared to water.[13] This meant that ertapenem had to be dissolved in water for all mixing experiments, and not mother liquor solution.

Another issue was that there had been previous issues with getting VIM-2 homogenous crystals using previous optimisation blocks mentioned in Chapter 2. Although the crystals outwardly look the same, some were in the space group *C* 1 2 1, there were some that were in the orthorhombic *I* 2 2 2 space group. If slurries of microcrystals contained crystals from both space groups, this could create problems when it comes to data processing, although it is still possible to get a dataset, although it is not impossible to process such data. A similar problem was seen with the optimisation block (magnesium chloride, PEG 8000 and Tris buffer) created by Dr. Gareth Langley, making this condition flawed. In either case both these space groups have relatively low symmetry, meaning that a lot of images would be needed for a complete dataset which meant using more protein.

Many broad screens were then set up to try and find VIM-2 crystallisation conditions that were low in PEG concentration and which potentially produced crystals in a different space group. Many crystals were produced across these broad screens, however, most conditions seemed to employ high concentrations of PEG. One crystal in a citrate-based condition was found (Wizard 3 and 4 B3: 1.6 M sodium citrate, (**Figure 6**), however, the crystal produced did not diffract to high resolution (3.3 Å) and the citrate had displaced the zinc ions in the active site (**Figure 5**).

Although the displacement of the zinc ions was frustrating, from a mechanistic perspective, it is interesting with regards to MBL inhibition because it implies that displacement of zinc ions by an organic inhibitor is a suitable mechanism of MBL inhibition. Due to time constraints, it was decided that the best course of action was to grow batch crystals in the magnesium formate PEG3350 condition.

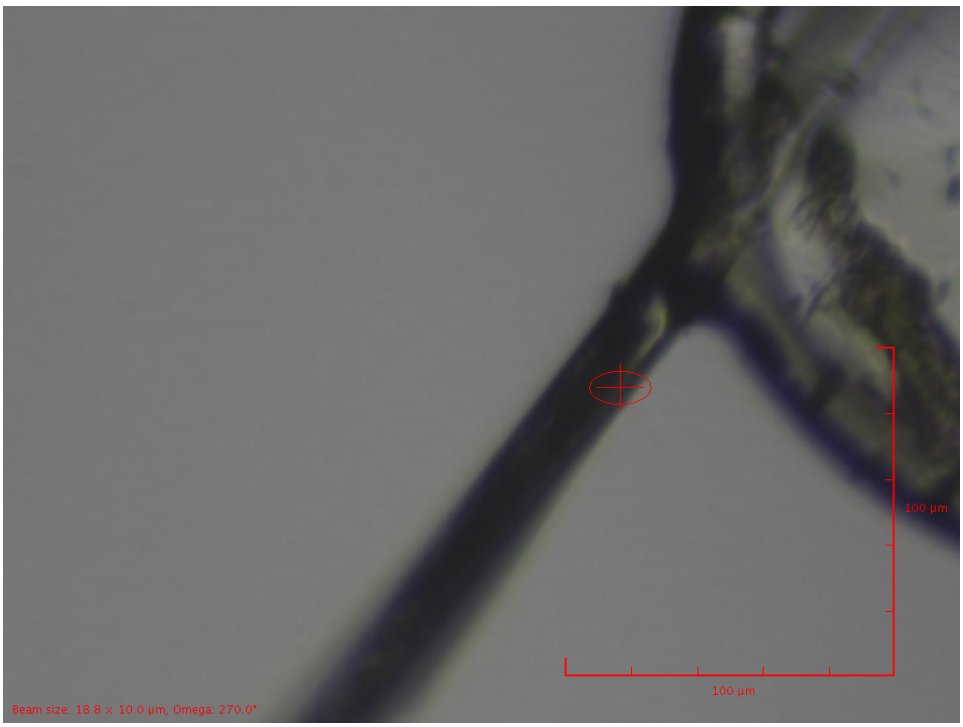


Figure 5: Image of crystal from the B3 condition in the Wizard 3 and 4 broad screens (1.6 M sodium citrate tribasic). The crystal diffracted to a resolution of 3.3Å. due to the low resolution, no room temperature data collection was attempted.

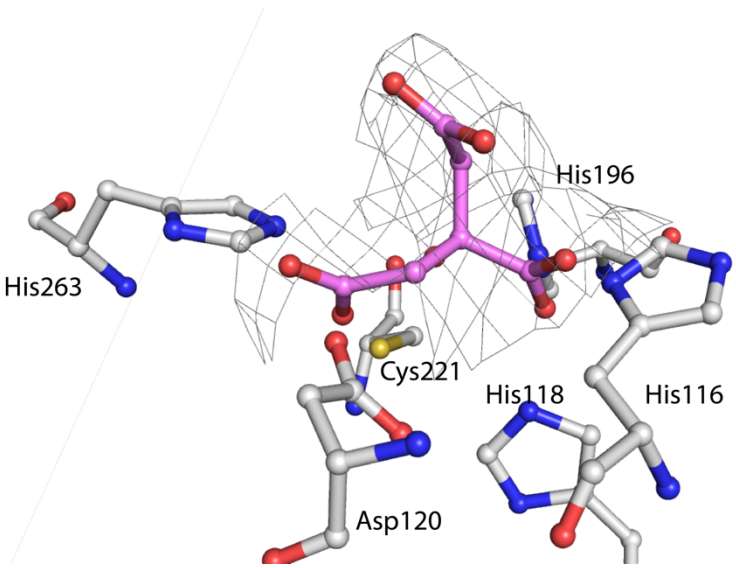


Figure 6: View from VIM-2 active site from the B3 Wizard 3&4 condition. The citrate molecule was modelled in, a mF_o-DF_c electron density map (contoured to 3σ). The citrate molecule has clearly displaced the zincs from the active site. Resolution was 3.3 Å, space group P 3_1 2 1.

Batch Crystallisation of VIM-2

Several more plates of VIM-2 macrocrystals were set up in order to produce the most concentrated seed stock possible. All the crystals were harvested and crushed using a standard seed bead made from Polytetrafluoroethylene (Hampton Research). VIM-2 was added to a well solution of 0.1 M magnesium formate and 26% (w/v) PEG3350 in a 1:2 protein reservoir ratio. 3 µL of the seed stock was also added to this mixture which was shaken at 700 rpm using a plate shaker. Microcrystals started to appear after overnight incubation and a clear increase in concentration was observed after another 24 hours of incubation (**Figure 7**). The slurries produced from this method had a crystal concentration in the range of ~10^7 crystals/mL.

The microcrystals had dimensions approximately between 10 to 20 x 5 x 5 µm.[32] This crystallisation method was repeated on site at the EuXFEL. However, due to a lack of available equipment a vortex shaker was used instead of the microplate shaker. The vortex mixer shook the crystals at a significantly higher speed compared to what was previously used for batch crystallisation, which lead to a decrease in crystal concentration. The crystals were then left to settle, and the well solution was removed in order to increase the crystal concentration. By the end of the EuXFEL beam time, a slurry with 8 times ($16x10^7$ crystals/mL) the original concentration was used for data collection, due to the high concentration needed for the mixing jet method.

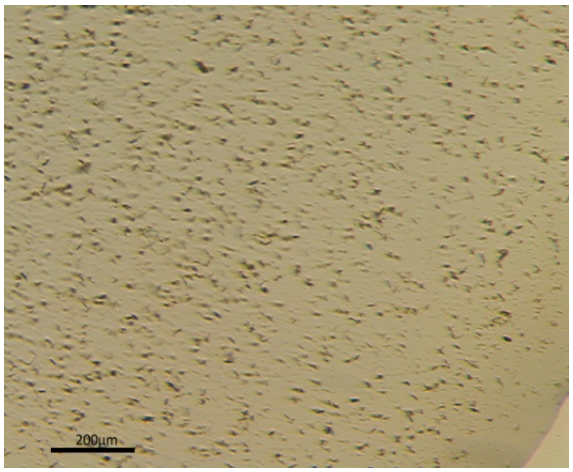


Figure 7: Batch method crystals of VIM-2 at EuXFEL. Crystals took 48 hours to reach the highest concentration possible ($2x10^7$ crystals/mL); and initially appeared homogenous in shape and size (10 x 5 x 5 µm). The latter is vital for harmonising potential substrate diffusion as differing rates of diffusion within the same batch of crystals can lead to unclear electron density maps.

VIM-2 Fixed Target Data Collection

Fixed target data collection of VIM-2 was performed at the I24 beamline at the Diamond Light Source with help from Dr. Pierre Aller, Dr. Robin Owen, Dr. Agata Butryn and Dr. Danny Axford. Data were collected on resting state crystals of VIM-2 and crystals soaked with 150 mM stock of ertapenem for 10 minutes. Several of the fixed target silicon chips were used to collect data for each dataset; in some cases, only half the chip was loaded in order to increase the concentration of microcrystals in the area

thus increasing the hit rate. Both the resting state and the soaked samples diffracted to around 2 Å resolution.

Data was processed by Dr. Pierre Aller. A mixture of unit cells was observed in both cases, although all appeared to be in the *C* 1 2 1 space group (**Figures 8-10**). The two different unit cells made data processing more difficult, however, complete datasets were produced for both. No ligand was observed in the active site of the sample that had been soaked with ertapenem, potentially due to the high concentration of PEG 3350 (26% w/v). The resting state structure was similar to those observed in previous cryo structures, with a similar unit cell and positioning of the zinc.

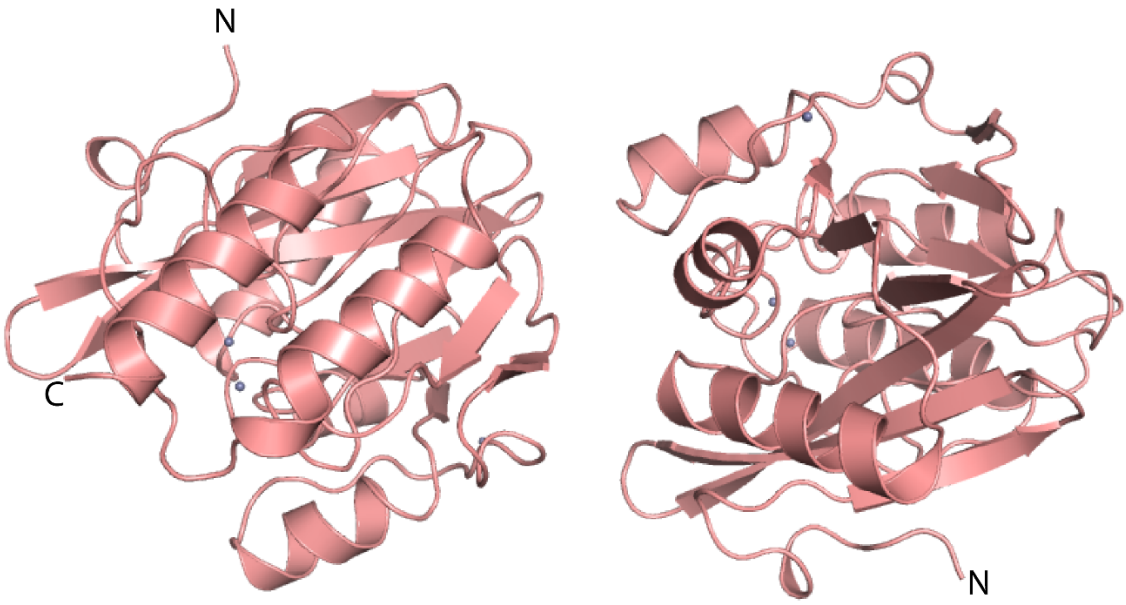


Figure 8: View of the two VIM-2 molecules in the asymmetric unit from the fixed target data collection. Zinc ions are shown as grey spheres. Note how the active sites are not pointed away from one another, something which has not been observed in previous VIM-2 datasets in the *C* 1 2 1 space group, where both active sites face each other. It is uncertain why this happened despite the similar data collection statistics. Further data processing maybe be necessary in different unit cells.[33]

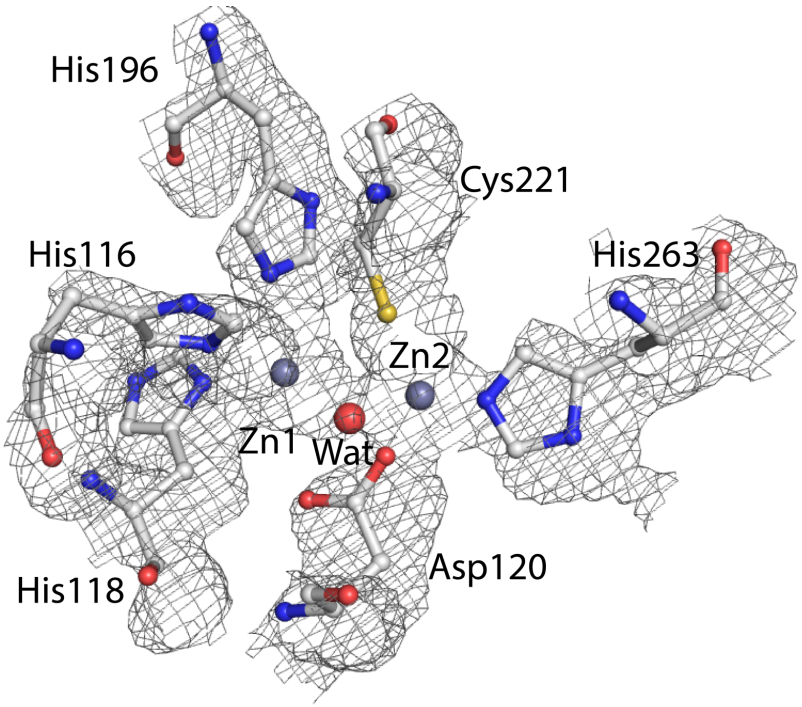


Figure 9: Active site electron density map ($2mF_o$-DF_C) from dataset collected at I24 Diamond Light Source using fixed target data collection at room temperature. Overall, the structure was comparable to previous cryo data sets collected. The map is contoured to 1σ to 2.1 Å.[33]

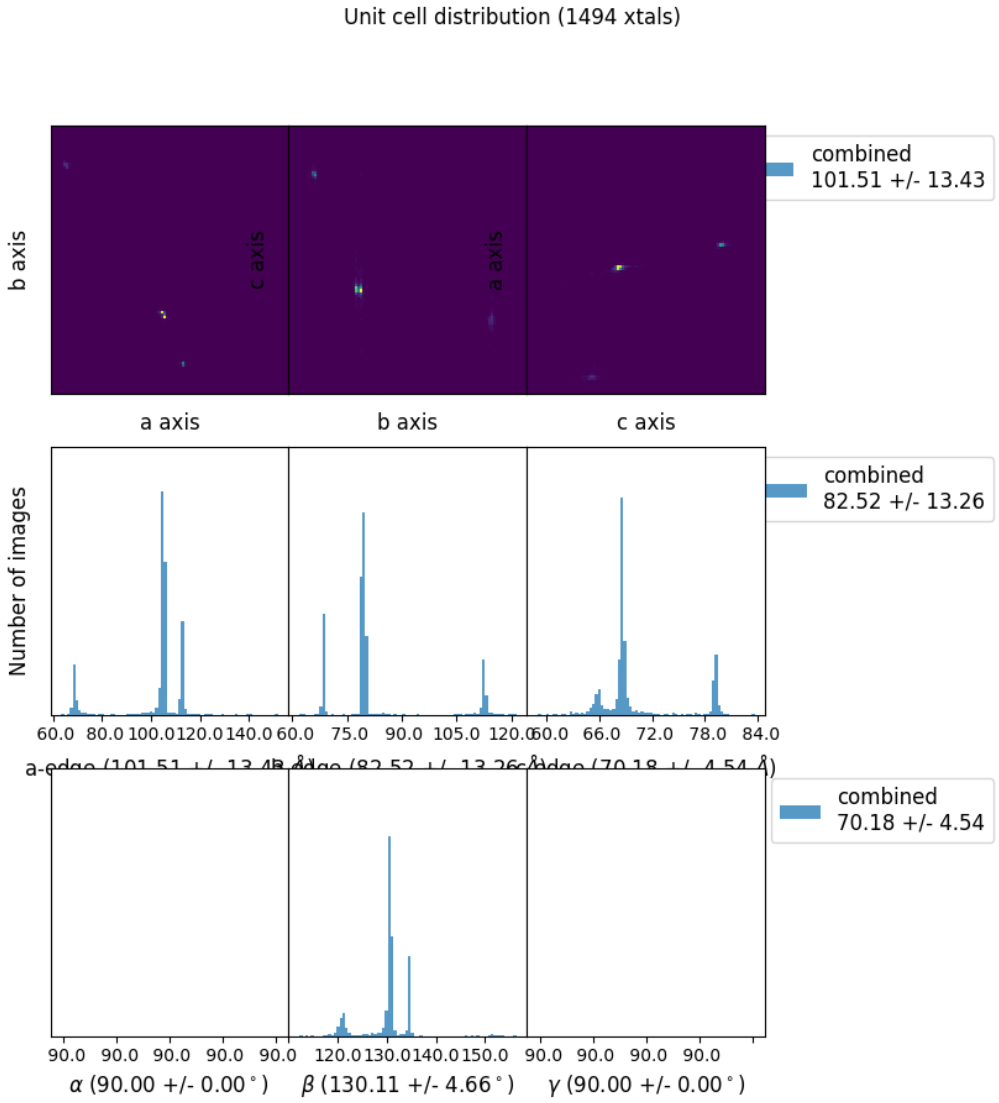


Figure 10: Unit cell distribution for fixed target data collection of VIM-2 crystals. Note the different values for β and a, b and c which lead to issues with regard to data processing. Average dimensions for a, b and c can be observed on the side of the image although they are obscured below the graphs for a, b

VIM-2 Data Collection at EuXFEL

Data collection was attempted at EuXFEL using the mixing jet sample delivery system.[13] A total of 120 mg of VIM-2 was used for this data collection. Due to initial problems when growing the microcrystals, the crystal concentration was lower than what would have been ideal. Consequently, the hit rate, calculated using OnDA and Cheetah,[19,27] during the data collection was very low (~0.1%). Moreover,

there were issues with regards to the focussing of the beam which meant that the beam size was 18 μm^2 rather than 5 μm^2. This is due to the fact that the last focusing mirrors had not been installed. It should be noted that the real time feedback produced may not have been entirely accurate as different OnDA and Cheetah seemed to report slightly different hit rates, with a 0.2% hit rate being reported from Cheetah and a 1.1% hit rate from OnDA. The crystals that did diffract produced high-resolution data and were in the space group *I* 1 2 1. Data was processed by Dr. Thomas White. A dataset of resting state VIM-2 was collected to 1.7 Å (**Figure 11**) however it was only 70% complete due to the low hit rate (**Table 1**). Despite this, the two zinc ions in the active site were clearly visible and there was some density between the two zincs which is most likely the nucleophilic water that is involved in the reaction.

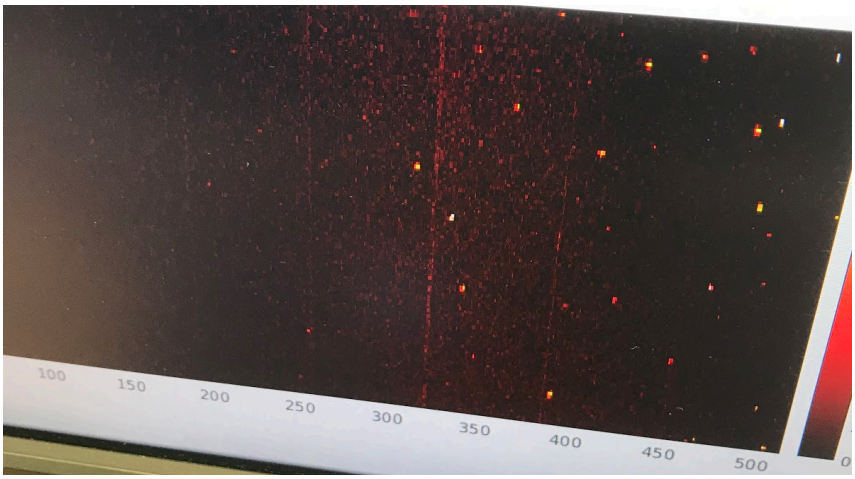


Figure 11: Diffraction pattern from VIM-2 data collection at the EuXFEL. Spots are clearly seen on the detector panel although the hit rate is low, indicating that the crystal concentration was not high enough.

Data were collected for VIM-2 crystals that had been soaked in 300 mM ertapenem dissolved in water in the mixing jet for 16 ms and 120 ms time points. These timepoints reflect the total time the samples had to equilibrate before the crystals interacted with the beam. One of the major downsides of these mixing experiments is that the crystal concentration becomes diluted once the substrate is added. It was very difficult to obtain a complete dataset within the time frame, since upon mixing the hit rate

further dropped. In the future, this should be of little concern, as up 3500 images can be collected at EuXFEL when it is working at full capacity. The dataset produced for the 120 ms was 30% complete (**Table 1**), which meant that the maps produced were of poor quality (**Figure 12A**). It did not appear there was any extra density in the active site (**Figure 12B**), indicating that the ertapenem had not entered through the solvent channels of most the crystals.

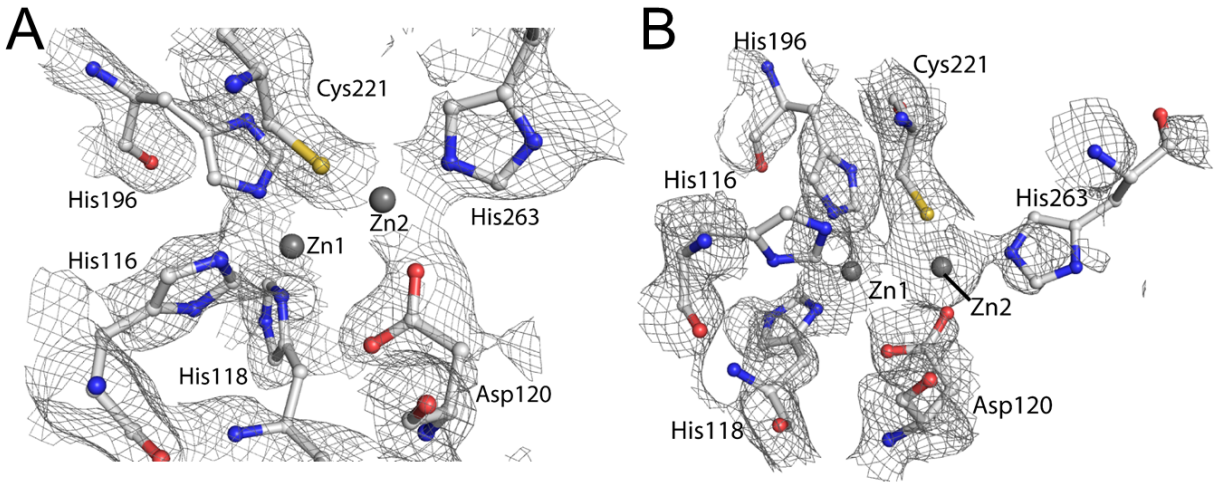


Figure 12: $2mF_o$-DF_c electron density map for data collected at EuXFEL around the active site. Maps were contoured to 1σ. A) Resting state T_0 density, water molecules were not modelled in due to the low completeness. Dataset resolution was to 1.5 Å. B) Density from data collected after 120 ms of mixing with ertapenem. Dataset resolution was to 1.4 Å. The completeness for this was very low which can be seen with the poor density and there was no density for ertapenem in the active site.[33]

Further issues occurred with the data processing, due to issues with characterising the photon energy. This meant that even after extensive refinement of the detector parameters the photon energy was still off, leading to problems with the unit cell which appeared to be expanded. In addition, it appeared that there was a mixture of two different unit cells in all the datasets, making merging and integrating the datasets significantly more complex. This could also have been why it was difficult to obtain a complete dataset. Other issues during the beam time, such as problems with the accelerator and the beam line failing meant that collecting more data was not possible.

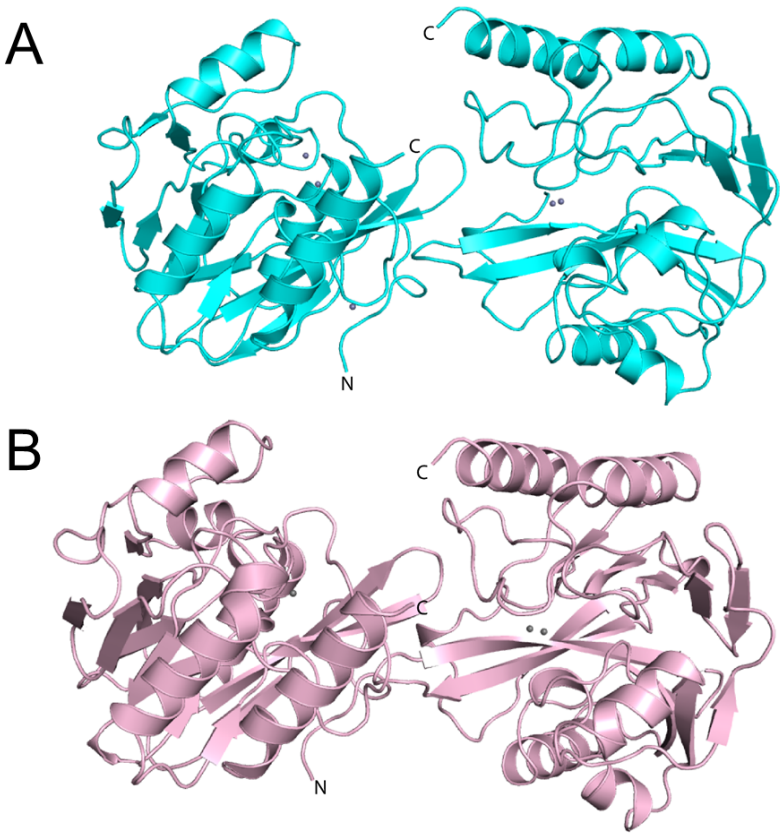


Figure 13: Secondary structure of VIM-2 in the asymmetric units of the datasets collected at EuXFEL. The top panel shows the secondary structure for T_0 structure and the bottom panel the structure collected after 120 ms of mixing with ertapenem. Zinc ions are shown as grey spheres. Both had two molecules in the asymmetric unit and were processed in the space group *I* 2.[33]

Data Collection at SACLA

80 mg of VIM-2 protein was sent to SACLA for data collection, the protein was crystallised using the batch method crystallisation as described in the methods section. The crystal concentration was in the range of 10^7 crystals/mL and appeared to be similar in shape and size to those produced at Oxford. Despite the high temperatures in the experimental area at SACLA (~34°C) the crystals did not appear to be affected. A dataset of VIM-2 in its resting state was successfully collected using the ADE method

to a resolution of 1.7 Å. A comparison of this structure with the fixed target structure shows that there is high similarity between the structures despite the difference in resolution (**Table 1**). This also true for the asymmetric unit, with the active sites facing away from each other in both resting state structures. This was not seen in the resting structure at the EuXFEL however, although it should be noted that data was processed in a different space group.

VIM-2 Data Collection at SACLA

Drop-on-drop mixing was then attempted with a solution of 1 M ertapenem dissolved in mother liquor (0.2 M magnesium formate and 26% (w/v) PEG 3350). Five 0.1 nL drops of ertapenem were ejected at 5 Hz during the data collection for from the PolyPico machine.[9] This was for every 4 nL droplet of crystal slurry, leading to an 8x dilution of ertapenem concentration (125 mM). The drops of ertapenem from the PolyPico appeared consistently, with some interacting with the droplet of microcrystal slurry on the Kapton tape. A downside to this drop on drop method is that not every drop released from the PolyPico would interact with the drop of microcrystal slurry, reducing the substrate concentration upon mixing.[9] This, in addition to the high viscosity of the sample meant that no electron density in the difference map was visible in the active site that could correspond to ertapenem (**Figures 14 and 15**). The PolyPico itself, however, was able to work with minor glitches during the beam time which can be expected with a new sample delivery system.

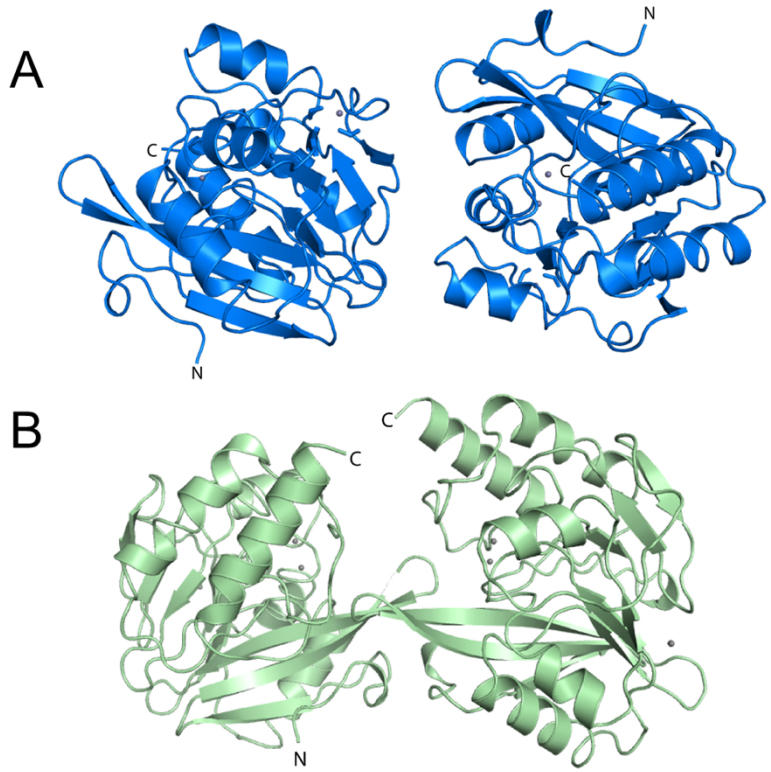


Figure 14: Asymmetric units of datasets collected from the SACLA beam time. Secondary structure is depicted as cartoons. A) Secondary structure of VIM-2 resting state data and B) Shows the secondary structure of VIM-2 after mixing with ertapenem. Note the different positioning of the molecules with the active sites facing away from each other in A and towards each other in B despite the fact that both were processed in the same space group (*C* 1 2 1).[33]

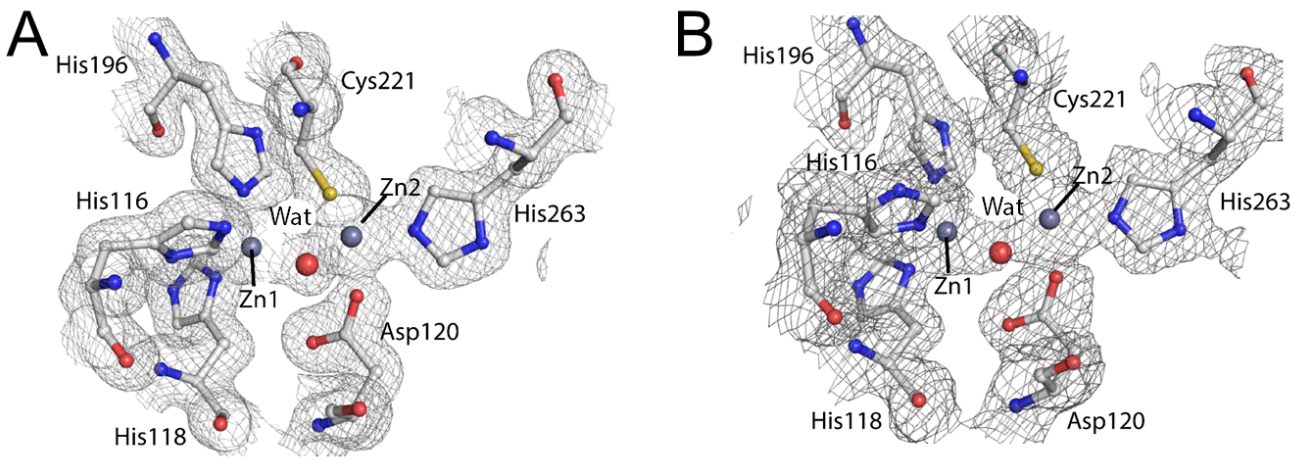


Figure 15: View from the VIM-2 active site from SACLA dataset. Significantly better resolution was observed for data collection in SACLA compare to a I24 Diamond Light Source data collection at room temperature. The $2mF_c$-DF_o map was contoured to 1σ. The bridging water was seen observed between the active site zinc ions. A) Is the T_0 dataset (resolution 1.7 Å) and B) is the data set collected after mixing the microcrystal slurry with ertapenem with a 300 mm/s belt speed (resolution 1.4 Å). Both datasets were processed in the same space group (*C* 1 2 1).[33]

	VIM-2 EuXFEL T_0	VIM-2: ertapenem 120 ms EuXFEL	VIM2: ertapenem SACLA	VIM-2 SACLA T_0	VIM-2 Fixed Target T_0
Beamline	SPB/SFX	SPB/SFX	BL2	BL2	I24
Temperature (K)	298	298	332	332	298
Space group	*I2*	*I2*	*C2*	*C2*	*C2*
Molecules/ASU	2	2	2	2	2
Total Reflections	75044	24566	5896522 (124606)	1384350 (42288)	672189 (12609)
Unique Reflections	75984 (1257)	11752 (30)	77652 (5354)	45095 (4518)	25033 (2494)
a b c (Å)	75.91 88.52 87.34	68.91 80.52 79.2	103.22 79.15 67.99	102.53 79.03 67.66	104.17 79.94 68.70
α β γ (°)	90.00 90.71 90.00	90.00 90.72 90.00	90 130.58 90	90.00 130.58 90.00	90.00 130.58 90.00
photon energy keV	10.5	10.5	10	10	12.8
Resolution (Å)	28.47 -1.49 (1.54 1.49)	21.19 - 1.36 (1.41 - 1.36)	39.2-1.4 (1.46 - 1.40)	31.32 -1.7(1.76 - 1.70)	52.18 - 2.1 (2.18 - 2.1)
R_{split}	50.92 (-622.38)	70.40 (145.40)	26.5 (98.30)	45.1 (109.70)	32.1 (73.40)
CC 1/2	82.01 (5.32)	23.9 (2.00)	93.5 (14.00)	78.1 (16.90)	89.2 (30.60)
I / σI	1.41	5.62	29.2 (1.10)	22.1 (1.20)	16.6 (3.40)
Completeness (%)	69.98 (10.40)	12.39 (0.30)	71.94 (25.99)	99.98 (99.98)	99.82 (99.28)
Multiplicity	12.55	3.00	116.69 (49.35)	36.08 (22.29)	26.82 (10.09)
Refinement					
Resolution (Å)	28.47 - 1.485	21.19 - 1.361	39.2 - 1.4	31.32 - 1.7	52.18 - 2.1
R_{work} / R_{free}	0.3010 0.3496	0.3133 0.3915	0.3102 0.3294	0.1927 0.2248	0.1980 0.2350
No. non-H atoms	3652	3676	3776	3935	3819
Protein	3469	3672	3672	3672	3594
Solvent	177		98	257	219
Ligand	6	4	6	6	6
B-factors (Å^2)	48.34	16.70	28.01	29.50	30.06
Protein	48.21	16.70	28.04	28.92	29.79
Solvent	51.06	22.39	27.47	38.02	34.68
Ligand	44.79		21.64	24.01	24.40
R.m.s. deviations					
Bond lengths (Å)	0.006	0.002	0.006	0.011	0.003
Bond angles (°)	0.75	0.54	0.65	1.07	0.51
Ramachandran Favoured (%)	87.77	95.41	96.94	98.03	97.38
Ramachandran outliers	2.18	0.87	0.44	0.44	0.44

Table 1: Data collection statistics for VIM-2 datasets. High resolution shell values are in brackets. R_{meas} was used for the cryo dataset.

Conclusions

Overall, it is clear that VIM-2, at least from some perspectives, is a good candidate for XFEL studies; it is clinically relevant and is capable of diffracting to high resolution. The studies report here show that slurries of VIM-2 microcrystals can be produced in a short period of time, that these crystals are relatively homogenous in size and can be produced in a highly concentrated form. Having homogenous, concentrated microcrystal slurries is important for XFEL data collection, as it not only improves hit rate, but ensures a more even diffusion of substrate throughout the microcrystal slurry.

Complete room temperature datasets have been collected for VIM-2 in its resting state, using two sample delivery methods (fixed target, Diamond Light Source 2.1 Å and ADE, SACLA 1.7 Å) and an incomplete resting state dataset was collected using a mixing jet. Despite the lack of success in getting a dataset with ertapenem in the active site, this should be possible to do with the right sample delivery system, crystallisation condition and a better understanding of substrate diffusion through crystals.

The first challenge is finding a condition that does not contain such a high concentration of PEG, which increases solution viscosity in comparison to water, this should enable the substrate to diffuse into the crystals and reach the active site more rapidly in addition to allowing easier dispensation of the microcrystal slurry. Finding a condition that produces crystals with less tight packing, could make it easier for substrates to diffuse through the solvent channels and enter the active site. Ideally, one would eventually develop multiple batch method conditions in order to produce crystals in separate space groups. Different space groups and crystal forms lead to different crystal packing which can affect the diffusion time for the substrate. Performing XFEL data collection on crystals of VIM-2 in different space groups could help in our understanding of diffusion in crystals by comparing and contrasting datasets and rates of substrate diffusion, something that would be useful for all crystallographers in regard to time resolved studies. Further developing the drop-on-drop PolyPico

system will help provide an option for mixing microcrystal slurries and substrates that uses small quantities of microcrystals and proteins.

The work described in this chapter and Chapter 3 used several different sample delivery methods (**Table 2**). The fixed target method not only used little sample comparatively, but also was simple to use, with sample change only taking a few minutes. However, currently, it is not possible to use mixing experiments using the fixed target method. The ADE method also does not require large quantities of a microcrystal slurry and there has been some progress with developing drop on drop mixing using ADE, however, larger quantities of substrate may need to be soaked into the microcrystal slurry droplets in order to obtain more enzyme: ligand structures.[34] Whilst mixing jets have been used in the past to collect datasets during β-lactamase reactions,[35] this method is not only wasteful in terms of the amount of protein (>200 mg) used but is also technically difficult to set up and fragile.[13,36,37] The jets are prone to clogging with high salt and viscous mother liquor and changing the nozzle can take a couple of hours. During a 12-hour shift of XFEL beamtime, this takes valuable time from data collection. Finding a durable method that is sample efficient is vital for performing regular mixing experiments.

Sample delivery method	Advantages	Disadvantages
ADE	Low sample consumption. Possible to do mixing experiments when you attach a PolyPico device.	Not user friendly, is complicated to maintain and set up. PolyPico ejects small droplets of substrate making it less likely that substrate will pass through the solvent channels.
Fixed Target	Low sample consumption. Easy to use and durable, any damaged chips can simply be replaced with a new one.	Currently not possible to do any enzyme: substrate mixing experiments.
Mixing Jets	Can do enzyme: substrate mixing experiments. High concentrations of substrate make it more likely substrate will pass through the crystals solvent channels	Not user friendly, is complicated to maintain and set up. Very high volumes and concentrations of microcrystal slurry needed to get a complete dataset.

Table 2. Table discussing the advantages and disadvantages of each sample delivery method mentioned in this chapter.

A key element of time resolved crystallography is understanding the kinetics of the reactions that are occurring in the crystals as the protein molecules are not in their native forms, affecting the turnover rate of the reaction and affinity. Obtaining data on the kinetics of ertapenem diffusion into the VIM-2 active site in crystals would be useful to validate kinetics parameters and define any intermediates that are observed in a given dataset. There are several ways that this may be done; one potential method would be to attach a fluorescent tag unto a substrate. The idea would be to use a fluorescent substrate where β-lactam hydrolysis can be monitored by changes in fluorescence. Substrates, such as BOCILLIN and FC5, have been developed previously to study PBPs and β-lactamases respectively.[38–

[40] BOCILLIN-FL is a derivative of penicillin with a boron-dipyrromethene (BODIPY) by modifying the side chain.[39,41] Unlike FC5 (a fluorescent cephalosporin[42]) the fluorescent probe in BOCILLIN-FL is not released upon binding, which makes it easier to detect any fluorescence inside a crystal for spectroscopic studies. Caged substrates and residues should also be investigated. Caged substrates are "inert substrates" that are activated upon their exposure to light whereas caged residues involve creating a photoactive residue in the protein active site that may trigger a reaction.[43–46]

References

(1) Nordmann, P.; Naas, T.; Poirel, L. Global Spread of Carbapenemase Producing *Enterobacteriaceae*. *Emerg. Infect. Dis.* **2011**, *17*, 1791–1798.

(2) Lagatolla, C.; Tonin, E. A.; Monti-Bragadin, C.; Dolzani, L.; Gombac, F.; Bearzi, C.; Edalucci, E.; Gionechetti, F.; Rossolini, G. M. Endemic Carbapenem-Resistant *Pseudomonas aeruginosa* with Acquired Metallo-Beta-Lactamase Determinants in European Hospital. *Emerg. Infect. Dis.* **2004**, *10*, 535–538.

(3) Zagorianou, A.; Sianou, E.; Iosifidis, E.; Dimou, V.; Protonotariou, E.; Miyakis, S.; Roilides, E.; Sofianou, D. Microbiological and Molecular Characteristics of Carbapenemase-Producing *Klebsiella Pneumoniae* Endemic in a Tertiary Greek Hospital during 2004-2010. *Eurosurveillance* **2012**, *17*, 20088.

(4) Poirel, L.; Naas, T.; Nicolas, D.; Collet, L.; Bellais, S.; Cavallo, J. D.; Nordmann, P. Characterization of VIM-2, a Carbapenem-Hydrolyzing Metallo-Beta-Lactamase and Its Plasmid- and Integron-Borne Gene from a *Pseudomonas Aeruginosa* Clinical Isolate in France. *Antimicrob. Agents Chemother.* **2000**, *44*, 891–897.

(5) Krajnc, A.; Brem, J.; Hinchliffe, P.; Calvopiña, K.; Panduwawala, T. D.; Lang, P. A.; Kamps, J. J. A. G.; Tyrrell, J. M.; Widlake, E.; Saward, B. G.; et al. Bicyclic Boronate VNRX-5133 Inhibits Metallo- and Serine-β-Lactamases. *J. Med. Chem.* **2019**, *62*, 8544–8556.

(6) Spence, J. C. H. XFELs for Structure and Dynamics in Biology. *IUCrJ* **2017**, *4*, 322–339.

(7) Johansson, L. C.; Stauch, B.; Ishchenko, A.; Cherezov, V. A Bright Future for Serial Femtosecond Crystallography with XFELs. *Trends Biochem. Sci.* **2017**, *42*, 749–762.

(8) Keating, G. M.; Perry, C. M. Ertapenem. *Drugs* **2005**, *65*, 2151–2178.

(9) Davy, B.; Axford, D.; Beale, J. H.; Butryn, A.; Docker, P.; Ebrahim, A.; Leen, G.; Orville, A. M.; Owen, R. L.; Aller, P. Reducing Sample Consumption for Serial Crystallography Using Acoustic Drop Ejection. *J. Synchrotron Radiat.* **2019**, *26*, 1820–1825.

(10) Parkova, A.; Lucic, A.; Krajnc, A.; Brem, J.; Calvopiña, K.; Langley, G. W.; McDonough, M. A.; Trapencieris, P.; Schofield, C. J. Broad Spectrum β-Lactamase Inhibition by a Thioether Substituted Bicyclic Boronate. *ACS Infect. Dis.* **2020**.

(11) Cahill, S. T.; Tarhonskaya, H.; Rydzik, A. M.; Flashman, E.; McDonough, M. A.; Schofield, C. J.; Brem, J. Use of Ferrous Iron by Metallo-β-Lactamases. *J. Inorg. Biochem.* **2016**, *163*, 185–193.

(12) Brem, J.; van Berkel, S. S.; Zollman, D.; Lee, S. Y.; Gileadi, O.; McHugh, P. J.; Walsh, T. R.; McDonough, M. A.; Schofield, C. J. Structural Basis of Metallo-β-Lactamase Inhibition by Captopril Stereoisomers. *Antimicrob. Agents Chemother.* **2016**, *60*, 142–150.

(13) Calvey, G. D.; Katz, A. M.; Schaffer, C. B.; Pollack, L. Mixing Injector Enables Time-Resolved Crystallography with High Hit Rate at X-Ray Free Electron Lasers. *Struct. Dyn.* **2016**, *3*, 054301.

(14) Overview https://www.xfel.eu/facility/overview/index_eng.html (accessed Nov 26, 2020).

(15) Zagorodnov, I.; Feng, G.; Limberg, T. Corrugated Structure Insertion for Extending the SASE Bandwidth up to 3% at the European XFEL. *Nucl. Instruments Methods Phys. Res. Sect. A Accel. Spectrometers, Detect. Assoc. Equip.* **2016**, *837*, 69–79.

(16) Mills, G.; Bean, R.; Mancuso, A. P. First Experiments in Structural Biology at the European X-Ray Free-Electron Laser. *Appl. Sci.* **2020**, *10*, 3642.

(17) Henrich, B.; Becker, J.; Dinapoli, R.; Goettlicher, P.; Graafsma, H.; Hirsemann, H.; Klanner, R.; Krueger, H.; Mazzocco, R.; Mozzanica, A.; et al. The Adaptive Gain Integrating Pixel Detector AGIPD a Detector for the European XFEL. *Nucl. Instruments Methods Phys. Res. Sect. A Accel. Spectrometers, Detect. Assoc. Equip.* **2011**, *633*, S11–S14.

(18) White, T. A.; Kirian, R. A.; Martin, A. V.; Aquila, A.; Nass, K.; Barty, A.; Chapman, H. N.; IUCr. *CrystFEL* : A Software Suite for Snapshot Serial Crystallography. *J. Appl. Crystallogr.* **2012**, *45*, 335–341.

(19) Mariani, V.; Morgan, A.; Yoon, C. H.; Lane, T. J.; White, T. A.; O'Grady, C.; Kuhn, M.; Aplin, S.; Koglin, J.; Barty, A.; et al. *OnDA* : Online Data Analysis and Feedback for Serial X-Ray Imaging. *J. Appl. Crystallogr.* **2016**, *49*, 1073–1080.

(20) White, T. A.; Barty, A.; Stellato, F.; Holton, J. M.; Kirian, R. A.; Zatsepin, N. A.; Chapman, H. N. Crystallographic Data Processing for Free-Electron Laser Sources. *Acta Crystallogr. Sect. D Biol. Crystallogr.* **2013**, *69*, 1231–1240.

(21) Duisenberg, A. J. M.; IUCr. Indexing in Single-Crystal Diffractometry with an Obstinate List of Reflections. *J. Appl. Crystallogr.* **1992**, *25*, 92–96.

(22) Leslie, A. G. W.; Powell, H. R. Processing Diffraction Data with Mosflm; Springer, Dordrecht, **2007**; pp 41–51.

(23) White, T. A. Processing Serial Crystallography Data with *CrystFEL* : A Step-by-Step Guide. *Acta Crystallogr. Sect. D Struct. Biol.* **2019**, *75*, 219–233.

(24) White, T. A.; Mariani, V.; Brehm, W.; Yefanov, O.; Barty, A.; Beyerlein, K. R.; Chervinskii, F.; Galli, L.; Gati, C.; Nakane, T.; et al. Recent Developments in *CrystFEL*. *J. Appl. Crystallogr.* **2016**, *49*, 680–689.

(25) Leslie, A. G. W.; IUCr. The Integration of Macromolecular Diffraction Data. *Acta Crystallogr. Sect. D Biol. Crystallogr.* **2006**, *62*, 48–57.

(26) White, T. A. Processing of XFEL Data; Humana Press, New York, NY, **2017**; pp 325–347.

(27) Barty, A.; Kirian, R. A.; Maia, F. R. N. C.; Hantke, M.; Yoon, C. H.; White, T. A.; Chapman, H.; IUCr. *Cheetah* : Software for High-Throughput Reduction and Analysis of Serial Femtosecond X-Ray Diffraction Data. *J. Appl. Crystallogr.* **2014**, *47*, 1118–1131.

(28) Yabashi, M.; Tanaka, H.; Ishikawa, T.; IUCr. Overview of the SACLA Facility. *J. Synchrotron Radiat.* **2015**, *22*, 477–484.

(29) Shintake, T.; Tanaka, T.; Hara, T.; Togawa, K.; Inagaki, T.; Kim, Y. J.; Ishikawa, T.; Kitamura, H.; Baba, H.; Matsumoto, H.; et al. Status of SPring-8 Compact SASE Source FEL Project. In *Nuclear Instruments and Methods in Physics Research, Section A: Accelerators, Spectrometers, Detectors and Associated Equipment*; North-Holland, **2003**; *507*, pp 382–387.

(30) Sauter, N. K.; Hattne, J.; Grosse-Kunstleve, R. W.; Echols, N. New Python-Based Methods for Data Processing. *Acta Crystallogr. Sect. D Biol. Crystallogr.* **2013**, *69*, 1274–1282.

(31) Brewster, A. S.; Young, I. D.; Lyubimov, A.; Bhowmick, A.; Sauter, N. K. *Processing Serial Crystallographic Data from XFELs or Synchrotrons Using the Cctbx.Xfel GUI*; **2019**; *10*.

(32) Mahon, B. P.; Kurian, J. J.; Lomelino, C. L.; Smith, I. R.; Socorro, L.; Bennett, A.; Hendon, A. M.; Chipman, P.; Savin, D. A.; Agbandje-McKenna, M.; et al. Microbatch Mixing: "Shaken Not Stirred", a Method for Macromolecular Microcrystal Production for Serial Crystallography. *Cryst. Growth Des.* **2016**, *16*, 6214–6221.

(33) DeLano, W. L. The PyMOL Molecular Graphics System. *Schrödinger LLC www.pymol.org* **2008**, http://www.pymol.org. https://doi.org/citeulike-article-id:240061.

(34) Fuller, F. D.; Gul, S.; Chatterjee, R.; Burgie, E. S.; Young, I. D.; Lebrette, H.; Srinivas, V.; Brewster, A. S.; Michels-Clark, T.; Clinger, J. A.; et al. Drop-on-Demand Sample Delivery for Studying Biocatalysts in Action at X-Ray Free-Electron Lasers. *Nat. Methods* **2017**, *14*, 443–449.

(35) Olmos, J. L.; Pandey, S.; Martin-Garcia, J. M.; Calvey, G.; Katz, A.; Knoska, J.; Kupitz, C.; Hunter, M. S.; Liang, M.; Oberthuer, D.; et al. Enzyme Intermediates Captured "on the Fly" by Mix-and-Inject Serial Crystallography. *BMC Biol.* **2018**, *16*, 59.

(36) DePonte, D. P.; Weierstall, U.; Schmidt, K.; Warner, J.; Starodub, D.; Spence, J. C. H.; Doak, R. B. Gas Dynamic Virtual Nozzle for Generation of Microscopic Droplet Streams. *J. Phys. D. Appl. Phys.* **2008**, *41*, 195505.

(37) Calvey, G. D.; Katz, A. M.; Pollack, L. Microfluidic Mixing Injector Holder Enables Routine Structural Enzymology Measurements with Mix-and-Inject Serial Crystallography Using X-Ray

Free Electron Lasers. *Anal. Chem.* **2019**, *91*, 7139–7144.

(38) June, C. M.; Vaughan, R. M.; Ulberg, L. S.; Bonomo, R. A.; Witucki, L. A.; Leonard, D. A. A Fluorescent Carbapenem for Structure Function Studies of Penicillin-Binding Proteins, β-Lactamases, and β-Lactam Sensors. *Anal. Biochem.* **2014**, *463*, 70–74.

(39) Zhao, G.; Meier, T. I.; Kahl, S. D.; Gee, K. R.; Blaszczak, L. C. BOCILLIN FL, a Sensitive and Commercially Available Reagent for Detection of Penicillin-Binding Proteins. *Antimicrob. Agents Chemother.* **1999**, *43*, 1124–1128.

(40) Park, M.; Sutherland, J. B.; Rafii, F. β-Lactam Resistance Development Affects Binding of Penicillin-Binding Proteins (PBPs) of Clostridium Perfringens to the Fluorescent Penicillin, BOCILLIN FL. *Anaerobe* **2020**, *62*, 102179.

(41) Schneider, K. D.; Bethel, C. R.; Distler, A. M.; Hujer, A. M.; Bonomo, R. A.; Leonard, D. A. Mutation of the Active Site Carboxy-Lysine (K70) of OXA-1 β-Lactamase Results in a Deacylation-Deficient Enzyme. *Biochemistry* **2009**, *48*, 6136–6145.

(42) van Berkel, S. S.; Brem, J.; Rydzik, A. M.; Salimraj, R.; Cain, R.; Verma, A.; Owens, R. J.; Fishwick, C. W. G.; Spencer, J.; Schofield, C. J. Assay Platform for Clinically Relevant Metallo-β-Lactamases. *J. Med. Chem.* **2013**, *56*, 6945–6953. https://doi.org/10.1021/jm400769b.

(43) Banala, S.; Arnold, A.; Johnsson, K. Caged Substrates for Protein Labeling and Immobilization. *ChemBioChem* **2008**, *9*, 38–41.

(44) Marriott, G.; Roy, P.; Jacobson, K. Preparation and Light-Directed Activation of Caged Proteins. *Methods Enzymol.* **2003**, *360*, 274–288.

(45) Swezey, R. R.; Epel, D. Caged Substrates for Measuring Enzymatic Activity in Vivo: Photoactivated Caged Glucose 6-Phosphate. *Methods Enzymol.* **1998**, *291*, 278–288.

(46) Mayer, G.; Hechel, A. Biologically Active Molecules with a “Light Switch.” *Angewandte Chemie - International Edition*., **2006**, pp 4900–4921.

Chapter 5 – Studies on Bicyclic Boronate Inhibitors with VIM-2

Some of the work described in this chapter has been reported in the academic literature.[1]

Abstract

Bicyclic boronates have shown considerable promise as inhibitors of both MBLs/SBLs and PBPs/transpeptidases, with several compounds showing broad-spectrum inhibitory activity against representatives of all classes of β-lactamases. All previously reported bicyclic boronates have an acylamino side chain, as present in penicillins and cephalosporins. This chapter describes work exploring the binding of three bicyclic boronates; one with a thioether sidechain and two with sulfonamide side chains, to better understand how this may affect inhibition of β-lactamases by boronates. Additional kinetic and microbiological studies are reported for the thioether boronate **3**. Crystal structures showed that all three compounds bind to the MBL VIM-2 in a comparable manner to previously studied 6,6-bicyclic boronates; the kinetics studies indicate that compound **3** has potential as a broad-spectrum inhibitor of both MBLs and SBLs.

Introduction

Despite the growth of antimicrobial resistance to β-lactam antibiotics due to the spread of MBLs and SBLs, there are currently no clinically useful broad spectrum β-lactamase inhibitors, i.e., those that inhibit most clinically relevant SBLs and MBLs. Several SBL and PBP inhibitors are available on the market such as clavulanic acid and sulbactam (**Figure 1**), these are administered together with β-lactam antibiotics in the form of combination therapy, e.g. amoxycillin and clavulanate in Augmentin (See Chapter 1 - Introduction).[2–4] All β-lactam based β-lactamase inhibitors have a narrow spectrum of activity being only capable of inhibiting some SBLs, notably class A SBLs, with little intrinsic broad spectrum activity.[2–4] Avibactam, the first non β-lactam β-lactamase inhibitor to enter the clinic (**Figure 1**), has a broader spectrum of activity but operates in the same way as previous β-lactamase inhibitors

by forming an acyl-enzyme complex with the nucleophilic serine of SBLs. Unlike with β-lactams however, the binding of avibactam is reversible.[5,6] Avibactam is not effective against MBLs and in some cases with SBLs (e.g. KPC-2) can be hydrolytically labile.[7] Because of this, it is critical that broad spectrum inhibitors against all three groups of enzymes, i.e. SBLs, MBLs, and transpeptidases are developed. One of the main challenges for the development of broad spectrum inhibitors is that MBLs are structurally and mechanistically unique compared to other β-lactamases (as well as PBPs/transpeptidases) therefore making it potentially difficult to develop inhibitors that effectively inhibit the various β-lactamase classes.[8,9] This makes a lack of broad spectrum inhibitors critical since many β-lactamases are co-expressed.[10]

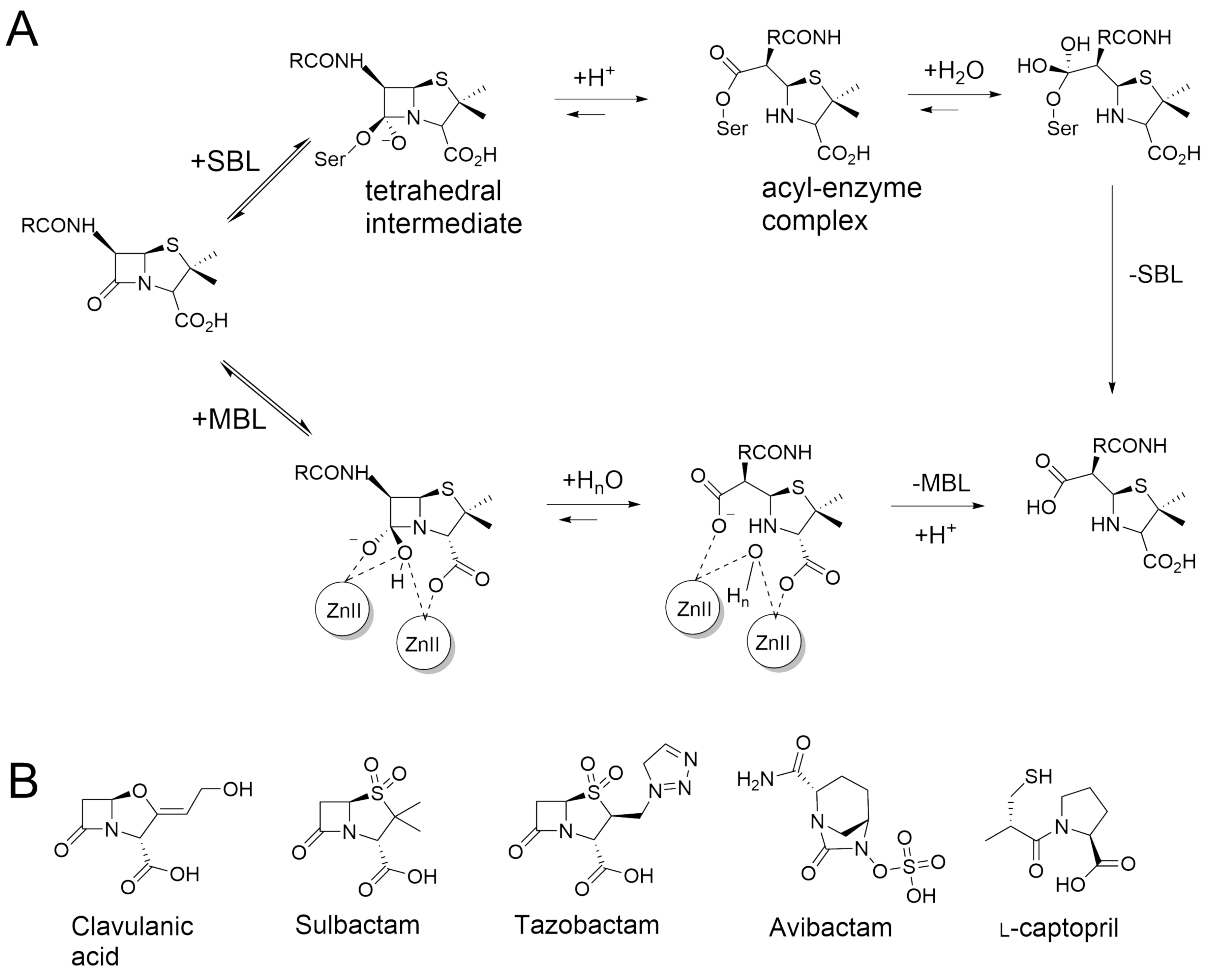


Figure 1: A) Outline of the SBL and MBL mechanisms with a penicillin substrate. (B) Clinically used SBL inhibitors (clavulanate, sulbactam, tazobactam, avibactam) which operate using acylation type mechanisms and L-captopril, a non-clinically used MBL inhibitor.[11]

Though there are differences in their respective mechanisms of the β-lactam hydrolysis, both SBLs and MBLs form a 'tetrahedral' intermediate with their substrates during the hydrolysis process.[12] It was therefore of interest to develop inhibitors that can successfully mimic this intermediate, which would then inhibit both groups of β-lactamases. Acyclic boronic acids (**Figure 2**) have previously shown promise as potential inhibitors of SBLs and PBPs.[13,14] Cyclic boronates have shown potential as broad spectrum inhibitors of β-lactamases, with the monocyclic boronate vaborbactam having been recently approved for clinical use. However, it has little efficacy against MBLs and extended spectrum SBLs (ESBLs).[15,16] Bicyclic boronates, such as taniborbactam (formerly VNRX-5133) and the cyclic boronate

2, previously developed in the Schofield group have been shown to inhibit several clinically important MBLs as well as SBLs and to a lesser extent PBPs (**Figure 2**).[17–20] Both taniborbactam and **2** have the standard acylamino side chain, as seen in cephalosporins and penicillins, little SAR studies have been done on potentially different side chains meaning further studies in this area are vital.

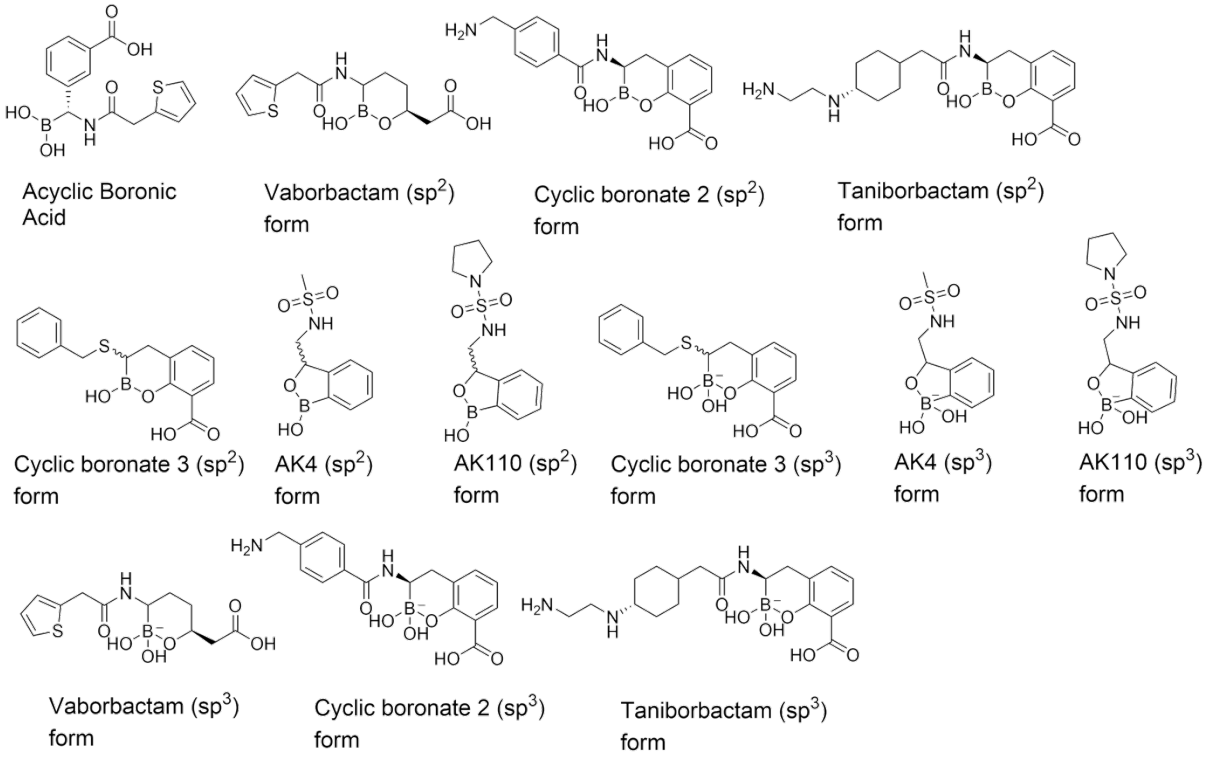


Figure 2: Boronate based β-lactamase inhibitors – the SBL inhibitor vaborbactam and the broader spectrum bicyclic boronates **2**, taniborbactam.[19–21] **3**, AK4 and AK110 are the subject of the current work. Note that both the penicillins, taniborbactam and **2** have an acylamino side chain.

In collaboration with the Latvian Institute of Organic Synthesis, the Schofield group has been studying a bicyclic boronate analogue bearing a thioether sidechain (**3**) instead of the 'usual' acylamino side chain.[1] Several kinetic, crystallographic and minimum inhibitory concentrations (MIC) studies have shown that cyclic boronate **3** has a broader range of inhibition than the previously reported compounds.[1]

In a separate, but related investigation line, two bicyclic boronates developed by Alen Krajnc (i.e., AK4 and AK110) were made (following high throughput screening by crystallography, unpublished data) to compare and contrast their interactions with those of **3** and other bicyclic boronates. These two boronates are, to date, unique in that they have a sulfonamide group; no potent β-lactam antibiotics / β-lactamase inhibitors with such a side chain have reported. Moreover, no carboxylate group is present on the second ring of the bicyclic boronate scaffolds of AK4 and AK110. Studying cyclic boronates with additions to their backbone allows scientists to explore which parts of the active site are the most important for tight binding. Overall, the results in this chapter show that further structural and solution studies need to be done on the bicyclic boronate scaffold to optimise binding and gain a deep understanding of the importance of the side chains in β-lactamase inhibition by bicyclic boronates.

Materials and Methods

Synthesis

The bicyclic boronates were synthesised by Dr. Anete Parkova (**3**) and Alen Krajnc (AK4 and AK110) as previously described. [1,20] Alen Krajnc's thesis has recently been submitted, which contains details about the synthesis of AK4 and AK110.

Protein Production and Purification

The purification of VIM-2 was performed as described in Chapter 2. The protein production was performed using Lemo21 (DE3) *E. coli* cells.

VIM-2 Crystallisation

Once VIM-2 was buffer exchanged into the appropriated crystallisation buffer (50 mM HEPES pH 7.5, 100 mM NaCl, 1 mM TCEP and 100 μM zinc chloride), crystal plates in the conditions mentioned in

Chapter 2 were set up. Once crystals appeared, soaking experiments were done with **3** (overnight)**,** AK4 (2 hours), and AK110 (30 minutes). The crystals were then harvested and cryo-cooled for data collection. Soaks during an overnight period were also done for compound **3.** AK4 and AK110 were soaked into the crystals for 40 minutes and overnight, respectively.

To obtain a high-resolution structure of VIM-2 complexed with **3** with clearer density, co-crystallisation experiments were set up. A 10 mM stock of **3** was added to 60 μL of VIM-2 to give a final concentration of 1 mM for the compound. The mixture was left on ice for 20 minutes and the 96-well crystallisation plate was set up as described in Chapter 2. An advantage of using co-crystallisation over soaking, is that the compound does not necessarily have to pass through any solvent channels in the crystal to reach the active site, rather they mix in solution beforehand.[22] This increases the likelihood of **3** binding to the active site of VIM-2. Since more molecules of VIM-2 may have the compound in the active site, this will lead to an improved occupancy / electron density map for the ligand, making it easier to observe its binding mode.

VIM-2 Data Collection and Refinement

Diffraction data for crystals were collected at (i) Diamond Light Source, and (ii) using an in-house diffractometer, i.e., a Rigaku FRE+ X-ray generator equipped with HF Varimax optics (300 μm collimator) and a Saturn 944+ CCD detector. Data collected at Diamond Light Source were processed as described in Chapter 2. Data collected in-house were processed manually using HKL2000.[23] The mtz files generated from this process were used for molecular replacement, which was done using a resting state model of VIM-2 (PDB: 4BZ3[11]) in Phaser software.[24] All refinements were done with phenix refine and the model building was done using COOT.[25,26]

Kinetic Studies

IC_{50} or pIC_{50} values are used to compare the efficacy of inhibitors are. To investigate if **3** is an inhibitor of β-lactamases, its pIC_{50} values needed to be determined. The IC_{50} values are the concentration of inhibitor that reduces the enzyme activity by half, with pIC_{50} value. IC_{50} values are calculated by adding increasing concentrations of the inhibitor to a solution of the enzyme being inhibited and a substrate. pIC_{50} values are the negative log of the IC_{50} value.[27] Therefore, the higher the pIC_{50} value is, the more potent the inhibitor. Ideally, to obtain information about the extent of inhibition the substrate and / or products would have a change in a property, such as absorption, that can be measured upon reaction.

The kinetic experiments for compound **3** were performed by Dr. Gareth Langley (of the Schofield group) using a reported method.[28] The substrate FC5 was used to measure changes in fluorescence that would be caused by the hydrolysis of the substrate when compound **3** was added to the enzyme substrate mixture.[28] FC5 is a fluorescent cephalosporin with an umbelliferone tag that is released upon hydrolysis giving a fluorescence readout. It is this fluorescence that is measured to monitor the effect inhibitors have on β-lactam hydrolysis. The fluorescence over time was measured using a Clariostar microplate reader (BMG Labtech); the results were used to calculate the pIC_{50} values as reported.[1] This protocol is not only suited for VIM-2 assays, but for a wide range of β-lactamase enzymes, comprising both MBLs and SBLs from all four Ambler classes. Experiments were also performed with established inhibitors to compare inhibitor efficacy. These included: avibactam, L-captopril (an MBL inhibitor), taniborbactam and cyclic boronate **2**.[1,5,11,19,20] Experiments involving OXA-10 and OXA-48 were performed in the presence and absence of sodium bicarbonate due to the lysine carbamylation that is required for OXA catalysis (**Figure 3**).[29]

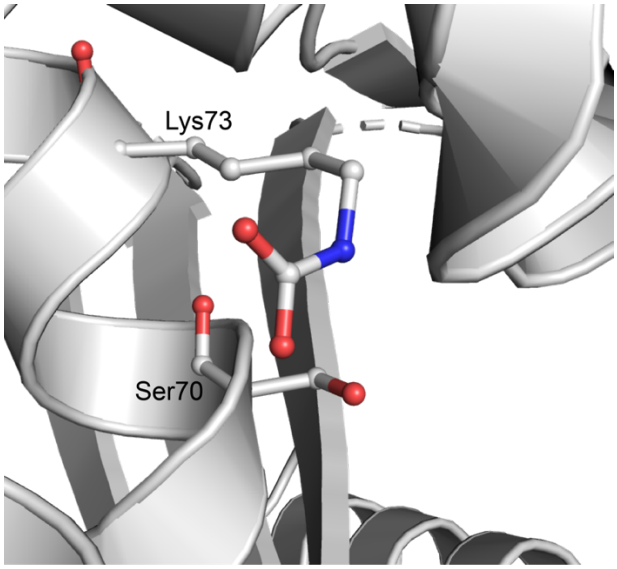


Figure 3: View from the active site of OXA-231 (PDB 6NZ8[30]). The active site lysine that is part of the SXXK motif is clearly carbamylated, which is a common feature of OXA SBLs.[31]

MIC Experiments

Minimum inhibitory concentration (MIC) experiments are microbiological experiments performed to test the lowest concentration of a drug or antimicrobial agent that prevents the visible growth of bacteria.[32] These can vary between different bacterial species for the same drug or inhibitor.[32] To measure the MIC values, separate solutions of bacteria are grown with different concentrations of the chemical in question. These results are then measured using a broth microdilution or agar dilution. The results can then be graded to three separate levels: susceptible, intermediate and resistant to an antimicrobial agent.[32]

The MIC experiments were performed by Dr. Karina Calvopiña (of the Schofield group) using an OXA-48 producing bacteria, *K. pneumoniae,* to assess its ability to restore the activity of meropenem. These results were compared with experiments performed with vaborbactam.[15] All experiments were performed in triplicate using microbroth dilution method in accordance with the CLSI guidelines.[33] Agar plates were incubated overnight at 37°C for 18 to 24 hours and the absorbance was measured at 600 nm using a ClarioSTAR plate reader.[1]

Results

Synthesis of boronates 3, AK4 and AK110

The thioether substituted cyclic boronate **3** was prepared *via* an eight-step stereoselective route from commercially available 3-methylsalicylic acid by Dr. Anete Parkova.[1] The synthesis gave the desired bicyclic boronate **3**, which was isolated as a mixture of (*R*/*S*)-enantiomers.[1,34] The estimation of the diastereoisomeric ratios for the stereoselective synthesis of **3** was performed by Alen Krajnc, along with the synthesis of AK4 and AK110. (thesis submitted)

Kinetics

3 was tested against several different β-lactamases (**Table 1**) from all four Ambler classes alongside previously developed inhibitors to compare of how effective **3** is as an inhibitor. Avibactam showed no inhibition against MBLs and L-captopril was not effective against SBLs, as anticipated based on its mode of action against MBLs.[7,11] It is clear from the results that **3** is effective against some members of all classes of β-lactamases (**Table 1**), but that the degree of inhibition varies between the different enzymes, something that was seen with previous bicyclic boronates. There are significant differences in the inhibition profiles for **2**, taniborbactam and **3** (**Table 1**). With the class A and C SBLs (TEM-116 and AmpC), **2** is more potent compared to **3** and taniborbactam against the A TEM-116 enzyme (pIC_{50} 8.5 compared to 6.7 with **3** and 6.92 with taniborbactam), but **3** is more potent than the other cyclic boronates against the AmpC enzyme from *P. aeruginosa* (pIC_{50} 7.8 compared to 6.9 with **2** and 6.5 with taniborbactam).

Notable results were also seen with the Class D OXA enzymes. Experiments with OXAs were done with and without sodium bicarbonate. This is because OXAs require carbamylated lysine residue for catalysis, which is formed in the presence of sodium bicarbonate or carbon dioxide.[29] Neither of the three bicyclic boronates were particularly potent against OXA-10 with or without sodium bicarbonate.

However, **3** was significantly more potent against OXA-48 (pIC_{50} 8.2) compared to **2** (pIC_{50} 4.6) and taniborbactam (pIC_{50} 6.3) as well as avibactam (pIC_{50} 6.2) (**Table 1**). This is important since OXA-48 is an ESBL with strong carbapenemase activity.[35] **3** also had a higher potency compared to **2** and taniborbactam with OXA-48 in the presence of sodium bicarbonate, with the pIC_{50} values being significantly higher when compared to taniborbactam and the acylamino cyclic boronate **2**. Further work is needed in this area, as recent studies have shown that different inhibitor classes have the potential to differently affect the carbamylation status of the active site lysine in OXA-inhibitor complexes.[29]

The results indicate that **3** has the ability to inhibit all subclasses of MBLs, further proving that bicyclic boronates can be effective broad-spectrum inhibitors for SBLs and MBLs.[18] **3** was considerably more potent against B1 MBLs compared to L-captopril (pIC_{50} 7.5 compared to 5.8).[1,11] When compared to **2**, however, **3** was of similar or reduced potency. In the case of NDM-1, the pIC_{50} was 7.4 with **3** but 7.5 with **2**. This is most likely due to slight variations in the active sites of these B1 MBLs, which may lead to differences in binding modes.[36,37] The increased potency of **3** compared to L-captopril was also seen with the monozinc B2 MBLs CphA, indicating that further SAR studies with regards to the side chain will expand the scope of potent inhibition by cyclic boronates against all three classes of MBLs.

pIC_{50} values						
Ambler Class	**β-Lactamase**	**avibactam[5] pIC_{50}**	**L-Captopril[11] pIC_{50}**	**3 pIC_{50}**	**2[19] pIC_{50}**	**Taniborbactam[20] pIC_{50}**
A	TEM-116	8.1	<3.4	6.7	8.5	6.92
B1	IMP-1	<3.4	5.0	6.9	6.0 (5.0)	5.6
B1	NDM-1	<3.4	5.8	7.4	7.5	8
B1	VIM-1	<3.4	5.6	7.1	7.0	8.1
B1	VIM-2	<3.4	6.1	7.2	8.5	9.3, 7.7
B2	CphA	<2.4	<5.0	6.3	>4	5.6
B3	L1	<4.7	5.6	5.3	Not inhibited	<5
C	AmpC (*P.aeruginosa*)	6.5	<4.4	7.8	6.9	6.5, 7.5
D	OXA-10	<4.7	<4.4	5.9	4.5	6.6
D	OXA-10 (+100mM $NaHCO_3$)	<4.7	<4.4	4.1	4.7 (5.2)	6.2
D	OXA-48	6.2	<4.4	8.2	4.6	6.3, 6.4
D	OXA-48 (+100mM $NaHCO_3$)	6.1	<4.4	8	4.8 (5.6)	5.6,

Table 1: pIC_{50} values for 3 with multiple SBLs and MBLs as well as pIC_{50} values for selected reported inhibitors. Inhibition assays for β-lactamases were performed as described.[19] The cephalosporin FC-5[28] was used as a substrate for VIM-1, VIM-2, IMP-1, NDM-1, SPM-1, TEM-116, OXA-10, and OXA-48; meropenem was used for CphA. Column 1 defines the Ambler class or MBL subclass of the β-lactamases used. Experiments involving inhibition of OXA-10 and OXA-48 by compound **2** were done with and without added bicarbonate. All *in vitro* assays except for taniborbactam, were freshly determined.[20]

Microbiology

MIC experiments were performed by Dr Karina Calvopiña using the *Klebsiella pneumoniae* NCTC 13442 strain, which produces OXA-48.[1] These experiments were done to assess whether **3** would be able to restore the antimicrobial activity of meropenem. The results were compared to those for vaborbactam. Meropenem on its own gave an MIC value of 4 μg mL^{-1} with the addition of vaborbactam having no effect. The addition of the thioether boronate **3** (concentration, 8 μg mL^{-1}) caused the

meropenem MIC value to drop to 1 μg mL^{-1}, which is in the susceptible range. These results further prove that additional studies of bicyclic boronates with different side chains will be important in developing potent, broad spectrum inhibitors of this class.

Crystallisation

Crystal structures were obtained with the three bicyclic boronates, i.e., compound **3,** AK110 and AK4, in complex with VIM-2. All three datasets were collected to high resolution (1.41 Å, 1.44 Å and 1.33 Å resolution respectively) at the Diamond Light Source and were auto processed using the software on iSpyB (**Table 2**).[39] Once this was completed, all three datasets were subjected to molecular replacement to solve their phase using Phaser and were refined using Phenix refine and COOT for manual model building.[24,25,40,41] CIF files were generated using ELBOW or Grade Web Server (**Table 2**).[42,43]

Structure Name	**VIM-2: 3 (PDB 6RPN)**	**VIM-2: AK110**	**VIM-2: AK4**
X-ray source (λ)	Rigaku FR-E+ Superbright (CuK_α)	I04-1 Diamond Light Source	I24 Diamond Light Source
Wavelength (Å)	1.54	0.9159	0.9686
Sample temperature (K)	100	100	100
Crystal size (μm)	150 x 50 x 50	100 x 50 x 75	200 x 50 x 50
Resolution range (Å)	31.34-1.41 (1.46-1.41) *	29.66-1.44 (1.491-1.44)*	49.76-1.33 (1.378-1.33)*
Space group	*C* 2	*I* 2 2 2	*C* 2
Unit cell (a, b, c) (Å)	101.081 79.155 67.746	63.653 74.086 78.739	100.462 79.210 67.218
Unit cell (α, β, γ) (°)	90, 130.3, 90	90 90 90	90 129.895 90
No. of reflections	75121 (6682) *	34047 (3375) *	92484 (9171)
R_{merge}	0.084 (0.365) *	0.086 (0.084) *	0.157 (1.506) *
I/σI	14.4 (1.85) *	20.2 (3.0) *	7.1 (1.5) *
CC1/2	0.725 (0.658) *	1.0 (0.9) *	1.0 (0.6) *
Completeness (%)	95.5 (85.1) *	99.9 (98.4) *	99.9 (97.2) *
Multiplicity	2.0 (1.4) *	13.2 (12.7) *	6.3 (6.2) *
Wilson B values ($Å^2$)	15.4	13.43	10.71
Refinement*			
R_{work}/R_{free}	0.1287/ 0.1556	0.1442/ 0.1747	0.2093/ 0.1828
Average B factors ($Å^2$)			
All Atoms	15.8	20.94	16.27
Enzyme Atoms	13.2	19.86	15.06
Ligand Atoms	22.4	16.21	21.40
Water Atoms	28.3	31.62	26.26
RMS Deviations			
Bond lengths (Å)	0.007	0.007	0.007
Bond angles (º)	1.086	0.91	0.97

Table 2: Data processing and refinement statistics for the VIM-2: Bicyclic boronate structures.

*Values from the highest resolution shell are in brackets.

Bicyclic Boronate 3

Initial soaking experiments with **3** showed some success, with electron density for compound **3** supporting **3'**s presence in the active site after 2 hours of soaking clearly being present. However, the density for the thioether side chain was poor, making it difficult to model the side chain and to determine the ratio of enantiomers are present in the structure. Several other attempts at soaking were performed, although little improvement was seen. It was thus decided that co-crystallisation should be attempted.

Crystals appeared in wells with a solution 0.2 M $MgCl_2$, 0.1 M Tris pH 8.25 and 25% (w/v) PEG 8000, with dimensions of approximately 150 µm x 50 µm x 30 µm.[1] The first crystal collected, diffracted to high resolution (1.41 Å), but partial oxidation of the Cys221 in the active site was observed. Such oxidation is well precedented in MBL structural biology, but its precise mechanism is unknown.[44] A new crystal plate was set up and a crystal was harvested from the same condition for data collection and diffracted to 1.44 Å resolution in the space group *C* 1 2 1 (**Table 2**). After performing molecular replacement (using a structure of VIM-2, PDB 4BZ3[11]) and refinement, it was clear that there were two molecules of VIM-2 in the asymmetric unit (**Figure 4**).

Moreover, the electron density showed evidence for the presence of both enantiomers (*R/S*) in the active site of both chains. Each of the enantiomers was refined to 50% occupancy in both molecules of the asymmetric unit. The electron density for **3** in both chains indicates that the 'tetrahedral' intermediate-type bicyclic boronate is in fact present (**Figure 5A**), as has been observed for structurally bicyclic boronates including **2** and taniborbactam.[18–20,45]

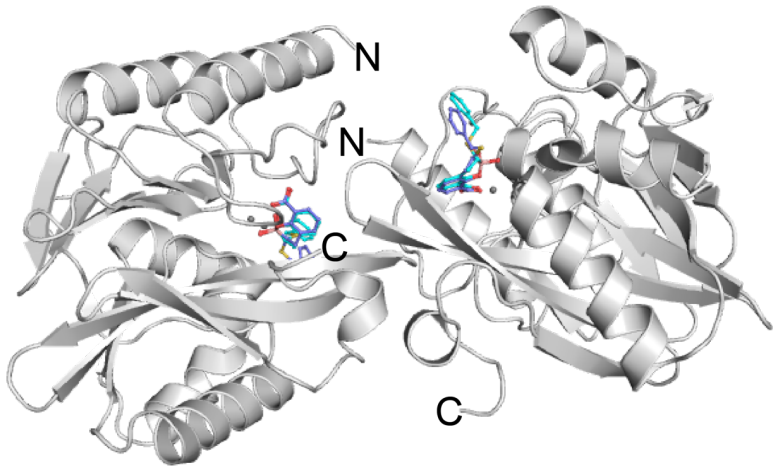


Figure 4: View from the asymmetric unit of VIM-2 complexed with 3, space *C* 1 2 1**.** Both enantiomers are modelled into the active site of both molecules in the asymmetric unit. PDB code: 6RPN.[1,31]

Upon analysis of the structure of VIM-2: **3**, it is clear that the binding modes of the bicyclic core and its carboxylate of **3** are very similar to structures reported for **2** and related compounds with VIM-2 and other MBLs such as NDM-1 (**Figure 5B**).[19,20,34] Unlike with taniborbactam, no evidence for tricyclisation[20] was observed crystallographically.

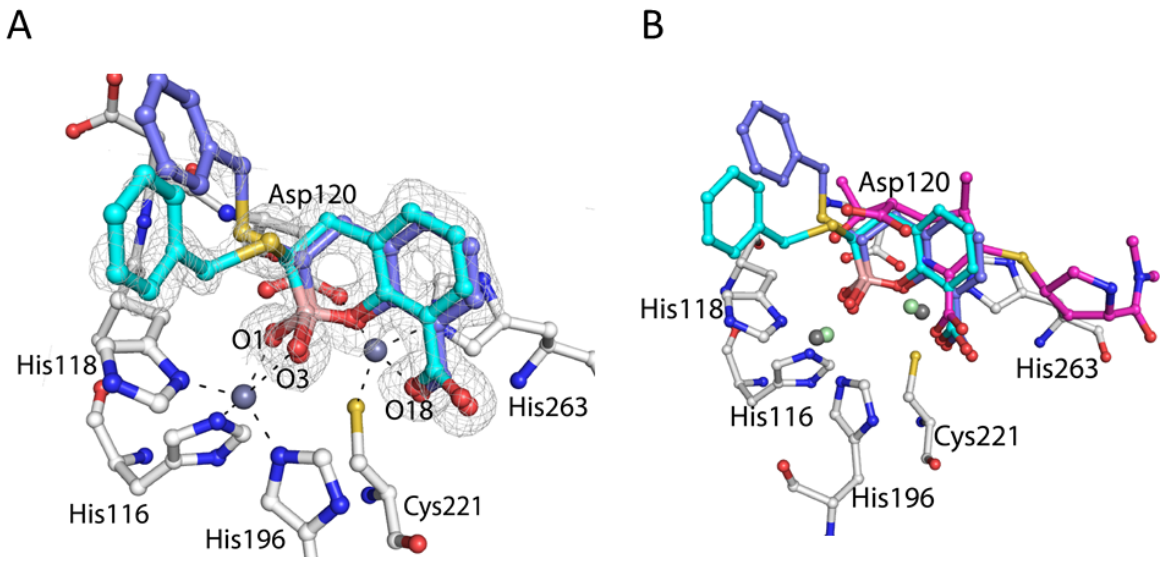


Figure 5: Mode of inhibition of the VIM-2 MBL by thioether 3. (A) View from a crystal structure of VIM-2 complexed with **3**. Both the (*R*)- (cyan) and (*S*)- (slate blue) enantiomers of **3** are observed in the structure. mF_o-DF_c OMIT electron density contoured to 3σ is shown as a grey mesh. Note: the density around the phenyl sidechain of **3** is weak in both the (*S*)- and (*R*)-enantiomers, likely due to the presence of multiple conformations. (B) Comparison of crystal structures of VIM-1 in complex with a meropenem derived product (pink)[47] along with the (*R*)-enantiomer (cyan) and the (*S*)-enantiomer (slate blue) of **3**. The zinc ions for VIM-1 (5N5I) are shown in green and in grey for VIM-2 (6RPN).[1,31,46]

Compared to the resting state structure of VIM-2 (4BZ3[11]), in the VIM-2: **3** structure there is significant zinc ion movement, with the distance increasing from ~ 3.5 Å as in the resting state to 4.3 Å as in 4BZ3[11] (**Figure 7B**). Moreover, the carboxylate oxygen atom HETATM O18 of **3** is positioned to coordinate Zn2 in the VIM-2 active site, as is the endocyclic boron ring oxygen. The observations are consistent with what has been observed in previous crystallographic and solution studies with bicyclic boronates, as well upon substrate binding (Chapter 2).[18–20,47] Movement of the L3 loop, which is important in VIMs, is also observed in the structure (**Figure 7A**).[37]

The overall binding mode of the bicyclic boronate core of **3** is very similar to the one observed for **2**,[19] although **2** binds at a slightly greater distance from the zinc ions compared to **3** (2.5Å compared to 2.3Å) (**Figure 7**).[19] Some similarities can be seen in the positioning of the side chains of **2** and **3**, with a similar binding mode to the acylamino side chain of cephalosporins and compound **2** (**Figure 6**). However, because **3** does not have the amido group that **2** has, there is no interaction between **3** and Asp119 (**Figure 8B**). Thus, the interaction between **3** and Asp119 is not essential for potent inhibition.

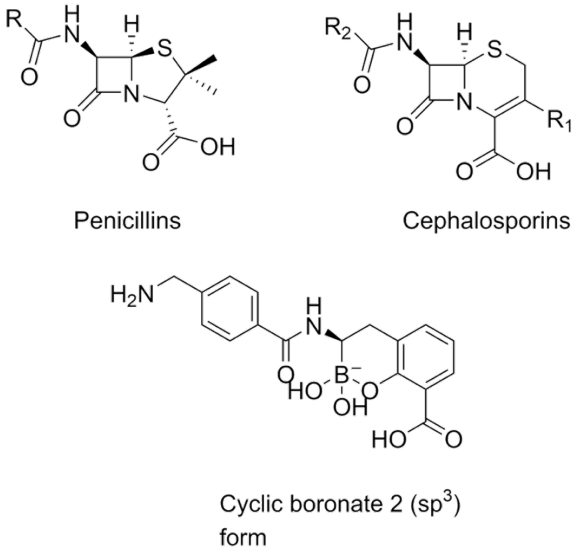


Figure 6: General structure of penicillins and cephalosporins compared to compound 2. Both of have an acylamino side chain, which is what has led to the development of bicyclic boronates with the same side chain.[19–21]

However, given the lower activity of **3** compared to **2** with regards to VIM-2**,** interaction with Asp119 could potentially promote binding. This lack of interaction with Asp119 potentially may affect inhibition potency of **3** compared to taniborbactam, and cyclic boronate **2.** There are also some similarities in the behaviour of the side chain and the non-zinc ion-ligating carboxylate oxygen (O19) for **2** and **3**. The carboxylate O19 atom in both boronates interacts with the amide nitrogen of the Asn233 main chain (**Figure 8A**).

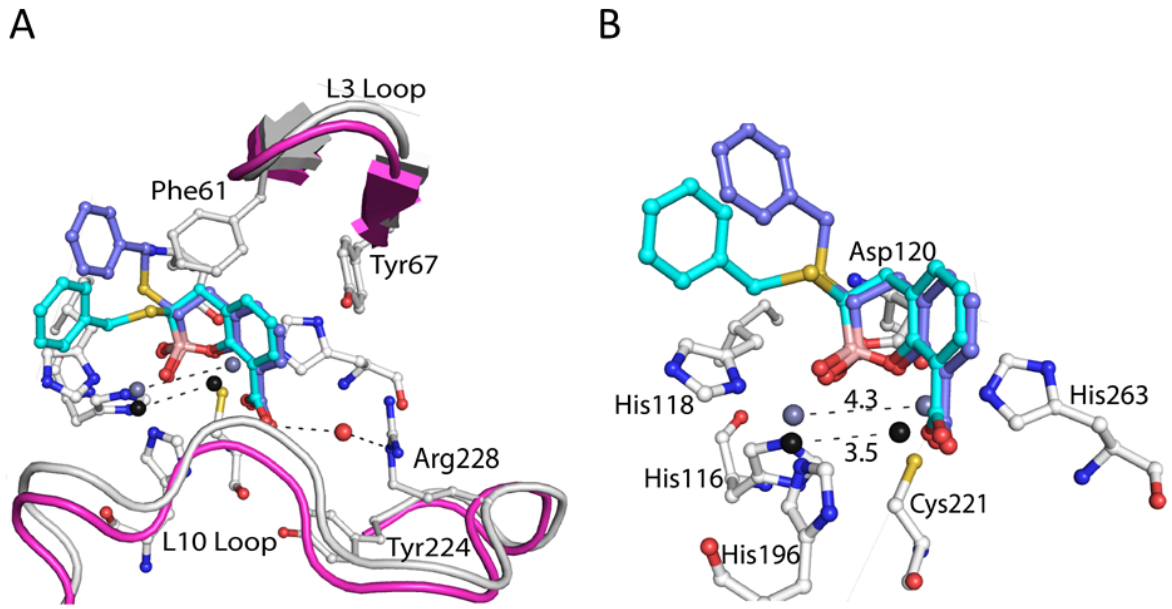


Figure 7: Comparison of the L3 and L10 loop conformations and zinc-zinc distances in the VIM-2 resting state (4BZ3[11]) (pink) and VIM-2 in complex with thioether 3 (white) (6RPN[1]). (A) Both L3 and L10 have shifted compared to the resting state structure (pink). (B) When **3** is bound to VIM-2, the zinc ions move further apart. VIM-2 (black, 3.5 Å) compared to VIM-2:**3** complex (grey, 4.3 Å).[31]

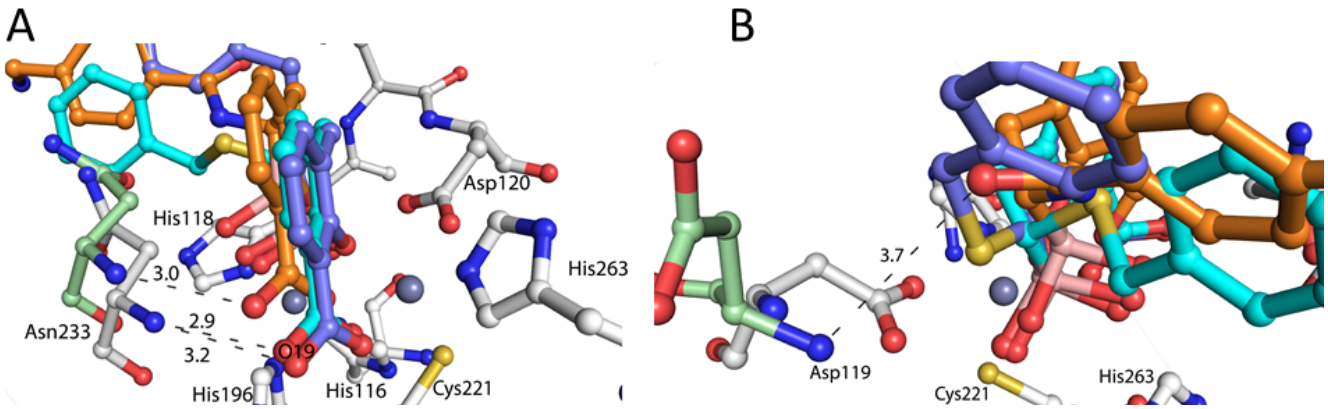


Figure 8: **Views from crystal structures of VIM-2 complexed the (*S*)- and (*R*)-enantiomers of 3 (blue and cyan respectively, 6RPN[1]) superimposed with 2 (orange, 5FQC[19]) a**. A) HETATM O18 of both **2** and **3** interacts with the main chain nitrogen of Asn233**.** B) The carbonyl group of the side chain in **2** interacts with the amide backbone NH of Asp119, unlike with **3**, due to the lack of acylamino side chain in the latter. Residues Asp119 and Asn233 from the VIM-2: **2** complex structure are coloured in green (PDB: 5FQC[19]).[31]

Structure of AK4 in complex with VIM-2

A crystal structure of VIM-2 with AK4 was obtained in a condition containing 0.2 M $MgCl_2$, 30% (w/v) PEG 8000 and 0.1 M Tris pH 7.25. The crystal diffracted to a high resolution (1.33 Å) in the space group *C* 1 2 1, with two protein molecules in the asymmetric unit (**Figure 10**), the same as observed with compound **3**. Upon refinement, it became clear that electron density corresponding to AK4 was present in the active site (**Figure 9**). The boron atom of the AK4 in both the active sites was in the sp^3 hybridised form, as indicated by the electron density.

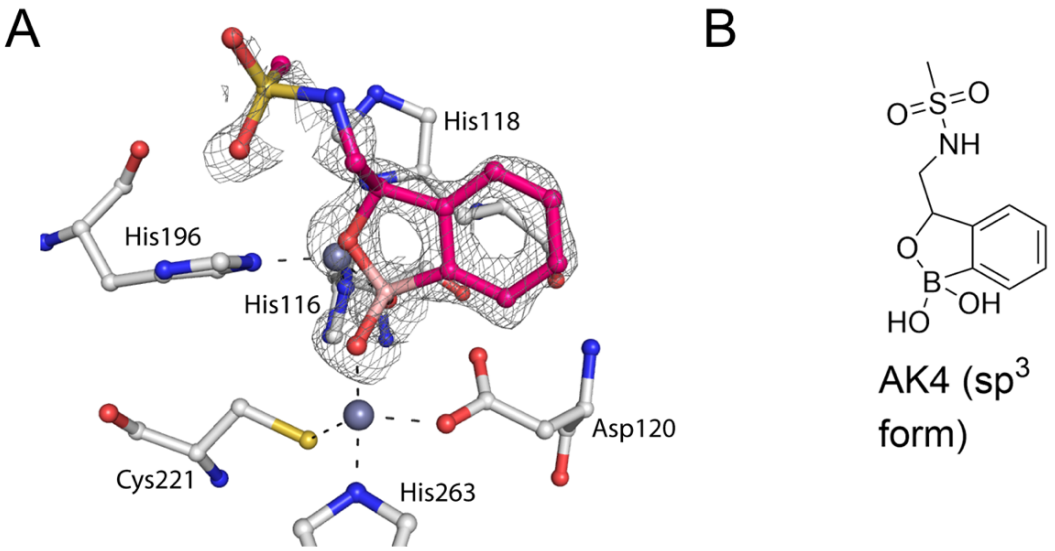


Figure 9: View from a crystal structure of VIM-2 complexed with the bicyclic boronate AK4. A) The mF_o-DF_c electron density map carved around AK4 contoured to 3σ, is shown as a grey mesh. The density around the side chain is clearly weaker compared to that surrounding the rest of the molecule. The lack of a carboxylate group in AK4, compared with **3** means there are fewer interactions with the zinc ions in the active site.[31] B) Schematic of AK4 (sp^3 form).

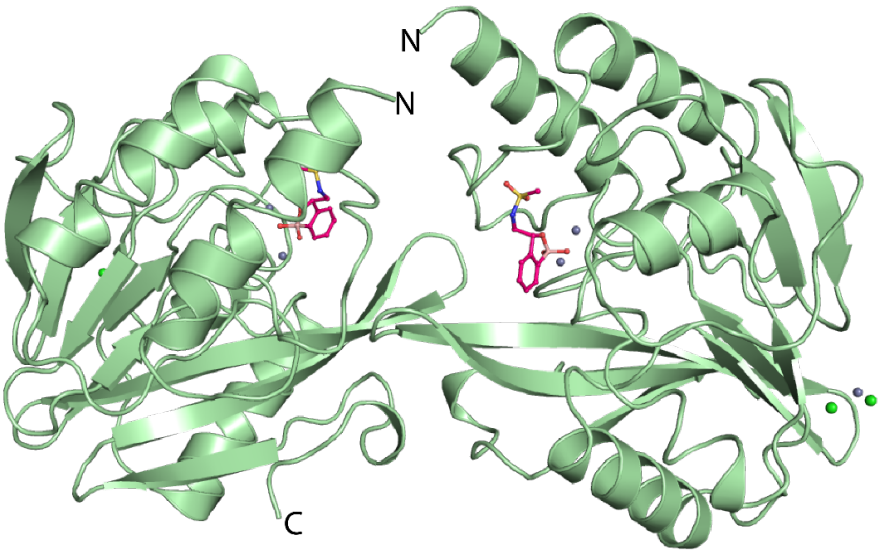


Figure 10: **Molecules in the asymmetric unit of VIM-2: AK4 structure**. Both this structure and the VIM-2: **3** complex structure are in the *C* 1 2 1 space group and have similar unit cells (**Table 2**).[31]

Comparing the structure of AK4 with that of compound **3**, it is clear that the two compounds make similar interactions. Both **3** and AK4 interact with the zinc ions in the VIM-2 active site. Moreover, both inhibitors interact with the amide of the Asn233 main chain, although AK4 interacts with the side chain in a way that is not seen with bicyclic boronate **3** (**Figure 11**)**.** No interactions are seen between AK4 and Asp119, due to the lack of an acylamino side chain on its bicyclic boronate structure. Hydrophobic interactions were also seen with residues and **2, 3** and taniborbactam on the L3 loop (Phe61 and Tyr67) and Trp87.

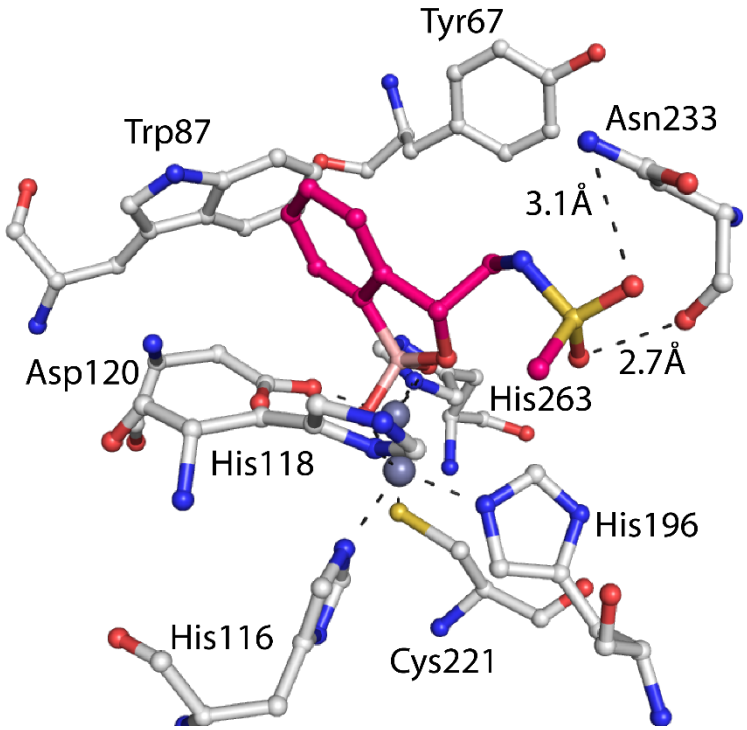


Figure 11: Interactions between VIM-2 and AK4 in the VIM-2 active site. The interactions observed are comparable with what was observed in the thioether **3:** VIM-2 complex structure, with Asn233 playing a key role in the enzyme inhibitor interaction.[31]

Structure of AK110 in complex with VIM-2

A crystal structure of VIM-2 complexed with the bicyclic boronate AK110 was also obtained. AK110 had the same sulfonamide side chain as AK4, but with an added pyrrolidine ring rather than a methyl group. Crystals appeared in the condition A11 of the new optimisation plate (0.2 M $MgCl_2$, 0.1 M Tris pH 7.0 and 32.5% (w/v) PEG 8000) and a dataset was collected to 1.44 Å in the space group *I* 2 2 2, with one protein molecule in the asymmetric unit. The data were processed using FastDP.[48] Upon refining the structure, it became clear that electron density corresponding to compound AK110 was present in the active site (**Figure 12**). The nucleophilic water that bridges the two zinc ions in the active site was clearly displaced due to the movement of the active site zincs, which is consistent with what was observed for previous bicyclic boronate structures **3** and AK4.[1]

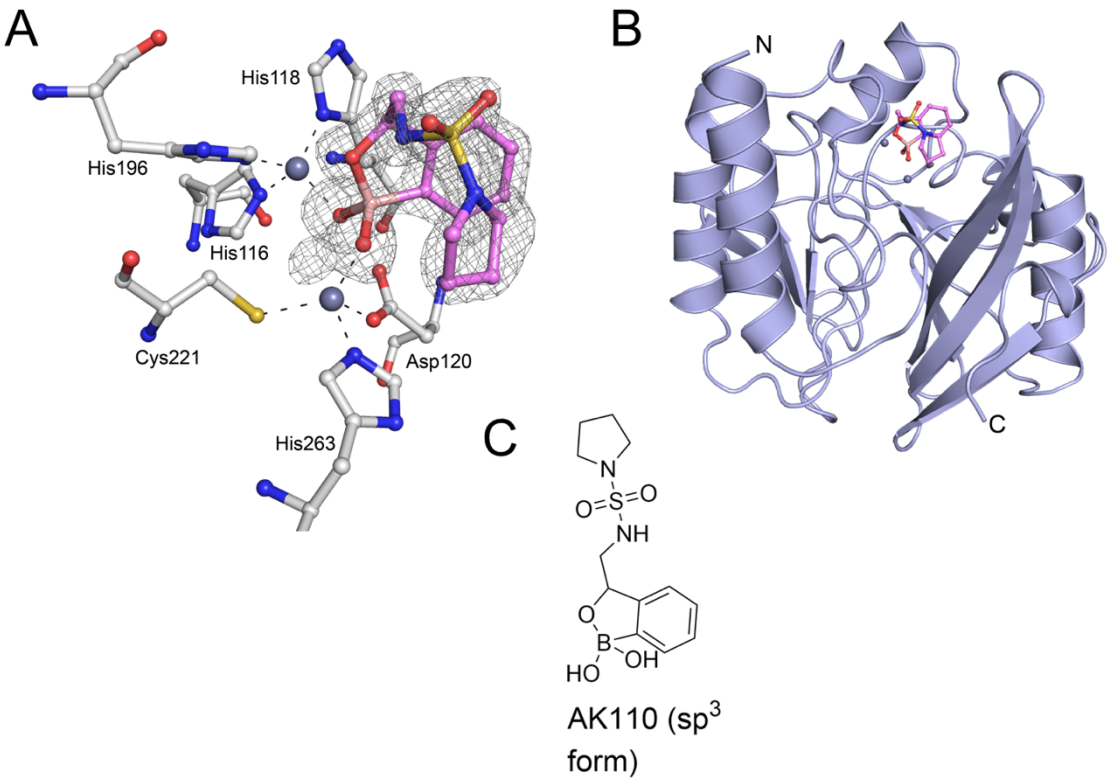


Figure 12: A) Views of from a structure of the VIM-2 active site complexed with AK110. A) The mF_c-DF_o density is shown in grey and is contoured to 3σ. B) The asymmetric unit of the VIM-2: AK110 structure. Unlike the other two structures (with **3** and AK4), there is only one protein molecule present in this asymmetric unit. The space group was *I* 2 2 2; see Table 2 for details.[31] C) Schematic of AK110 in its sp^3 form.

Upon analysis of the VIM-2: AK110 structure, it was clear that many of the interactions made by AK110 and VIM-2 are consistent with those for the other studied bicyclic boronates. The NH group of the Asn233 side chain is positioned to form polar interactions with the sulfonamide group of AK110, although the main chain oxygen of Asn233 does not interact with the side chain of AK110 as Asn233 does with AK4 (**Figure 13**). The carboxyl attached to the five membered *N*-ring of AK110 interacts with the zinc ions, as seen with **3** and AK4.[1] Hydrophobic interactions are observed between the side chain of AK110 and L3 residues (Phe61 and Tyr67) and Trp87 (**Figure 13**).

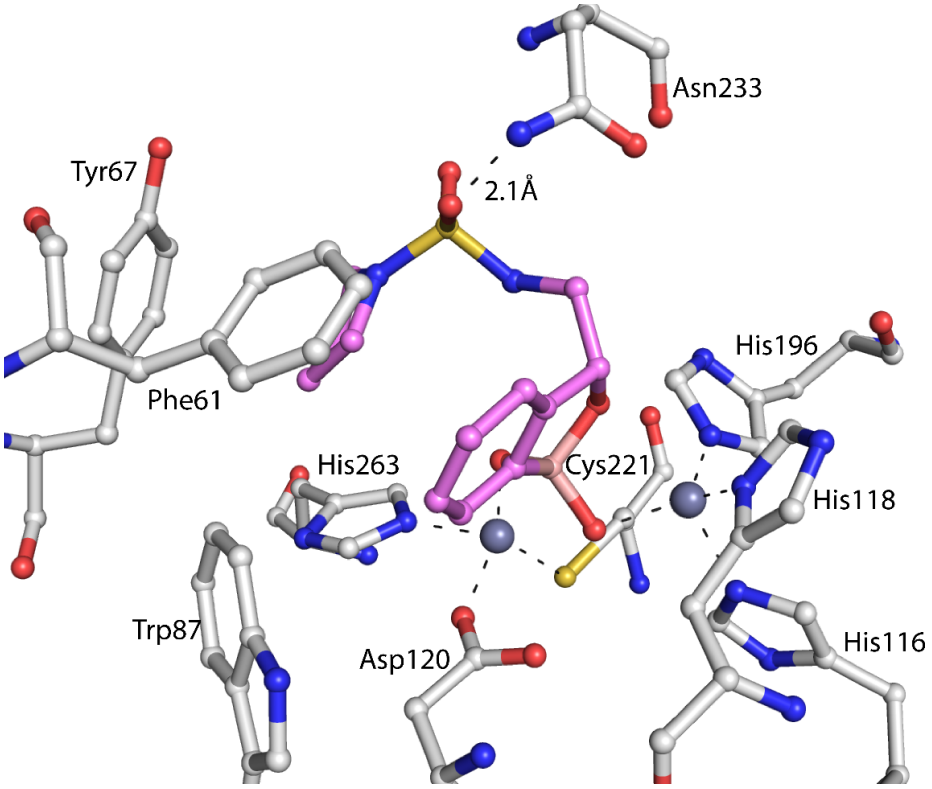


Figure 13: Interactions between AK110 and VIM-2. Note the lack of interactions between Asn233 main chain and AK110 when compared to the previous structures for β-lactamases with bicyclic boronates, despite the similar positioning of the side chain between AK4 and AK110.[1,19,20,31,34]

Conclusions

The combined crystallographic, kinetic and microbiological studies support previous work indicating that bicyclic boronates are capable of acting as broad-spectrum inhibitors of both SBLs and MBLs.[17,19,20,47] Several cases have shown that bicyclic boronates can undergo unexpected reactions, such as the formation of a tricyclic ring of taniborbactam in complex with NDM-1 (**Figure 14**).[20] However, as is the case here, most of the time the bicyclic boronates form a sp^3 hybridised complex with both SBLs and MBLs.

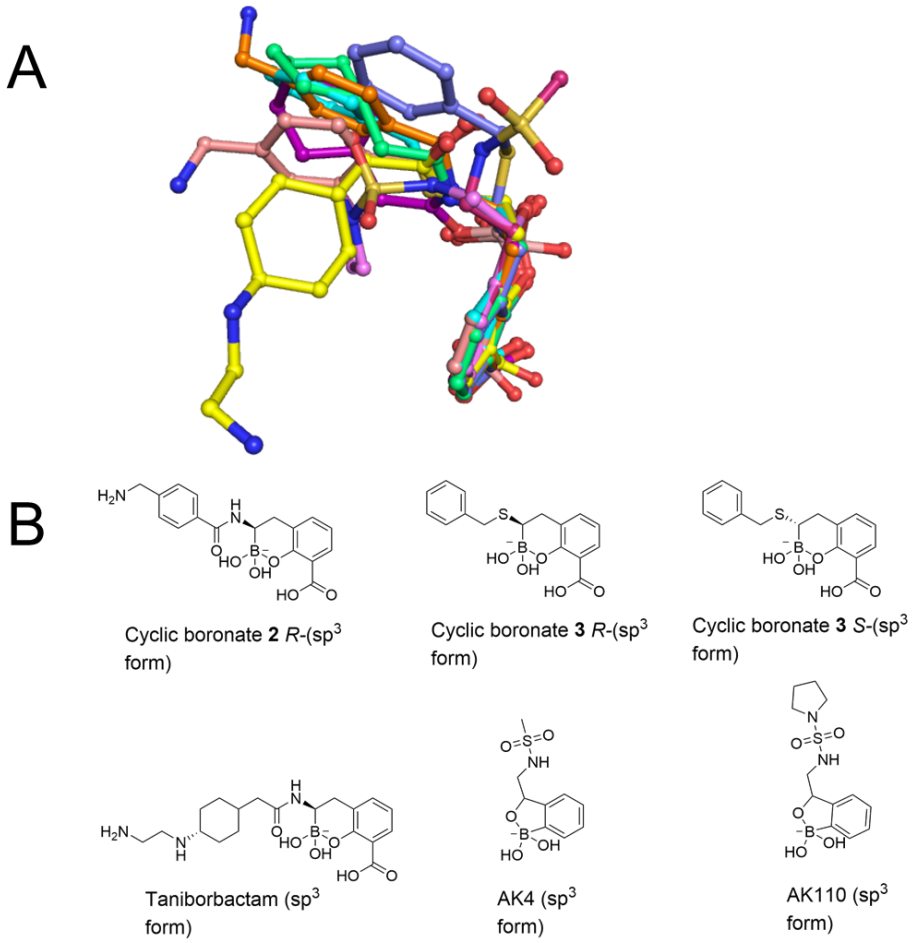


Figure 14: **Figure showing the different binding modes of various cyclic boronates in complex with β-lactamases and a PBP**. (A) conformations of the (*R*) and (*S*)-enantiomers of compound **3** in complex with VIM-2 are shown as cyan and blue respectively (PDB: 6RPN[1]); compound **2** bound to VIM-2 (5FQC[19]) shown in orange; compound **2** complexed with PBP5 (5J8X[19]) shown in pink; taniborbactam interacting NDM-1 (6RMF[20]) in its bicyclic and tricyclic forms, (Green and purple respectively); taniborbactam with OXA-10 (6RTN) in yellow;[19,20] Violet: VIM-2 bound to AK110 and dark pink indicates VIM-2 bound to AK4. The different side chain conformations observed imply that there is scope for optimisation to extend the spectrum of activity of cyclic boronates. All compounds are observed in the sp^3 form.[31]

Despite the limited structural studies on the potential side chains of bicyclic boronates in the academic literature,[1] the current study clearly shows that the alteration of the bicyclic boronate side chain can significantly affect the potency of a bicyclic boronate β-lactamase inhibitors (**Table 1**). Therefore, even

though **3** was less potent than **2** against some β-lactamases, **3** was more potent against others, most notably against the mono zinc ion B2 MBL CphA and the B3 MBL L1 (**Table 1**). The pIC_{50} assays, along with crystallographic and microbiological studies, demonstrate the potential of bicyclic boronates, with different types of side chain, for potent inhibition of all three subclasses of MBLs. Although **3** was a potent inhibitor in the biochemical assays, it was less potent than **2** in the cell-based activity assays potentially due to a lack of cell penetration.

Overall, these results indicate not only that further structure-activity relationship (SAR) studies are needed on the side chains of bicyclic boronates, but that it may also be useful to revisit side chain chemistry of the established types of β-lactam containing SBL/transpeptidase inhibitors, the SARs of which mostly reflects cell-based studies. A combination of kinetic, crystallographic and microbiological studies would give great insight into how alterations to the bicyclic boronates side chain affects inhibition. In addition, the crystallographic observations support the use of cyclic boronates as inhibitors of β-lactamases that have potential to both mimic binding of the β-lactamase substrates (the sp^2 boron form) and, once bound, the high energy 'tetrahedral' intermediates (sp^3 boron form) (**Figure 15**).

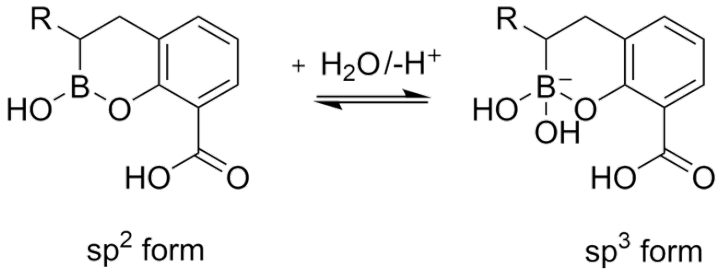


Figure 15: Scheme of sp^2 to sp^3 hybridisation as observed. Reported crystal structures of β-lactamases complexed with bicyclic boronates show the bicyclic boronate in the sp^3 form .[1,17,19,20,45]

In the case of clinically established β-lactam based class A SBL inhibitors, the range of C6 penicillin equivalent side chains is limited to either none or the hydroxyethyl chain, as seen in carbapenems.[49–51] The suggestion that further work on side chain optimisation should be done is supported by on-

going work concerning derivatives of avibactam, wherein substitution of the avibactam $CONH_2$ side chain has been shown to lead to improved activity, including with respect to conferring transpeptidase inhibition / antibacterial activity.[5,6]

References

(1) Parkova, A.; Lucic, A.; Krajnc, A.; Brem, J.; Calvopiña, K.; Langley, G. W.; McDonough, M. A.; Trapencieris, P.; Schofield, C. J. Broad Spectrum β-Lactamase Inhibition by a Thioether Substituted Bicyclic Boronate. *ACS Infect. Dis.* **2020**,

(2) Reading, C.; Cole, M. Clavulanic Acid: A Beta-Lactamase-Inhiting Beta-Lactam from Streptomyces Clavuligerus. *Antimicrob. Agents Chemother.* **1977**, *11*, 852–857.

(3) Campoli-Richards, D. M.; Brogden, R. N. Sulbactam/Ampicillin. *Drugs* **1987**, *33*, 577–609.

(4) Bryson, H. M.; Brogden, R. N. Piperacillin/Tazobactam. *Drugs* **1994**, *47*, 506–535.

(5) Ehmann, D. E.; Jahic, H.; Ross, P. L.; Gu, R.-F.; Hu, J.; Kern, G.; Walkup, G. K.; Fisher, S. L.; Designed, S. L. F.; Performed, G. K. W. Avibactam Is a Covalent, Reversible, Non-β-Lactam β-Lactamase Inhibitor. *PNAS* **2012**, *109*, 11663–11668.

(6) Wang, D. Y.; Abboud, M. I.; Markoulides, M. S.; Brem, J.; Schofield, C. J. The Road to Avibactam: The First Clinically Useful Non-β-Lactam Working Somewhat like a β-Lactam. *Future Med. Chem.* **2016**, *8*, 1063–1084.

(7) Abboud, M. I.; Damblon, C.; Brem, J.; Smargiasso, N.; Mercuri, P.; Gilbert, B.; Rydzik, A. M.; Claridge, T. D. W.; Schofield, C. J.; Frère, J.-M. Interaction of Avibactam with Class B Metallo-β-Lactamases. *Antimicrob. Agents Chemother.* **2016**, *60*, 5655–5662.

(8) Bush, K. Metallo-Beta-Lactamases: A Class Apart. *Clin. Infect. Dis.* **1998**, *27 Suppl 1*, S48-53.

(9) Walsh, T. R.; Toleman, M. A.; Poirel, L.; Nordmann, P. Metallo-Beta-Lactamases: The Quiet before the Storm? *Clin. Microbiol. Rev.* **2005**, *18*, 306–325.

(10) Weldhagen, G. F. Integrons and β-Lactamases—a Novel Perspective on Resistance. *Int. J.*

Antimicrob. Agents **2004**, *23*, 556–562.

(11) Brem, J.; van Berkel, S. S.; Zollman, D.; Lee, S. Y.; Gileadi, O.; McHugh, P. J.; Walsh, T. R.; McDonough, M. A.; Schofield, C. J. Structural Basis of Metallo-β-Lactamase Inhibition by Captopril Stereoisomers. *Antimicrob. Agents Chemother.* **2016**, *60*, 142–150.

(12) Lisa, M.-N.; Palacios, A. R.; Aitha, M.; González, M. M.; Moreno, D. M.; Crowder, M. W.; Bonomo, R. A.; Spencer, J.; Tierney, D. L.; Llarrull, L. I.; et al. A General Reaction Mechanism for Carbapenem Hydrolysis by Mononuclear and Binuclear Metallo-β-Lactamases. *Nat. Commun.* **2017**, *8*, 538.

(13) Zervosen, A.; Herman, R.; Kerff, F.; Herman, A.; Bouillez, A.; Prati, F.; Pratt, R. F.; Frère, J.-M.; Joris, B.; Luxen, A.; et al. Unexpected Tricovalent Binding Mode of Boronic Acids within the Active Site of a Penicillin-Binding Protein. *J. Am. Chem. Soc.* **2011**, *133*, 10839–10848.

(14) Morandi, F.; Caselli, E.; Morandi, S.; Focia, P. J.; Blázquez, J.; Shoichet, B. K.; Prati, F. Nanomolar Inhibitors of AmpC Beta-Lactamase. *J. Am. Chem. Soc.* **2003**, *125*, 685–695.

(15) Lomovskaya, O.; Sun, D.; Rubio-Aparicio, D.; Nelson, K.; Tsivkovski, R.; Griffith, D. C.; Dudley, M. N. Vaborbactam: Spectrum of Beta-Lactamase Inhibition and Impact of Resistance Mechanisms on Activity in Enterobacteriaceae. *Antimicrob. Agents Chemother.* **2017**, *61*.

(16) Langley, G. W.; Cain, R.; Tyrrell, J. M.; Hinchliffe, P.; Calvopiña, K.; Tooke, C. L.; Widlake, E.; Dowson, C. G.; Spencer, J.; Walsh, T. R.; et al. Profiling Interactions of Vaborbactam with Metallo-β-Lactamases. *Bioorg. Med. Chem. Lett.* **2019**, *29*, 1981–1984.

(17) Cahill, S. T.; Tyrrell, J. M.; Navratilova, I. H.; Calvopiña, K.; Robinson, S. W.; Lohans, C. T.; McDonough, M. A.; Cain, R.; Fishwick, C. W. G.; Avison, M. B.; et al. Studies on the Inhibition of AmpC and Other β-Lactamases by Cyclic Boronates. *Biochim. Biophys. Acta - Gen. Subj.* **2019**, *1863*, 742–748.

(18) Cahill, S. T.; Cain, R.; Wang, D. Y.; Lohans, C. T.; Wareham, D. W.; Oswin, H. P.; Mohammed, J.; Spencer, J.; Fishwick, C. W. G.; McDonough, M. A.; et al. Cyclic Boronates Inhibit All Classes of β-Lactamases. *Antimicrob. Agents Chemother.* **2017**, *61*.

(19) Brem, J.; Cain, R.; Cahill, S.; McDonough, M. A.; Clifton, I. J.; Jiménez-Castellanos, J.-C.; Avison, M. B.; Spencer, J.; Fishwick, C. W. G.; Schofield, C. J. Structural Basis of Metallo-β-Lactamase, Serine-β-Lactamase and Penicillin-Binding Protein Inhibition by Cyclic Boronates. *Nat. Commun.* **2016**, *7*, 12406.

(20) Krajnc, A.; Brem, J.; Hinchliffe, P.; Calvopiña, K.; Panduwawala, T. D.; Lang, P. A.; Kamps, J. J. A. G.; Tyrrell, J. M.; Widlake, E.; Saward, B. G.; et al. Bicyclic Boronate VNRX-5133 Inhibits Metallo- and Serine-β-Lactamases. *J. Med. Chem.* **2019**, *62*, 8544–8556.

(21) Liu, B.; E. Lee Trout, R.; Chu, G.-H.; McGarry, D.; W Jackson, R.; Hamrick, J.; Daigle, D.; Cusick, S.; Pozzi, C.; De Luca, F.; et al. Discovery of Taniborbactam (VNRX-5133): A Broad-Spectrum Serine- and Metallo-β-Lactamase Inhibitor for Carbapenem-Resistant Bacterial Infections. *J. Med. Chem.* **2019**.

(22) Hassell, A. M.; An, G.; Bledsoe, R. K.; Bynum, J. M.; Carter, H. L.; III; Deng, S.-J. J.; Gampe, R. T.; Grisard, T. E.; Madauss, K. P.; et al. Crystallization of Protein–Ligand Complexes. *Acta Crystallogr. Sect. D Biol. Crystallogr.* **2007**, *63*, 72.

(23) Gewirth, D.; Otwinowski, Z.; Minor, W. *THE HKL MANUAL Denzo XDisplayF Scalepack An Oscillation Data Processing Suite for Macromolecular Crystallography*.

(24) McCoy, A. J.; Grosse-Kunstleve, R. W.; Adams, P. D.; Winn, M. D.; Storoni, L. C.; Read, R. J.; IUCr. *Phaser* Crystallographic Software. *J. Appl. Crystallogr.* **2007**, *40*, 658–674.

(25) Emsley, P.; Cowtan, K.; IUCr. *Coot* : Model-Building Tools for Molecular Graphics. *Acta Crystallogr. Sect. D Biol. Crystallogr.* **2004**, *60*, 2126–2132.

(26) Afonine, P. V.; Grosse-Kunstleve, R. W.; Echols, N.; Headd, J. J.; Moriarty, N. W.; Mustyakimov, M.; Terwilliger, T. C.; Urzhumtsev, A.; Zwart, P. H.; Adams, P. D. Towards Automated Crystallographic Structure Refinement with *Phenix.Refine*. *Acta Crystallogr. Sect. D Biol. Crystallogr.* **2012**, *68*, 352–367.

(27) Stewart, M. J.; Watson, I. D. Standard Units for Expressing Drug Concentrations in Biological Fluids. *Br. J. Clin. Pharmacol.* **1983**, *16*, 3–7.

(28) van Berkel, S. S.; Brem, J.; Rydzik, A. M.; Salimraj, R.; Cain, R.; Verma, A.; Owens, R. J.; Fishwick, C. W. G.; Spencer, J.; Schofield, C. J. Assay Platform for Clinically Relevant Metallo-β-Lactamases. *J. Med. Chem.* **2013**, *56*, 6945–6953.

(29) Golemi, D.; Maveyraud, L.; Vakulenko, S.; Samama, J. P.; Mobashery, S. Critical Involvement of a Carbamylated Lysine in Catalytic Function of Class D Beta-Lactamases. *Proc. Natl. Acad. Sci. U. S. A.* **2001**, *98*, 14280–14285.

(30) VU, A.; EE, L.; FNDC, V.; Y, L. de L. S.; RJ, O.; N, L.; CS, F.; N, D.; A, M.; DC, F. Importance of the B5-B6 Loop for the Structure, Catalytic Efficiency, and Stability of Carbapenem-Hydrolyzing Class D β-Lactamase Subfamily OXA-143. *Biochemistry* **2019**, *58*.

(31) DeLano, W. L. The PyMOL Molecular Graphics System. *Schrödinger LLC www.pymol.org* **2008**, http://www.pymol.org. https://doi.org/citeulike-article-id:240061.

(32) Andrews, J. M. Determination of Minimum Inhibitory Concentrations. *J. Antimicrob. Chemother.* **2001**, *48*, 5–16.

(33) *M100 Performance Standards for Antimicrobial Susceptibility Testing An Informational Supplement for Global Application Developed through the Clinical and Laboratory Standards Institute Consensus Process*.

(34) Lang, P. A.; Parkova, A.; Leissing, T. M.; Calvopiña, K.; Cain, R.; Krajnc, A.; Panduwawala, T. D.; Philippe, J.; Fishwick, C. W. G.; Trapencieris, P.; et al. Bicyclic Boronates as Potent Inhibitors of AmpC, the Class C β-Lactamase from Escherichia Coli. *Biomolecules* **2020**, *10*.

(35) Poirel, L.; Potron, A.; Nordmann, P. OXA-48-like Carbapenemases: The Phantom Menace. *J. Antimicrob. Chemother.* **2012**, *67*, 1597–1606.

(36) Bebrone, C. Metallo-β-Lactamases (Classification, Activity, Genetic Organization, Structure, Zinc Coordination) and Their Superfamily. *Biochem. Pharmacol.* **2007**, *74*, 1686–1701.

(37) Makena, A.; Düzgün, A. O. ¨; Brem, J.; Mcdonough, M. A.; Rydzik, A. M.; Abboud, M. I.; Saral, A. A.; Ays¸egül, A.; Çiçek, Ç.; Sandalli, C.; et al. Comparison of Verona Integron-Borne Metallo-Lactamase (VIM) Variants Reveals Differences in Stability and Inhibition Profiles. **2016**.

(38) Bebrone, C. *Metallo-β-Lactamases (Classification, Activity, Genetic Organization, Structure, Zinc Coordination) and Their Superfamily*; **2007**; *74*.

(39) Fisher, S. J.; Levik, K. E.; Williams, M. A.; Ashton, A. W.; McAuley, K. E.; IUCr. *SynchWeb* : A Modern Interface for *ISPyB*. *J. Appl. Crystallogr.* **2015**, *48*, 927–932.

(40) Adams, P. D.; Afonine, P. V.; Bunkóczi, G.; Chen, V. B.; Davis, I. W.; Echols, N.; Headd, J. J.; Hung, L.-W.; Kapral, G. J.; Grosse-Kunstleve, R. W.; et al. *PHENIX* : A Comprehensive Python-Based System for Macromolecular Structure Solution. *Acta Crystallogr. Sect. D Biol. Crystallogr.* **2010**, *66*, 213–221.

(41) Afonine, P. V.; Grosse-Kunstleve, R. W.; Echols, N.; Headd, J. J.; Moriarty, N. W.; Mustyakimov, M.; Terwilliger, T. C.; Urzhumtsev, A.; Zwart, P. H.; Adams, P. D. Towards Automated Crystallographic Structure Refinement with *Phenix.Refine*. *Acta Crystallogr. Sect. D Biol. Crystallogr.* **2012**, *68*, 352–367.

(42) Moriarty, N. W.; Grosse-Kunstleve, R. W.; Adams, P. D.; IUCr. *Electronic Ligand Builder and Optimization Workbench* (*ELBOW*): A Tool for Ligand Coordinate and Restraint Generation. *Acta Crystallogr. Sect. D Biol. Crystallogr.* **2009**, *65*, 1074–1080.

(43) Grade Web Server http://grade.globalphasing.org/cgi-bin/grade/server.cgi (accessed Jan 3, 2021).

(44) Garcia-Saez, I.; Docquier, J.-D.; Rossolini, G. M.; Dideberg, O. The Three-Dimensional Structure of VIM-2, a Zn-β-Lactamase from Pseudomonas Aeruginosa in Its Reduced and Oxidised Form. *J. Mol. Biol.* **2008**, *375*, 604–611.

(45) Lang, P. A.; Parkova, A.; Leissing, T. M.; Calvopiña, K.; Cain, R.; Krajnc, A.; Panduwawala, T. D.; Philippe, J.; Fishwick, C. W. G.; Trapencieris, P.; et al. Bicyclic Boronates as Potent Inhibitors of AmpC, the Class C B-lactamase from Escherichia Coli. *Biomolecules* **2020**, *10*, 1–15.

(46) Salimraj, R.; Hinchliffe, P.; Kosmopoulou, M.; Tyrrell, J. M.; Brem, J.; van Berkel, S. S.; Verma, A.; Owens, R. J.; McDonough, M. A.; Walsh, T. R.; et al. Crystal Structures of VIM-1 Complexes Explain Active Site Heterogeneity in VIM-Class Metallo-β-Lactamases. *FEBS J.* **2019**, *286*, 169–

183.

(47) Krajnc, A.; Lang, P. A.; Panduwawala, T. D.; Brem, J.; Schofield, C. J. Will Morphing Boron-Based Inhibitors Beat the β-Lactamases? *Curr. Opin. Chem. Biol.* **2019**, *50*, 101–110.

(48) Winter, G. *Xia2* : An Expert System for Macromolecular Crystallography Data Reduction. *J. Appl. Crystallogr.* **2010**, *43*, 186–190.

(49) Bush, K.; Bradford, P. A. β-Lactams and β-Lactamase Inhibitors: An Overview. *Cold Spring Harb. Perspect. Med.* **2016**, *6*.

(50) Singh, G. S. Beta-Lactams in the New Millennium. Part-I: Monobactams and Carbapenems. *Mini Rev. Med. Chem.* **2004**, *4*, 69–92.

(51) GS, S. β-Lactams in the New Millennium. Part-II: Cephems, Oxacephems, Penams and Sulbactam. *Mini-Reviews Med. Chem.* **2004**, *4*, 93–109.

Chapter 6 - Discussion and Future Work

In recent times, the field of antibiotic development has received relatively little attention in comparison to other areas of medical research, such as cancer treatment and genetic manipulation.[1] In part, this may be due a lack of financial incentive as well as the seemingly inevitable long-term failure of any new antibiotic; once an antibiotic starts to be used in the clinic or in agriculture, bacteria will always eventually develop a mechanism of resistance.[1] The lack of antibiotic development makes research in the area of resistance to existing antibiotic drugs of critical importance, with millions of deaths predicted to be caused by a lack of effective antimicrobials every year by 2050.[2,3] To date, no single antibiotic compound has demonstrated the ability to inhibit both mechanistic groups of β-lactamases, i.e. serine- and metallo-β-lactamases, and penicillin binding proteins.[4] The work described in this thesis has set out to answer the following questions: How do MBLs catalyse hydrolysis of the clinically important carbapenem family of β-lactams? What can we do to further understand our mechanistic understanding of β-lactamases? What needs to be done to produce improved broad spectrum β-lactamase inhibitors? Considerable progress has been made in answering these questions, but further work is still needed, as outlined in this chapter.

Carbapenems and Penems

Understanding the hydrolysis of β-lactam antibiotics may be key to the development of effective, broad spectrum resistance combatting agents. It is clear from the literature studies that penems and carbapenems have demonstrated clinically useful properties as antibiotics as well as being β-lactamase substrates and, in some cases, inhibitors. As described in Chapter 2, both faropenem and biapenem can be hydrolysed to give multiple products with the amounts and product identities depending on the particular β-lactamase enzyme. In most cases, an enamine is the likely major nascent product, which is formed due by active site mediated protonation of the β-lactam ring derived

nitrogen; this can then be converted to an imine product upon the tautomerisation of the enamine. In some cases, enamine-imine tautomerisation may occur at the active site.

With faropenem, further potential for reaction is possible due to the potential of its THF ring to be opened (**Figures 1 and 2**). No C5/C6 fragmentation of faropenem was observed with the transpeptidase Ldt_{Mt2}.[5] Moreover, no lactone products were observed with class D SBLs and faropenem, indicating that lactone formation is a phenomenon associated with class D SBL mediated reaction with carbapenems.[6] The reason for the lack of β-lactone formation with faropenem may relate to the conformation of the C6 hydroxyethyl group in the acyl-enzyme complex, which may differ for carbapenems versus penems. With carbapenems, β-lactone formation is favoured by the presence of a C1 β-methyl group, though with some class D SBLs, β-lactone formation may occur without a C1 β-methyl group.[6] Further work thus needs to be carried out to investigate the molecular basis for this difference. However, if β-lactone formation is indeed an important resistance mechanism as has been proposed, use of penems may be a way to overcome it. The formation of multiple products with penems and carbapenems should also be further pursued and studied - it is of interest to see if one or more of these compounds could be an inhibitor of MBLs (perhaps most likely *via* active site Zn(II) chelation), SBLs, or transpeptidases.

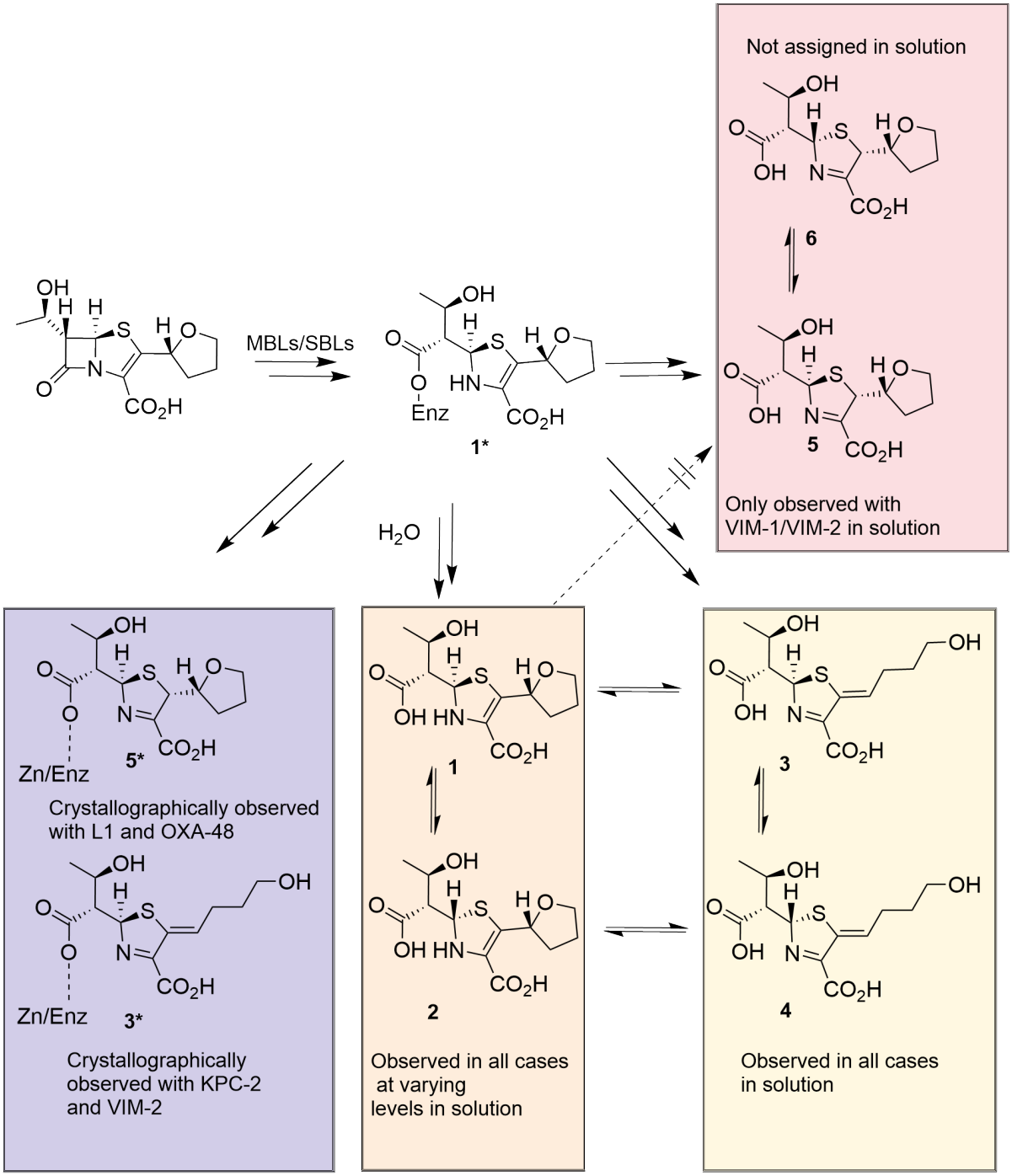


Figure 1: Summary of proposed mechanisms and products of faropenem hydrolysis. Products **1-4** have been observed in solution in all cases, though at varying levels. Product **5** was only observed in the cases of VIM-1 and VIM-2. **2** and **4** are produced by epimerisation of **1** and **3**, respectively.

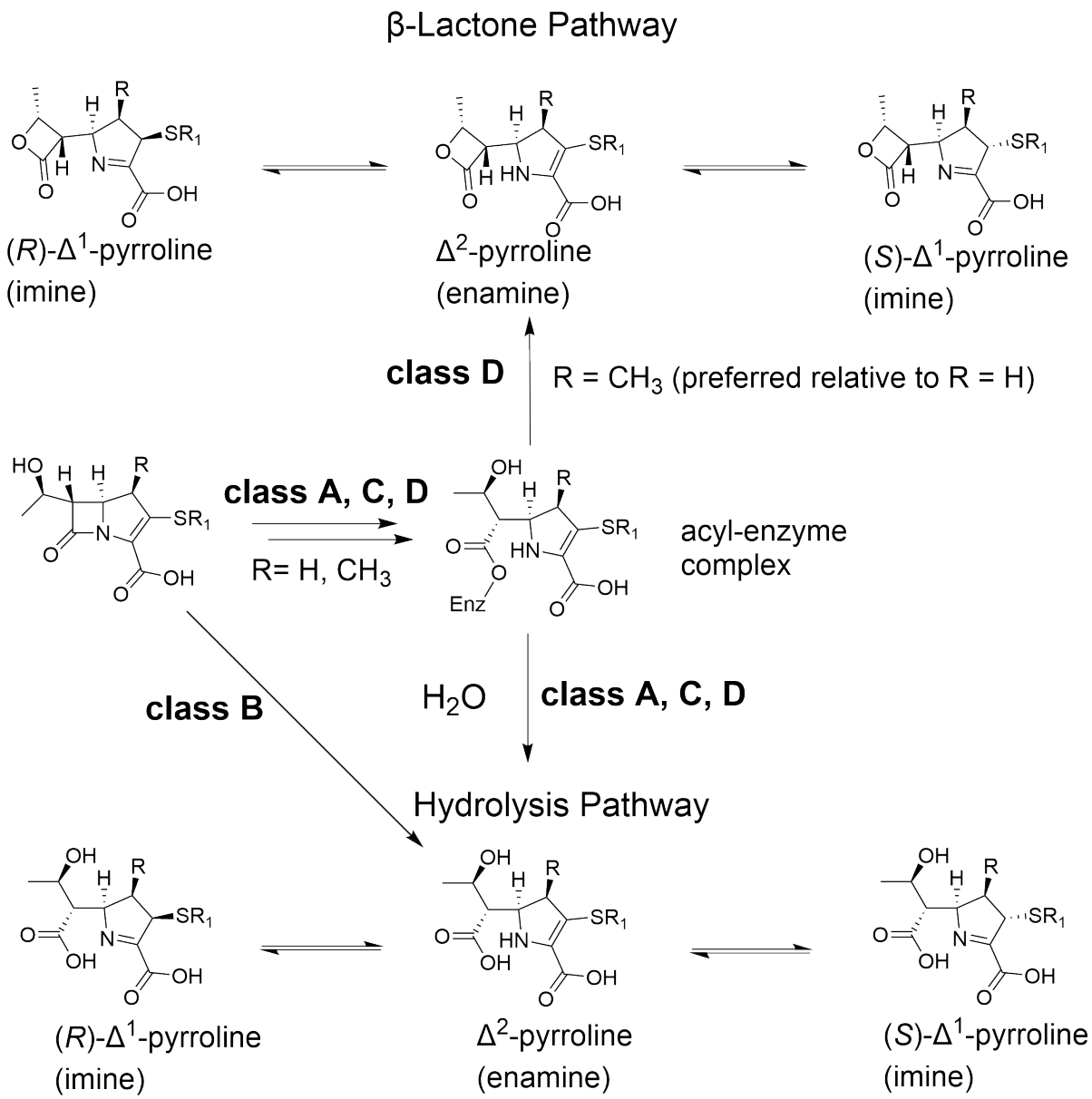


Figure 2: Summary of carbapenem hydrolysis mechanism by SBLs and MBLs. Only class D SBLs form β-lactone products and this is only observed (to date) with carbapenems (not penems). The NMR studies conducted in this thesis indicated that no β-lactone products were formed upon faropenem hydrolysis.

Despite their potential as β-lactamase inhibitors, penems are not as clinically significant as their carbapenem counterparts; this could be due to issues including difficulties associated with their synthesis.[7] Further development of penems which would be tested against multiple clinically relevant β-lactamases, would potentially aid in the development of new antibiotics and β-lactamases.

Moreover, crystallographic studies and solution studies with other penems, such as sulopenem and ritipenem, should be performed to compare and contrast their hydrolysis mechanisms with those of carbapenems and faropenem in order to inform on the development of improved β-lactamase inhibitors.[8,9]

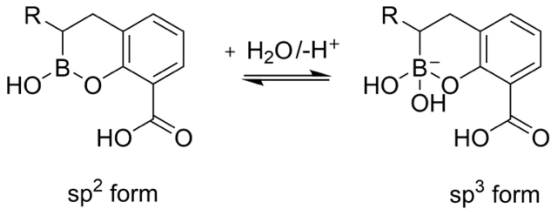
Bicyclic Boronates

Despite the success of β-lactam based SBL inhibitors, which work *via* formation of stable acyl-enzyme complexes, there are no reported potent β-lactam based inhibitors of MBLs. This has prompted the research for other classes of MBL inhibitors, with the bicyclic boronates being a very promising class.[10–15] One such compound, taniborbactam (previously known as VNRX-5133), is in clinical development. A key feature of the bicyclic boronate is their ability to potently inhibit many SBLs and MBLs. However, there is relatively little SAR on bicyclic boronate SBL and MBL inhibitors reported.

The results described in Chapter 5 concerning bicyclic boronate **3**, indicated that alteration of its C2 side chain does indeed have an impact on the behaviour of these inhibitors and that the is likely scope for further studies. Using IC_{50} studies, it was observed that, compared to previously developed bicyclic boronates that have an acylamino side chain (compound **2** and taniborbactam), **3** was able to inhibit the B3 MBL L1 which **2** did not do and was a more potent inhibitor of the class C SBL AmpC compared to taniborbactam and **2.**[11-14] Moreover, **3** was shown to be a more potent inhibitor of OXA-48 compared to previous bicyclic boronates and avibactam, a non β-lactam β-lactamase inhibitor that is clinically important.[16] Further kinetics experiments on AK4 and AK110, indicate the importance of the carboxylate that is attached to the bicyclic backbone at C2. Overall, the kinetics studies described here and elsewhere imply that bicyclic boronates have considerable potential as a new class of SBL and MBL inhibitors, possibly with antibacterial activity.[12,15]

High resolution crystal structures of **3**, AK4, and AK110 complexed with VIM-2 reveal that the bicyclic boronates bind in a manner in which the boron atom is in its sp^3 hybridised form (**Figure 3**), i.e., they appear to mimic the tetrahedral intermediate in β-lactam hydrolysis common to both SBL and MBL catalysis.

A



B

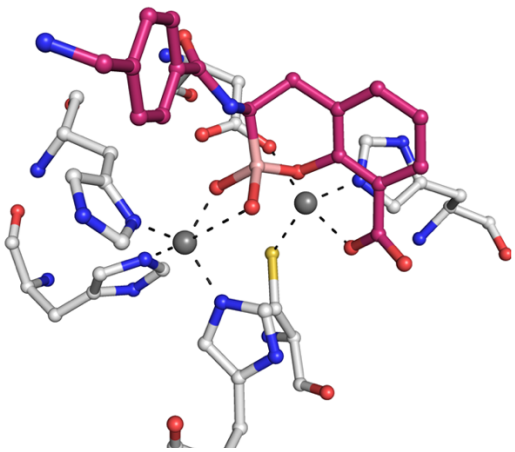


Figure 3: sp^2 and sp^3 hybridisation states of the boron atom in the bicyclic boronate. A) All crystal structures with bicyclic boronate so far have shown the bicyclic boronates in the sp^3 form, though it cannot be ruled out that the boronates (sometimes) bind to the active site in there sp^2 form. The sp^3 form may mimic the tetrahedral intermediate in catalysis whereas the sp^2 form may mimic the unreacted β-lactam substrate. B) Crystal structure of VIM-2 complexed with bicyclic boronate **2** in the sp^3 form (PDB 5FQC).[14,17]

The overall studies strongly indicate that further SAR studies will be critical for the development of broad spectrum boronate containing β-lactamase inhibitors as shown in the work reported here alterations to the side chain clearly impact the behaviour of these compounds. It can be concluded that bicyclic boronates show great promise as broad spectrum inhibitors, as highlighted by the fact that taniborbactam is currently in phase 3 clinical trials.[10,11,13,18]

Changes to the bicyclic boronate scaffold and its appendages may also lead to a different mechanism of inhibition. In this regard, it should be noted that upon binding to the MBL NDM-1, taniborbactam takes on a tricyclic form as well as the well-established bicyclic form – at least as observed crystallographically (**Figure 4**).[11] Since taniborbactam is a potent inhibitor of NDM-1, developing a tricyclic boronate backbone could potentially yield promising results.[11] However, having a good understanding of the structural changes that occur in SBLs and MBLs during the hydrolysis reaction and a clear proof of tetrahedral intermediate formation, will likely be key in aiding the production of more potent antimicrobials

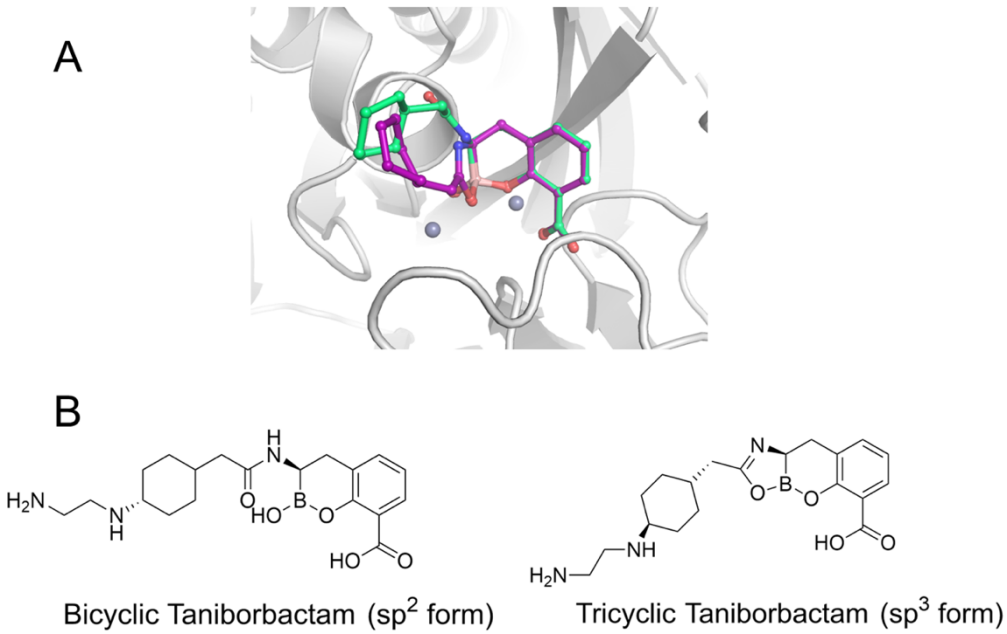


Figure 4: Active site of NDM-1 with taniborbactam (PDB code: 6RMF[11]). Note the presence of both bicyclic and tricyclic boronate forms (green and purple respective) of taniborbactam. It is of interest to study constrained tricyclic boronates to compare how they might bind and inhibit compared to bicyclic boronates.[17]

XFELs and Serial crystallography

There remains a lack of understanding with regards to how and why certain intermediates and products are formed with some SBLs/MBLs, but not others, e.g. the formation of β-lactones with only certain class D SBLs and carbapenem combinations.[6] Most MBL and SBL reactions happen on the millisecond timescale,[19,20] making it difficult to capture an enzyme: intermediate structure using standard crystallographic methods at a synchrotron. It is for this reason that it was decided to expand mechanistic studies of β-lactamases to the field of dynamic structural biology with a particular focus on XFELs, as described in Chapters 3 and 4. The ultimate aim is to produce a "molecular movie" of β-lactamase catalysis, employing clinically relevant substrates, in my case ertapenem, which was selected because of its clinical relevance, cost, and solubility. The fast pulses of the XFEL (femtosecond

timescale) in principle allow for the visualisation of the structures of intermediates that could not previously be observed *in crystallo*.[21] Moreover, the bright pulse of XFELs mean that crystals much smaller than what is normally used at a synchrotron can be used for XFEL data collection, a property that is useful for time resolved studies as obtaining high occupancy *via* diffusion is normally easier with smaller crystals.[22] Gaining deep insight into the reaction mechanisms of SBLs and MBLs, could be a key element in aiding the formation of effective truly broad spectrum β-lactamase inhibitors.

The aim of the initial XFEL studies was to optimise methods of batch crystallisation for different experiments, test which sample delivery methods may be best suited to β-lactamase / PBP studies and to test these methods at an XFEL (See Chapter 3). PBP5 was used for these initial trials due to its gene being highly expressed in comparison to that of VIM-2 (Chapters 3 and 4). Since large amounts of proteins are used for most XFEL sample delivery methods, it was thus simpler and less time consuming to use PBP5 rather than VIM-2. Following optimisation, it was shown that large batches of microcrystals can be produced of PBP5, with subsequent work showing this was also possible for VIM-2. The key to success was the use of highly concentrated seedstocks and shaking the crystal plates; this combination increased the concentration of microcrystals present in the slurry and prevented the crystals from growing too large.

Upon testing the fixed target and gel extruder sample delivery methods at Diamond Light Source,[23–25] it was clear that the gel extruder method had a negative impact on the crystals, with diffraction quality decreasing throughout the data collection (Chapter 3). Furthermore, the gel extruder method of sample delivery does not (readily) allow for mixing experiments, making it less practical than other methods for any future time resolved XFEL studies.[25,26] The fixed target method produced significantly higher quality datasets and required small quantities of samples compared to other sample delivery methods.[23,24,27] It is a simple sample delivery method to use, requiring little technological expertise on the user's part. There has been little development in terms of mixing when it comes to the fixed target

method;[28] future experiments could involve adding drops of substrate solution onto the fixed target chip using a PolyPico machine, a droplet dispenser that releases very small droplets (up to pL in size).[23] The fixed target method also allowed for the collection of a room temperature dataset of VIM-2 in its resting state using microcrystal diffraction, albeit with lower resolution compared to previous cryo-synchrotron structures.[29]

During two separate XFEL beamtime data collection studies, resting state datasets were collected for both VIM-2 and PBP5 (Chapters 3 and 4), however, no enzyme-substrate complex structures were successfully collected. Enzyme-substrate mixing was done using the ADE method, as developed at Lawrence Berkley National Laboratory (also known as the ADE tape drive).[30] The ADE tape drive machine uses a small amount of sample compared to Gas Dynamic Virtual Nozzle (GDVN),[31] meaning that less time is needed to be spent on protein production compared to other methods such as mixing jets.[32,33] However, the ADE tape drive method is technically more complex than the fixed target or the gel extruder methods and requires a substantial machine and expert attention if something goes wrong.[30]

Whilst mixing jets have been used in the past to attempt to collect datasets during β-lactamase reactions,[32,34,35] this method is not only wasteful in terms of the amount of protein used, but is also technically difficult to set up and fragile.[30] The jets are prone to clogging with high salt and viscous well solutions and changing the nozzle can take a couple of hours, which cuts into precious time during a 12-hour XFEL shift. Finding a durable sample delivery method that is sample and enzyme efficient, is vital for performing regular mixing experiments for time resolved β-lactamase work.

Unfortunately, no enzyme: substrate VIM-2 structures were collected at the XFEL beamtime. Moreover, it was clear that the microcrystals in the VIM-2 slurry existed in two separate space groups and unit cells. This complicated the data processing, meaning that a new microcrystal growth

condition should be found if possible. The current growth conditions for VIM-2 microcrystals also employ a high concentration of PEG 3350 (26% (w/v)), which impacts on diffusion rates due to the high viscosity of the mother liquor. Unfortunately, no conditions with low PEG concentrations were found that could produce VIM-2 crystals that diffracted to a high resolution. To address this challenge, it would be worth concentrating VIM-2 to a higher concentration before setting up crystal plates, making it easier for the protein to nucleate. Moreover, being able to produce crystals with a higher solvent content would potentially make it easier to diffuse substrates into the crystals.[36] It is therefore vital that new broad screens are performed with VIM-2 to find conditions that can produce a high concentration of homogenous microcrystals quickly and reliably.

A dataset of PBP5 complexed with ertapenem was collected at Diamond Light Source at cryo temperatures and at room temperatures using the fixed target method.[37–39] However, the PBP5: ertapenem dataset collected at room temperature was of relatively low resolution (2.9 Å) and the crystals were in multiple unit cells. As discussed in Chapter 3, this drastically reduced the number of viable images that could be used for data processing, thus reducing the quality of the dataset. The unit cell alterations could be caused by soaking the ertapenem solution into the crystal, with the crystal shape altering upon ertapenem binding. Ideally, finding a condition where PBP5 could be co-crystallised *via* batch method with a substrate (in this case ertapenem) would increase homogeneity and prevent the presence of multiple unit cells.

Future work

Two key questions surrounding XFEL studies, in particular in studies on β-lactamases where substrates are diffused into the active site are: a) how long it takes for a substrate to diffuse through a crystal matrix to the active site and b) how reactions in crystals differ to those that occur in solution. Indeed, with the faropenem studies, different products were observed in the L1 crystal structure compared to the solution L1 studies employing NMR (Chapter 2). Understanding this in more detail would allow

for a better estimation of what time points would need to be collected at an XFEL in order to create a reliable picture of catalysis. Currently, there is no clear answer to either of these questions and the available evidence is that they need to be answered on a case-by-case basis. A small, soluble substrate will (normally) diffuse into a crystal faster than a large, hydrophobic compound.[36] The mother liquor that the crystal slurry is in is also important. Any solution with a high concentration of PEG or other viscous precipitants will make it more difficult for substrates to diffuse into the crystal quickly. The space group, unit cell and solvent content in the crystals are also key, with tightly packed structures making it harder for substrates to enter the active site.[36] All of these things need to be taken into consideration when undertaking any time resolved experiments involving substrate diffusion.

A potentially simple way to measure diffusion would be to produce an active site binding fluorescent probe (either a substrate or an inhibitor) that can be soaked into either a slurry of microcrystals or a single crystal. Measuring the fluorescence of the crystals during and immediately after soaking would give crystallographers an idea of how long the diffusion process takes. Moreover, this could be tested with crystals in various different well solutions, space groups and unit cells to see how these factors affect the diffusion rate. Because of the high volumes of substrates needed in mixing experiments, any probe used for this sort of experiment needs to be easy to synthesise in high yields. It should also be very soluble so that it does not clog any jets or dispensers during data collection.

There are several potential fluorescent β-lactam substrates that have been produced such as FC5 and some fluorescent carbapenems.[40] In most of these cases, the fluorescent probe is released upon the hydrolysis of the β-lactams, making it possible to monitor catalysis. However, this would make it difficult to track active site binding in a highly concentrated microcrystal slurry. Furthermore, some of the enzyme will likely not have crystallised and could be turning over the substrate in solution. The microcrystal slurry would potentially need to be “washed” with fresh well solution to remove any excess protein – a technically difficult task.

Several fluorescent antibiotic conjugates are commercially available. One of these is BOCILLIN-FL, which is a derivative of penicillin V that is linked to a fluorescent probe boron-dipyrromethene (BODIPY) *via* modifications to the side chain (**Figure 5**).[41] BOCILLIN-FL is also a broad spectrum binder of PBPs and several β-lactamases and has been used for several SAR studies with PBPs and OXA-10 as well as in cell biology studies.[42–44] Binding of BOCILLIN-FL can be detected using SDS-PAGE as well as through fluorescent spectroscopy. Unlike FC5, the fluorescent probe is not released upon β-lactam hydrolysis, making it easier to detect fluorescence inside a crystal. Moreover, the fact that the compound is commercially available through ThermoFisher, makes it easy to access. However, BOCILLIN-FL is a large molecule, which could make it difficult for the substrate to enter the active site via solvent channels (**Figure 5**). Currently, the Schofield lab is developing bicyclic boronates (AK110) with a fluorescent probe, which could potentially be used for diffusion studies. Such compounds could be ideal for diffusion studies as they are relatively small, and it has been proven they can be soaked into crystals from the work described in Chapter 4.

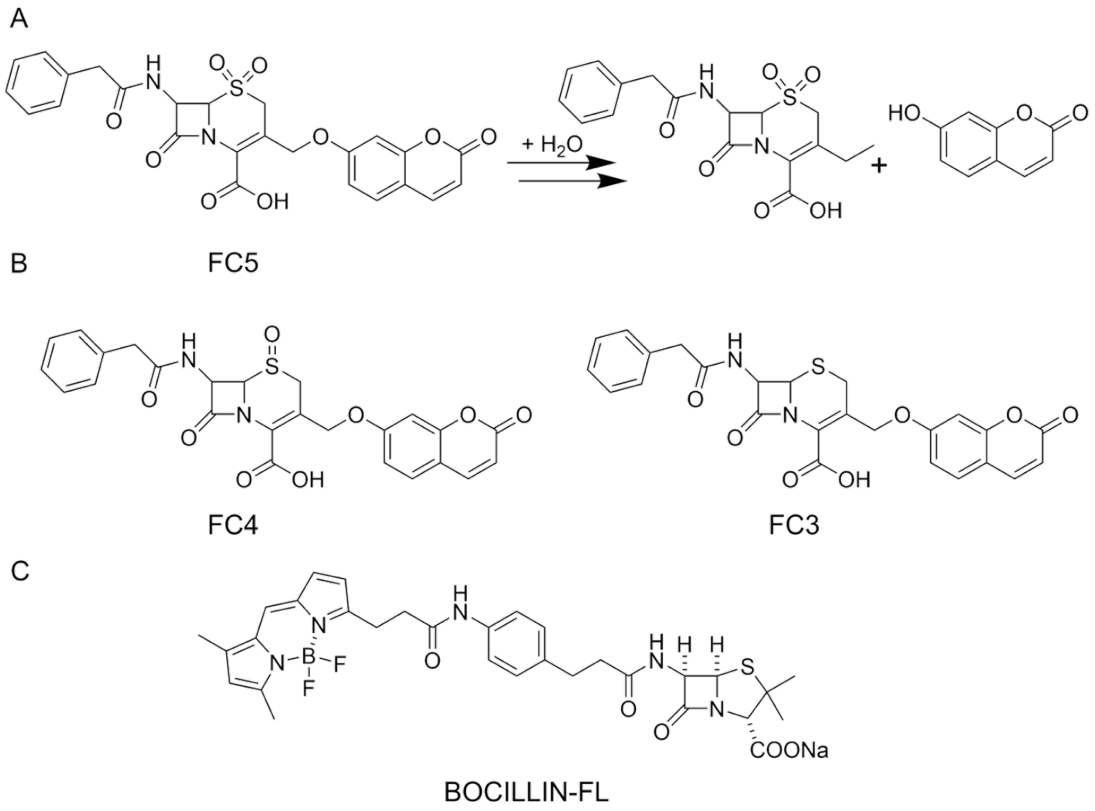


Figure 5: Structures of various fluorescent β-lactams. A) Outline of mechanism of FC5, which contains an umbelliferone tag that is released upon the hydrolysis of the cephalosporin backbone.[40] **B)** Structures of FC3 and FC4 which use the same mechanism as FC5. FC5 is the most commonly used of the three.[40] The release of the fluorescent 'tag' makes it easy to use this probe for kinetic and inhibition studies.[40] **C)** Structure of the commercially available BOCILLIN-FL which contains a BODIPY tag rather than an umbelliferone tag.[43] This compound has also been used for various cell biological and kinetic studies.

Raman spectroscopy is another potential spectroscopic technique that could be used to monitor the diffusion and turnover of substrates in crystals. Raman spectroscopy works by determining vibrational of molecules; laser light interacts with the vibrations in a molecule, which alters the energy in the laser.[45] Raman spectroscopy is often used in cellular biology and to analyse tissues, but its possibility to follow reactions in crystals has not been explored.[45,46]

Another issue that arises in capturing an enzyme: substrate complex of VIM-2 (or indeed most other β-lactamases) at an XFEL is that VIM-2 has a high turnover rate making it very difficult to capture an enzyme-substrate complex structure due to the very efficient hydrolysis of the β-lactam ring. Ideally, VIM-2, or any other β-lactamase enzyme, might be crystallised with some of an initially "inert" substrate that is triggered by an outside source such as light.[47] This could be done with a caged substrate. Indeed, this has been used in the past to study the activity of various enzymes *in vivo*. Such a substrate could have a photolabile switch which can be activate by light to remove the photolabile group. One of the most common of such groups is the *ortho*-nitrobenzyl group which has often been used for creating photoactive substrates.[47,48] Caged substrates have been used to study proteins potentially involved in malaria and various hormonal pathways.[49] However, the presence of a photolabile group will likely hinder productive active site binding and the photo-release mechanism may cause damage.

An alternative is to create a photoactivatable form of the enzyme, with catalytically important residues in the active site being "caged", so the enzyme is inactive until being triggered by photo irridation, which has previously been done to study actin binding protein.[50] There are a few advantages to using a caged protein over a caged substrate. In terms of dynamic structural biology studies, the most important of these is that caged proteins may be more specific than a caged substrate, since the mode of modifications is more clearly defined. Photocaging is most commonly done on a lysine or cysteine residue employing the 2-nitrophenyl group, though there are other possibilities.[51] Creating a caged protein, however is often technically difficult (particularly if involving production of unnatural residues in recombinant proteins) and expression yields tend to be low upon modification of residues. This is not ideal as most sample delivery methods used at XFELs require a relatively high quantity of protein compared to other chemical biology experiments.

Using non-native metals in the MBL active sites could also be used as a strategy to obtain enzyme: substrate complex structures. VIM-2 has previously been purified with different metals such as cobalt and iron;[51] the enzyme is still active with these metals, however, the turnover rate is slower.[50] In principle, this would provide more time for the substrate to diffuse into the active site prior to extensive hydrolysis (**Figure 6**). A structure of the MBL BcII with two iron ions instead of two zinc ions reveals almost identical metal ion binding modes, including with respect to the presence of the metal ion bridging water, indicating that MBLs complexed with non-native metals would behave a similar way to the native protein.[51] In the BcII iron structure, Cys221 residue was modelled as being oxidised to a sulfonic acid; however,[51] this is most likely a crystallographic / purification artefact as this oxidation has previously been seen in other MBLs.[52] Thus, in principle, VIM-2 and other MBLs could be purified with a different metal in order to alter the turnover rate of VIM-2 and other MBLs, some enabling the determination of MBL: substrate complex structures as previously reported with VIM-2 and iron.

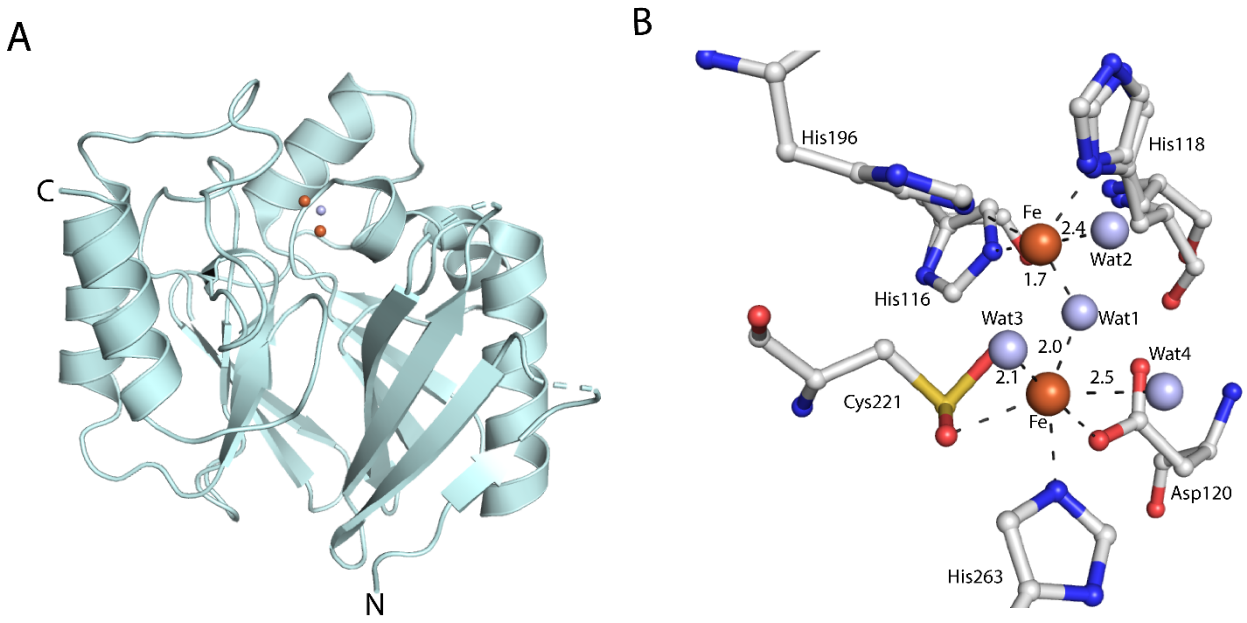


Figure 6: Views from a structure of BcII (PDB code 5FQA[51]) complexed with iron. A) The fold of the BcII structure - some residues were not modelled in due to poor density. The iron atoms are shown in reddish brown and the waters in blue. Distances are shown in Å. Very little difference is seen between this structure and the BcII: zinc structure (PDB code: 4C09[29]).[17]

It is of interest to produce a crystal structure of PBP5 with its substrate, which contains a D-Ala- D-Ala unit,[53] to compare differences in the binding modes between substrate and inhibitor. This would provide a better structural understanding of how β-lactams interact with their original target proteins compared to their substrates, which could aid in the development of future antimicrobials.

To conclude, the work described in this thesis has made several steps towards a detailed understanding of the mechanisms of β-lactamases and has identified steps that need to be taken to combat antibiotic resistance due to β-lactamases. However, more needs to be done to comprehend the dynamic structural biology of their mechanisms in order to gain an understanding of how β-lactamases work. The results show that multiple products can be formed during the hydrolysis mechanism with penems and carbapenems. Both in the cases of faropenem and biapenem, the enamine and imine products were formed by both SBLs and MBLs. In both cases, the major (though

not necessarily the exclusive) initial product appears to be an enamine (Chapter 2). No β-lactone products were observed upon faropenem hydrolysis with the enzymes studied in this thesis as well as no C5/C6 fragmentation products, indicating that β-lactone formation may not occur in penems, in contrast with carbapenems, at least in the case of their interactions with class D SBLS. Thus, further SAR studies on penems are merited.

Studies on penems such as ritipenem and sulopenem would test the lack of lactone formation with penems as being of general relevance. Such studies should preferably be performed on multiple MBLs and SBLs from all Ambler classes to get a broad picture of the kinetics and structural changes that occur, broadening our understanding of how different penems are hydrolysed in comparison to the carbapenems. Further research needs to be performed to understand what triggers the hydrolysis of the biapenem THF ring as occurs in the case of some, but not all β-lactamases. Time resolved studies employing XFEL methods may inform on such mechanisms – though these should be combined with solution studies.

The crystallographically observed interactions between the faropenem/biapenem derived intermediates were similar to those seen in MBL: inhibitor structures, including bicyclic boronates. Indeed, the results further indicate that bicyclic boronates have strong potential to act as broad spectrum β-lactamase inhibitors of clinical utility. Studies on bicyclic boronate **3** support a need for further SAR studies on the impact of sidechain variation on bicyclic boronate potency, with studies on other thioether boronates already taking place in the Schofield lab in collaboration with other groups. It is hoped that the combined studies will lead to a future where antimicrobial resistance is tackled in a more efficient and targeted manner, and eventually lead to the production of new potent, broad spectrum antimicrobial agents.

References

(1) Ventola, C. L. The Antibiotic Resistance Crisis: Causes and Threats. *P T J.* **2015**, *40*, 277–283.

(2) Hutchings, M. I.; Truman, A. W. Antibiotics: Past, Present and Future. *Curr. Opin. Microbiol.* **2019**, *51*, 72–80.

(3) Antimicrobial resistance https://www.who.int/news-room/fact-sheets/detail/antimicrobial-resistance (accessed Dec 22, 2020).

(4) Buynak, J. D. β-Lactamase Inhibitors: A Review of the Patent Literature (2010 – 2013). *Expert Opin. Ther. Pat.* **2013**, *23*, 1469–1481.

(5) Lohans, C. T.; Chan, H. T. H.; Malla, T. R.; Kumar, K.; Kamps, J. J. A. G.; McArdle, D. J. B.; van Groesen, E.; de Munnik, M.; Tooke, C. L.; Spencer, J.; et al. Non-Hydrolytic β-Lactam Antibiotic Fragmentation by l,d -Transpeptidases and Serine β-Lactamase Cysteine Variants. *Angew. Chemie Int. Ed.* **2019**, *58*, 1990–1994.

(6) Lohans, C. T.; van Groesen, E.; Kumar, K.; Tooke, C. L.; Spencer, J.; Paton, R. S.; Brem, J.; Schofield, C. J. A New Mechanism for β-Lactamases: Class D Enzymes Degrade 1β-Methyl Carbapenems through Lactone Formation. *Angew. Chemie Int. Ed.* **2018**, *57*, 1282–1285.

(7) Penems and Related Substances. *Philos. Trans. R. Soc. London. B, Biol. Sci.* **1980**, *289*, 239–250.

(8) Okamoto, K.; Gotoh, N.; Nishino, T. Pseudomonas Aeruginosa Reveals High Intrinsic Resistance to Penem Antibiotics: Penem Resistance Mechanisms and Their Interplay. *Antimicrob. Agents Chemother.* **2001**, *45*, 1964–1971.

(9) Karlowsky, J. A.; Adam, H. J.; Baxter, M. R.; Denisuik, A. J.; Lagacé-Wiens, P. R. S.; Walkty, A. J.; Puttagunta, S.; Dunne, M. W.; Zhanel, G. G. In Vitro Activity of Sulopenem, an Oral Penem, against Urinary Isolates of Escherichia Coli. *Antimicrob. Agents Chemother.* **2019**, *63*.

(10) Liu, B.; E. Lee Trout, R.; Chu, G.-H.; McGarry, D.; W Jackson, R.; Hamrick, J.; Daigle, D.; Cusick, S.; Pozzi, C.; De Luca, F.; et al. Discovery of Taniborbactam (VNRX-5133): A Broad-Spectrum

Serine- and Metallo-β-Lactamase Inhibitor for Carbapenem-Resistant Bacterial Infections. *J. Med. Chem.* **2019**,.

(11) Krajnc, A.; Brem, J.; Hinchliffe, P.; Calvopiña, K.; Panduwawala, T. D.; Lang, P. A.; Kamps, J. J. A. G.; Tyrrell, J. M.; Widlake, E.; Saward, B. G.; et al. Bicyclic Boronate VNRX-5133 Inhibits Metallo- and Serine-β-Lactamases. *J. Med. Chem.* **2019**, *62*, 8544–8556.

(12) Parkova, A.; Lucic, A.; Krajnc, A.; Brem, J.; Calvopiña, K.; Langley, G. W.; McDonough, M. A.; Trapencieris, P.; Schofield, C. J. Broad Spectrum β-Lactamase Inhibition by a Thioether Substituted Bicyclic Boronate. *ACS Infect. Dis.* **2020**.

(13) Lang, P. A.; Parkova, A.; Leissing, T. M.; Calvopiña, K.; Cain, R.; Krajnc, A.; Panduwawala, T. D.; Philippe, J.; Fishwick, C. W. G.; Trapencieris, P.; et al. Bicyclic Boronates as Potent Inhibitors of AmpC, the Class C B-lactamase from Escherichia Coli. *Biomolecules* **2020**, *10*, 1–15.

(14) Brem, J.; Cain, R.; Cahill, S.; McDonough, M. A.; Clifton, I. J.; Jiménez-Castellanos, J.-C.; Avison, M. B.; Spencer, J.; Fishwick, C. W. G.; Schofield, C. J. Structural Basis of Metallo-β-Lactamase, Serine-β-Lactamase and Penicillin-Binding Protein Inhibition by Cyclic Boronates. *Nat. Commun.* **2016**, *7*.

(15) Cahill, S. T.; Cain, R.; Wang, D. Y.; Lohans, C. T.; Wareham, D. W.; Oswin, H. P.; Mohammed, J.; Spencer, J.; Fishwick, C. W. G.; McDonough, M. A.; et al. Cyclic Boronates Inhibit All Classes of β-Lactamases. *Antimicrob. Agents Chemother.* **2017**, *61*.

(16) Ehmann, D. E.; Jahic´, H.; Ross, P. L.; Gu, R.-F.; Hu, J.; Kern, G.; Walkup, G. K.; Fisher, S. L.; Designed, S. L. F.; Performed, G. K. W. Avibactam Is a Covalent, Reversible, Non-β-Lactam β-Lactamase Inhibitor. *PNAS* **2012**, *109*, 11663–11668.

(17) DeLano, W. L. The PyMOL Molecular Graphics System. *Schrödinger LLC www.pymol.org* **2008**, http://www.pymol.org. https://doi.org/citeulike-article-id:240061.

(18) Krajnc, A.; Lang, P. A.; Panduwawala, T. D.; Brem, J.; Schofield, C. J. Will Morphing Boron-Based Inhibitors Beat the β-Lactamases? *Curr. Opin. Chem. Biol.* **2019**, *50*, 101–110.

(19) Lassaux, P.; Traoré, D. A. K.; Loisel, E.; Favier, A.; Docquier, J.-D.; Sohier, J. S.; Laurent, C.;

Bebrone, C.; Frè, J.-M.; Ferrer, J.-L.; et al. Biochemical and Structural Characterization of the Subclass B1 Metallo-Lactamase VIM-4. *Antimicrob. Agents Chemother.* **2011**, *55*, 1248–1255.

(20) Tooke, C. L.; Hinchliffe, P.; Lang, P. A.; Mulholland, A. J.; Brem, J.; Schofield, C. J.; Spencer, J. Molecular Basis of Class A β-Lactamase Inhibition by Relebactam. *Antimicrob. Agents Chemother.* **2019**, *63*.

(21) Spence, J. C. H. XFELs for Structure and Dynamics in Biology. *IUCrJ* **2017**, *4*, 322–339.

(22) Fromme, P. XFELs Open a New Era in Structural Chemical Biology. *Nature Chemical Biology*. Nature Publishing Group December 1, 2015, pp 895–899.

(23) Davy, B.; Axford, D.; Beale, J. H.; Butryn, A.; Docker, P.; Ebrahim, A.; Leen, G.; Orville, A. M.; Owen, R. L.; Aller, P. Reducing Sample Consumption for Serial Crystallography Using Acoustic Drop Ejection. *J. Synchrotron Radiat.* **2019**, *26*, 1820–1825.

(24) Rabe, P.; Beale, J. H.; Butryn, A.; Aller, P.; Dirr, A.; Lang, P. A.; Axford, D. N.; Carr, S. B.; Leissing, T. M.; McDonough, M. A.; et al. Anaerobic Fixed-Target Serial Crystallography. *IUCrJ* **2020**, *7*, 901–912.

(25) Nogly, P.; James, D.; Wang, D.; White, T. A.; Zatsepin, N.; Shilova, A.; Nelson, G.; Liu, H.; Johansson, L.; Heymann, M.; et al. Lipidic Cubic Phase Serial Millisecond Crystallography Using Synchrotron Radiation. *IUCrJ* **2015**, *2*, 168–176.

(26) Kovácsová, G.; Grünbein, M. L.; Kloos, M.; Barends, T. R. M.; Schlesinger, R.; Heberle, J.; Kabsch, W.; Shoeman, R. L.; Doak, R. B.; Schlichting, I. Viscous Hydrophilic Injection Matrices for Serial Crystallography. *IUCrJ* **2017**, *4*, 400–410.

(27) Ebrahim, A.; Appleby, M. V.; Axford, D.; Beale, J.; Moreno-Chicano, T.; Sherrell, D. A.; Strange, R. W.; Hough, M. A.; Owen, R. L.; IUCr. Resolving Polymorphs and Radiation-Driven Effects in Microcrystals Using Fixed-Target Serial Synchrotron Crystallography. *Acta Crystallogr. Sect. D Struct. Biol.* **2019**, *75*, 151–159.

(28) Mehrabi, P.; Schulz, E. C.; Agthe, M.; Horrell, S.; Bourenkov, G.; von Stetten, D.; Leimkohl, J.-P.; Schikora, H.; Schneider, T. R.; Pearson, A. R.; et al. Liquid Application Method for Time-

Resolved Analyses by Serial Synchrotron Crystallography. *Nat. Methods* **2019**, *16*, 979–982.

(29) Brem, J.; van Berkel, S. S.; Zollman, D.; Lee, S. Y.; Gileadi, O.; McHugh, P. J.; Walsh, T. R.; McDonough, M. A.; Schofield, C. J. Structural Basis of Metallo-β-Lactamase Inhibition by Captopril Stereoisomers. *Antimicrob. Agents Chemother.* **2016**, *60*, 142–150.

(30) Fuller, F. D.; Gul, S.; Chatterjee, R.; Burgie, E. S.; Young, I. D.; Lebrette, H.; Srinivas, V.; Brewster, A. S.; Michels-Clark, T.; Clinger, J. A.; et al. Drop-on-Demand Sample Delivery for Studying Biocatalysts in Action at X-Ray Free-Electron Lasers. *Nat. Methods* **2017**, *14*, 443–449.

(31) Martiel, I.; Müller-Werkmeister, H. M.; Cohen, A. E.; IUCr. Strategies for Sample Delivery for Femtosecond Crystallography. *Acta Crystallogr. Sect. D Struct. Biol.* **2019**, *75*, 160–177.

(32) Calvey, G. D.; Katz, A. M.; Schaffer, C. B.; Pollack, L. Mixing Injector Enables Time-Resolved Crystallography with High Hit Rate at X-Ray Free Electron Lasers. *Struct. Dyn.* **2016**, *3*, 054301.

(33) Wang, D.; Weierstall, U.; Pollack, L.; Spence, J. Double-Focusing Mixing Jet for XFEL Study of Chemical Kinetics. *J. Synchrotron Radiat.* **2014**, *21*, 1364–1366.

(34) Olmos, J. L.; Pandey, S.; Martin-Garcia, J. M.; Calvey, G.; Katz, A.; Knoska, J.; Kupitz, C.; Hunter, M. S.; Liang, M.; Oberthuer, D.; et al. Enzyme Intermediates Captured “on the Fly” by Mix-and-Inject Serial Crystallography. *BMC Biol.* **2018**, *16*, 59.

(35) DePonte, D. P.; Weierstall, U.; Schmidt, K.; Warner, J.; Starodub, D.; Spence, J. C. H.; Doak, R. B. Gas Dynamic Virtual Nozzle for Generation of Microscopic Droplet Streams. *J. Phys. D. Appl. Phys.* **2008**, *41*

(36) McNae, I. W.; Kan, D.; Kontopidis, G.; Patterson, A.; Taylor, P.; Worrall, L.; Walkinshaw, M. D. Studying Protein–Ligand Interactions Using Protein Crystallography. *Crystallogr. Rev.* **2005**, *11*, 61–71.

(37) Oghbaey, S.; Sarracini, A.; Ginn, H. M.; Pare-Labrosse, O.; Kuo, A.; Marx, A.; Epp, S. W.; Sherrell, D. A.; Eger, B. T.; Zhong, Y.; et al. Fixed Target Combined with Spectral Mapping: Approaching 100% Hit Rates for Serial Crystallography. *Acta Crystallogr. Sect. D Struct. Biol.*

2016, *72*, 944–955.

(38) Owen, R. L.; Axford, D.; Sherrell, D. A.; Kuo, A.; Ernst, O. P.; Schulz, E. C.; Miller, R. J. D.; Mueller-Werkmeister, H. M. Low-Dose Fixed-Target Serial Synchrotron Crystallography. *Acta Crystallogr. Sect. D, Struct. Biol.* **2017**, *73*, 373–378.

(39) Hunter, M. S.; Segelke, B.; Messerschmidt, M.; Williams, G. J.; Zatsepin, N. A.; Barty, A.; Henry Benner, W.; Carlson, D. B.; Coleman, M.; Graf, A.; et al. Fixed-Target Protein Serial Microcrystallography with an X-Ray Free Electron Laser. *Sci. Rep.* **2014**, *4*, 1–5.

(40) van Berkel, S. S.; Brem, J.; Rydzik, A. M.; Salimraj, R.; Cain, R.; Verma, A.; Owens, R. J.; Fishwick, C. W. G.; Spencer, J.; Schofield, C. J. Assay Platform for Clinically Relevant Metallo-β-Lactamases. *J. Med. Chem.* **2013**, *56*, 6945–6953.

(41) Zhao, G.; Meier, T. I.; Kahl, S. D.; Gee, K. R.; Blaszczak, L. C. BOCILLIN FL, a Sensitive and Commercially Available Reagent for Detection of Penicillin-Binding Proteins. *Antimicrob. Agents Chemother.* **1999**, *43*, 1124–1128.

(42) June, C. M.; Vaughan, R. M.; Ulberg, L. S.; Bonomo, R. A.; Witucki, L. A.; Leonard, D. A. A Fluorescent Carbapenem for Structure Function Studies of Penicillin-Binding Proteins, β-Lactamases, and β-Lactam Sensors. *Anal. Biochem.* **2014**, *463*, 70–74.

(43) Schneider, K. D.; Bethel, C. R.; Distler, A. M.; Hujer, A. M.; Bonomo, R. A.; Leonard, D. A. Mutation of the Active Site Carboxy-Lysine (K70) of OXA-1 β-Lactamase Results in a Deacylation-Deficient Enzyme. *Biochemistry* **2009**, *48*, 6136–6145.

(44) Park, M.; Sutherland, J. B.; Rafii, F. β-Lactam Resistance Development Affects Binding of Penicillin-Binding Proteins (PBPs) of Clostridium Perfringens to the Fluorescent Penicillin, BOCILLIN FL. *Anaerobe* **2020**, *62*, 102179.

(45) Tu, A. T. Raman Spectroscopy in Biology: Principles and Applications. *undefined* **1982**.

(46) Aljakouch, K.; Lechtonen, T.; Yosef, H. K.; Hammoud, M. K.; Alsaidi, W.; Kötting, C.; Mügge, C.; Kourist, R.; El-Mashtoly, S. F.; Gerwert, K. Raman Microspectroscopic Evidence for the Metabolism of a Tyrosine Kinase Inhibitor, Neratinib, in Cancer Cells. *Angew. Chemie - Int. Ed.*

2018, 7250–7254.

(47) Banala, S.; Arnold, A.; Johnsson, K. Caged Substrates for Protein Labeling and Immobilization. *ChemBioChem* **2008**, *9*, 38–41.

(48) Swezey, R. R.; Epel, D. Caged Substrates for Measuring Enzymatic Activity in Vivo: Photoactivated Caged Glucose 6-Phosphate. *Methods Enzymol.* **1998**, *291*, 278–288.

(49) DeGraw, A. J.; Hast, M. A.; Xu, J.; Mullen, D.; Beese, L. S.; Barany, G.; Distefano, M. D. Caged Protein Prenyltransferase Substrates: Tools for Understanding Protein Prenylation. *Chem. Biol. Drug Des.* **2008**, *72*, 171–181.

(50) Marriott, G.; Roy, P.; Jacobson, K. Preparation and Light-Directed Activation of Caged Proteins. *Methods Enzymol.* **2003**, *360*, 274–288.

(51) Cahill, S. T.; Tarhonskaya, H.; Rydzik, A. M.; Flashman, E.; McDonough, M. A.; Schofield, C. J.; Brem, J. Use of Ferrous Iron by Metallo-β-Lactamases. *J. Inorg. Biochem.* **2016**, *163*, 185–193.

(52) Garcia-Saez, I.; Docquier, J.-D.; Rossolini, G. M.; Dideberg, O. The Three-Dimensional Structure of VIM-2, a Zn-β-Lactamase from Pseudomonas Aeruginosa in Its Reduced and Oxidised Form. *J. Mol. Biol.* **2008**, *375*, 604–611.

(53) Sauvage, E.; Kerff, F.; Terrak, M.; Ayala, J. A.; Charlier, P. The Penicillin-Binding Proteins: Structure and Role in Peptidoglycan Biosynthesis. *FEMS Microbiol. Rev.* **2008**, *32*, 234–258.

Appendix

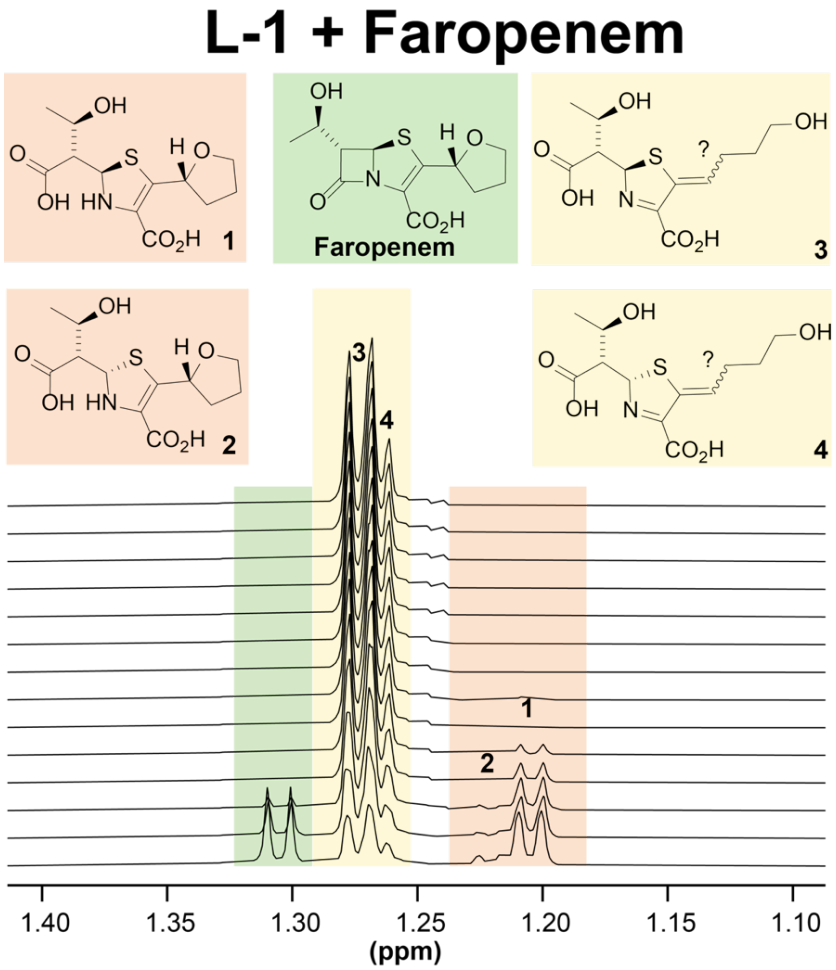


Figure S1: ^{1}H-NMR (AVIII700) reaction time course spectra of L1 treated with faropenem. Faropenem (5 mM, green) was treated with purified L1 (125 nM) in 50 mM sodium phosphate, pH 7.5, 10% (v/v) D_2O in H_2O. Enamine **1** and **2** (orange) and imines **3** and **4** (yellow) products were observed. **1**, which reacts to give **2,** is initially formed and then reacts to give **3,** which then reacts to give **4**. Note the presence of evidence for unassigned degraded faropenem products at 1.24-1.26 ppm. Spectra were stacked from bottom (earliest time point 5 minutes) to top with each spectra acquired in 2.5 minute intervals (number of scans =32).

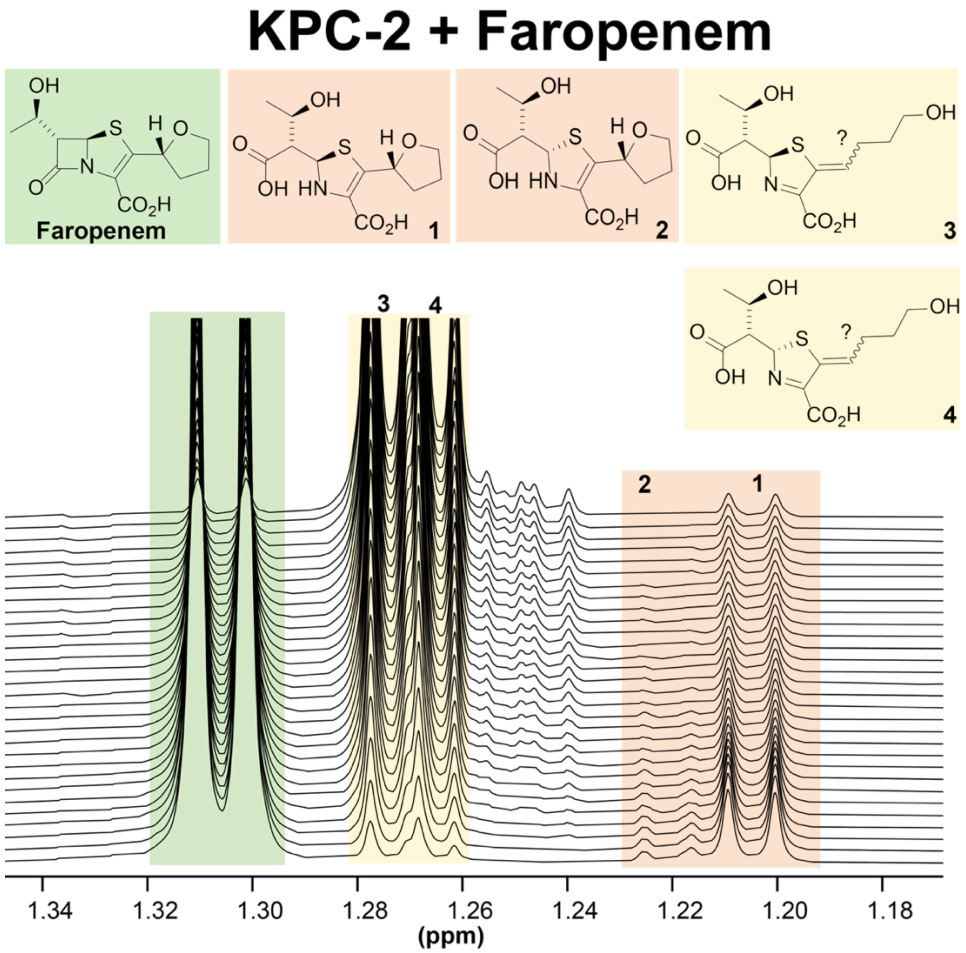


Figure S2: ^{1}H-NMR (AVIII700) reaction time course spectra of KPC-2 treated with faropenem. Faropenem (5 mM, green) was treated with purified KPC-2 (125 nM) in 50 mM sodium phosphate, pH 7.5, 10% (v/v) D_2O in H_2O. Enamine **1** and **2** (orange) and imines **3** and **4** (yellow) products were observed. **1**, which reacts to give **2,** is initially formed and then reacts to give **3,** which then likely reacts to give **4**. Note the presence of evidence for unassigned degraded faropenem products at 1.24-1.26 ppm. Spectra were stacked from bottom (earliest time point 5 minutes) to top with each spectra acquired in 2.5 minute intervals (number of scans =32).

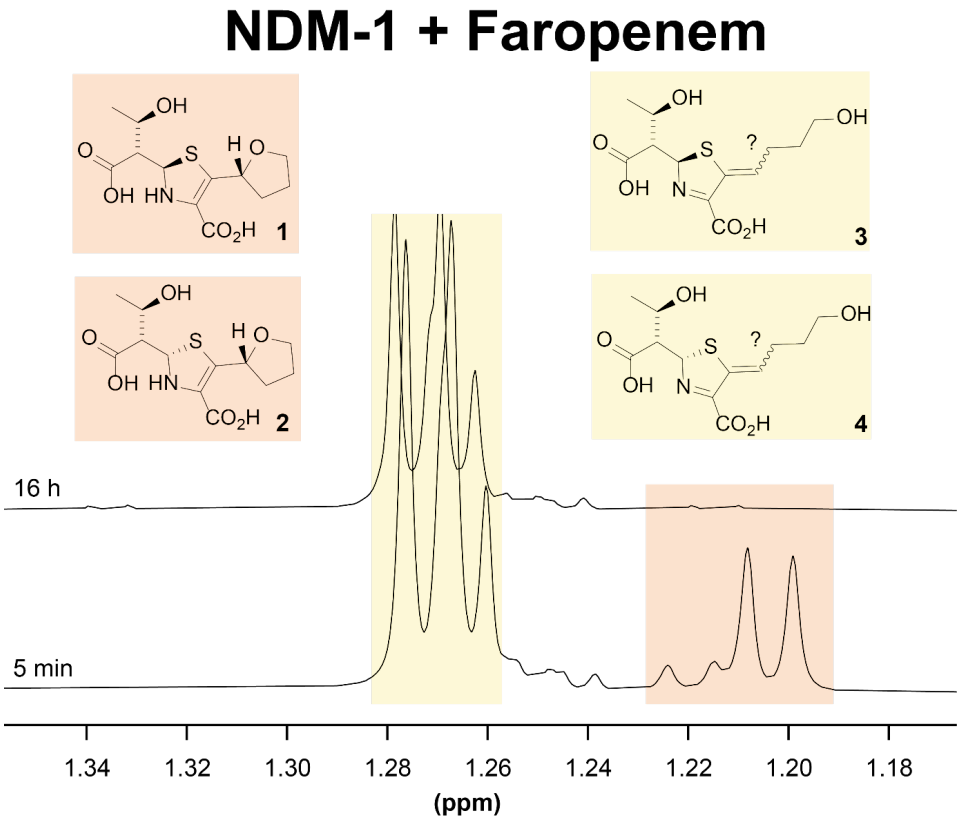


Figure S3: ^{1}H-NMR (700 MHz) spectra of NDM-1 treated with faropenem. Faropenem (5 mM) was treated with NDM-1 (5 µM) in 50 mM sodium phosphate, pH 7.5, 10% (v/v) D_2O in H_2O. Enamine **1** and **2** (orange) and imines **3** and **4** (yellow) products were observed. **1**, which reacts to give **2,** is initially formed and then reacts to give **3,** which then likely reacts to give **4**. Note the presence of evidence for unassigned degraded faropenem products at 1.24-1.26 ppm. Spectra were stacked from bottom (earliest time point 5 minutes) to top with each spectra acquired in 2.5 minute intervals (number of scans =32).

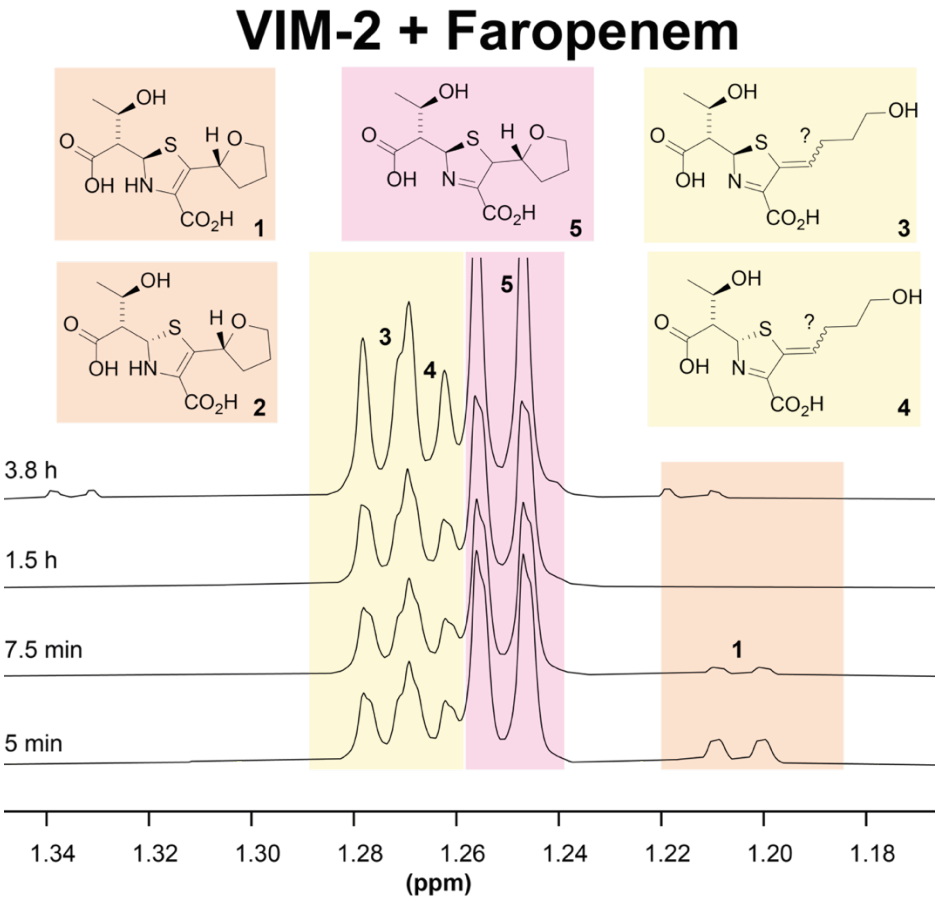


Figure S4: ^{1}H-NMR (700 MHz) spectra of VIM-2 treated with faropenem. Faropenem (5 mM) was treated with purified VIM-2 (280 nM) in 50 mM sodium phosphate, pH 7.5, 10% (v/v) D_2O in H_2O. Enamine **1** and **2** (orange) and imines **3** and **4** (yellow) products were observed. **1**, which reacts to give **2,** is initially formed and then reacts to give **3,** which then likely reacts to give **4**. Note the presence of unassigned degraded faropenem product signals at 1.24-1.26 ppm. Spectra were stacked from bottom (earliest time point 5 minutes) to top with each spectra was acquired in 2.5 minute intervals (number of scans =32).

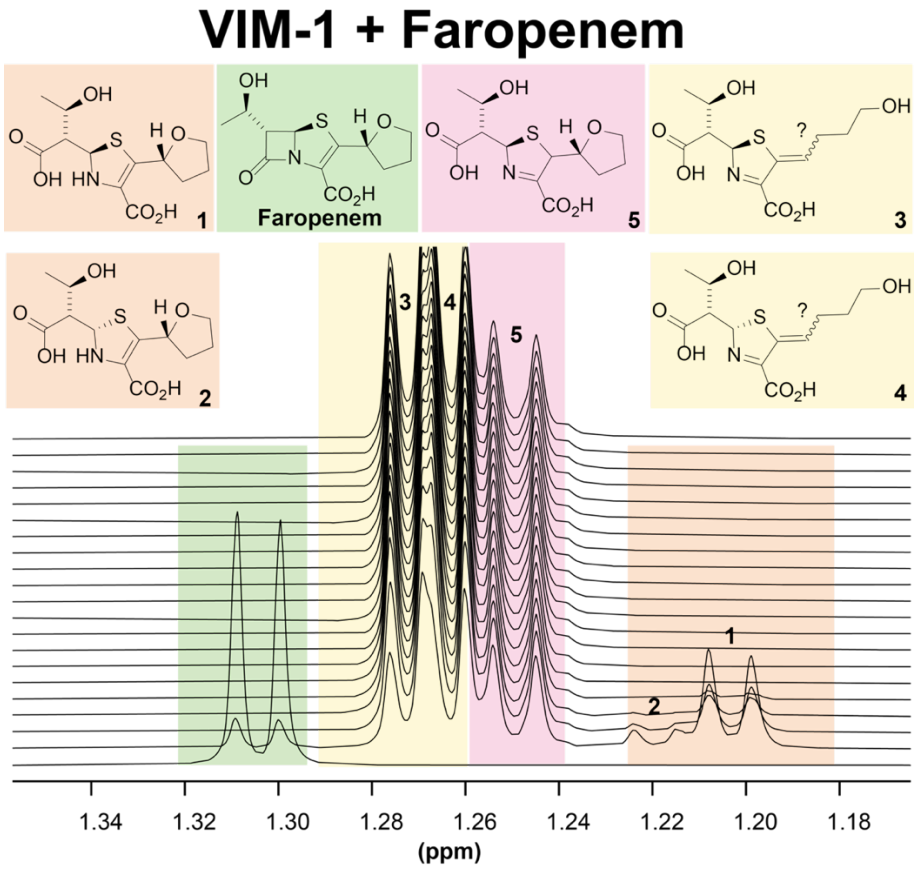


Figure S5: ^{1}H-NMR (700 MHz) time course spectra of VIM-1 treated with faropenem. Faropenem (5 mM, green) was treated with VIM-1 (280 nM) in 50 mM sodium phosphate, pH 7.5, 10% (v/v) D_2O in H_2O. Enamine **1** and **2** (orange) and imines **3** and **4** (yellow) products were observed. **1**, which reacts to give **2,** is initially formed and then reacts to give **3,** which then likely reacts to give **4**. Spectra are stacked from bottom (earliest time point 5 minutes) to top with each spectra was acquired in 2.5 minute intervals (number of scans =32).

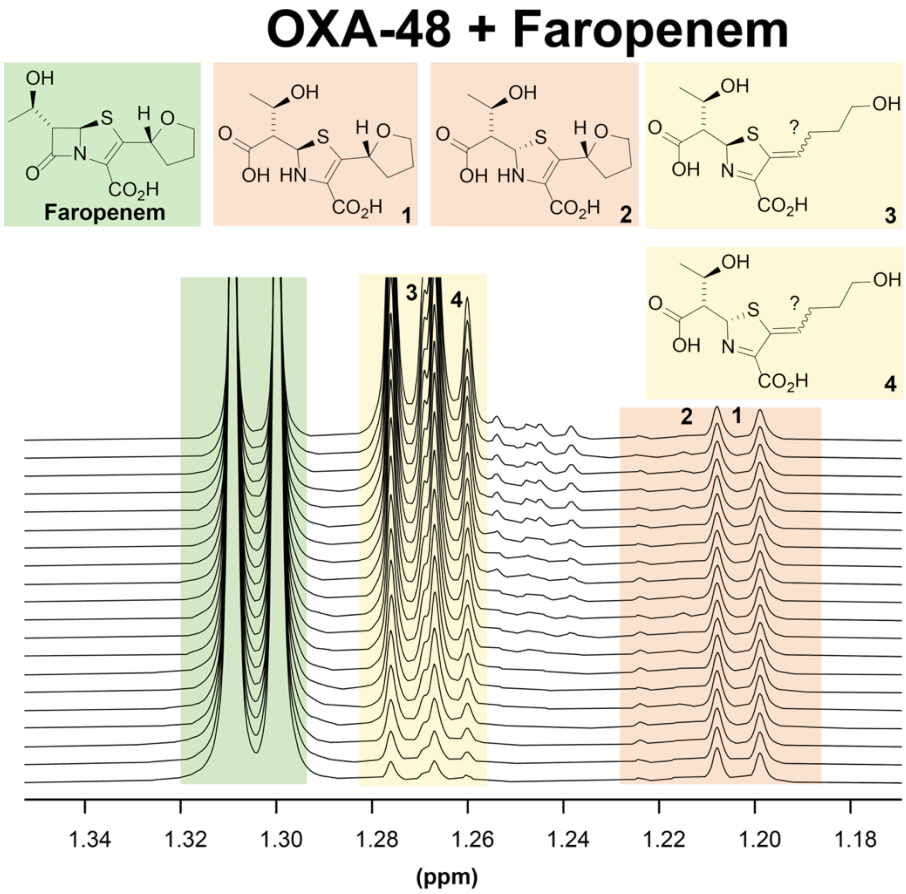


Figure S6: ^{1}H-NMR (700 MHz) time course spectra of OXA-48 treated with faropenem. Faropenem (5 mM, green) was treated with OXA-48 (280 nM) in 50 mM sodium phosphate, pH 7.5, 10% (v/v) D_2O in H_2O. Enamine **1** and **2** (orange) and imines **3** and **4** (yellow) products were observed. **1**, which reacts to give **2,** is initially formed and then reacts to give **3,** which then likely reacts to give **4**. Spectra were stacked from bottom (earliest time point 5 minutes) to top with each spectra was acquired in 2.5 minute intervals (number of scans =32). Note the presence of unassigned products with resonances 1.24-1.26 ppm.

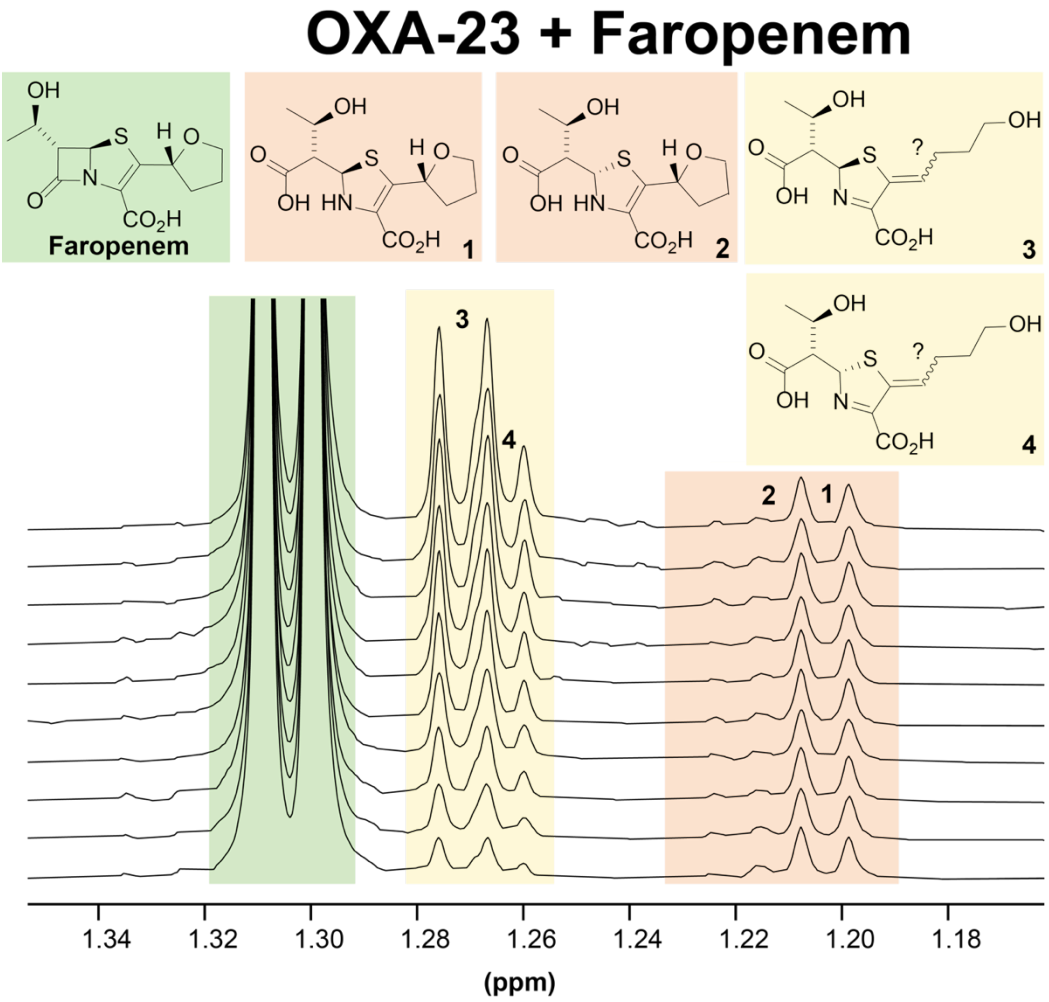


Figure S7: ^{1}H-NMR (700 MHz) time course spectra for reaction of OXA-23 with faropenem. Faropenem (2 mM, green) was treated with OXA-23 (5 µM) in 50 mM sodium phosphate, pH 7.5, 10% (v/v) D_2O in H_2O. Enamine **1** and **2** (orange) and imines **3** and **4** (yellow) products were observed. **1**, which reacts to give **2,** is initially formed and then reacts to give **3,** which then likely reacts to give **4**. Spectra are stacked from bottom (earliest time point 5 minutes) to top with each spectra was acquired at 2.5 minute intervals (number of scans =32).

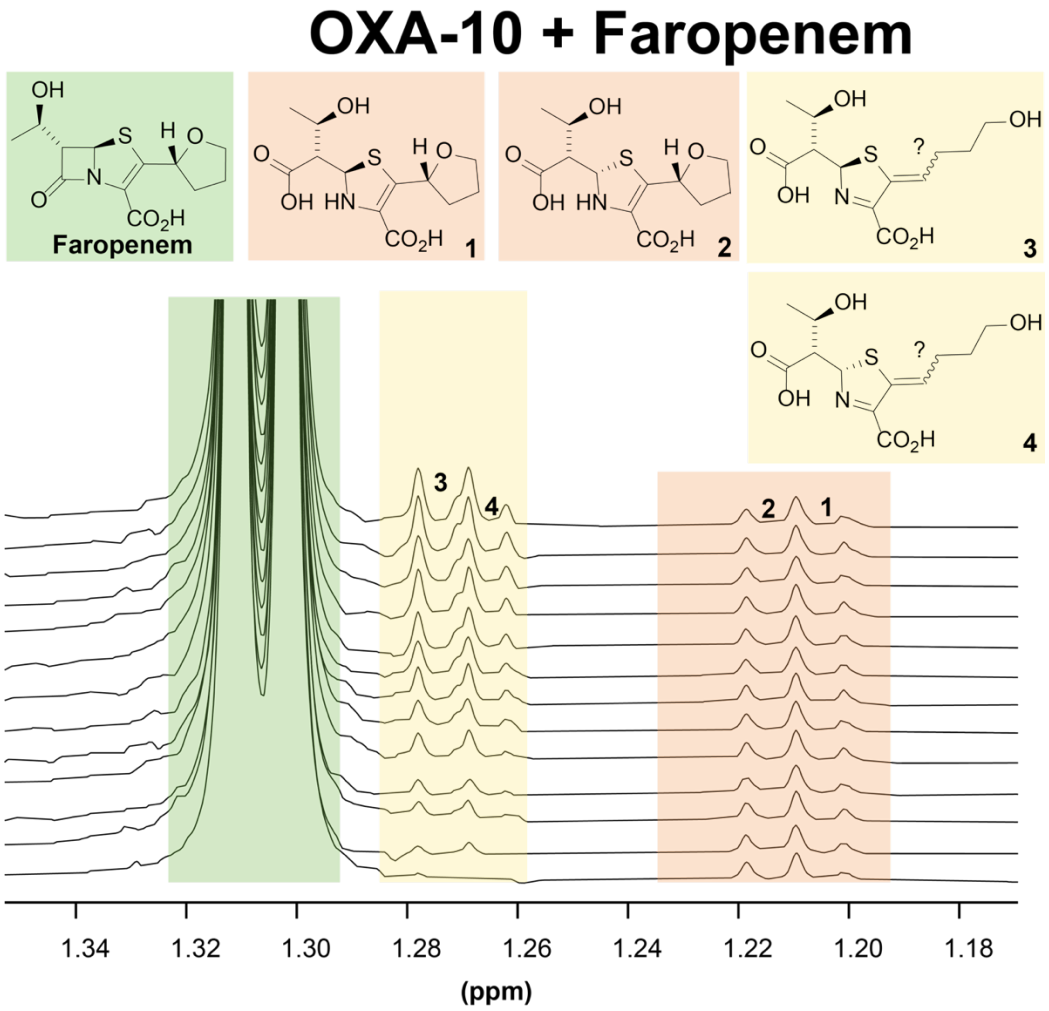


Figure S8: ^{1}H-NMR (700 MHz) reaction time course for OXA-10 treated with faropenem. Faropenem (5 mM, green) was treated with OXA-10 (5 µM) in 50 mM sodium phosphate, pH 7.5, 10% (v/v) D_2O in H_2O. Enamine **1** and **2** (orange) and imines **3** and **4** (yellow) products were observed. **1**, which reacts to give **2,** is initially formed and then reacts to give **3,** which then likely reacts to give **4**. Spectra are stacked from bottom (earliest time point 5 minutes) to top with each spectra acquired at 2.5 minute intervals (number of scans =32).

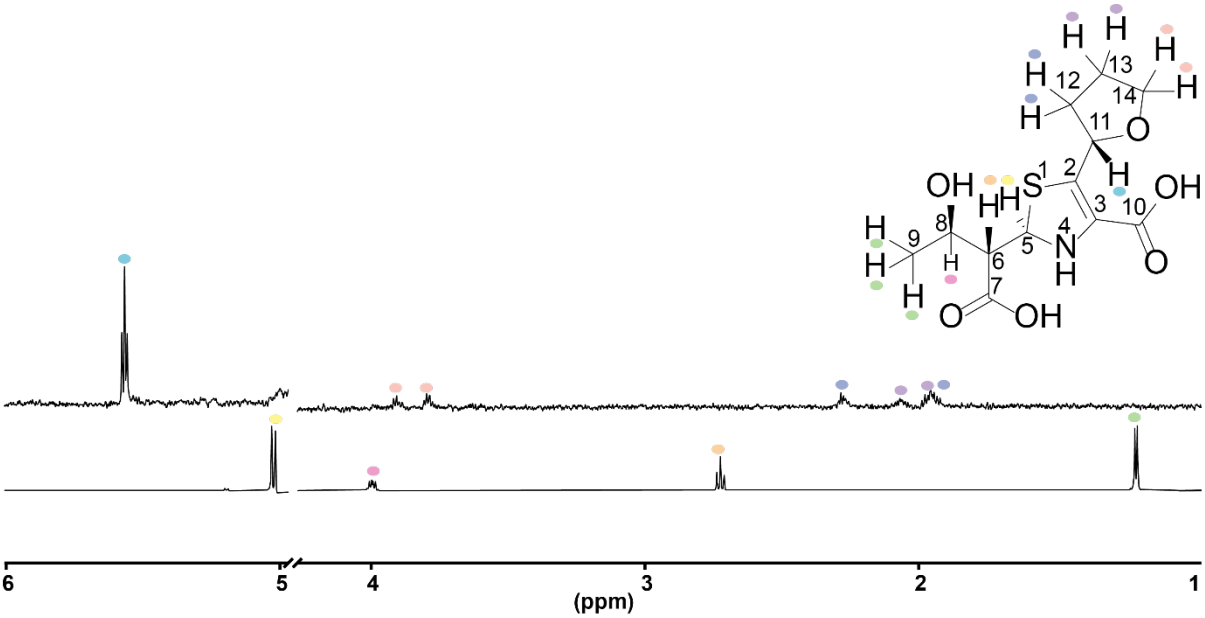


Figure S9: 1D-TOCSY of 1, an enamine product of faropenem. The C11 proton (light blue) was irradiated at 5.57 ppm (top) and the C9 protons (green) were irradiated at 1.2 ppm (bottom spectrum). Water suppression peaks were removed using MestreNova. Two distinct signals are obtained for the C14 protons (orange), adjacent to the oxygen in the tetrahydrofuran ring supporting the assignment of a closed tetrahydrofuran ring. The proton attached to C11 (light blue) position is visible as a triplet and that at C5 as a duplet. Each spectrum was acquired directly from freshly prepared 5 mM faropenem treated with purified 125 nM L1 in 50 mM sodium phosphate, pH 7.5, 10% (v/v) D_2O in H_2O.

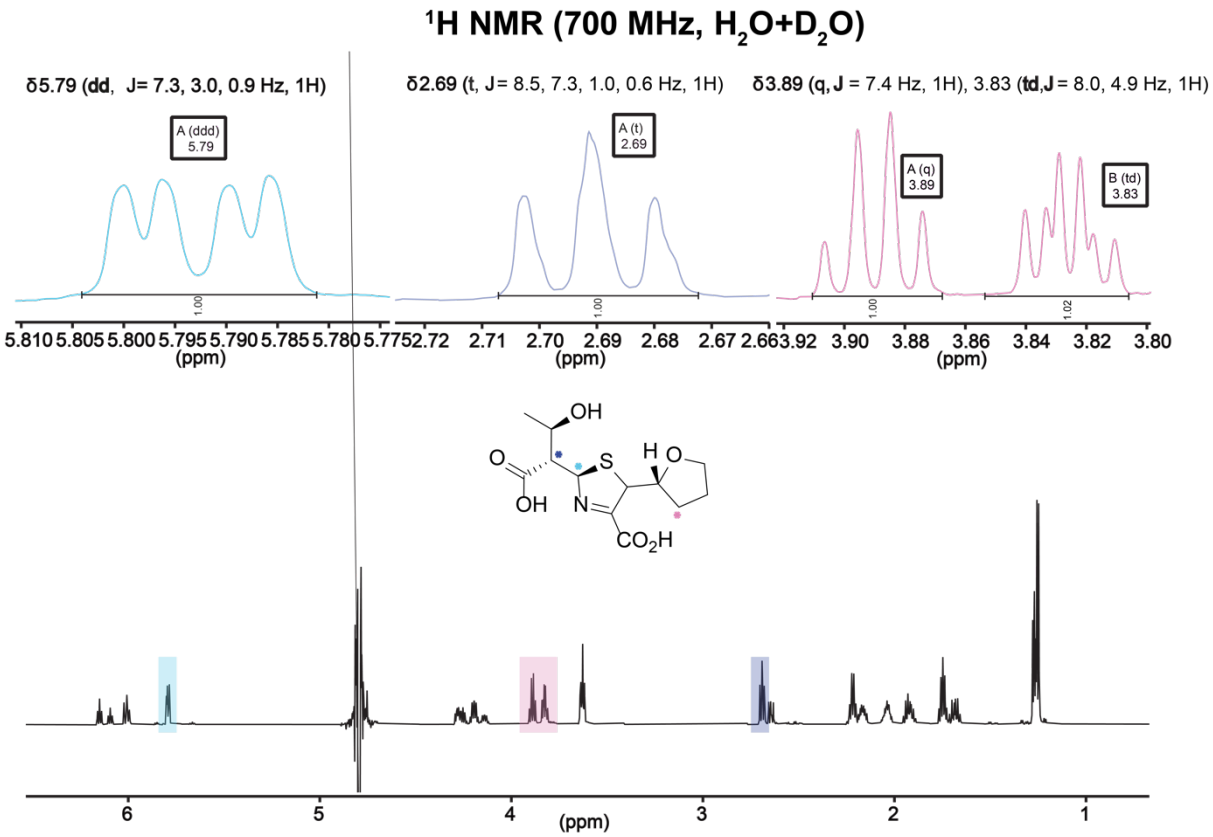


Figure S10: ^{1}H-NMR (700 MHz) of VIM-2 (847 nM) with 5 mM faropenem in 50 mM sodium phosphate, pH 7.5, 10% (v/v) D_2O in H_2O.

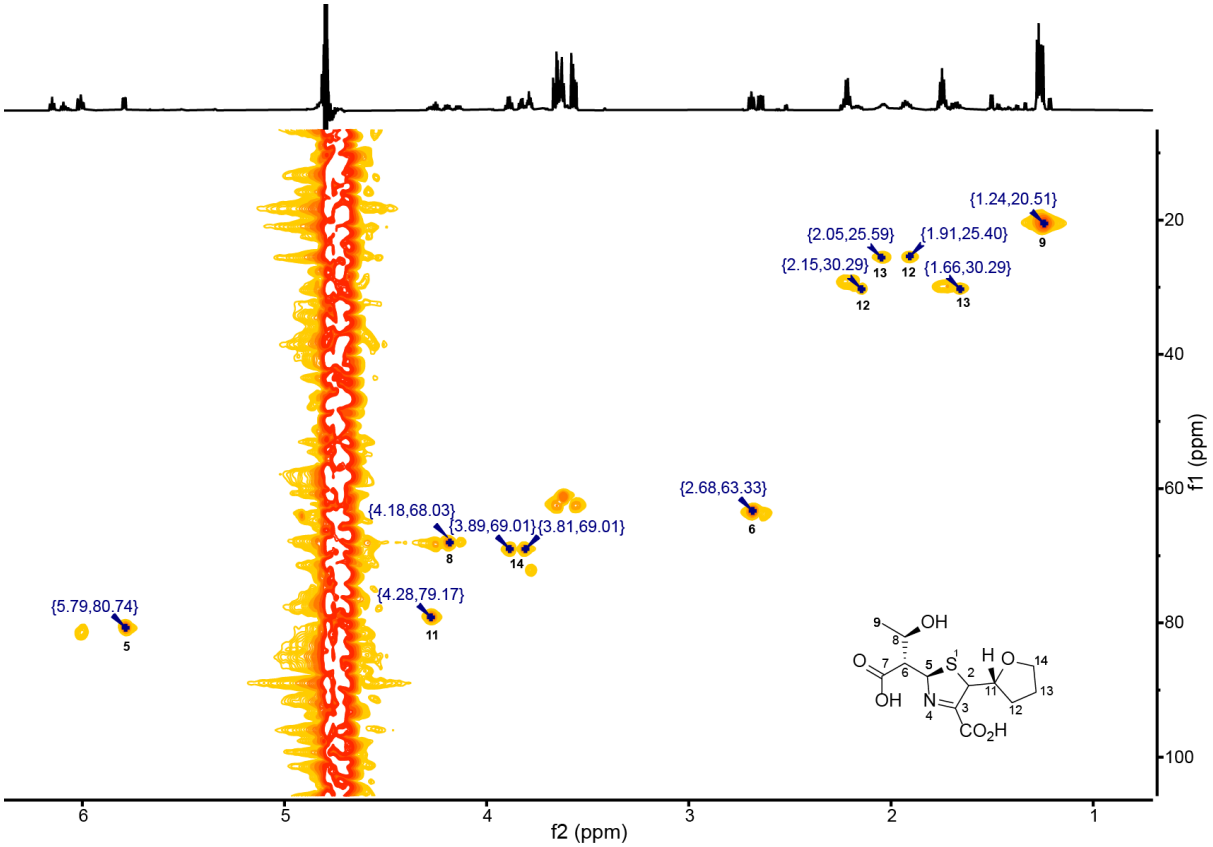


Figure S11: ^{1}H-^{13}C HSQC spectrum (AV700 MHz) of the major faropenem derived product 5 with VIM-2. 5 mM faropenem was incubated with 847 nM VIM-2 in 50 mM sodium phosphate buffer, pH 7.5, 10% (v/v) D_2O in H_2O. Note, also the products **3** and **4,** along with **5** in a ratio of ~3:2:6, respectively.

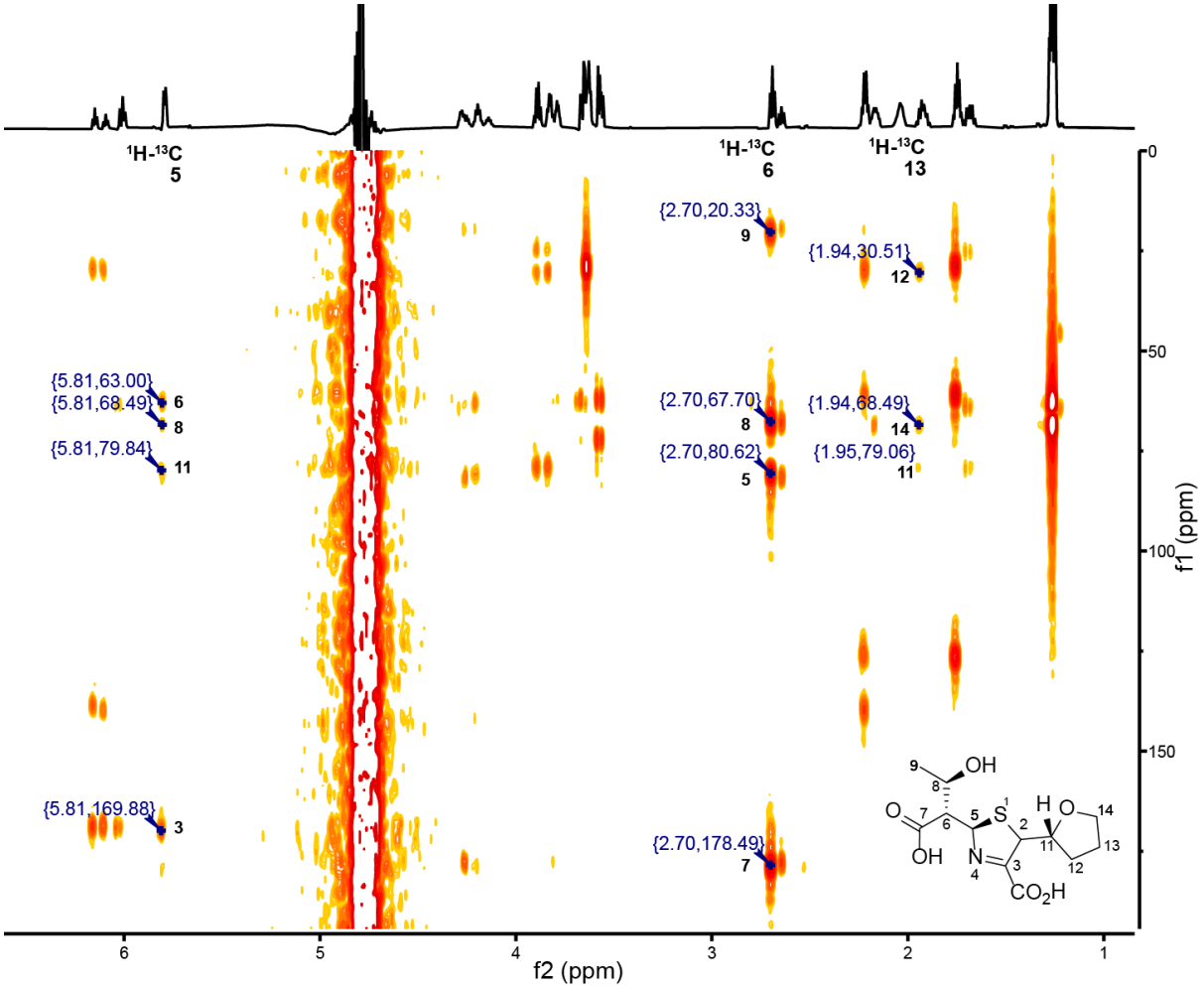


Figure S12: ^{1}H-^{13}C HMBC spectrum (700 MHz) of the major faropenem degradation product 5 with VIM-2. 5 mM faropenem was incubated with 847 nM VIM-2 in 50 mM sodium phosphate buffer, pH 7.5, 10% (v/v) D_2O in H_2O. Note the presence of **3** and **4** along with **5** in a ratio of ~3:2:6, respectively.

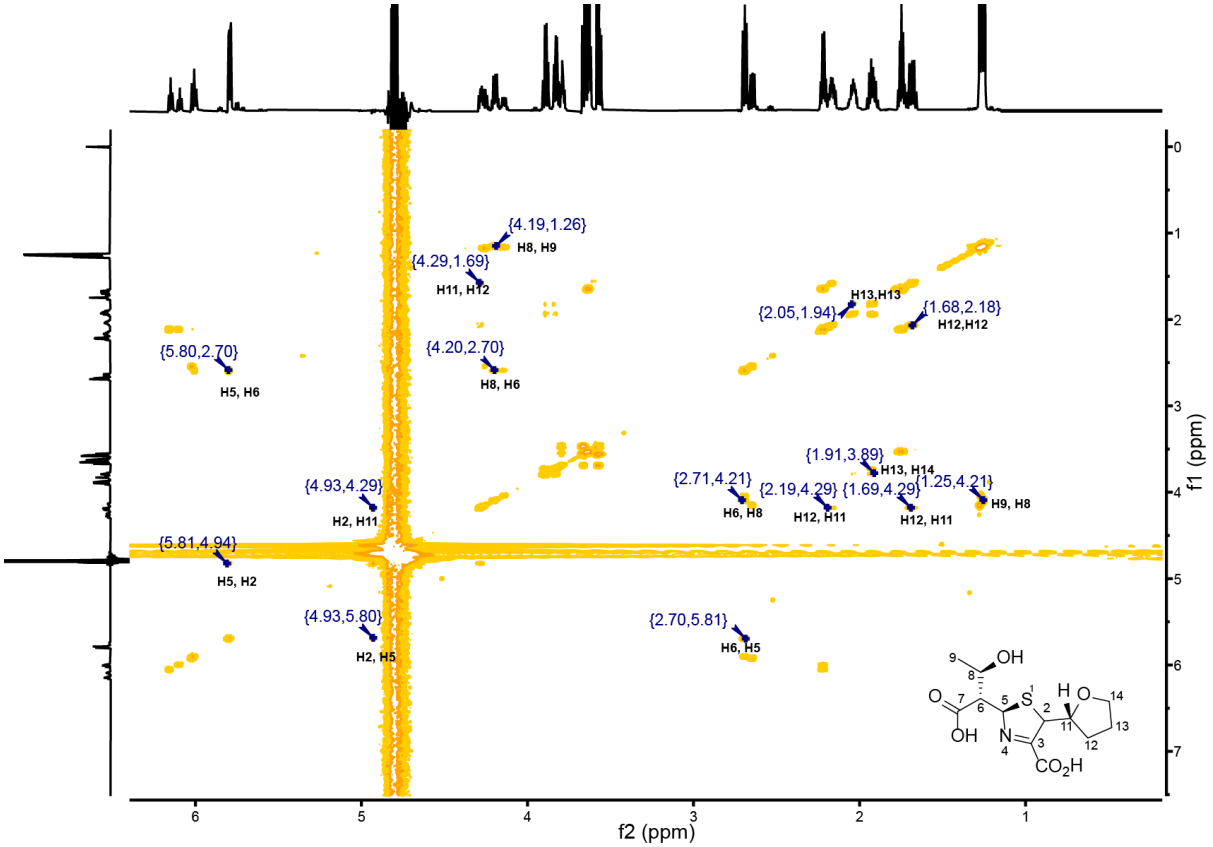


Figure S13: TOCSY spectrum (700 MHz) of the major faropenem derived product 5 with VIM-2. 5 mM faropenem was incubated with 847 nM VIM-2 in 50 mM sodium phosphate buffer, pH 7.5, 10% (v/v) D_2O in H_2O. Note also the presence of hydrolysis products **3** and **4,** along with **5, in** a ratio of ~3:2:6, respectively.

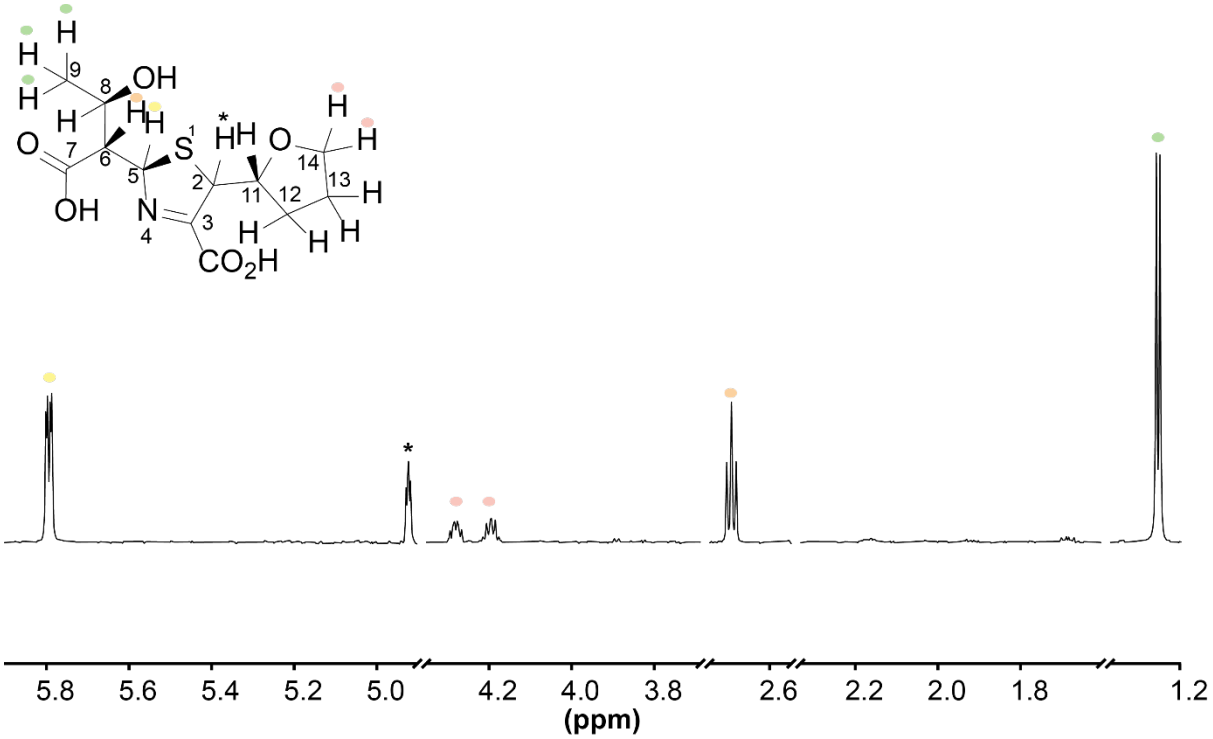
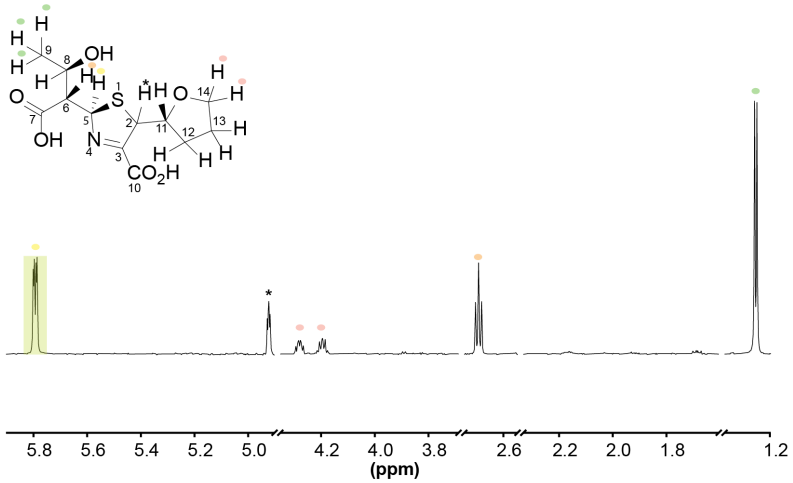
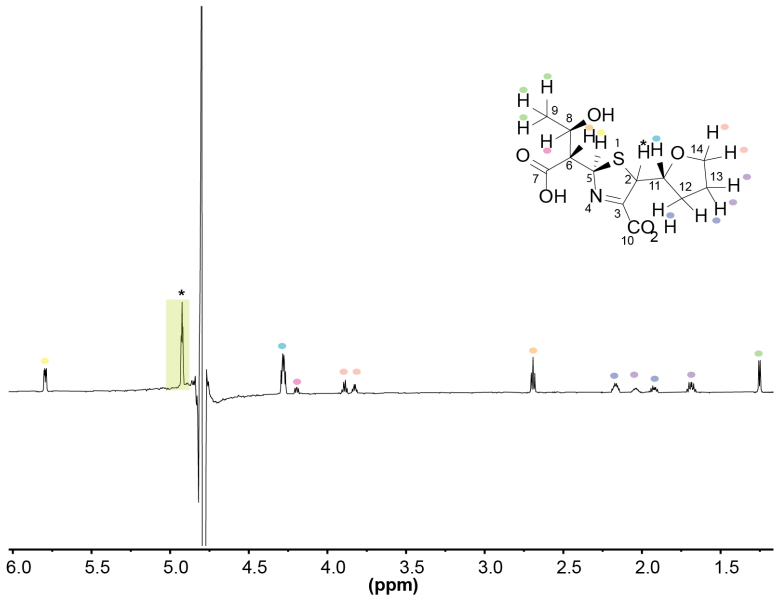


Figure S14: 1D-TOCSY characterisation of 5, a faropenem derived product. The proton at 5.79 ppm was irradiated and a new signal at 4.9 ppm (asterisk), previously unseen in the 1D spectra due to water suppression, is observed. The change in signal suggested the proton could correspond to the proton attached to C2. Water suppression peaks were removed from the spectrum using MestreNova. The spectrum was acquired directly from 5 mM faropenem treated with purified 280 nM VIM-2 in 50 mM sodium phosphate, pH 7.5, 10% (v/v) D_2O in H_2O.

A


5.8
5.6
5.4
5.2
5.0
4.2
4.0
3.8
2.6
2.2
2.0
1.8
1.2
(ppm)

B


6.0
5.5
5.0
4.5
4.0
3.5
3.0
2.5
2.0
1.5
(ppm)

C

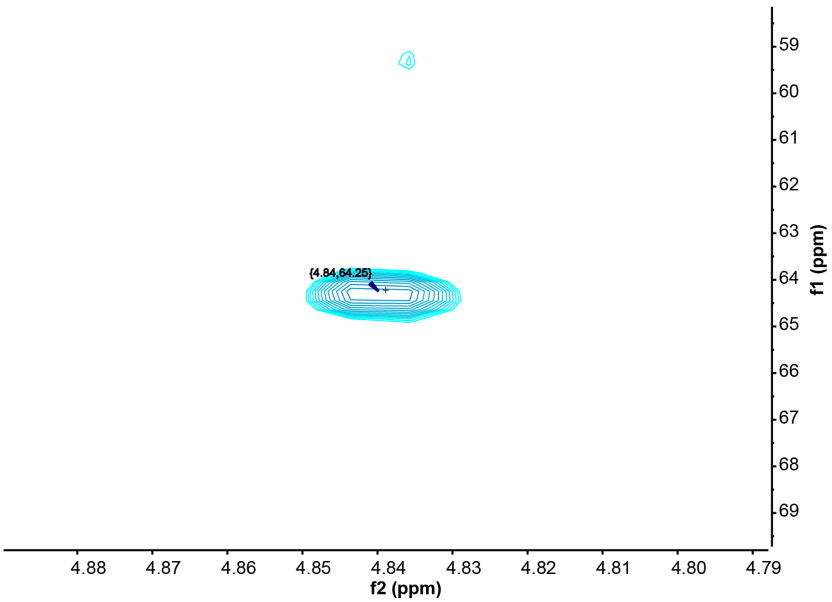

(4.84,64.25)
59
60
61
62
63
64
65
66
67
68
69
f1 (ppm)
4.88
4.87
4.86
4.85
4.84
4.83
4.82
4.81
4.80
4.79
f2 (ppm)

Figure S15: 1D-TOCSY spectrum of 5 generated by irradiation of the H3 proton at 5.79 ppm. Note that, a signal at 4.9 ppm (*), previously unobserved in the 1D spectra due to water suppression, is now observed. This resonance corresponds to the C2 proton. Water suppression peaks were removed from the spectrum using MestreNova. The spectrum was acquired directly from 5 mM faropenem mixed with purified 280 nM VIM-2 in 50 mM sodium phosphate, pH 7.5, 10% (v/v) D_2O in H_2O**. (B)** 1D-TOCSY experiment monitoring the spin transfer of the H2 proton of 5. The proton attached to C2 (*) was irradiated at 4.91 ppm. Spin transfer was observed with protons attached to C5 (yellow), C11 (sky blue), C8 (pink), C14 (peach), C6 (orange), C12 (blue) and C13 (purple). The spectrum was acquired using the same method as described in A. **(C)** ^{1}H-^{13}C HSQC (700 MHz) of VIM-2 catalysed crude faropenem products in D_2O for assigning the chemical shift of C2 carbon in 5. A chemical shift of 4.83 ppm for H2 and 64.18 ppm for the C2 carbon was observed. Note the sample analysed was a crude mixture of faropenem products arising from reaction of 280 nM VIM-2 with 5 mM faropenem in D_2O.

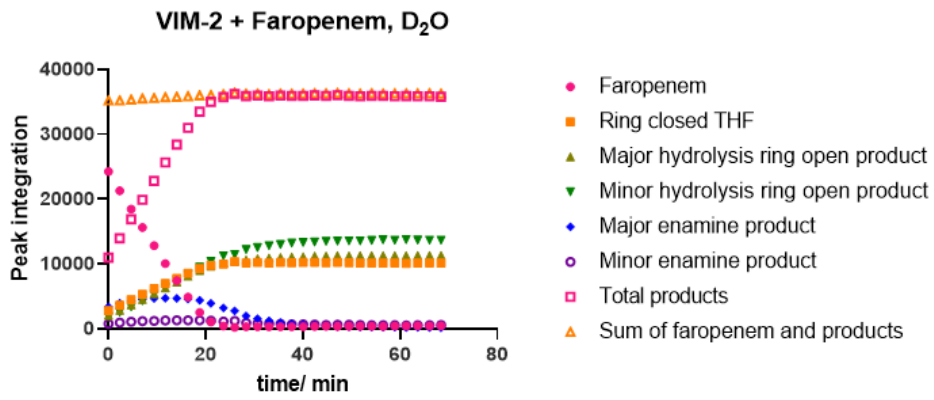


Figure S16: Faropenem (5 mM) turnover by VIM-2 (280 nM) giving rise to a THF ring closed hydrolysis product (orange square, **5**), a THF ring open major hydrolysis product yellow (green triangle, **3**), minor THF ring opened hydrolysis product (green triangle, **4**), major enamine product (blue diamond, **1**) and minor enamine product (purple open circle, **2**). The total amount of product at any time is shown in closed magenta circle and the total sum of faropenem and faropenem derived product in orange triangle. Experiment performed in 50 mM sodium phosphate, pH 7.5, D_2O. The peak corresponding to one of the methyl resonances for each chemical species was integrated, to measure the concentration of specific compounds.

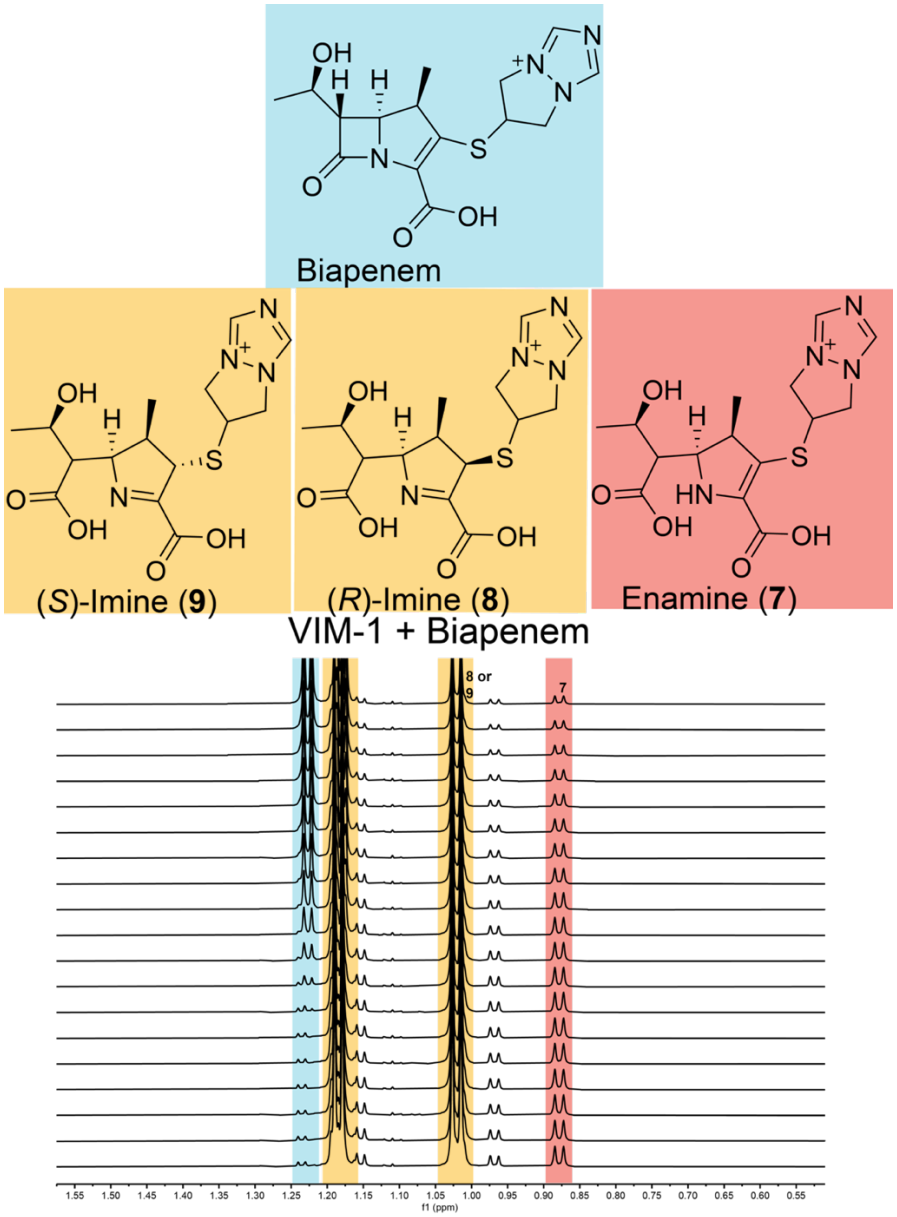


Figure S17*:* NMR spectrum of VIM-1: biapenem reaction time course spectra of the methyl group regions. The time course was measured using Bruker AVIIIHD 600 MHz. Biapenem (light blue) was treated with purified VIM-1 in 50 mM sodium phosphate pH 7.5. Both imine (**8** and **9**) and enamine (**7**) products were observed (orange and purple, respectively). Note the presence of unassigned products at 0.97 and 1.15 ppm. Spectra are stacked with earliest time point on top and last time point bottom.

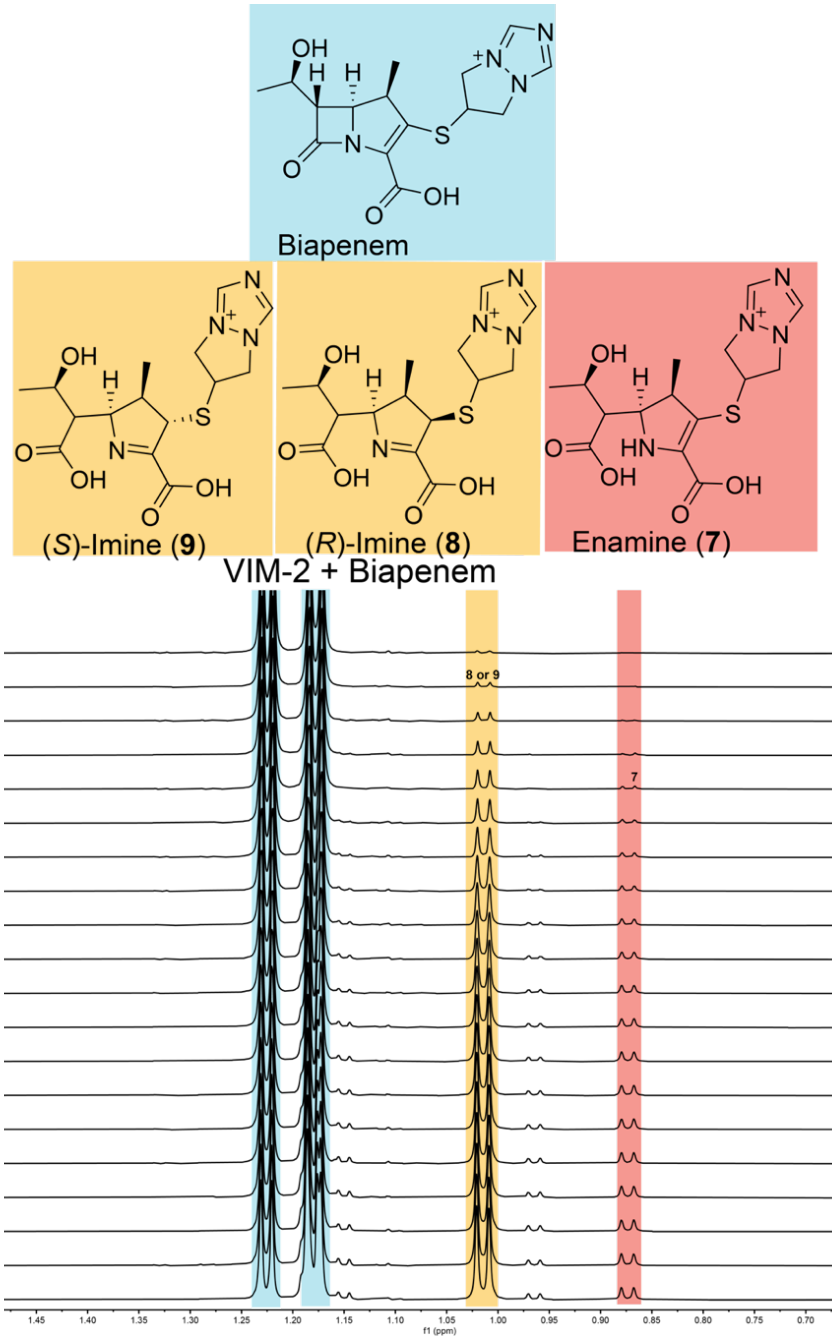


Figure S18*:* NMR spectrum of VIM-2: biapenem reaction time course spectra of the methyl group regions. The time course was measured using Bruker AVIIIHD 600 MHz. Biapenem (light blue) was treated with purified VIM-2 in 50 mM sodium phosphate pH 7.5. Both imine (**8** and **9**) and enamine (**7**) products were observed (orange and purple respectively). Note the presence of unassigned products at 0.97 and 1.15 ppm. Spectra are stacked with earliest time point on top and last time point bottom.

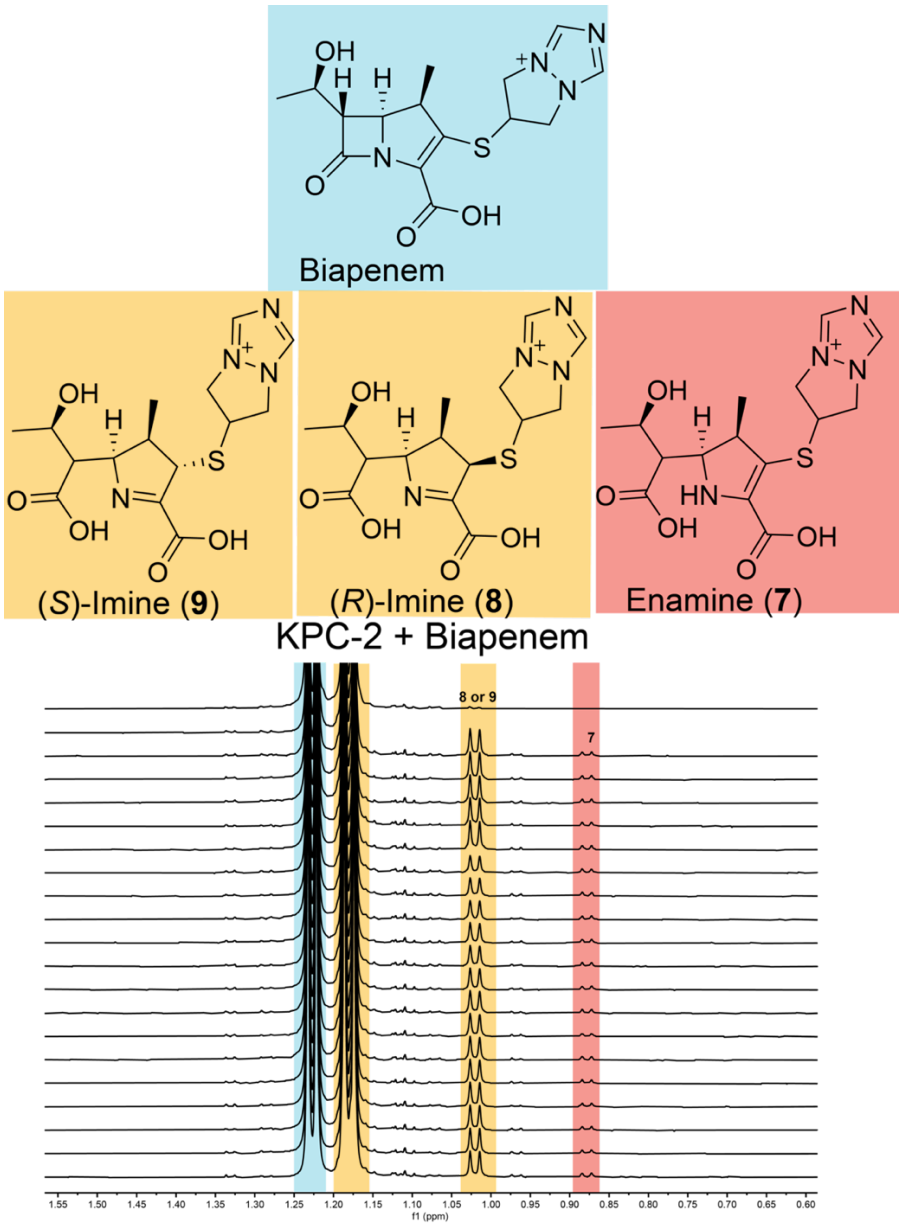


Figure S19: NMR spectrum of VIM-2: biapenem reaction time course spectra of the methyl group regions. Time course was measured using Bruker AVIIIHD 600 MHz. Biapenem (light blue) was treated with purified VIM-2 in 50 mM sodium phosphate pH 7.5. Both imine (**8** and **9**) and enamine (**7**) products were observed (orange and purple respectively). Note the presence of unassigned products at 0.97 and 1.15 ppm. Spectra are stacked with earliest time point on top and last time point bottom.